Lattice Models of Nucleation from Solution

by

Yuri Lifanov

Thesis

Submitted to the University of Warwick

for the degree of

Doctor of Philosophy in

Physics and Complexity Science

Department of Physics and Centre for Complexity Science

THE UNIVERSITY OF
WARWICK

February 2017

CONTENTS

List of Figures viii

List of Tables xi

Acknowledgements xii

Declaration xiii

Abstract xiv

List of Abbreviations xv

List of Symbols xvii

1 INTRODUCTION 1

- 1.1 Overview of the Work 2

2 THEORETICAL BACKGROUND 3

- 2.1 Equilibrium Statistical Mechanics 3
  - 2.1.1 State Space 4
  - 2.1.2 Dynamics 4
  - 2.1.3 Microscopic Quantities 5
  - 2.1.4 Entropy and Macroscopic Quantities 6
- 2.2 Markov Chain Monte Carlo 7
  - 2.2.1 Stochastic Dynamics 7
  - 2.2.2 Detailed Balance 8
  - 2.2.3 Random Site Update 8
  - 2.2.4 Important Properties 9
  - 2.2.5 Kinetic Monte Carlo 11
  - 2.2.6 Constant Jump Rate Kinetics 13
- 2.3 Phase Transitions 14
  - 2.3.1 Classification 14
  - 2.3.2 Coexistence and Metastability 15
  - 2.3.3 Landau Theory 16
  - 2.3.4 Coarse-graining via Order Parameter 16
  - 2.3.5 Theories of Reaction Kinetics 18
- 2.4 Nucleation Theory 22
  - 2.4.1 Homogeneous Nucleation Rate 22
  - 2.4.2 Droplet Free Energy 23
  - 2.4.3 Cluster Size as Order Parameter and Reaction Coordinate 25
  - 2.4.4 Limitations of the Classical Theory 25

3 RECENT DEVELOPMENTS 27

- 3.1 Nucleation in Atomistic and Molecular Models 27
  - 3.1.1 Selected Systems 27
  - 3.1.2 Overview of Methodology for Studies of Nucleation Kinetics 28
  - 3.1.3 Quantitative Comparison of Simulation and Experiment . . . 30
  - 3.1.4 Quantitative Comparison of Simulation and Theory 31
  - 3.1.5 Nonclassical Nucleation 32
- 3.2 Nucleation in Lattice Models 34
  - 3.2.1 The Ising Model 34
  - 3.2.2 Microscopic Kinetics 35
  - 3.2.3 Homogeneous Nucleation in Ising Models 36
  - 3.2.4 The Potts Model 37
  - 3.2.5 The Potts Lattice Gas Model 39
  - 3.2.6 Other Models 41
  - 3.2.7 Heterogeneous Nucleation 41

4 MODEL AND PHASE BEHAVIOUR 43
- 4.1 The Extended Potts Lattice Gas Model 43
  - 4.1.1 Particle Interactions 43
  - 4.1.2 The Hamiltonian 44
  - 4.1.3 Monte Carlo Move Sets 45
  - 4.1.4 Low Temperature Equilibrium States 45
- 4.2 Coexistence Point Calculations 45
  - 4.2.1 Flat Histogram Method 46
  - 4.2.2 Histogram Reweighting 47
  - 4.2.3 Validation for Ising-like Lattice Gas 48
- 4.3 Approximate Coexistence Points 49
  - 4.3.1 Mean Field Solute Phase Coexistence points 50
  - 4.3.2 Solvent-Solute Coexistence in the Extended PLG 51
- 4.4 Phase Diagrams 53
  - 4.4.1 Solute Fugacity and Concentration 53
  - 4.4.2 Low Temperature Metastability of Disordered States 54

5 EQUILIBRIUM CLUSTER DISTRIBUTIONS 55
- 5.1 Order Parameters 55
- 5.2 Enhanced Sampling Method 56
  - 5.2.1 Equilibrium Path Sampling 57
  - 5.2.2 Recovering Marginal Distributions 58
  - 5.2.3 Validation 59
- 5.3 Equilibrium Cluster Distributions in the Extended PLG 61
  - 5.3.1 Cluster Size Distributions 61
  - 5.3.2 Equilibrium Internal Orientational Order of Nuclei 63
- 5.4 Sampling Equilibrium Cluster Configurations 66

5.4.1 Constrained Cluster Size Ensemble 66
5.4.2 Committor Distributions 68
5.5 Chapter Summary 70
6 SEEDING METHOD 72
6.1 Langevin Equation for the Reaction Coordinate 73
6.1.1 Estimators and Their Properties 73
6.1.2 Drifts, Diffusion Coefficients and Escape Rates 74
6.2 Seeding Method In the Context of CNT 76
6.2.1 Estimation of Drifts and Diffusivities along the Cluster Size Coordinate 77
6.2.2 Fitting of a CNT model 79
6.2.3 Quotient of Noncentral Normal Variates 80
6.3 Nucleation Barrier Reconstruction 81
6.3.1 Nucleation Rate Estimates 83
7 EXPLICIT RATE CALCULATIONS 86
7.1 Irreducible Markov Chains 86
7.1.1 The Fundamental Matrix 87
7.1.2 Mean First Passage Times 87
7.1.3 Absorption Probabilities 88
7.1.4 General Applicability 88
7.2 Transition Path Theory 88
7.2.1 Rate and Effective Reactive Current 88
7.2.2 Paths, Hitting Times and Committors 89
7.2.3 Escape Rates and Quasi-equilibrium 91
7.2.4 Application to the Ising Model 91
7.3 Rare Event Methods 95
7.3.1 Connection to Transition Path Theory 95
7.3.2 Distinctions between Sampling Strategies 97
7.3.3 Application to the Ising Model 98
7.4 Modelling Open System Kinetics 101
7.4.1 Random Walker on $\mathbb{Z}^d$ 101
7.4.2 Density Autocorrelation Function 102
7.4.3 Implications for Modelling 103
7.5 Explicit Rates for the Extended PLG 103
7.5.1 Validation at High Solute Concentration 104
7.5.2 Estimates at Lower Solute Concentrations 105
7.6 Chapter Summary 107
8 SUMMARY AND CONCLUSIONS 109
8.1 Summary and Discussion of Key Findings 109

8.2 Conclusions 112
8.3 Future Work 112

LIST OF FIGURES

2.1 Visualisations of system states for the Ising model in $d \in \{2, 3\}$ dimensions, illustrating the site indexing scheme for a cubic lattice. 5
2.2 Sample and analytical spin autocorrelation sequences for whole and thinned spin value time series. 11
3.1 Schematic phase diagram and typical configurations of the two low temperature equilibrium states of the Ising model. 35
3.2 Schematic phase diagram and typical configurations of the two equilibrium states of the Potts model. 39
3.3 Schematic phase diagram and configurations of nuclei in coexistence with solvent in the Potts lattice gas model. 40
4.1 Visualisation of a cubic lattice cell showing site nearest and diagonal neighbour positions. 44
4.2 Visualisations of the bulk structures of the three solute rich states in the extended Potts lattice gas model. 46
4.3 Validation of the flat histogram sampling method for an Ising-like lattice gas model. 50
4.4 Comparison of numerically computed solute phase coexistence points with those obtained via mean field theory for the extended Potts lattice gas model. 51
4.5 Comparison of numerically computed solute-solvent coexistence points with those obtained via an approximate analytical treatment of the extended Potts lattice gas model. 52
4.6 Phase diagrams for the extended Potts lattice gas model. 53
4.7 Plots of solute concentration against solute fugacity and solute-solvent chemical potential difference. 54
5.1 Visualisations of small solute nuclei of varying degree of internal structural order, showing the corresponding values of the cluster orientational order parameter. 56
5.2 Validation of the path based enhanced sampling method using the Potts lattice gas model of Duff and Peters. 60
5.3 Comparison of the weighted histogram analysis and the least squares methods for free energy landscape reconstruction. 60
5.4 Free energy barriers as functions of the largest solute cluster size coordinate for the extended Potts lattice gas model. 61

5.5 Fitted parameters of the classical nucleation theoretic droplet model and heights of free energy barriers to nucleation in the extended Potts lattice gas model. 62
5.6 Size dependence of preferred nuclei internal orientational order. 63
5.7 Distributions of internal orientational order parameter for critical nuclei. 64
5.8 Free energy barriers to nucleation of the three solute structures. 65
5.9 Distributions of orientational order parameter for the extended Potts lattice gas model on small cubic lattices. 67
5.10 Short time and long time cluster configurations as generated by the constrained cluster size Monte Carlo algorithm. 68
5.11 Distributions of nuclei internal orientational order parameter sampled under the constrained cluster size Monte Carlo scheme. 69
5.12 Estimates of committor distributions for configurations of critical nuclei sampled via the constrained cluster size Monte Carlo scheme. . . . 70
6.1 Probability densities of the diffusivity estimator for a coordinate evolving according to Brownian dynamics. 74
6.2 Mean displacements and squared deviations from the mean for short trajectories of Brownian motion in a bistable potential. 75
6.3 Averages of drift and diffusivity estimators, and escape rates for trajectories of Brownian motion in a bistable potential. 76
6.4 Short time average trajectories and mean displacements along the largest cluster size coordinate in seeded simulations of the extended Potts lattice gas model. 78
6.5 Estimation of diffusivity of the largest solute cluster size coordinate from seeded simulations of the extended Potts lattice gas model. 79
6.6 Distributions of the quotient of noncentral normal variates. 80
6.7 Fits of the classical nucleation theoretic droplet model to the data obtained from seeded simulations of the extended Potts lattice gas model. 82
6.8 Comparison of free energy barrier height estimates obtained via the "seeding" method to those based on explicit free energy calculations. . 83
6.9 Comparison of nucleation rate estimates obtained via the "seeding" method to those obtained via the Auer and Frenkel approach. 84
7.1 Validation of the jump matrix for the 3 × 3 Ising model. 92
7.2 Averages and probability density distributions of metastable state escape times in the 3 × 3 Ising model. 93
7.3 Committor, mean first passage time and rate values for the 3 × 3 Ising model as given by Markov chain and transition path theories. 94
7.4 Probability densities of first passage times in the 3 × 3 Ising model in regimes of low and high free energy barriers. 94

7.5 Monte Carlo estimates of transition probabilities in collective variable space for the 3×3 Ising model compared to values given by transition path theory. 100
7.6 Comparison of nucleation rate estimates given by three distinct rare event Monte Carlo schemes to values given by transition path theory in the 3×3 Ising model. 101
7.7 Particle density autocorrelation functions for $d \in \{1, 3\}$ open systems of random walkers. 103
7.8 First passage time distribution and cumulative product of transition probabilities in the collective variable space for the extended Potts lattice gas model at high supersaturation. 105
7.9 Visualisations of typical solute nuclei configurations sampled by the rare event scheme used for calculation of nucleation rates in the extended Potts lattice gas model. 106
7.10 Cumulative products of transition probabilities in the collective variable space as sampled by the rare event scheme applied to the extended Potts lattice gas model. 107
7.11 Comparison of the explicitly computed values of approximate nucleation rates to those obtained via the approach of Auer and Frenkel. . . 108

LIST OF TABLES

3.1 Listing of studies quantitatively comparing the nucleation rate estimation approach of Auer and Frenkel with other rate calculation methods. 31
3.2 Listing of studies quantitatively comparing the classical nucleation theoretic form of free energy barriers with explicit free energy calculations. 33
4.1 Listing of the stationary states in the extended Potts lattice gas model at low temperatures. 46

ACKNOWLEDGEMENTS

I am very thankful to the Engineering and Physical Sciences Research Council (grant No. EP/E501311/1) and the Complexity Doctoral Traning Centre (DTC) (now Mathematics for Real-World Systems Centre for Doctoral Training) for providing the opportunity to carry out this project. I would also like to thank the members of the Complexity DTC staff, in particular Heather Robson and Deborah Walker, for the incredible administrational and academic effort in maintaining the DTC.

Without the guidance of my academic supervisors this project would not be possible and I am grateful to David Quigley, Bart Vorselaars and Stefan Grosskinsky for their continued support and patience.

I also greatly appreciate the help and advice I have received from my friends and colleagues, and I would like to thank, in particular, Ellen Webborn, Michael Maitland, Sara Jennings, Kirstyleigh Kendall, James Kendall, Gladys Ng'weno, Miriam Zehnter and Jasmin Rückert for sharing their perspective, words of encouragement and solidarity.

I am fortunate to have a very caring and understanding family: Svetlana Kletsova, Ksenya Kletsova and Lyubov Lifanova, who have, on countless occasions, given me the energy to stay optimistic and focused.

I am extremely grateful to Tatiana Nicholson for believing in my abilities and motivating me to seek challenge while, at the same time, giving me a sense of security and hope.

I am profoundly thankful to Carina Karner for her wisdom, kindness and academic insight, and, above all, for constantly challenging me on a personal and intellectual level.

DECLARATION

This thesis is submitted to the University of Warwick in support of the author's application for the degree of Doctor of Philosophy. It has been composed solely by the author and has not been submitted in any previous application for any degree. Portions of the material presented in Chapters 4, 5 and 6 appear in the following publication: "Y. Lifanov, B. Vorselaars, and D. Quigley. Nucleation barrier reconstruction via the seeding method in a lattice model with competing nucleation pathways. *J. Chem. Phys.*, 145(21):211912, 2016"

ABSTRACT

In this work we consider nucleation in existing and novel lattice models of particles in solution, reviewing, testing and applying the modern methodology for free energy calculation and calculation of nucleation rates based on elements of classical nucleation, reaction rate and transition path theories. We introduce a multi-component lattice model where, at low temperatures, the solute phase can form three distinct solid structures, for which we accurately map the phase diagram, discussing the relevance of the model to the study of nucleation of polymorphic minerals. By analysing multi-dimensional free energy profiles, computed via a path sampling based Monte Carlo protocol, we demonstrate that solute precipitation in the developed model can proceed via nonclassical pathways, where the formation of nuclei of unstable solute phases is followed by their transformation into the thermodynamically preferred structure. Despite the existence of nonclassical nucleation pathways, we show that the conceptual framework of classical nucleation theory provides an adequate quantitative treatment of the nucleation process in our model over a broad range of parameter space.

LIST OF ABBREVIATIONS

ACF	Autocorrelation Function
CNT	Classical Nucleation Theory
DR	Diffusion-Reorientation
EPS	Equilibrium Path Sampling
EQSM	Equilibrium Statistical Mechanics
FES	Free Energy Surface
FFS	Forward Flux Sampling
FPT	First Passage Time
HS	Hard Sphere
LD	Langevin Dynamics
LJ	Lennard-Jones
LSQ	Least Squares
MCMC	Markov Chain Monte Carlo
MCS	Monte Carlo Sweep
MC	Monte Carlo
MD	Molecular Dynamics
MFPT	Mean First Passage Time
PLG	Potts Lattice Gas
PPTIS	Partial Path Transition Interface Sampling
RC	Reaction Coordinate
TIS	Transition Interface Sampling
TPS	Transition Path Sampling
TPT	Transition Path Theory

TR	Transmutation-Reorientation
TST	Transition State Theory
US	Umbrella Sampling
WHAM	Weighted Histogram Analysis Method
WLS	Wang–Landau Sampling
fcc	face-centred cubic
kMC	Kinetic Monte Carlo
rhcp	random hexagonal close-packed

LIST OF SYMBOLS

$\lvert . \rvert$	Cardinality of a set
$. \setminus .$	Set relative complement (set-theoretic difference)
$\delta_{.,.}$	Kronecker delta function
$\delta(.)$	Dirac delta function
$\langle . \rangle$, $\mathbb{E}[.]$	Ensemble average of a microscopic quantity
k_B	Boltzmann constant
$T \in \mathbb{R}$	Temperature
$\beta = (k_B T)^{-1}$	Thermodynamic beta (inverse temperature)
Λ	Configuration space of a particle system
$A \subset \Lambda$	Reactant or metastable state of a particle system
$B \subset \Lambda$	Product or thermodynamically preferred state of a particle system
$\sigma \in \Lambda$	Configuration of a particle system
$\sigma(t) \in \Lambda$	Continuous time trajectory of a particle system through its configuration space; continuous time jump process on Λ
$\sigma_m, \sigma(m) \in \Lambda$	Discrete time trajectory of a particle system through its configuration space; discrete time jump process on Λ
$d \in \{1, 2, 3\}$	Dimension of a particle system
$N \in \mathbb{N}$	Number of lattice sites
$s_i \in \mathbb{Z}$	Spin value or species label of lattice site $i \in \{0, \dots, N-1\}$
$Q \in \mathbb{N}$	Number of possible discrete orientations of an anisotropic particle in a lattice gas model
$q_i \in \{1, \dots, Q\}$	Spin value or orientation label of lattice site $i \in \{0, \dots, N-1\}$
$\vec{l} \in \mathbb{R}^d$	Dimensions of a d-dimensional hyperrectangular particle system

$l \in \mathbb{R}$	Linear dimension of a d-dimensional hypercubic particle system
$E(\sigma) \in \mathbb{R}$	Energy of a particle system in configuration σ
$\mathcal{K} \in \mathbb{N}$	Number of chemical components in a multi-component particle system
$\vec{\mu} \in \mathbb{R}^{\mathcal{K}}$	Vector of reservoir chemical potential values for a particle system with $\mathcal{K}$ chemical components
$\mu_k \in \mathbb{R}$	Reservoir chemical potential of particle species $k \in \{1, \ldots, \mathcal{K}\}$
$\Delta\mu \in \mathbb{R}$	Difference between chemical potentials of solute and solvent particle reservoirs
$f \in (0, \infty)$	Solute fugacity: $f = \exp[\beta\Delta\mu]$
$f_* \in (0, \infty)$	Solute fugacity at solute-solvent coexistence
$\Delta\mu_{\text{coex}} \in \mathbb{R}$	Difference between chemical potentials of solute and solvent
$\rho \in [0, 1]$	Particle density or solute concentration
$N_k(\sigma) \in \mathbb{N}$	Number of particles of species $k \in \{1, \ldots, \mathcal{K}\}$ in configuration σ of a particle system
$N_s(\sigma) \in \mathbb{N}$	Number of solute particles in configuration σ of a particle system
$\mathcal{S}(\beta, \vec{\mu}) \in [0, \infty)$	Entropy of a multi-component particle system at point $(\beta, \vec{\mu})$ of the parameter space
$H(\sigma\|\vec{\mu}) \in \mathbb{R}$	Value of the Hamiltonian of a particle system in configuration σ, given reservoir chemical potentials $\vec{\mu}$
$Z(\beta, \vec{\mu}) \in \mathbb{R}$	Value of the partition function of a multi-component particle system at point $(\beta, \vec{\mu})$ of the parameter space
$\mathcal{F}(\beta, \vec{\mu}) \in \mathbb{R}$	Value of the thermodynamic free energy of a multi-component particle system at point $(\beta, \vec{\mu})$ of the parameter space
$r(\sigma) \in [0, \infty)$	Jump rate at microstate σ for a continuous time Markov process $\sigma(t)$
$R \in [0, \infty)$	Jump rate for a continuous time Markov process $\sigma(t) : r(\sigma) = R \, \forall \sigma \in \Lambda$

$F(\lambda) \in \mathbb{R}$	Free energy as a function of parameter λ: $F(\lambda) = -k_B T \ln \mathbb{P}(\lambda)$
$n \in \mathbb{N}$	Number of particles in a nucleus or a solute particle cluster in a particle system
$n(\sigma) \in \mathbb{N}$	Size of the largest particle cluster or solute particle cluster in a particle system in configuration σ
$n(t) \in \mathbb{N}$	Continuous time trajectory of the largest particle cluster size coordinate; continuous time process $n(t) = n[\sigma(t)]$
$\Delta F(n) \in \mathbb{R}$	Height of the free energy barrier along the solute cluster size coordinate: $\Delta F(n) = F(n) - F(1)$
$n^\dagger \in \mathbb{N}$	Value of the cluster size coordinate at the top of the barrier $\Delta F(n)$; $n^\dagger = \operatorname{argmax}_n\{\Delta F(n)\}$
$n^* \in \mathbb{N}$	Estimated value of the cluster size coordinate yielding the slowest variation (drift) in $\langle n(t) \vert n(0) = n^* \rangle$ with t
$J(A \to B) \in [0, \infty)$	Rate (probability per unit time) of transition of a particle system from initial metastable state A to thermodynamically preferred state B
$\Delta F_{\text{CNT}}(n) \in \mathbb{R}$	Free energy as a function of the cluster size coordinate in the CNT droplet model
$\gamma_{\text{CNT}} \in \mathbb{R}$	Surface term coefficient of the CNT droplet model
$\Delta\mu_{\text{CNT}} \in \mathbb{R}$	Volume term coefficient of the CNT droplet model
$n^*_{\text{CNT}} \in \mathbb{R}$	Critical nucleus size as defined by the CNT droplet model: $n^*_{\text{CNT}} = \operatorname{argmax}_n\{\Delta F_{\text{CNT}}(n)\}$
$J_{\text{CNT}} \in [0, \infty)$	Value of the nucleation rate as given by CNT
$c \in [0.5, 1]$	Solute anisotropic interaction strength parameter in the extended PLG model; $c = 1$ unless otherwise specified
$\Gamma(a, b)$	Gamma distribution with shape parameter a and scale parameter b
$\mathcal{N}(a, b)$	Normal distribution with mean a and variance b
$D_x \in [0, \infty)$	Diffusivity of a Brownian motion process $x(t)$: $D_x = \langle [x(t) - \langle x(t) \rangle]^2 \rangle / (2t)$

1

INTRODUCTION

Nucleation is one of the fundamental mechanisms governing the early stages of first order phase transitions, and the underlying microscopic process is understood as fluctuation-driven formation of microdomains of one phase within a macroscopic domain of another [1]. Due to the small length and time scales involved, at present, it is difficult to obtain detailed insight into the microscopic kinetics of nucleation phenomena empirically, yet such insight is crucial in numerous industrial applications [2]. Although significant progress in molecular and atomistic modelling of nucleation processes has been achieved over the recent years, open questions remain abundant even in the simplest model systems [3].

Much of the quantitative understanding of nucleation phenomena is provided by the phenomenological framework of Classical Nucleation Theory (CNT) [4], which employs a simple one-dimensional model in order to derive closed form expressions for the key quantities used for characterising the nucleation processes (Sec. 2.4). Despite introducing a considerable list of simplifying assumptions, the CNT approach for calculating nucleation rates appears to yield estimates in good agreement with those obtained via state of the art numerical methods. Thorough application of the advanced numerical methods for rate estimation, however, has, so far, only been attempted in relatively simple single component model systems.

The more complex particle systems, such as solutions of polymorphic minerals, e.g. calcium carbonate, are thought to exhibit a richer variety of microscopic dynamics which significantly complicate the expected nucleation mechanisms [5]. The associated phase transformation mechanisms typically fall into the category of nonclassical nucleation (Sec. 3.1.5), where the quantitative framework of CNT is thought to break down under the typical assumptions used in its application. Due to the difficulties and the computational expense of numerical modelling of multi-component systems, no quantitatively rigorous studies of nonclassical nucleation in molecular systems have been reported to date. Consequently, the interest in capturing nonclassical nucleation behaviours in computationally tractable models has spiked over the recent years, forming the core of the motivation for this work.

In the present study, we will develop and analyse a novel multi-component lattice model of anisotropic particles in solution, based largely on the combination of the well known Ising and Potts models as implemented in the Potts Lattice Gas (PLG) model of Duff and Peters [6]. Employing state of the art numerical methods, we will demonstrate the presence of nonclassical nucleation behaviours in the introduced model while providing evidence for Potts-like lattice models not being ideal candidates for modelling nonclassical nucleation pathways of polymorphic minerals. Based on results of our application of rare event and enhanced sampling methodology, we will also argue that the quantitative treatment of CNT can adequately describe the nucleation kinetics of the introduced model over a considerable range of parameter space. As an aside, we will provide detailed discussions of the employed numerical methodology as well as relevant issues in modelling of multi-component systems.

1.1 OVERVIEW OF THE WORK

We will start by briefly outlining the relevant to this study theoretical background and the recent literature in Chapters 2 and 3, covering the key aspects of statistical mechanics, Markov chain and reaction rate theories as well as discussing the current status of nucleation theory in the context of lattice models and molecular simulation.

We will then move on to the discussion of equilibrium properties of the extended PLG model. In Chapter 4 we will develop the model, discuss its phase behaviour and produce accurate estimates as well analytical expressions for the relevant phase coexistence lines. Applying a path based enhanced sampling protocol in Chapter 5, we will analyse the equilibrium structures of nuclei in our model, illustrating the potential nonclassical nucleation pathways.

In the second half of the study, we will focus on quantitative analysis of nucleation kinetics. Chapter 6 will be dedicated to application of the currently popular "seeding" method for nucleation rate estimation based, in part, on the analytical framework of CNT. The more rigorous rate calculation approaches will be discussed in Chapter 7, where we will provide explicit quantitative treatment of nucleation kinetics and discuss the results in the context of CNT.

Finally, in Chapter 8 will present the summary and the main conclusions of this work, outlining the potential future research directions.

2

THEORETICAL BACKGROUND

In this chapter we will give a brief overview of the core theory relevant to studies of phase behaviour and transitions in stochastic systems of interacting particles. A thorough critical review of the subject would require consideration of the underlying mathematical and philosophical constructs, which alone would span the entire volume of the thesis. We will therefore restrict ourselves to a relatively naive view of the more complex topics, e.g. dynamical systems and ergodic theory, referring to the more in-depth literature where possible. The key purpose of this chapter is to introduce the core concepts and notation.

2.1 EQUILIBRIUM STATISTICAL MECHANICS

The importance of statistical mechanics lies in its success at providing a microscopic basis for the theory of equilibrium thermodynamics [7]. Although the traditional definitions of equilibrium statistical mechanics (EQSM) may have limited use in the treatment of nonequilibrium phenomena, the theory does provide a convenient conceptual framework on which we will rely throughout the following sections and chapters.

The conception of statistical mechanics is commonly attributed to Maxwell, Boltzmann and Gibbs, who put forward different, largely intuitive, justifications for statistical treatment of molecular systems. The resultant analytical framework faced criticism as early as 1911 [8], particularly with respect to the "Ergodic hypothesis". Further mathematical study of the hypothesis arguably lead to the establishment of the field of ergodic theory, where the formal mathematical basis for EQSM is a subject of much ongoing research [9].

Despite the considerable volume of, so far, unresolved mathematical and philosophical criticisms [10–12], the theory of EQSM appears successful in explaining a wide range of physical phenomena. The traditional formulations, commonly used in statistical physics texts [7, 13–16], however, do little to highlight the underlying mathematical detail of EQSM. While such detail extends beyond the scope of this work, we will attempt to cite the important considerations, since our list of modelling assumptions begins here.

2.1.1 *State Space*

In an abstract sense, a model particle system can be defined by a state space Λ and a set of dynamical rules, expressed as a transformation $\mathcal{T} : \Lambda \to \Lambda$, which describe the system's time evolution. We use the notation $\mathcal{T} : \Lambda \to \Lambda$ to state that $\mathcal{T}$ maps Λ on to itself, i.e. there exist $\sigma, \sigma' \in \Lambda$ such that $\sigma' = \mathcal{T}(\sigma)$. In classical systems under Hamiltonian or Langevin dynamics, the state space is typically taken as the set of all possible positions and momenta of some number N of particles in a 3 dimensional container – a subset of $\mathbb{R}^3$. In the case of overdamped Langevin dynamics and systems of Brownian particles, the momenta are treated as random and, hence, do not appear explicitly in Λ. In both cases, however, Λ is an uncountable set of system states. A crucial distinction of the lattice models presented in this work is that their state spaces are discrete and finite – a factor which significantly simplifies the necessary mathematical considerations.

We can consider a d dimensional particle system on a lattice as a collection of coordinates in $\mathbb{Z}^d$. However, for the majority of this work, we will focus on (hyper) rectangular systems with a finite number, N, of lattice sites (or finite volume, $V = N$). Therefore, for our purposes, a lattice is a finite subset of $\mathbb{Z}^d$ and each lattice site can be assigned a unique index, $i \in \{0, \ldots, N-1\}$. Given a set of integer valued lattice lengths, $(l_j > 0 : j \in \{1, \ldots, d\}, \prod_{j=1}^{d} l_j = N)$, the conversion between the site index, i, and its coordinate, $\vec{x} = (x_1, \ldots, x_d), x_j \in \{0, \ldots, l_j - 1\}$, can be achieved through:

$$i = x_1 + \sum_{j=2}^{d} x_j \prod_{k=1}^{j-1} l_k, \quad x_j = \left\lfloor \frac{i}{\prod_{k=1}^{j-1} l_k} \right\rfloor \bmod l_j, \tag{2.1}$$

where $\lfloor A \rfloor$ is the integral (whole) part of A, and $A \bmod B = A - B\lfloor A/B \rfloor$ (Fig. 2.1c).

Typically, each lattice site, i, possesses a state, s_i, which may have one, e.g., $s_i \in \{-1, 1\}$ as in the Ising model, or multiple degrees of freedom. A collection, $\sigma = (s_0, \ldots, s_{N-1})$, of the N site states, fully specifies the microstate of the system. The state space of the system, $\Lambda = \{\sigma\}$, is then the set of all of its possible microstates. In our discussion of multicomponent systems of anisotropic particles, we will extend the state space to accommodate particles' identities and model their orientational degrees of freedom.

2.1.2 *Dynamics*

With the abstract notation $(\Lambda, \mathcal{T})$, the time evolution of the system, $\sigma_t \in \Lambda$, from some initial microstate $\sigma_0 \in \Lambda$, can be expressed as: $\sigma_t = \mathcal{T}(\ldots \mathcal{T}(\sigma_0) \ldots) = \mathcal{T}^t(\sigma_0)$. It is worth pointing out that such notation implies memorylessness of $\mathcal{T}$, since: $\sigma_t = \mathcal{T}(\sigma_{t-\delta t})$, i.e. the future state of the system depends only on its current

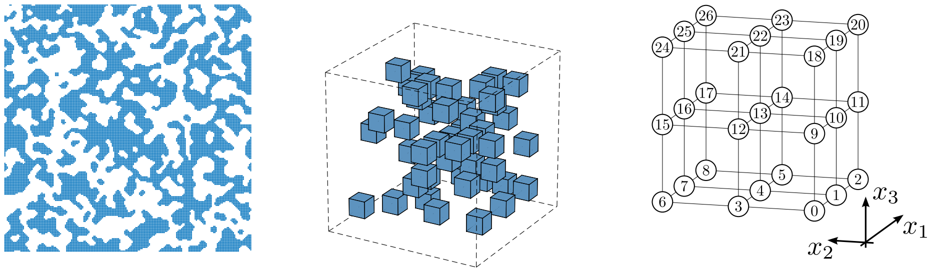

(a) Ising model ($d = 2$). **(b)** Ising model ($d = 3$). **(c)** Site indexing scheme.

Figure 2.1: Examples of visualisations of system states for the Ising model in $d = 2$ (a) and $d = 3$ (b) dimensions on, respectively, $\vec{l} = (128, 128)$ and $\vec{l} = (6, 6, 6)$ lattices, illustrating the site indexing scheme for $d = 3$ lattice with $\vec{l} = (3, 3, 3)$ in (c). The configurations of the Ising model ($\sigma \in \{-1, 1\}^N$) are shown with $s = 1$ spins represented by blue dots (a) and blue cubes (b), omitting $s = -1$ spins. In (c), each lattice site is represented by a circle, labelled by an integer $i \in \{0, \dots, N-1\}$, $N = 3^3$ corresponding to the site index in accordance with (2.1).

state and not on its history. The framework of EQSM relies on the proposition that the macroscopic behaviour of the system, as $t \to \infty$, can be studied with the help of a unique time invariant probability measure $\mathbb{P}(\sigma)$. In the language of ergodic theory, such proposition can be justified based on certain properties of $\mathcal{T}$, notably [11]: 1) Measure preservation. 2) Ergodicity. 3) Mixing. Owing to plethora of analytical results [11, 17], such an approach does allow a rigorous mathematical formulation of EQSM. However, as every other school of thought in statistical mechanics [10–12], the ergodic theory formulation faces strong criticisms. For instance, a peculiar property of many systems which admit EQSM treatment is that they violate the conditions set out by the "Ergodicity Programme" [11], casting doubt on the explanatory power of ergodic theory with respect to EQSM [18].

In the case of Markov chains on finite discrete state spaces, e.g. the lattice models we will discuss in this work, conditions on $\mathcal{T}$ granting measure preservation, ergodicity and convergence are, as we will see, relatively clear [19]. In addition, mixing properties of finite lattice gas models have been established [20], which implies ergodicity and convergence properties for the general class of such models. It is important to note, however, that nonergodic lattice model dynamics are possible [21], particularly in spin glass systems [22] or under conditions of critical slowing down [23].

2.1.3 *Microscopic Quantities*

A microstate of the system is usually characterised by some lower dimensional projection of the kind: $\Lambda \to \mathbb{R}^k$. One example of such projection is the system's internal energy: $E : \Lambda \to \mathbb{R}$, which typically encodes the information describing particle interactions. The chemical composition of a multicomponent system, i.e.

a system containing particles of $\mathcal{K}$ distinct chemical species, is simply given by the corresponding particle counts: $N_k : \Lambda \to \mathbb{N},\ k \in \{1, \ldots, \mathcal{K}\}$. While the precise definitions of internal energy, $E(\sigma)$, and composition, $N_k(\sigma)$, for multicomponent systems can be largely a modelling choice, the microstate probabilities, $\mathbb{P}(\sigma) : \Lambda \to (0, 1)$, must be assigned in such a way as to satisfy the following conditions:

$$\begin{aligned} 1 &= \sum_{\sigma\in\Lambda} \mathbb{P}(\sigma), \\ \langle E\rangle = \mathbb{E}(E) &= \sum_{\sigma\in\Lambda} E(\sigma)\mathbb{P}(\sigma), \\ \langle N_k\rangle = \mathbb{E}(N_k) &= \sum_{\sigma\in\Lambda} N_k(\sigma)\mathbb{P}(\sigma), \end{aligned} \tag{2.2}$$

where $\langle E\rangle$ and $\langle N_k\rangle$ are the macroscopic averages of E and N_k respectively.

2.1.4 *Entropy and Macroscopic Quantities*

The formalism of ergodic theory can, in some cases, prove the existence and uniqueness of an ergodic probability measure $\mathbb{P}(\sigma)$, however no general criteria for construction of the measure arise. The principle of entropy maximisation serves as an additional constraint on $\mathbb{P}(\sigma)$, which happens to be sufficient to construct the unique measure.

If the microstate, σ, of the system is to be treated as a stochastic variable, the entropy, $\mathcal{S}$ of the system can be viewed as a measure of the uncertainty in the system's microstate. More specifically, entropy is a functional $\mathcal{S} : \mathbb{P} \to \mathbb{R}$ of the form:

$$\mathcal{S} = -k_B \sum_{\sigma\in\Lambda} \mathbb{P}(\sigma) \ln \mathbb{P}(\sigma). \tag{2.3}$$

Compelling arguments for the above definition exist [24, 25], although the mathematical connection between the given expression and the dynamics of particle systems is only partially understood [26]. A large body of empirical evidence, however, shows that dynamics of particle systems lead to equilibrium states which maximise the quantity $\mathcal{S}$ by adopting the Boltzmann distribution $\mathbb{P}(\sigma|\beta, \vec{\mu})$:

$$\mathbb{P}(\sigma|\beta, \vec{\mu}) = Z(\beta, \vec{\mu})^{-1} \exp\left[-\beta H(\sigma|\vec{\mu})\right], \quad Z(\beta, \vec{\mu}) = \sum_{\sigma\in\Lambda} \exp\left[-\beta H(\sigma|\vec{\mu})\right], \tag{2.4}$$

where $Z(\beta, \vec{\mu})$ is termed the partition sum (or function) and $H(\sigma|\vec{\mu})$ is the system's Hamiltonian:

$$H(\sigma|\vec{\mu}) = E(\sigma) - \sum_{k=1}^{\mathcal{K}} \mu_k N_k(\sigma). \tag{2.5}$$

In the language of the Gibbsian formulation of EQSM, the above expression corresponds to the distribution of the grand canonical (μVT) ensemble. We will later introduce the semigrand μVT and canonical (NVT) ensembles as particular subsets of the grand μVT ensemble. Quantities $\beta = (k_B T)^{-1}$ – the inverse temperature – and $(\mu_k,\ k \in \{1, \ldots, \mathcal{K}\})$ – the reservoir chemical potential of chemical species k – correspond to Langrange multipliers in the maximum entropy formulation of EQSM [25]. In the physical sense, these quantities dictate the equilibrium properties of the particle system, e.g. the average energy $\mathbb{E}[E|\beta, \vec{\mu}]$ and composition $\mathbb{E}[N_k|\beta, \vec{\mu}]$. It is straightforward to show that the thermodynamic information, characterising the equilibrium state of the particle system, is completely encoded in the quantity $Z(\beta, \vec{\mu})$.

2.2 MARKOV CHAIN MONTE CARLO

Direct computation of the partition sum is impractical even for the simplest and modestly sized lattice models, even if one exploits the symmetries of the system. In studies of nonequilibrium processes we often must consider the properties of sequences of the system's states, i.e. trajectories. Keeping in mind the already significant difficulty of obtaining thermodynamic information, it is clear that sufficient kinetic information cannot be obtained via direct enumeration of the possible trajectories.

Monte Carlo (MC) avoids the problem of microstate enumeration entirely. Central to the method is the idea of sampling the target distribution $\mathbb{P}(\sigma|\beta, \vec{\mu})$ by generating lattice configurations $\sigma \in \Lambda$ in their correct relative proportions as dictated by the target distribution. Although absolute quantities, such as the partition sum, remain unknown, the approach can still be used to estimate various thermodynamic quantities. The MC procedure is typically implemented as a Markov chain sampler, whose stationary distribution is exactly the MC target distribution – a property which is guaranteed by the balance conditions as discussed below.

2.2.1 *Stochastic Dynamics*

The dynamics of a Markov chain are defined by transition probabilities: $\mathbb{P}(\sigma \to \sigma') : \sum_{\sigma' \in \Lambda} \mathbb{P}(\sigma \to \sigma') = 1$, between members of the state space $\sigma, \sigma' \in \Lambda$. By Markov property, the transition probabilities are independent of the history of the chain and we make the additional assumption that the transition probabilities are time invariant.

For discrete systems, the time evolution can be expressed as a matrix equation: $\vec{p}_m = \vec{p}_{m-1}\boldsymbol{P}$, where, using some enumeration $i, j \in \{1, \ldots, |\Lambda|\}$ of the possible microstates, $P_{i,j} = \mathbb{P}(\sigma_i \to \sigma_j)$ is the matrix of transition probabilities and $p_m^{(i)}$ is the probability of finding the chain in state σ_i after m MC moves. Given some initial distribution of states $\vec{p}_0$, the state of the chain after m MC moves is characterised by: $\vec{p}_m = \vec{p}_0 \prod_{i=1}^{m} \boldsymbol{P} = \vec{p}_0 \boldsymbol{P}^m$. The chain is said to be irreducible if there exists an integer m for which all entries of $\boldsymbol{P}^m$ are greater than zero. If $P_{i,i} > 0\ \forall i \in \{1, \ldots, |\Lambda|\}$, the chain is also aperiodic, which, together with irreducibility, implies ergodicity and mixing properties with respect to the unique stationary measure: $\vec{p}^* = \vec{p}^* \boldsymbol{P}$. The mixing property dictates that any initial distribution $\vec{p}_0$ will approach the stationary distribution $\vec{p}^*$ under the action of $\boldsymbol{P}$ [19].

2.2.2 *Detailed Balance*

The stationary distribution can be expressed in terms of the transition probabilities $P_{i,j} = \mathbb{P}(\sigma_i \to \sigma_j)$ by solving the eigenvalue problem: $\vec{p}^* = \vec{p}^* \boldsymbol{P}$. More intuitively, the setting can be viewed in the form of a discrete master equation, noting that $p_m^{(i)} \sum_{j=1}^{|\Lambda|} P_{i,j} = p_m^{(i)}$:

$$p_{m+1}^{(i)} - p_m^{(i)} = \sum_{j=1}^{|\Lambda|} p_m^{(j)} P_{j,i} - \sum_{j=1}^{|\Lambda|} p_m^{(i)} P_{i,j}. \tag{2.6}$$

which, after substituting $\vec{p}_{m+1} = \vec{p}_m = \vec{p}^*$ and noting that the stationary distribution should correspond to the target distribution $\mathbb{P}(\sigma|\beta, \vec{\mu})$, leads to the global balance equation for the Markov Chain Monte Carlo (MCMC) sampler of the Boltzmann distribution:

$$\sum_{\sigma' \in \Lambda} \mathbb{P}(\sigma'|\beta, \vec{\mu}) \mathbb{P}(\sigma' \to \sigma) = \sum_{\sigma' \in \Lambda} \mathbb{P}(\sigma|\beta, \vec{\mu}) \mathbb{P}(\sigma \to \sigma'). \tag{2.7}$$

A reversible Markov chain is obtained by enforcing the detailed balance condition:

$$\mathbb{P}(\sigma'|\beta, \vec{\mu}) \mathbb{P}(\sigma' \to \sigma) = \mathbb{P}(\sigma|\beta, \vec{\mu}) \mathbb{P}(\sigma \to \sigma'), \quad \forall \sigma, \sigma' \in \Lambda, \tag{2.8}$$

which guarantees that the dynamics of the chain at equilibrium are statistically invariant under time reversal – a property useful for path sampling protocols.

2.2.3 *Random Site Update*

The microscopic dynamics of the model are specified by a set of local MC moves – a set of random lattice site updates. A random site i is chosen and its state s_i is altered to be s_i' with some probability $\mathbb{P}_{\text{gen}}(s_i \to s_i')$. Thus, from an initial lattice configuration σ a new configuration σ' is created with probability $\mathbb{P}_{\text{gen}}(\sigma \to \sigma') = \mathbb{P}_{\text{gen}}(s_i \to s_i')$. The MC move is accepted with probability $\mathbb{P}_{\text{acc}}(\sigma \to \sigma')$, hence:

$$\mathbb{P}(\sigma \to \sigma') = \mathbb{P}_{\text{acc}}(\sigma \to \sigma') \mathbb{P}_{\text{gen}}(\sigma \to \sigma'). \tag{2.9}$$

Since the target probability distribution is known up to the normalising constant, we can write the single site perturbation acceptance probability as:

$$\mathbb{P}_{\text{acc}}(\sigma \to \sigma') = \mathbb{P}_{\text{acc}}(\sigma' \to \sigma) \frac{\mathbb{P}_{\text{gen}}(\sigma' \to \sigma)}{\mathbb{P}_{\text{gen}}(\sigma \to \sigma')} \exp\left\{-\beta \left[H(\sigma'|\vec{\mu}) - H(\sigma|\vec{\mu})\right]\right\}. \tag{2.10}$$

For symmetric site perturbation probabilities $\mathbb{P}_{\text{gen}}(s_i \to s_i') = \mathbb{P}_{\text{gen}}(s_i' \to s_i)$, the common choices of $\mathbb{P}_{\text{acc}}(\sigma \to \sigma')$ are respectively the Metropolis and the Glauber functions:

$$\mathbb{P}_{\text{acc}}(\sigma \to \sigma') = \min\left\{1, e^{-\beta\Delta H}\right\} \text{ and } \mathbb{P}_{\text{acc}}(\sigma \to \sigma') = \left[1 + e^{-\beta\Delta H}\right]^{-1}, \qquad (2.11)$$

with the latter sometimes written as: $\left[1 - \tanh\left(\beta\Delta H/2\right)\right]/2$, where $\Delta H = H(\sigma'|\vec{\mu}) - H(\sigma|\vec{\mu})$ [27, 28]. While the Metropolis choice may be marginally more computationally efficient, unlike the Glauber choice, it could set $\mathbb{P}(\sigma \to \sigma) = 0\ \forall\sigma \in \Lambda$ at $\beta = 0$, thus breaking the aperiodicity property of the chain. Although this would complicate the mixing properties of the chain, the associated stochastic process would remain ergodic with respect to the Boltzmann distribution. In most discrete models (except the Ising model), however, the site perturbation is chosen at random from a discrete set of possibilities, thereby allowing a nonzero probability of leaving the state of the lattice unchanged and, hence, keeping the chain aperiodic.

2.2.4 *Important Properties*

Having established the microscopic transition probabilities, we can now discuss the statistical properties of the stochastic process σ_m. From the Markov property $\mathbb{P}(\sigma_m|\sigma_{m-1}, \ldots, \sigma_0) = \mathbb{P}(\sigma_m|\sigma_{m-1})$, it follows that the probability of any trajectory is given by:

$$\mathbb{P}(\sigma_m, \sigma_{m-1}, \ldots, \sigma_0) = \mathbb{P}(\sigma_0)\prod_{i=1}^{m}\mathbb{P}(\sigma_{i-1} \to \sigma_i), \qquad (2.12)$$

and the Chapman–Kolmogorov equation is satisfied:

$$\mathbb{P}(\sigma_{m-2} \to \sigma_m) = \sum_{\sigma_{m-1}\in\Lambda}\mathbb{P}(\sigma_{m-2} \to \sigma_{m-1})\mathbb{P}(\sigma_{m-1} \to \sigma_m). \qquad (2.13)$$

The ergodic theorem [19] for irreducible Markov chains asserts that for any function $g : \Lambda \to \mathbb{R}$:

$$\lim_{m\to\infty}\frac{1}{m}\sum_{i=1}^{m} g(\sigma_i) = \sum_{\sigma\in\Lambda} g(\sigma)\mathbb{P}(\sigma), \qquad (2.14)$$

and, in addition, the quantity $m^{-1}\sum_{i=1}^{m} g(\sigma_i)$ for large m can be shown to be a good estimator for the average $\langle g\rangle$ by the Central Limit theorem [7].

Convergence properties of the above quantities are related to the property of mixing. The mixing time of the Markov chain can be viewed as a lower bound on the number of MC steps necessary for the chain to approach its stationary distribution [19]. Away from criticality, mixing times for a broad class of lattice models are known to be $\mathcal{O}(N \ln N)$, where N is the number of lattice sites as before [20]. In practical settings, some initial portion of a sequence of MCMC observations is treated as the "burn-in" period, and is, therefore, discarded as it may not accurately represent the target distribution. The necessary duration of the "burn-in" period may be reduced by appropriately choosing the initial state of the Markov chain.

At equilibrium the system is well mixed and we are, sometimes, interested in obtaining uncorrelated samples from the Boltzmann distribution. A useful quantity for this purpose is the autocorrelation function:

$$\mathcal{R}_g(\tau) = \frac{\langle g(\sigma_m) g(\sigma_{m+\tau}) \rangle - \langle g(\sigma_m) \rangle^2}{\langle g^2(\sigma_m) \rangle - \langle g(\sigma_m) \rangle^2}. \tag{2.15}$$

Under typical conditions, the decay of $\mathcal{R}_g(\tau)$ is exponential. As an illustration, it is useful to consider the example of a simple lattice gas model under Glauber dynamics, i.e. $s_i \in \{0,1\}\ \forall i \in \{1,\dots,N\}$ and $\mathbb{P}(s_i \to s_i') = 0.5\ \forall s_i, s_i' \in \{0,1\}$. For $\beta = 0$ we can ignore the spin interactions and the equilibrium spin distribution is known: $\mathbb{P}(s) = 0.5\ \forall s \in \{0,1\}$. It is straightforward to show that the spin autocorrelation function is given by:

$$\mathcal{R}_s(\tau) = 4\mathbb{P}(s_i^{(m)} = 1, s_i^{(m+\tau)} = 1) - 1. \tag{2.16}$$

Making use of the Markov property and the Chapman–Kolmogorov equation, the joint probability can be written as:

$$\mathbb{P}(s_i^{(m)} = 1, s_i^{(m+\tau)} = 1) = \mathbb{P}(s_i^{(m)} = 1)\mathbb{P}(s_i^{(m)} \to s_i^{(m+\tau)} = 1) = \frac{1}{4}\left[1 + \left(1 - \frac{1}{N}\right)^{\tau}\right], \tag{2.17}$$

hence $\mathcal{R}_s(\tau) = \left(1 - N^{-1}\right)^{\tau} = \exp\left[\tau \ln\left(1 - N^{-1}\right)\right]$ (Fig. 2.2). A decay, $\exp(-\tau/\tau_r)$, of correlations is characterised by the relaxation time τ_r and correlation time τ_c, with one unit of time representing N MC moves [29]:

$$\tau_c = \int_0^{\infty} \mathcal{R}(\tau) d\tau = \int_0^{\infty} \exp(-\tau/\tau_r) d\tau = \tau_r. \tag{2.18}$$

In the above example, the correlation time τ_c scales approximately linearly with system size N. For finite temperatures ($\beta > 0$), the form of the autocorrelation function is not trivial and some parameter regimes give rise to extremely long correlation times $\tau_c/N \propto L^z$, where z is the dynamical critical exponent and L is the linear size of the system such that $N = L^d$ [30,31].

Sample independence becomes important when one is concerned with higher moments of observables computed on Λ. Standard estimators for such quantities become biased due to temporal correlations in the sample, and elimination of bias requires knowledge of the autocorrelation sequence [32] which is only available under certain conditions (e.g. $\beta = 0$). A common rule of thumb is to consider the sample autocorrelation in relation to that of a sample of white noise. For a white noise sequence of length u, the standard error on the autocorrelation sequence is approximated by:

$$\text{S.E.}\left[\mathcal{R}(\tau > 0)\right] \approx u^{-1/2}. \tag{2.19}$$

By keeping only every kth sample, such that $\mathcal{R}_s(k\tau > 0) < u^{-1/2}$, a thinned sample sequence is obtained, where temporal correlations are statistically indistinguishable from correlations in samples of white noise [32], and hence standard moment estimators approximately apply. Generally, however, the practice of thinning is discouraged as it is unnecessary for calculation of sample means and MC integration purposes, while sample variances and standard errors can be obtained from multiple independent MC runs [33].

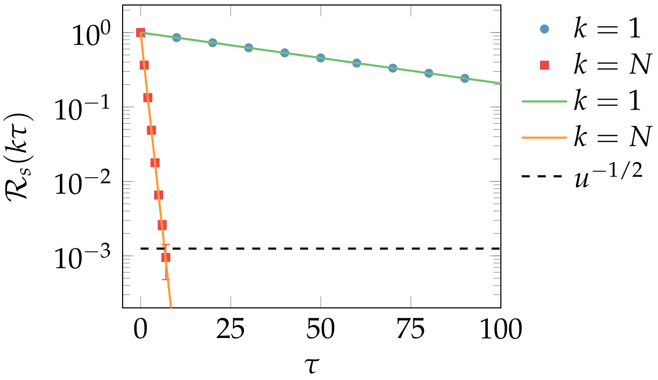

Figure 2.2: Sample ($N = 64$, $u = N \times 10^4$) and analytical spin autocorrelation sequences for whole and thinned time series $s_i^{(m)}$, in a lattice gas with $s_i \in \{0,1\}, \forall i \in \{1,\ldots,N\}$ and $\mathbb{P}(s_i \to s_i') = 0.5, \forall s_i, s_i' \in \{0,1\}$, where u is the length of the sample sequence for both thinned ($k = N$) and unthinned ($k = 1$) sequences. Solid lines are the plots of $\left(1 - N^{-1}\right)^{k\tau}$, while markers show the simulation data. The $u^{-1/2}$ threshold indicates the magnitude of the autocorrelation coefficient below which the correlations can be treated as insignificant, according to (2.19). Here, achieving the acceptable level of correlations requires thinning by roughly $k = 10N$, i.e. observations of $s_i^{(m)}$, obtained at time intervals equivalent to 10 lattice sweeps, can be treated as statistically independent.

2.2.5 *Kinetic Monte Carlo*

The primary motivation for use of kinetic Monte Carlo (kMC) is the need for continuous time modelling of physical processes. The continuous time stochastic process $\sigma(t)$, $t \in [0, \infty)$, $\sigma(0) = \sigma_0$ can be viewed as a sequence of states $\{\sigma_m\}$ accompanied by a sequence of arrival times $\{t_m \geq 0, t_0 = 0\}$, with transitions:

$$\begin{aligned}\mathbb{P}\left[\sigma(t_{m+1}) = \sigma_{m+1} | \{\sigma(t_m) = \sigma_m\}\right] &= \mathbb{P}\left[\sigma_{m+1}, t_{m+1} | \{\sigma_m, t_m\}\right] \\ &= \mathbb{P}\left[\sigma_{m+1} | \{\sigma_m, t_m\}\right] \mathbb{P}\left[t_{m+1} | \{\sigma_m, t_m\}\right],\end{aligned} \tag{2.20}$$

conditional on the histories of the process. Note that the arrival time t_{m+1} is independent of σ_{m+1}, since the time spent in σ_m must be independent of σ_{m+1}. The Markov property reads [34]:

$$\mathbb{P}\left[\sigma(t_{m+1}) = \sigma_{m+1} | \{\sigma(t_m) = \sigma_m\}\right] = \mathbb{P}\left[\sigma(t_{m+1}) = \sigma_{m+1} | \sigma(t_m) = \sigma_m\right], \tag{2.21}$$

implying Markov properties for both $\{\sigma_m\}$ and $\{t_m\}$:

$$\mathbb{P}\left[\sigma_{m+1} | \{\sigma_m, t_m\}\right] = \mathbb{P}\left[\sigma_{m+1} | \sigma_m, t_m\right], \quad \mathbb{P}\left[t_{m+1} | \{\sigma_m, t_m\}\right] = \mathbb{P}\left[t_{m+1} | \sigma_m, t_m\right]. \tag{2.22}$$

As before, we assume that the state transition probabilities are stationary with time, hence the Markov chain is homogeneous:

$$\mathbb{P}\left[\sigma(t + \Delta t) | \sigma(t)\right] = \mathbb{P}\left[\sigma(\Delta t) | \sigma(0)\right]. \tag{2.23}$$

From the Markov property for $\{t_m\}$ it follows that the residence times $h_{m+1} = t_{m+1} - t_m$ are independent, conditional on $\{\sigma_m\}$:

$$\mathbb{P}\left[t_{m+1} | \{\sigma_m, t_m\}\right] = \mathbb{P}\left[t_{m+1} | \sigma_m, t_m\right] = \mathbb{P}\left[h_{m+1} | \{\sigma_m, h_m\}\right] = \mathbb{P}\left[h_{m+1} | \sigma_m\right]. \tag{2.24}$$

We can consider the properties of $\mathbb{P}\left[h_{m+1} | \sigma_m\right]$ by evaluating the cumulative distribution:

$$\begin{aligned} \mathbb{P}\left[\sigma(t_m + a + b) = \sigma_m | \sigma(t_m + a) = \sigma_m, \sigma(t_m) = \sigma_m\right] \\ = \mathbb{P}\left[h_{m+1} > a + b | h_{m+1} > a, \sigma_m\right]. \end{aligned} \tag{2.25}$$

From (2.24) it is clear that the residence time h_{m+1} depends only on the current state of the system and not on the elapsed time a, hence we arrive at the memorylessness property for $\mathbb{P}\left[h_{m+1} | \sigma_m\right]$:

$$\mathbb{P}\left[h_{m+1} > a + b | h_{m+1} > a, \sigma_m\right] = \mathbb{P}\left[h_{m+1} > b | \sigma_m\right]. \tag{2.26}$$

It can be shown that the above property is only satisfied by the exponential distribution [34]: $\mathbb{P}\left[h | \sigma\right] = r(\sigma) \exp\left[-r(\sigma) h\right]$, with $r(\sigma) > 0$ being the rate at which the system leaves the state σ. It further follows that the jumping times between states $\sigma, \sigma' \in \Lambda$ are exponentially distributed with some rate $r(\sigma \to \sigma') \in [0, \infty)$, and, by examining the joint distribution of independent exponentially distributed variables, we see that:

$$r(\sigma) = \sum_{\sigma' \in \Lambda} r(\sigma \to \sigma'). \tag{2.27}$$

For technical reasons, it is useful to set $r(\sigma \to \sigma) = 0$ and define the continuous time process via the generator $\boldsymbol{Q} : Q_{i,j} = r(\sigma_i \to \sigma_j), Q_{i,i} = -r(\sigma_i)$, whose properties allow one to elegantly express the dynamics of the process [34]. For practical considerations, we will assume $r(\sigma \to \sigma) \geq 0$.

Intuitively, a transition from state σ to some other state σ' occurs if the event $\sigma \to \sigma'$ happens to trigger sooner than any other possible event $\sigma \to \sigma^{\dagger} \in \Lambda$ [35]. Applying the properties of the exponential distribution, we can, thus, relate the transition rates of the continuous time Markov chain to the jump probabilities of its embedded discrete time analogue [36]:

$$\mathbb{P}(\sigma \to \sigma') = r(\sigma \to \sigma') \Big/ r(\sigma). \tag{2.28}$$

Clearly, any choice of rates $\nu(\sigma \to \sigma') \propto \mathbb{P}(\sigma \to \sigma')$ yields the correct set of transition probabilities, hence a continuous Markov process is uniquely specified by either a set of transition rates $r(\sigma \to \sigma')$ or a set of transition probabilities $\mathbb{P}(\sigma \to \sigma')$ combined with the state escape rates $r(\sigma)$ [37].

Kinetic MC methods can be classified as standard (rejection, e.g. Metropolis) or rejection-free (e.g. BLK, Gillespie). In the standard construction, an event $\sigma \to \sigma'$ is selected uniformly on the set of possible events and accepted with probability $\mathbb{P}(\sigma \to \sigma')$, with the MC time variable being updated by a randomly drawn time increment $h : \mathbb{P}[h|\sigma] = r(\sigma) \exp[-r(\sigma)h]$, regardless of acceptance or rejection of σ'. The rejection-free approach is to, effectively, compute the probability distribution over the set of possible events and, thus, sample the event directly, incrementing the time variable by h [38]. The two classes of algorithms can be shown to be equivalent, in the sense that, given a set of rates $r(\sigma)$, both correctly model the physical time scale of the process [37].

2.2.6 *Constant Jump Rate Kinetics*

Computer simulations of general kMC models typically track the state σ of the system as well as the value of the stochastic time variable t to sample trajectories $\sigma(t)$. In this work we will only consider kMC models where the escape rates $r(\sigma)$ are equal to some constant R for all $\sigma \in \Lambda$, which implies that all time increments h_m, as defined above, are independent and identically distributed. Under these conditions, the stochastic time variable t_m, tracking the system's time after m MC updates (jumps), follows the gamma distribution $\Gamma(m, R^{-1})$, which converges to the normal distribution with the mean mR^{-1} for large m and any $R \in (0, \infty)$. Thus, for any long sequence $\{\sigma_m\}$ of observations of the system's microstate, the corresponding time values $\{t_m\}$ can be sampled independently and are represented sufficiently well by the averages $\langle t_m \rangle = mR^{-1}$. In this work, we, therefore, avoid tracking the values of t_m explicitly, using instead the standard time metric of MC sweeps (MCS): $t_m = mN^{-1}$, which associates one time unit with N Metropolis MC updates, thus tracking the stochastic process $\sigma(t)$ under the condition of $r(\sigma) = N$, $\forall \sigma \in \Lambda$.

2.3 PHASE TRANSITIONS

A thermodynamic phase of the system can be broadly defined as some subset $A \subseteq \Lambda$ of its state space, all elements of which share common physical properties, e.g. microscopic structure, composition or density. Any distinct phase $B \subset \Lambda : B \neq A$ must possess distinct physical characteristics to A and is, therefore, a set of microscopic configurations necessarily disjoint from A. Since any equilibrium state of the system corresponds to either one of the thermodynamically preferred phases or a phase coexistence regime, it follows that distinct equilibrium states possess distinct physical characteristics.

In the framework of thermodynamics, the equilibrium states of the system are distinguished based on the macroscopic quantities, e.g. the average internal energy $\langle E|\beta, \vec{\mu}\rangle$ and composition $\langle N_i|\beta, \vec{\mu}\rangle, i \in \{1, \ldots, \mathcal{K}\}$. One can, in theory, establish a complete picture of the phase behaviour of the system by evaluating the macroscopic averages at each point $(\beta, \vec{\mu})$ in the parameter space. Parameter points $(\beta^*, \vec{\mu}^*)$, at which at least one of the macroscopic quantities exhibits a discontinuity, correspond to points of abrupt change in the system's equilibrium state and are, therefore, phase transitions.

The focus of this work is primarily on the composition driven phase transitions in multicomponent mixtures, which correspond to $\vec{\mu}$ driven transitions in the μVT ensemble of model systems. The relevant microscopic processes are also studied in canonical (NVT) and isothermal–isobaric (NPT) ensembles [2], where the respective driving variables are the particle density ρ and the system's pressure P. While all three ensembles can be realised in lattice models, in the following discussion we will consider a system in the μVT ensemble for simplicity, although the theory we will cover can be applied to other statistical ensembles.

2.3.1 *Classification*

Thermodynamic quantities are typically related to derivatives of the free energy function $\mathcal{F}(\beta, \vec{\mu}) = -k_B T \ln Z(\beta, \vec{\mu}) = \langle H|\beta, \vec{\mu}\rangle - T\mathcal{S}(\beta, \vec{\mu})$. Modern classification of phase transitions recognises two broad categories [39]: 1) First-order – characterised by a discontinuities or divergences in first derivatives of $\mathcal{F}(\beta, \vec{\mu})$, and 2) Continuous – characterised by a discontinuities or divergences in second or higher order derivatives of $\mathcal{F}(\beta, \vec{\mu})$ with all first-order derivatives being continuous. It can be shown that, due to the functional form of $Z(\beta, \vec{\mu})$, discontinuities in the derivatives of $\mathcal{F}(\beta, \vec{\mu})$ occur only in the infinite system limit $N \to \infty$ [40], which makes the above treatment of phase transitions problematic from the practical point of view. The concept of "thermodynamic limit" $N \to \infty$ is currently a subject of academic debate [41] and arguments for existence of phase transitions in finite systems exist [42].

Although the underlying microscopic mechanisms of either class of phase transitions, in general, remain only partially understood, both classes appear to exhibit unique characteristics. So, for instance, continuous phase transitions are associated with phenomena of scale-invariance and divergence of correlation lengths, while metastability and hysteresis typically signal the onset of first-order phase transitions [43]. Nucleation and spinodal decomposition are thought to be the two major microscopic mechanisms of first-order phase transitions [44].

2.3.2 *Coexistence and Metastability*

At equilibrium, the likelihood of observing the system in phase A at the parameter point $(\beta, \vec{\mu})$ is simply given by the total equilibrium measure in A: $\mathbb{P}(\sigma \in A|\beta, \vec{\mu}) = \sum_{\sigma' \in A} \mathbb{P}(\sigma'|\beta, \vec{\mu})$. For a system comprising only two phases – A and B, the set of points $(\beta^*, \vec{\mu}^*)$:

$$\mathbb{P}(\sigma \in A|\beta^*, \vec{\mu}^*) = \mathbb{P}(\sigma \in B|\beta^*, \vec{\mu}^*), \tag{2.29}$$

forms the set of phase coexistence points. Due to finite size effects, the coordinates of coexistence points vary with system size and we typically estimate the true coexistence points by extrapolating to the $N \to \infty$ limit.

In some region of parameter space close to coexistence, with $\mathbb{P}(\sigma \in A|\beta, \vec{\mu}) < \mathbb{P}(\sigma \in B|\beta, \vec{\mu})$, phase A may persist despite it not being thermodynamically preferred. Such a scenario is termed a metastable equilibrium with A being the metastable state. Metastability often arises due to presence of high energetic or entropic barriers along the kinetic pathways to transformation of phase A to phase B. Such transformation, therefore, requires large, and hence improbable, thermal fluctuations – rare events. A commonly observed barrier crossing phase transition process is nucleation and growth, where microscopic droplets of a more thermodynamically stable phase, forming and vanishing due to thermal fluctuations, must exceed a certain critical size before continuing to grow [39].

Sufficiently far away from the coexistence point, the energetic barriers to transformation of A to B become negligible or vanish completely. Under such conditions, phase A is said to have reached or crossed its limit of metastability – the spinodal point, and the barrierless transformation to phase B proceeds via spinodal decomposition, whereby arbitrarily small domains of a more stable phase grow freely throughout the system [45].

Although nucleation and spinodal decomposition are two very distinct processes, the crossover from one microscopic transition mechanism to the other does not always occur sharply at the spinodal point [39, 45]. In addition, the limit of metastability of a phase is often dictated by the system's kinetics and not thermodynamics alone, making it difficult to define the spinodal point rigorously [46]. In this work, we will employ a purely heuristic view of the limit of metastability, corresponding to the parameter point at which the frequency and magnitude of fluctuations carrying the system away from the metastable state exceed certain arbitrarily specified thresholds, as, for instance, shown in Ref. [6].

2.3.3 *Landau Theory*

Much of the intuition behind the methodology of this work originates from Landau theory – a phenomenological treatment of phase transitions. Initially, the approach was applied to the study of continuous phase transitions, particularly critical phenomena, however, it has also proven useful in the context of first order phase transitions [39].

Central to Landau theory is the concept of the order parameter: $\lambda : \Lambda \to \mathbb{R}^k$ – some lower dimensional, often scalar, projection of the state space of the system. A well chosen order parameter quantifies the microscopic state of the system in such a fashion as to allow the various phases of the system to be quantitatively distinguished. The thermodynamics of a phase transition are modelled by assuming the functional form of the partition function to be:

$$Z(\beta, \vec{\mu}) = \exp\left[-\beta \mathcal{F}(\beta, \vec{\mu})\right] = \int_{\mathbb{R}^k} d\lambda \exp\left[-\beta F_{\mathrm{L}}(\lambda | \beta, \vec{\mu})\right], \tag{2.30}$$

in the vicinity of the phase transition, with $F_{\mathrm{L}}(\lambda | \beta, \vec{\mu})$ being the Landau free energy which is assumed to be a smooth function. Choosing λ to be a small valued quantity around the phase transition, one writes down a truncated Taylor expansion of the free energy in powers of λ, keeping only the terms of the expansion which are consistent with the symmetries of λ in the given system. The integral is assumed to be sharply peaked at the minima of $F_{\mathrm{L}}(\lambda | \beta, \vec{\mu})$, leading to an expression for $Z(\beta, \vec{\mu})$ in terms of the coefficients of the Taylor expansion of $F_{\mathrm{L}}(\lambda | \beta, \vec{\mu})$, whose $(\beta, \vec{\mu})$ dependence can be established empirically [13, 47, 48].

The analytical framework gives little insight into the kinetics of the phase transition process, but, despite its bold assumptions and poor predictive power, it does adequately illustrate the concepts of phase coexistence, metastability and spinodal point.

2.3.4 *Coarse-graining via Order Parameter*

The concept of order parameter is frequently employed in computational physics methodology for study of phase behaviour and kinetics of phase transitions in model particle systems. Instead of obtaining a phenomenological expression for the partition function, one typically estimates the probability distribution $\mathbb{P}(\lambda|\beta,\vec{\mu})$ of the order parameter:

$$\mathbb{P}(\lambda'|\beta,\vec{\mu}) = \sum_{\sigma\in\Lambda} \delta_{\lambda(\sigma),\lambda'} \mathbb{P}(\sigma|\beta,\vec{\mu}) = \frac{1}{Z(\beta,\vec{\mu})} \sum_{\sigma\in\Lambda} \delta_{\lambda(\sigma),\lambda'} \exp\left[-\beta H(\sigma|\vec{\mu})\right], \quad (2.31)$$

where $\delta_{\lambda(\sigma),\lambda'}$ is the Kronecker delta function which restricts the sum over state space to configurations yielding $\lambda(\sigma) = \lambda'$.

Certain choices of λ lead to straightforward expressions relating $\mathbb{P}(\lambda|\beta,\vec{\mu})$ to thermodynamic quantities. Using, for instance, the energy of the configuration as the order parameter, i.e. $\lambda(\sigma) = E(\sigma)$, in the canonical ($NVT$) ensemble, i.e. keeping the composition of the system fixed: $N_k = \text{const}\,\forall k \in \{1,\ldots,\mathcal{K}\}$, we obtain:

$$\mathbb{P}(E|\beta) = \frac{e^{-\beta E}}{Z(\beta)}\Omega(E),\ Z(\beta) = \int_{\mathbb{R}} dE\Omega(E)e^{-\beta E},\ \Omega(E') = \sum_{\sigma\in\Lambda} \delta_{E(\sigma),E'}. \quad (2.32)$$

where $\Omega(E)$ is termed the degeneracy of E, i.e. the density of states in energy. Noting that $\mathbb{P}(E|\beta=0) \propto \Omega(E)$ yields $Z(\beta) \propto \int_{\mathbb{R}} dE\mathbb{P}(E|0)e^{-\beta E}$, which provides a means of, for example, estimating the system's entropy $S(\beta)$ and heat capacity $\mathcal{C}(\beta)$:

$$S(\beta) = \frac{\partial}{\partial T}\left[k_B T \ln Z(\beta)\right], \quad \mathcal{C}(\beta) = \frac{1}{k_B T^2}\frac{\partial^2}{\partial \beta^2}\left[\ln Z(\beta)\right], \quad (2.33)$$

at all points along β based on the information about the system at infinite temperature $\beta = 0$. In fact, the probability distribution of a coupled quantity, in this case E, can be reweighted between any two finite parameter values (β, β') via:

$$\frac{\mathbb{P}(E|\beta)}{\mathbb{P}(E|\beta')} \propto \exp[-\Delta\beta E], \quad (2.34)$$

where $\Delta\beta = \beta - \beta'$. We will cover the practical approach to the reweighting property of the Boltzmann distribution in more detail in Chapter 4.

The coordinates of temperature driven phase transitions can be determined by locating discontinuities of $\mathcal{C}(\beta)$. While a similar approach can be formulated for other choices of $\lambda(\sigma)$, e.g. $\lambda(\sigma) = N_k(\sigma)$, in the case of arbitrary λ it may be more appropriate to study the system's phase behaviour by considering $\mathbb{P}(\lambda|\beta,\vec{\mu})$. Defining basins $\mathcal{A},\mathcal{B} \subset \mathbb{R}^k$ as portions of the order parameter space corresponding to phases A and B respectively, we can estimate the coexistence points $(\beta^*,\vec{\mu}^*)$ of A and B via:

$$\int_{\mathcal{A}} d\lambda\mathbb{P}(\lambda|\beta^*,\vec{\mu}^*) = \int_{\mathcal{B}} d\lambda\mathbb{P}(\lambda|\beta^*,\vec{\mu}^*), \quad (2.35)$$

assuming $\mathcal{A}$ and $\mathcal{B}$ are disjoint, in which case the above expression follows directly from (2.29). The task of defining order parameters satisfying $\mathcal{A}\cap\mathcal{B} = \emptyset$ poses significant difficulties for many model systems [49]. In addition, employing an order parameter as a coarse-grained description of the system is subject to various practical considerations, particularly in study of the system's kinetics, which we will discuss in detail.

2.3.5 *Theories of Reaction Kinetics*

The decay of the metastable state in a first-order phase transition is commonly modelled as an activated process, where the system undergoes an activation stage, i.e. fluctuation driven crossing of the energetic barrier (nucleation), followed by transformation stage (growth). If the duration of the activation stage is much shorter than the lifetime of the metastable state, i.e. activation occurs spontaneously, the activation process can be viewed as a rare event.

Under this condition of clear separation of timescales, the system has sufficient time to reachieve metastable equilibrium between subsequent unsuccessful activation "attempts". Thus, any given activation attempt retains no memory of the history of the system, and the equation (2.26) applies to the distribution of system's residence times $\tau_A = \tau_{\mathrm{fp}}$ in metastable state A, where τ_{fp} is the time of first arrival into the stable state B [50]. Hence, the distribution of first passage times τ_{fp} is Poissonian:

$$\mathbb{P}\left(\tau_{\mathrm{fp}}|\beta,\vec{\mu}\right) = J(A \to B|\beta,\vec{\mu}) \exp\left[-J(A \to B|\beta,\vec{\mu})\tau_{\mathrm{fp}}\right], \tag{2.36}$$

where $J(A \to B|\beta,\vec{\mu}) = \langle\tau_{\mathrm{fp}}\rangle^{-1}$, is the probability per unit time of occurrence of a transition from phase A to phase B.

The conceptual treatment of activated processes often resembles that of the theory of gas-phase and solution reaction kinetics, where the motion of the system through its configuration space during a chemical reaction is captured by a reactive pathway through the system's potential energy surface [51, 52]. While this energetics centred view remains useful for treatment of systems with small numbers of important degrees of freedom, the formalism of transition path theory (TPT) provides a more general and rigorous framework for treatment of activated processes [53]. Within TPT, the reaction process is represented by a kinetically and energetically informed statistical ensemble of the system's trajectories, which can be visualised as a complex set of reactive channels through the high dimensional configuration space of the system.

Under the assumptions of ergodic [Eq. (2.14)], Markov [Eq. (2.21)] and equilibrium (stationarity) properties of the system, TPT is readily applicable to the continuous time processes covered in section 2.2.5 [54]. In order to study the microscopic mechanism of the transition, TPT defines the backward and forward committor functions q^-_σ and q^+_σ for every $\sigma \in \Lambda$ as:

$$q^-_\sigma = \mathbb{P}[\tau^-_A(\sigma) < \tau^-_B(\sigma)], \quad q^+_\sigma = \mathbb{P}[\tau^+_A(\sigma) > \tau^+_B(\sigma)], \tag{2.37}$$

where $\tau^-_C(\sigma)$ and $\tau^+_C(\sigma)$ are, respectively, the first backward and forward hitting times of subset $C \subset \Lambda$ by the, respectively, backward and forward trajectories $\tilde{\sigma}(t) : \tilde{\sigma}(0) = \sigma$ and $\sigma(t) : \sigma(0) = \sigma$, defined as:

$$\tau^-_C(\sigma) = \inf\{t > 0 : \tilde{\sigma}(t) \in C\}, \quad \tau^+_C(\sigma) = \inf\{t > 0 : \sigma(t) \in C\}. \tag{2.38}$$

By the reversibility property [Eq. (2.8)], i.e. the statistical equivalence of $\sigma(t)$ and $\tilde{\sigma}(t)$, we can state that a generic trajectory $\sigma(t)$, passing through the state σ at some time t', has visited A more recently than B with probability q^-_σ and will arrive at B before visiting A again with probability q^+_σ. Recalling that the equilibrium probability of $\sigma(t)$ visiting state σ is $\mathbb{P}(\sigma)$, one can derive the equilibrium probability distribution $\mathcal{P}(\sigma)$ of system configurations in the ensemble of reactive trajectories:

$$\mathcal{P}(\sigma) \propto q^-_\sigma \mathbb{P}(\sigma) q^+_\sigma \ . \tag{2.39}$$

Further noting that the probability per unit time of the system jumping from state σ to state σ' is given by $r(\sigma \to \sigma')$ [Eq. (2.28)], it is possible to show that the reactive probability current $\mathcal{J}(\sigma \to \sigma')$ flowing from A to B along the transition $\sigma \to \sigma'$ is given by:

$$\mathcal{J}(\sigma \to \sigma') = \begin{cases} \mathbb{P}(\sigma) r(\sigma \to \sigma') q^-_\sigma q^+_{\sigma'} & \text{if } \sigma \neq \sigma', \\ 0 & \text{otherwise}, \end{cases} \tag{2.40}$$

and satisfies the conservation property:

$$\sum_{\sigma' \in \Lambda} \left[\mathcal{J}(\sigma \to \sigma') - \mathcal{J}(\sigma' \to \sigma) \right] = 0, \ \forall \sigma \in \Lambda \setminus (A \cup B). \tag{2.41}$$

To facilitate an intuitive understanding of the ensemble of reactive trajectories it is useful to consider the system and its microscopic kinetics in the form of a graph $G(\Lambda, \Psi)$, where every microstate $\sigma \in \Lambda$ of the system is represented by a node and a directed edge $\psi_{\sigma,\sigma'} \in \Psi$ is drawn with weight $r(\sigma \to \sigma')$ between pairs of nodes $\sigma, \sigma' \in \Lambda : \sigma \neq \sigma'$ for which $r(\sigma \to \sigma') > 0$. By this construction, any walk, i.e. arbitrary alternating sequence of nodes and edges respecting the direction of each edge, through G constitutes a generic trajectory of the system. The ensemble of reactive trajectories is a subset of these walks, which we can construct by considering the subgraph $G_R(\Lambda, \Psi') \subset G$ whose directed edges $\psi'_{\sigma,\sigma'}$

form the subset of those of G, drawn with weight $\mathcal{J}^+(\sigma \to \sigma')$ under the condition $\mathcal{J}^+(\sigma \to \sigma') > 0$, where:

$$\mathcal{J}^+(\sigma \to \sigma') = \max\{\mathcal{J}(\sigma \to \sigma') - \mathcal{J}(\sigma' \to \sigma), 0\}. \tag{2.42}$$

Since $\mathcal{J}^+(\sigma \to \sigma')$ is the effective reactive current through the edge $\psi_{\sigma,\sigma'}$, noting that the only sources and sinks of reactive current in G_R are respectively the groups of nodes A and B, the total probability per unit time of the reaction can be written as the sum of weights $\mathcal{J}^+(\sigma \to \sigma')$ of edges connecting the nodes in A to the rest of G_R:

$$J(A \to B|\beta, \vec{\mu}) = \sum_{\sigma \in A} \sum_{\sigma' \in \Lambda} \mathcal{J}^+(\sigma \to \sigma'|\beta, \vec{\mu}), \tag{2.43}$$

where the restriction to the specified set of edges is implicit, since $\mathcal{J}^+(\sigma \to \sigma') = 0$ for all $\sigma, \sigma' \in A$ by definition of q^+_σ. In Eq. (2.43) the set of edges connecting the groups of nodes A and $\Lambda \setminus A$ corresponds to a dividing surface in the language of transition state theory (TST), with the total effective reactive current from A to B expressed as the sum of all effective currents leaving A through the dividing surface, i.e. the boundary of A in this case. Any subset of edges $\Psi^* \subset \Psi'$ is a valid choice of a dividing surface if removal of Ψ^* from G_R partitions G_R into two subgraphs $G_A(\Lambda_A, \Psi_A)$, $G_B(\Lambda_B, \Psi_B)$ with $A \subseteq \Lambda_A$ and $B \subseteq \Lambda_B = (\Lambda \setminus \Lambda_A)$. By properties of $\mathcal{J}^+(\sigma \to \sigma')$, one can show that the total reactive current through the edges Ψ^* leading from G_A to G_B yields $J(A \to B)$, hence the reaction rate is invariant under the choice of the dividing surface, so long as the product (B) and reactant (A) states are well defined.

A conceptually equivalent result to (2.43) can be obtained within the framework of TST [55], though TPT offers a more general and exhaustive treatment of the reaction process by considering the flow of $\mathcal{J}^+(\sigma \to \sigma')$ through the whole of the state space rather than the dividing surface alone [53]. While a rigorous application of the TPT can grant a complete understanding of the reaction mechanism, it requires estimation of q^-_σ and q^+_σ over a considerable portion of the state space, which has, so far, only been attempted in the context of simple systems [56, 57]. At present, studies of reaction kinetics in complex systems rely on less general approaches which can be understood as approximations to TPT. A common feature of many of such approaches is the attempt to model the microscopic kinetics of the system over the course of the reaction as motion of a reaction coordinate (RC) – an order parameter capturing the relevant to the reaction degrees of freedom of the system.

A coarse grained effective free energy surface of the system can be constructed from the equilibrium probability distribution of any order parameter:

$$F(\lambda|\beta,\vec{\mu}) = -k_B T \ln \mathbb{P}(\lambda|\beta,\vec{\mu}), \tag{2.44}$$

where $F(\lambda|\beta,\vec{\mu})$ is termed the free energy of λ, despite not having an explicit link to either the Landau free energy or the thermodynamic potential $\mathcal{F}(\beta,\vec{\mu})$. In a scenario where the system undergoes a transformation from phase A to phase B, we expect the surface $F(\lambda|\beta,\vec{\mu})$ to present at least two basins: a local minimum corresponding to the metastable state A and a global minimum corresponding to the stable state B. For various choices of kinetics of the order parameter, the activation rate of the reaction can be expressed in the form:

$$J(A \to B|\beta,\vec{\mu}) \propto \exp\left[-\beta \Delta F(A \to B|\beta,\vec{\mu})\right], \tag{2.45}$$

with $\Delta F(A \to B|\beta,\vec{\mu})$ being the activation energy of the process [58]. In the simple case where basins A and B are separated by a single free energy barrier, the activation energy is given by the height of the barrier relative to the minimum of free energy in basin A:

$$\Delta F(A \to B|\beta,\vec{\mu}) = F(\lambda^*|\beta,\vec{\mu}) - F(\lambda_A|\beta,\vec{\mu}), \tag{2.46}$$

where λ_A is the point minimising $F(\lambda|\beta,\vec{\mu})$ in the basin corresponding to phase A and λ^* is the value of the order parameter maximising $F(\lambda|\beta,\vec{\mu})$ along a suitably chosen path from A to B through the order parameter space. The set of configurations realising the order parameter value λ^* is referred to as the set of transition states (activated complexes). Combining the above, the expression for the activation rate $J(A \to B|\beta,\vec{\mu})$ takes a form similar to the expression for the rate of state transition in a Markov process (2.28):

$$J(A \to B|\beta,\vec{\mu}) = v(\beta,\vec{\mu}) \frac{\mathbb{P}(\lambda^*|\beta,\vec{\mu})}{\mathbb{P}(\lambda_A|\beta,\vec{\mu})}, \tag{2.47}$$

with $v(\beta,\vec{\mu})$ being the kinetic prefactor.

Theoretical justifications for (2.45) and (2.46) typically invoke extensive assumptions regarding the microscopic kinetics of the reaction process. Specifically, to derive (2.45) one assumes that the projection of the system's kinetics in the configuration space Λ on to the low dimensional coordinate λ yields an evolution $\lambda(t)$ which is well described by a variant of the Langevin equation over the course of the reaction [58]. As we will see in Chapter 3, it is not, in general, clear to what extent this assumption must be satisfied in order to qualify (2.45) as a reasonable approximation for complex systems. In addition, there exists no rigorous procedure for construction of reaction coordinates in complex systems, although various methods for assessment of order parameters as candidate RCs have been proposed [59,60].

2.4 NUCLEATION THEORY

Modern studies of nucleation phenomena continue to refer back to the theoretical developments of the early-to-mid 20th century, collectively termed Classical Nucleation Theory (CNT). Although developed independently, CNT follows largely the same reasoning as the conventional reaction rate theory [58] and, therefore, suffers from the same drawbacks.

Assuming that the transformation from the metastable phase A to the stable phase B proceeds via formation of microscopic nuclei or droplets of the stable phase, we first argue that nucleus size plays the key role in the kinetics of the process. Further assuming that a nucleus can be precisely defined as a compact, typically spherical, aggregate of particles, and the nucleus size is given simply by the number of particles n in the aggregate, we attempt to coarse grain the kinetics of the process via a master equation for n.

2.4.1 *Homogeneous Nucleation Rate*

We model the formation of a droplet of size n in a homogeneous medium, i.e. a system free of impurities and other preferential nucleation sites, as a process of uncorrelated attachment of monomers. Thus, we ignore the details of particle motion, particle depletion and the possibility of attachment of dimers and larger aggregates. Denoting the time dependent distribution of nuclei sizes as $P_n(t)$ ($n \geq 1$) and the nucleus size dependent rates of monomer attachment and detachment as J_n^+ and J_n^- respectively ($J_1^- = 0$), we write down the master equation as:

$$\frac{d}{dt}P_n(t) = P_n'(t) = J_{n-1}^+ P_{n-1}(t) + J_{n+1}^- P_{n+1}(t) - (J_n^+ + J_n^-)P_n(t), \tag{2.48}$$

which is analogous to the equation for the birth-death process. Assuming the distribution of nuclei sizes is quasi–stationary over the course of the phase transition, we set $P_n'(t) = 0$ and define the overall probability flux J_{CNT} as:

$$J_{\mathrm{CNT}} = J_{n-1}^+ P_{n-1} - J_n^- P_n = J_n^+ P_n - J_{n+1}^- P_{n+1}, \tag{2.49}$$

which is equivalent to stating that there is a steady state size independent rate J_{CNT} of formation of nuclei. The equilibrium distribution $\mathbb{P}(n) \neq P_n$ of nucleus sizes is recovered by setting $J_{\mathrm{CNT}} = 0$, yielding:

$$\frac{\mathbb{P}(n)}{\mathbb{P}(1)} = \prod_{i=1}^{n-1} \frac{J_i^+}{J_{i+1}^-} = \exp\left\{-\beta\left[F(n) - F(1)\right]\right\} = \exp\left[-\beta \Delta F(n)\right], \tag{2.50}$$

via the detailed balance condition, which relates the rate coefficients of the master equation to the cluster free energy $F(n)$. While it is possible to obtain a closed form expression for J_{CNT} in terms of attachment and detachment rates from (2.49) [61], a more straightforward approach is to substitute: $J_{n+1}^{-} = J_n^{+}\mathbb{P}(n)/\mathbb{P}(n+1)$, obtaining:

$$\frac{J_{\mathrm{CNT}}}{J_n^{+}\mathbb{P}(n)} = \frac{P_n}{\mathbb{P}(n)} - \frac{P_{n+1}}{\mathbb{P}(n+1)} \Rightarrow J_{\mathrm{CNT}} \sum_{n=1}^{n_{\max}} \frac{1}{J_n^{+}\mathbb{P}(n)} = \frac{P_1}{\mathbb{P}(1)} - \frac{P_{n_{\max}}}{\mathbb{P}(n_{\max})}, \quad (2.51)$$

by summing equations (2.49) up to an arbitrary value $n = n_{\max}$.

To make further progress we are forced to introduce a number of crude approximations. Truncating the quasi–stationary distribution P_n by setting $\lim_{n\to\infty} P_n/\mathbb{P}(n) = 0$, we arrive at:

$$J_{\mathrm{CNT}} = P_1 \left(\sum_{n=1}^{\infty} \frac{1}{J_n^{+}} \exp\left[\beta \Delta F(n)\right] \right)^{-1}, \quad (2.52)$$

which can be approximated as a Gaussian integral by Taylor expanding $\Delta F(n)$ about an assumed sharp peak at the critical cluster size n^*. Additionally treating $J_n^{+} \approx J_*^{+}$ as a constant, we arrive at the classical nucleation rate expression:

$$J_{\mathrm{CNT}} = \rho J_*^{+} \mathcal{Z} \exp\left[-\beta \Delta F(n^*)\right], \quad \mathcal{Z} = \left[-\frac{\beta}{2\pi} \left. \frac{\partial^2 \Delta F(n)}{\partial n^2} \right|_{n=n^*} \right]^{\frac{1}{2}}, \quad (2.53)$$

where $\rho = P_1$ is the monomer concentration, J_*^{+} is the rate of monomer attachment to the critical cluster, $\mathcal{Z}$ is the Zeldovich factor and the $(\beta, \vec{\mu})$ dependencies of ρ, J_+^{*}, $\mathcal{Z}$ and $\Delta F(n)$ are implicit [4].

2.4.2 *Droplet Free Energy*

A phenomenological expression: $\Delta F_{\mathrm{CNT}}(R) = bA_R - aV_R$, for the free energy as a function of the radius R of a spherical droplet can be obtained by means of thermodynamic considerations [4], where A_R and V_R are, respectively, the surface area and the volume of the droplet, and the coefficients a and b are, respectively, the volume and surface formation free energies of nuclei of phase B in the medium of phase A. For compact, e.g. spherical or cubic, nuclei of characteristic length R, it is straightforward to show that the number of monomers in the nucleus is related to R via: $R \propto n^{1/3}$ [4,62], hence the expression for $\Delta F_{\mathrm{CNT}}(n)$ is often written in the form:

$$\Delta F_{\mathrm{CNT}}(n) = \gamma_{\mathrm{CNT}} n^{2/3} - n \Delta \mu_{\mathrm{CNT}}, \quad (2.54)$$

where γ_{CNT} and $\Delta\mu_{\mathrm{CNT}}$ are temperature and saturation dependent scalars related to, respectively, the free energetic cost per unit area of formation of an interface between the nucleus of B in the medium of phase A, and the free energetic gain per additional monomer of phase B. In cases where the shape of the nucleus is known, the coefficient γ_{CNT} can be written in terms of the interfacial surface tension, i.e. surface formation free energy per unit area, and the nucleus shape factor, i.e. the approximate contribution of a single monomer to the surface area of the nucleus. Generally, the droplet shape is not known a priori, thus, to avoid additional assumptions, we will keep the shape factor implicit in γ_{CNT}.

Both γ_{CNT} and $\Delta\mu_{\mathrm{CNT}}$ are often inferred from the bulk properties of A and B, i.e. γ_{CNT} is approximated as the surface tension of a macroscopic planar interface of A and B, while $\Delta\mu_{\mathrm{CNT}}$ is taken as the difference per monomer of phase B between the free energies of the system in state B and in state A – the difference between the chemical potentials of B and A. This treatment assumes curvature independence of the interfacial free energy, and unambiguous definitions of monomer and nucleus of phase B, all of which, along with the general applicability of bulk phase properties to microscopic nuclei, are problematic in practice.

The mathematical simplicity of Eq. (2.54), however, offers a number of testable predictions and provides a means of nucleation rate estimation based largely on the thermodynamic properties of the system. The maximum of $F_{\mathrm{CNT}}(n)$ occurs at the critical nucleus size n^*_{CNT}:

$$n^*_{\mathrm{CNT}} = \left[\frac{2\gamma_{\mathrm{CNT}}}{3\Delta\mu_{\mathrm{CNT}}}\right]^3 \quad \Rightarrow \quad \Delta F_{\mathrm{CNT}}(n^*_{\mathrm{CNT}}) = \frac{4\gamma^3_{\mathrm{CNT}}}{27\left(\Delta\mu_{\mathrm{CNT}}\right)^2} = \frac{1}{2}n^*_{\mathrm{CNT}}\Delta\mu_{\mathrm{CNT}}, \tag{2.55}$$

leading to the relations: $n^*_{\mathrm{CNT}} \propto \left(\Delta\mu_{\mathrm{CNT}}\right)^{-3}$ and $F_{\mathrm{CNT}}(n^*_{\mathrm{CNT}}) \propto \left(\Delta\mu_{\mathrm{CNT}}\right)^{-2}$. Noting that:

$$\mathcal{Z}_{\mathrm{CNT}} = \left[-\frac{\beta}{2\pi}\frac{\partial^2 \Delta F_{\mathrm{CNT}}(n)}{\partial n^2}\bigg|_{n=n^*_{\mathrm{CNT}}}\right]^{\frac{1}{2}} = \left[\frac{\beta}{9\pi}\gamma_{\mathrm{CNT}}\left(n^*_{\mathrm{CNT}}\right)^{-4/3}\right]^{\frac{1}{2}}, \tag{2.56}$$

we obtain the expression for J_{CNT} in terms of $\Delta\mu_{\mathrm{CNT}}$:

$$J_{\mathrm{CNT}} = \frac{1}{3}\rho J^+_*\left(n^*_{\mathrm{CNT}}\right)^{-2/3}\exp\left[-\beta\frac{4\gamma^3_{\mathrm{CNT}}}{27\left(\Delta\mu_{\mathrm{CNT}}\right)^2}\right]\sqrt{\gamma_{\mathrm{CNT}}\beta\pi^{-1}}. \tag{2.57}$$

Assuming the attachment rate J^+_* is proportional to the surface area of the nucleus, i.e. $J^+_* \propto (n^*_{\mathrm{CNT}})^{2/3}$ [63], and the monomer density is related to the chemical potential difference: $\ln\rho \propto \beta\Delta\mu_{\mathrm{CNT}}$, one can argue that there is an approximately linear relationship between $\ln J_{\mathrm{CNT}} - \beta\Delta\mu_{\mathrm{CNT}}$ and $\left(\beta\Delta\mu_{\mathrm{CNT}}\right)^{-2}$ at fixed temperature [2].

In light of the numerous assumptions and simplifications implicit in Eq. (2.54) it is not surprising that the predictive capability of the expression is, as we shall discuss in Chapter 3, highly sensitive to the microscopic properties of the system. Numerous criticisms, modifications and corrections to the classical expression have been put forward, reaching various degrees of improvement [4]. Alternative expressions for the droplet formation free energy can also be found in the more recent literature [64–66], and improvements over Eq. (2.54) have been reported for various systems [67–72], yet the classical formula remains widely in use.

2.4.3 *Cluster Size as Order Parameter and Reaction Coordinate*

In the Section 2.3 we have considered order parameters as projections of the configuration space on to some lower dimensional coordinate. In practice, this definition also applies to the cluster order parameter: we typically define $n(\sigma)$ as the number of particles in the largest nucleus present in the system in microstate σ, which conflicts with the CNT definition of $\mathbb{P}(n)$ [73].

In the context of CNT, we treat $\mathbb{P}(n = 1)$ as the concentration of monomers in the system – the population of particle clusters of size 1. Employing the projection $n(\sigma)$ leads to $\mathbb{P}[n(\sigma) = 1]$ giving the probability of observing a microstate of the system in which the largest cluster of particles contains exactly one particle. Since configurations with $n(\sigma) = 1$ may contain more than one cluster of $n = 1$, clearly $\mathbb{P}(n = 1) \neq \mathbb{P}[n(\sigma) = 1]$. The same reasoning applies for cluster sizes $n : 1 < n < n^\dagger$, where $n^\dagger$ is system size dependent, which follows the intuition that, in sufficiently small systems, occurrence of multiple clusters of size $n : n \geq n^\dagger$ is extremely unlikely, and $\mathbb{P}(n|n \geq n^\dagger) \approx \mathbb{P}[n(\sigma)|n(\sigma) \geq n^\dagger]$.

In practice, accurate evaluation of $\mathbb{P}(n)$ is limited to a narrow range of small nuclei – unlike the case for $\mathbb{P}[n(\sigma)]$. Thus the system size must be chosen to not only accurately model the nucleation process, i.e. avoid percolation effects for clusters of size $n : n > n^*$, but also allow accurate computation of $\mathbb{P}(n|n \leq n^\dagger)$.

It is also worth pointing out that in spatially continuous systems the definition of $n(\sigma)$ can be ambiguous and, in general, it is not always clear whether a given definition is kinetically relevant [74]. On the other hand, a kinetically relevant choice of $n(\sigma)$ may not be compatible with the CNT framework, which may contribute to the quantitative discrepancies between nucleation theory and simulation [75]. Arguably, even in spatially discrete systems, e.g. the Ising model [1,76], the appropriate definition of the nucleus size metric remains a subject of debate.

2.4.4 *Limitations of the Classical Theory*

So far, we have discussed CNT in the context of a transition between two well defined thermodynamic states A (reactant) and B (product) in a spatially homogeneous system, where we have modelled the transition as a one-step process, i.e. direct nucleation of the product phase B. Many complex systems exhibit polymorphism, i.e. existence of multiple, often comparably thermodynamically stable, forms of the product phase B, giving rise to more involved multi-step activation pathways.

Two extensions to the one-step model have been put forward to account for the possibility of intermediate states along the phase transition process, namely:

1. The Ostwald conjecture: intermediate states appear in the order of their relative thermodynamic stability, i.e. the next appearing state is closest in free energy to the previous.
2. The Stranski-Totomanov conjecture: transitions between intermediate states occur in the order of the heights of corresponding free energetic barriers, i.e. the next appearing state is separated from the previous by the lowest free energy barrier.

Although these conjectures appear to hold in some cases, both are without any rigorous theoretical basis and cannot be viewed as universal rules, as it has been demonstrated that thermodynamic information alone is not always sufficient to determine the transition pathway [77,78].

By modifying the interfacial free energy term to account for the reduced surface area of the nucleus due to contact with an impurity, the CNT framework has also been extended to facilitate studies of heterogeneous nucleation, i.e. nucleation in systems with spacial heterogeneities [2,4]. Growing evidence, however, suggests that such an approach is not always adequate, and the variations in surface properties and chemical composition of impurities may strongly affect the kinetics of nucleation [79]. Considering the abundance of complex nucleation mechanisms, e.g. pre-nucleation clusters and multi-step nucleation [5,80], along with the prevalence of systematic errors and unphysical predictions of CNT [4,81], it is clear that CNT can serve as, at best, a theoretical basis for more detailed system specific theories rather than a general predictive theory of nucleation processes.

3

RECENT DEVELOPMENTS

Having introduced the core concepts of nucleation theory we will now discuss the current state of the art in computational study of condensation, freezing and solution precipitation processes. We will start by reviewing the recent studies of nucleation kinetics in MC and molecular dynamics (MD) models of several physical systems, e.g. colloidal suspensions, noble gasses and solutions. Following a brief outline of the computational methodology, we will explore the current status of atomistic and molecular simulation in relation to theory and experiment. In the second half of the chapter, our discussion will move towards studies of nucleation in lattice models.

3.1 NUCLEATION IN ATOMISTIC AND MOLECULAR MODELS

A number of approaches to atomistic and molecular modelling of physical systems exist. A common feature to all of them is that the system of interest is represented by a collection of N particles in a finite, often cubic, volume with periodic boundaries, yielding a model with a minimum of $3N$ degrees of freedom. Additional degrees of freedom may be introduced due to particle anisotropy, inclusion of particle inertia, and/or inclusion of energy and volume fluctuations (”thermostatting” and ”barostatting” in MD). Particle interactions are modelled by pair or many-body potentials, typically calibrated empirically or semi-empirically to accurately capture the thermodynamic and transport properties of the modelled system. Time evolution and appropriate sampling of the desired statistical ensemble are achieved by Metropolis style MC moves or integration of the appropriate equations of motion for MD and Langevin dynamics (LD) [7].

3.1.1 *Selected Systems*

Although a great number of atomistic and molecular model systems have been developed, quantitative studies of nucleation kinetics enabling comparison of experimental observations and theoretical predictions are rare. While a number of model systems have been studied, at present we find only four classes of models whose nucleation kinetics have been considered extensively by multiple research groups and via multiple approaches:

1. Crystallisation of hard spherical colloids – isotropic particles interacting via hard-core repulsion or modifications thereof.
2. Condensation, deposition, and crystallisation transitions in the Lennard-Jones (LJ) model – system of point particles interacting via the pairwise Lennard-Jones potential.
3. Ice nucleation in water models – namely TIP4P/2005 [82], TIP4P/Ice [83] and mW [84].
4. Precipitation from solution in Tosi-Fumi [85], Smith-Dang [86] and Joung-Cheatham [87] models of sodium chloride (NaCl).

Although the four classes of models are deemed accurate enough approximations to their physical counterparts to allow comparison between nucleation kinetics in experiment and simulation, they are not free from criticisms. The LJ system, for instance, is considered, in many respects, a reasonable approximation to the system of liquid argon (Ar), yet it is known to significantly misrepresent the bulk viscosity of the fluid [88]. The hard-core repulsion of the hard sphere (HS) pair potential is difficult to realise in an experimental setting [89]. In addition particle polydispersity and hydrodynamic interactions are typically ignored in conventional HS models, yet are thought to affect the transport properties of the physical systems [3]. Accurately capturing the thermodynamics and transport properties of the more complex physical systems in models for which statistical treatment is amenable remains a substantial challenge, and performance of the commonly used interatomic potentials for modelling of such systems as water [90] and aqueous solution of NaCL [91, 92] is still lacking in this respect.

Several less extensive nucleation studies have been carried out on models of charged colloids [93, 94], anisotropic colloids [95, 96], molten silica [97] and silicon [98], offering quantitative assessment of CNT. By comparison, qualitative studies of nucleation kinetics are much more numerous, and we cannot hope to cover a representative portion of these in this review. Instead, we will address the common topics of nucleation from solution by reviewing some of the archetypical systems, namely calcium carbonate ($CaCO_3$), NaCl and natural gas hydrates [2].

3.1.2 *Overview of Methodology for Studies of Nucleation Kinetics*

A wide range of rare event simulation methods have been applied to the study of nucleation kinetics over the recent years [99, 100]. The vast majority of these loosely fall into the following four categories:

1. Direct/Brute force – characterisation of nucleation kinetics based on direct observation of nucleation events, e.g. mean first passage time (MFPT) formalism [101].

2. Indirect/CNT based – measurement of nucleation rates based on equations of CNT, e.g. umbrella sampling (US) [63] and the "seeding" method [102].
3. Path based – study of nucleation kinetics via sampling of reactive trajectories or their segments, e.g. transition path sampling (TPS) [103], forward flux sampling (FFS) [104], transition interface sampling (TIS) [105].
4. Free energy surface (FES) based – characterisation of nucleation pathways via complete or partial reconstruction of the FES in the coarse grained space of collective variables, e.g. metadynamics [106, 107] and string method [108, 109].

Each of the four classes of methods have their advantages and drawbacks. Brute force methods, for example, offer a simple approach to characterisation of the nucleation process, which, unlike all other methods, do not rely on the notion of a reaction coordinate to a large extent. Direct calculations of MFPT, however, are only feasible at conditions where nucleation events are sufficiently frequent to allow adequate collection of statistics. Such conditions correspond to parameter regions of short lived metastability of the reactant phase A, i.e. far away from coexistence of A and the product phase B.

The remaining three groups of methods are applicable over a wider range of parameter space, but employ the concept of a reaction coordinate and additional assumptions. Methods based on CNT aim to estimate the terms of Eqs. (2.53) and (2.54) from free energy calculations and kinetic properties of the assumed reaction coordinate, thereby producing estimates of nucleation rates and barrier heights. Metadynamics and related methods attempt to obtain a projection of the FES on to a low dimensional coordinate space by introducing a history dependent bias into the energetics of the system or computing the local gradient of the FES. Based on the resultant thermodynamic information, various low dimensional kinetic models of the transition can be explored, potentially yielding quantitative insight.

Path based methods attempt to achieve a purely kinetic treatment of the transition process by sampling energetically unbiased trajectories through the system's state space. With the exception of TPS, all methods of this category enhance the sampling of rare events by indirectly guiding the system's kinetics along a, typically, one dimensional order parameter in a ratchet-like or milestoning manner. The choice of the guiding order parameter is often argued to play a weak role in the observed kinetics, though it is difficult to provide a rigorous justification for such arguments.

At present a detailed systematic comparison of the above rare event methods is lacking, although a reasonable degree of agreement between a selection of methods has been reported in various models [93, 96, 97, 110–112]. Due to their relative simplicity, MFPT and CNT based methods have been overwhelmingly popular in nucleation literature, while among the more advanced approaches there is a clear preference towards FFS at present. We will return to the subject of rare event methodology for a detailed discussion in Chapter 7.

3.1.3 *Quantitative Comparison of Simulation and Experiment*

Direct comparison of results of simulation and experiment in complex systems remains a major challenge due to the stark differences in the capabilities of the two methods of study. Recent advancements in imaging and simulation techniques, however, provided the opportunity for direct comparisons of computational and empirical studies of HS [89], LJ [113], water [3] and NaCl [114] systems. Large deviations between rate measurements via simulation and experiment have been widely reported for the four systems, and no general consensus regarding their origin has been established so far, although various contributing factors have been discussed.

Disagreement between computational and experimental studies of the HS system at conditions far away from liquid-solid coexistence is relatively small (factor of 10^2) and is attributed to statistical uncertainties in nucleation rate measurement and determination of the packing fraction – values of the single parameter governing the thermodynamic state of the ideal HS system – in experiment [115]. At lower packing fractions, i.e. closer to coexistence, however, the discrepancies are much greater [110, 111], suggesting existence of systematic errors in rate estimates due to simulation. Recently, roles of several modelling assumptions, made in computational studies of HS, have been examined, including effects of particle polydispersity [110], plasticity [111], sedimentation [116] and hydrodynamic interactions [117], showing some promise in resolving the existing disagreements.

The situation in LJ and NaCL systems is less clear due to the lack of computational and experimental studies at comparable parameter values. While indirect comparison can be achieved by extrapolating the computational measurements, performed at high supersaturations and undercoolings, into regions of parameter space probed by experiment, the resultant data have been shown to be highly sensitive to the choice of the necessary analytical models leading to spectacular discrepancies up to a factor of 10^{26} [69], although the role of uncertainties in experimental approach is not clear. The more recent study of freezing of LJ fluids [113] demonstrated reasonable qualitative consistency with previous investigations as well as remarkable agreement with two experimental measurements in close proximity to the considered parameter points. Results of the few available computational studies of NaCl at realistic conditions range from drastic disagreement [114] (in the case of precipitation from aqueous solution) to remarkable consistency [118] (in the case of nucleation from the melt) with experiment, though the quantity of reference data is scarce.

In the case of water models, discrepancies are common not only between simulation and experiment [3] but also among computational studies utilizing the same interatomic potentials and rate measurement procedures, as can be seen from a comparison of Refs. [119, 120] and [121]. Despite criticism of models' accuracy in capturing water thermodynamics [122], realistic computational nucleation rate estimates have been reported [123, 124], although the accuracy of these is debatable [3].

3.1.4 *Quantitative Comparison of Simulation and Theory*

Quantitative studies have compared CNT predictions given by Eqs. (2.53) and (2.54) with results of explicit nucleation rate and free energy calculations respectively. Despite the widespread criticism of CNT assumptions [3, 89], the rate estimation approach based on Eq. (2.53), as pioneered by Auer and Frenkel [125] in their study of nucleation in the HS model, has received largely favourable reviews over the recent years, as summarised in Table 3.1.

Study	**Model**	**Methods**
Filion *et al.* [110]	HS	US, MFPT, FFS
Filion *et al.* [111]	WCA potential [126]	US, MFPT, FFS
Mithen *et al.* [93]	Gaussian core [127]	US, FFS
Ni and Dijkstra [96]	Hard colloidal dumbbells	US, MFPT
Malek *et al.* [128]	LJ	US, MFPT
Saika-Voivod *et al.* [97]	BKS silica [129]	US, MFPT

Table 3.1: Listing of studies quantitatively comparing the nucleation rate estimation approach of Auer and Frenkel [125], i.e. Eq. (2.53) parametrised by explicit estimates of the free energy barrier (via US) and the kinetic prefactor, with other rate calculation methods. All listed studies report good agreement between the employed methods to within statistical errors.

Universal agreement between rare event methods, however, is not present. Discrepancies between results of TIS, FFS and related methods were reported in a study of a one-dimensional system [130]. Very recently, Jungblut and Delago [131] demonstrated the subtle effects of structural relaxation between consecutive nucleation attempts in the LJ system on MFPT based rate estimates, concluding that discrepancies between rate estimation methods, in specific systems or conditions, may arise due to the non-Markovian nature of the transition process. It is frequently highlighted in the literature that rate estimates can be highly sensitive to minor implementation details [132] as well as the choice of the order parameter. Critical surveys of the existing methods and systematic evaluations of performance of different implementations are still lacking.

A wide range of studies have addressed the accuracy of Eq. (2.54) in describing nuclei formation free energies. Direct comparisons (Table 3.2) with explicitly computed free energy barriers to nucleation show that the functional form of the CNT expression, although qualitatively reasonable, can yield erroneous estimates of barrier heights and sizes of critical nuclei. While certain qualitative predictions, e.g. scaling of nucleation rates, barrier heights and critical nuclei sizes with driving force to nucleation, appear to hold in many cases [112, 133–135], the predictive power of Eq. (2.54) is widely regarded as poor when employing reasonable estimates of the bulk surface free energy coefficient γ_{CNT} [98, 107, 128, 136]. Applicability of well defined macroscopic values of γ_{CNT} and $\Delta\mu_{\mathrm{CNT}}$ to microscopic nuclei is frequently challenged on the basis of nuclei anisotropy and compressibility as well as curvature and diffuse nature of nucleus surface [137, 138], yielding an abundance of corrections and alternatives to Eq. (2.54). More recently [75], it was pointed out that the commonly employed choice of order parameter, used in identifying microscopic nuclei and calculating their sizes, implicitly leads to a definition of nucleus interface with the surrounding medium, which may not correspond exactly to the thermodynamic definition implied in Eq. (2.54), contributing at least partially to the frequently reported discrepancies between microscopically and macroscopically estimated values of γ_{CNT} and $\Delta\mu_{\mathrm{CNT}}$.

In light of the above, it is fair to conclude that the limited capacity of CNT, in prediction of rates of homogeneous nucleation in molecular models, is largely attributable to the difficulty of obtaining precise estimates for nuclei formation free energies based solely on the thermodynamic properties of the models. Considering the questionable accuracy of the present methodology, it is not clear whether the quantitative framework of CNT can be completely ruled out as adequate, despite the mounting evidence against the framework's underlying assumptions. Particularly striking evidence in favour of the CNT formalism was recently provided by Espinosa *et al.*, who have shown that the "seeding" approach [102] to nucleation rate estimation, which wholly relies on Eqs. (2.53) and (2.54), can yield remarkable agreement with the previously reported direct measurements across a wide range of parameter space in various models [112].

3.1.5 *Nonclassical Nucleation*

The classical caricature of the phase transition process, where compact nuclei of the stable phase appear and grow in the medium of the metastable phase, does not fully capture the detail of nucleation processes in even the simplest molecular models [3, 144]. An overwhelming number of studies report that the qualitative character of the transition processes is more involved, and a variety of intricate multi-stage nucleation pathways have been observed in a range of systems, including HS, LJ, water, NaCl, $CaCO_3$ and natural gas hydrates [2,3,5,80,145]. Such

Study	Model	Methods
Filion *et al.* [110]	HS	US
Jungblut and Delago [139]	LJ	TIS, PPTIS [140]
Lundrigan and Saika-Voivod [141]	LJ	US, MFPT [142]
Saika-Voivod *et al.* [97] $*$	BKS silica [129]	US
Valeriani *et al.* [143] $*$	Tosi-Fumi NaCL	US
Cuetos and Dijkstra [95]	Colloidal hard rods	US

Table 3.2: Listing of studies quantitatively comparing the CNT form [Eq. (2.54)] of the free energy barrier with explicit free energy calculations. Studies marked with asterisk ($*$) report exceptionally good fits of Eq. (2.54) to explicitly computed barrier data. The remaining studies report that the CNT expression produces reasonable qualitative trends but yields substantial quantitative discrepancies.

processes typically do not comply with the standard assumptions of CNT regarding, for example, free energy barrier shapes and internal structures of nuclei, and, for this reason, are commonly referred to as "nonclassical" in the recent literature.

Both computational and experimental studies report evidence of amorphous precursor pathways to crystallisation in HS systems, where, prior to emergence of the stable face-centred cubic (fcc) structure, the colloidal suspension appears to exhibit formation of dense positionally disordered domains, which subsequently mature into random hexagonal close-packed (rhcp) stackings [146, 147]. Transition mechanisms involving metastable intermediate states were also identified in LJ [148], Yukawa [77], Gaussian core [93] and other particle systems, revealing a broad range of possible kinetic pathways to crystallisation, e.g. dissolution-recrystallisation, cross-nucleation and solid-state transformation. How such evident departure from the CNT model reflects in the quantitative metrics is, however, not clear as we do not find any studies reporting breakdown of Eq. (2.53), as applied by Auer and Frenkel, for one-component particle systems (see Table 3.1).

Consequently, it is not surprising that nonclassical nucleation mechanisms are abundant in more complex systems. Amorphous and metastable intermediates are widely reported in studies of multi-step crystallisation pathways in models of NaCl [149], $CaCO_3$ [150] and gas hydrates [151]. Particularly topical are the various system specific phenomena, such as dehydration of the amorphous precursor [152] and existence and role of pre-nucleation clusters [153] in precipitation of calcite from solution. At present, computational studies of nucleation from solution cannot examine directly the complete kinetic pathways to crystallisation at realistic conditions, due to the long timescales of solution relaxation, prohibitive system size requirements for simulation of realistic supersaturations as well as absence of methodology for modelling of open systems eliminating effects of solute depletion [2]. Meanwhile, experimental verification of computational findings remains a challenge due to the limitations of the modern microscopy and scattering techniques [3], though indirect evidence continues to emerge [154].

In this work we will explore lattice models of anisotropic particles in solution, where solute nuclei undergo structural transformations from low to high internal orientational order over the course of growth limited solute crystallisation pathways. Such behaviour falls into the broad category of multi-stage nucleation and will be considered as nonclassical throughout this work.

3.2 NUCLEATION IN LATTICE MODELS

It has been well documented that fundamental physical phenomena and processes can sometimes be captured by models including minimal physical detail, to which the Ising model is an excellent example in the field of statistical physics. Due to their remarkable simplicity, lattice models provide a platform for in depth exploration of generic nucleation mechanisms as well as system specific features at a greatly reduced computational expense. Additionally, the simplistic view of particle interactions offers an intuitive means to tune the model thermodynamics and phase behaviour, possibly utilising the body of analytical results available for some of the well established models. In the context of nucleation from solution, the relevant order parameters and initial system configurations can be constructed with relative ease. As we will see in this section, despite their simplicity, minimal models display a rich array of phase transition behaviours often challenging the established theoretical framework.

3.2.1 *The Ising Model*

Numerous studies have considered the Ising lattice gas as a simple model of vapour-to-liquid nucleation or precipitation from solution. In this model, each site of the simple square or simple cubic lattice represents either a vapour/solvent particle ($s'_i = -1$ – spin "down") or a liquid/solute particle ($s'_i = 1$ – spin "up"). For a given configuration $\sigma' \in \Lambda' = \{-1, 1\}^N$, the Hamiltonian is typically written as: $H_I(\sigma') = -\sum_{\{(i,j)\}} s'_i s'_j - h \sum_{k=1}^{N} s'_k$, where the first sum carries over all pairs (i, j) of nearest neighbouring lattice sites and h represents the strength of particle interaction with an external field.

For consistency with the later chapters, we write the above Hamiltonian in the equivalent form:

$$H_I(\sigma) = -\sum_{\{(i,j)\}} K_{s_i,s_j} - \sum_{k=0}^{1} \mu_k N_k, \quad \boldsymbol{K} = \begin{bmatrix} 1 & -1 \\ -1 & 1 \end{bmatrix}, \quad N_k = \sum_{i=1}^{N} \delta_{s_i,k}, \qquad (3.1)$$

where we replace the spins $s'_i \in \{-1, 1\}$ with $s_i = (s'_i + 1)/2$ and the pairwise interactions are given by the zero-based indexed symmetric matrix $\boldsymbol{K}$. Noting that $\sum_{k=1}^{N} s'_k = N_1 - N_0$ and $N_1 + N_0 = N$, the field interaction strength h can be related to the chemical potentials μ_0, μ_1 of respectively the solvent and solute particle reservoirs via:

$$2hN_1 - hN = (\mu_1 - \mu_0)N_1 - \mu_0 N = \Delta\mu N_1 - \mu_0 N. \tag{3.2}$$

hence, without loss of generality, we can take $\mu_0 = h$ and, therefore, $\Delta\mu = 2h$.

The $(\beta, \Delta\mu)$ phase diagrams of the model are well known in dimensions $d = 2, 3$ (Fig. 3.1a). A typical phase diagram consists of a single coexistence line $\Delta\mu = 0$, separating the vapour and liquid phases, which terminates at a system dimension dependent critical point $k_B T = k_B T_c(d)$. Beyond the critical point, the mechanisms of phase transformation no longer admit nucleation theoretic treatment. Within some region of $\Delta\mu > 0$ close to $\Delta\mu = 0$ and $T < T_c$ the vapour phase is metastable and nucleation of the liquid phase occurs. In addition to the ferromagnetic transition, the interface roughening transition, marking the gradual change between the regimes of cubical ($T < T_R$) and spherical ($T > T_R$) equilibrium crystal shapes [155], is known to occur at $T_R : 0.5T_c < T_R < 0.6T_c$ (for $d \in \{2, 3\}$) [156].

The Ising model presents an ideal testbed for CNT since most of the important macroscopic quantities, e.g. bulk surface tension, phase chemical potential difference at coexistence and $T_c(d)$, are known exactly or are well approximated. Furthermore, the simplicity of the Hamiltonian allows for implementation of highly efficient MC codes.

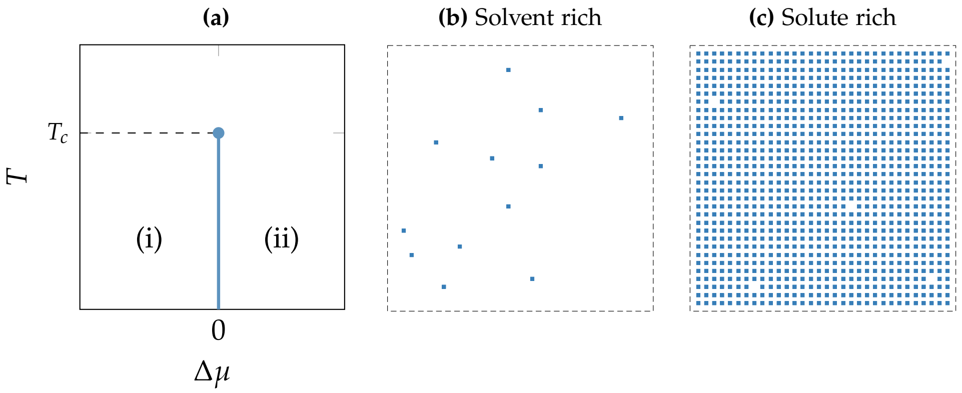

Figure 3.1: Schematic phase diagram for the Ising model in (a), and typical configurations of the two low temperature equilibrium states in (b) and (c) for $d = 2, \vec{l} = (32, 32)$. In (a), the solvent rich and solute rich regions are labelled (i) and (ii) respectively, and the solvent-solute coexistence line is shown in blue, with the critical point marked by a blue circle. In (b) and (c), the solute (spin "up") sites $s_i = 1$ are shown as blue squares, while the solvent (spin "down") $s_i = 0$ sites are omitted.

3.2.2 *Microscopic Kinetics*

The spin-flip kinetics (e.g. Glauber dynamics) have been a popular choice in studies of Ising models since they provide a reasonable microscopic model for magnetisation and condensation processes as well as avoid global depletion of liquid particles (solute) during formation and growth of the nucleus, thus keeping the $\Delta\mu$ constant over the course of the phase transformation process. In the context of a model of a solution, such kinetics, however, do not realistically treat particle transport or the effects of local solute depletion/augmentation due to particle attachment/detachment from the forming nucleus. The widely used single spin alternative – the local spin exchange (e.g. Kawasaki dynamics [157]) – allows spins to perform random walks on the lattice, effectively modelling particle diffusion. Pure Kawasaki dynamics does conserve particle counts and, therefore, suffers from the global solute depletion effects. Although various methods have been proposed to overcome these [158], as we will discuss in Chapter 7, accurate modelling of nucleation in the Ising system under realistic particle transport remains a challenge due to difficulties in modelling of particle density fluctuations of open systems.

It is well known that both choices of kinetics lead to breakdown of the Markov assumption on $n(t)$ – the stochastic process governing the evolution of the nucleus – as made by CNT [159, 160]. Unlike under Kawasaki dynamics, the behaviour of $n(t)$ under spin-flip dynamics appears approximately Markovian on a sufficiently long time scale [160]. While the consequences of the non-Markovian nature of $n(t)$ are still to be studied, earlier works [161, 162] have pointed out that the short time cluster kinetics of the Ising model under Kawasaki dynamics can be captured with surprising accuracy by (2.48) using explicit estimates of the cluster size dependent coefficients J_n^+, J_n^-. To our knowledge, however, the full nucleation kinetics in the Ising model under Kawasaki dynamics have not been studied in detail.

3.2.3 *Homogeneous Nucleation in Ising Models*

In absence of advanced methods for study of rare events, early MC simulations of nucleation in Ising models were largely restricted to conditions of high supersaturation, where the nucleation rates are relatively high. Under these conditions, the entire process of the phase transition is observable in a typical MC trajectory and nucleation rates can be estimated directly by computing the FPT distributions. The majority of these studies considered Glauber or equivalent spin-flip dynamics in $d \in \{2, 3\}$ systems evaluating the quality of the central prediction of CNT: $\ln J_{\text{CNT}} \propto (\beta\Delta\mu)^{-d+1}$. Despite the possibility of systematic errors due to nonstationarity, i.e. rapid decay of the metastable state [163], and effects of cluster coagulation [164–166], an overall reasonable agreement with the CNT prediction was widely reported [163, 167–172].

Studies focusing on the functional form of the expression for the free energy (2.54) reached less favourable conclusions. Simulations of liquid droplets in equilibrium with pure vapour showed that the average surface areas of small clusters obey a different scaling to the usual $n^{1-1/d}$ [173]. Although some evidence for cubical shapes of nuclei for $T < T_R$ is present [172], the validity of the compact nucleus assumption and the role of the roughening transition are questionable since for $T > T_R$ rough and anisotropic critical nuclei were reported [174–176]. Estimates of surface free energies of liquid clusters in coexistence with saturated vapour were also found to deviate from the CNT prediction [177, 178]. Explicit computations of droplet free energies, via thermodynamic integration in the constrained droplet size ensemble, suggested that (2.54) lacks a temperature dependent $\ln n$ term in $d = 2$ dimensions as well as a $n^{1/3}$ term in $d = 3$ dimensions [179,180]. Similar corrections were also proposed to explain brute force estimates of equilibrium cluster size distributions [181] and results of umbrella sampling calculations [66, 175, 176]. However, excellent fits of the classical expression to brute force estimates of $\Delta F(n)$ have been reported in $d = 2$ dimensions [182], leaving the overall status of (2.54) inconclusive.

Rate calculation methods relying on the basic elements of CNT have been explored. By examining the temperature and h dependence of J_{CNT} in (2.52), Vehkamäki and Ford developed a method of nucleation rate calculation based on estimates of critical cluster size and system's excess internal energy due to presence of a critical cluster [165]. Brendel *et al.* [182] considered an alternative approach to the master equation (2.48), expressing the nucleation rate in terms of the cluster size distribution and cluster attachment/detachment rates. Both methods produced rate estimates which were in reasonable agreement with available FPT based data.

More recently the Ising model has seen application of the rare event methodology, results of which appear to further support the general CNT framework. Results of a transition path sampling study [174] suggest that the CNT gives a reasonable estimate of the transmission coefficient, however the parameter dependence of this quantity was not examined. Ryu and Cai [175, 176] reported excellent agreement over a broad range of parameter space between nucleation rate estimates obtained via forward flux sampling and those given by (2.53), using explicitly computed cluster attachment rates and free energy barriers.

3.2.4 *The Potts Model*

The Potts model can be thought of as a generalisation of the Ising model to arbitrary number $Q \geq 2$ of site states $q_i \in \{1, \dots, Q\}$, with the following Hamiltonian:

$$H_P(\sigma) = -\sum_{\{(i,j)\}} \delta_{q_i,q_j} - \sum_{k=1}^{Q} h_k \sum_{i=1}^{N} \delta_{q_i,k}, \tag{3.3}$$

where $\{(i,j)\}$ is the set of all nearest neighbouring lattice site pairs and h_k is the strength of an applied external magnetic field of along the spin "direction" k.

Written in this form, the Hamiltonian is equivalent to a Q-component lattice gas, although often the one-field regime $h = h_{q^*} > 0, h_k = 0\,\forall k \neq q^*$ is considered in the literature. Generally, the above definition gives rise to two equilibrium states: (1) The low energy "ordered" state, where all spins assume some common value $q \in \{1, \ldots, Q\}$ (Fig. 3.2c); (2) The high entropy "disordered" state, where no long range order among spin values exists, i.e. spins assume random values in $\{1, \ldots, Q\}$ (Fig. 3.2b).

The model exhibits a temperature driven order-disorder phase transition which is believed to be first order for $Q \geq 5, d = 2$ and $Q \geq 3$, $d = 3$ [183]. Although the general phase diagram of the one-field model is not known exactly, reasonable numerical estimates for large Q in $d = 2$ exist (Fig. 3.2a) and qualitatively similar form can be expected in $d = 3$ [184]. The order-disorder coexistence line is the line $T^*(h \geq 0|d, Q)$ of first order phase transitions, terminating at the critical point $[h_c(d, Q), T_c(d, Q)]$. At zero field, the transition temperature is known exactly for $d = 2$ [184] and is approximately estimated via the mean-field approach in $d = 3$ for $Q \geq 3$ [185]:

$$T^*(0|2, Q \geq 4) = [\ln(1 + \sqrt{Q})]^{-1}, \quad T^*(0|3, Q \geq 3) = 3\frac{Q-2}{Q-1}[\ln(Q-1)]^{-1}. \tag{3.4}$$

At present, existence of metastable states in the vicinity of $T^*(h, d, Q)$ continues to be debated, and the lifetimes of the metastable states are thought to be system size dependent [186, 187]. Thus, in contrast to the field driven transition of the Ising model, the kinetics of the order-disorder transition in the Potts model cannot be quantified unambiguously, though the system size dependence of nucleation rates or free energy barriers has not been studied.

In the vicinity of the line $h_k = 0$, $k \in \{1, \ldots, Q\}$ below the order-disorder transition temperature – the line of coexistence points for the Q ordered phases – various field driven nucleation scenarios occur. Studies of nucleation kinetics over the course of field driven transitions in the Potts model have been carried out in $d = 2$ dimensions under spin-flip dynamics. Rutkevich reported good qualitative agreement of mean FPT estimates with the CNT prediction in the model with $h_k = 0$, $k \in \{1, 3, \ldots, Q\}$ [188]. Sanders *et al.* explored "multi-step" and competitive nucleation scenarios by including interactions between differently valued spins [189]. For this purpose, the Hamiltonian takes the equivalent to (3.1) form, with $\boldsymbol{K}$ being a $Q \times Q$ symmetric matrix with entries $K_{i,i} = 1$, $i \in \{1, \ldots, Q\}$. In a $Q = 3$ setting with $K_{1,2} = K_{1,3} > 0$, $K_{2,3} < 0$ and $0 = h_1 < h_2 \leq h_3$, Sanders *et al.* showed that ordered phase $q = 2$ has a nonzero probability of nucleating from phase $q = 1$ before nucleation of phase $q = 3$ takes place, thus pointing out the need for probabilistic interpretation of the Ostwald and Stranski-Totomanow conjectures, particularly in the regime where the free energy barriers to nucleation

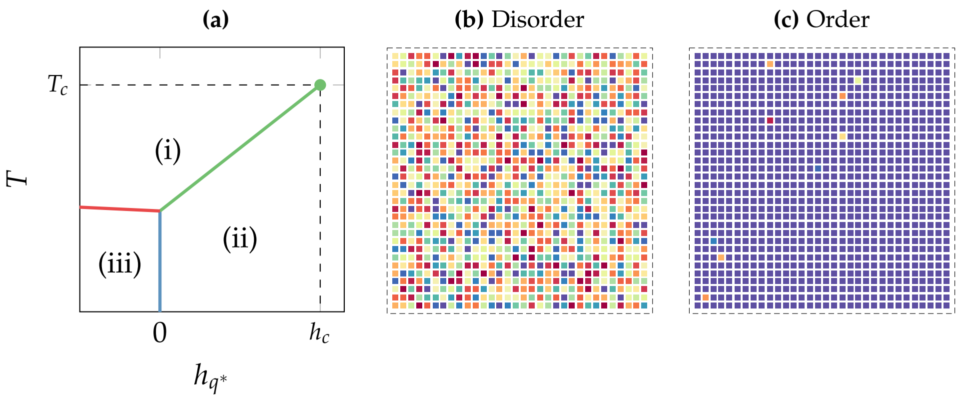

Figure 3.2: Schematic phase diagram (adapted from [184]) for the Potts model in (a), and typical configurations of the two equilibrium states in (b) and (c) for $d = 2$, $\vec{l} = (32, 32)$, $Q = 24$, $h_k = 0\,\forall k \neq q^*$. The three regions of (a) are: (i) Disordered state; (ii) Ordered state rich in spin values q^*; (iii) Ordered state poor in spin values q^*. In (b) and (c), lattice sites are represented by square markers with each spin value $q_i \in \{1, \dots, Q\}$ assigned one of $Q = 24$ colours. The critical point (h_c, T_c) is marked by a green circle.

of competing phases are comparable. Okamoto *et al.* employed a similar approach to model nucleation of polymorphic minerals from solution [190].

3.2.5 *The Potts Lattice Gas Model*

In order to explore mechanisms of crystal nucleation via amorphous precursors, several lattice models of anisotropic particles were formulated by combining elements of the Ising and Potts models [6,191,192]. In this work we will extend the Potts lattice gas (PLG) model of Duff and Peters [6,193], where solvent $(s_i = 0)$ and solute $(s_i = 1)$ particles are anisotropic, with their orientational degrees of freedom represented by an integer $q_i \in \{1, \dots, Q\}$. In addition to the usual (isotropic) nearest neighbour interaction, orientationally aligned, i.e. $q_i = q_j$, neighbouring particles i and j in the PLG model receive an energetic bonus A_{s_i,s_j}, thus:

$$H_{\text{PLG}}(\sigma) = -\sum_{\{(i,j)\}} \left[K_{s_i,s_j} + \delta_{q_i,q_j} A_{s_i,s_j}\right] - \sum_{k=0}^{1} \mu_k N_k, \tag{3.5}$$

where $\boldsymbol{K}$ and $\boldsymbol{A}$ are 2×2 matrices specifying the strengths of isotropic and anisotropic interaction between particles. For $Q \geq 3$ in $d = 3$ and:

$$\boldsymbol{K} = \begin{bmatrix} 1 & 0 \\ 0 & 1 \end{bmatrix}, \quad \boldsymbol{A} = \begin{bmatrix} 0 & 0 \\ 0 & 1 \end{bmatrix}, \tag{3.6}$$

we expect three distinct equilibrium states: (1) Solvent rich (low f); (2) Amorphous solute (low β, high f); (3) Crystalline solute (high β, high f); where we define the fugacity ratio f as:

$$f = \exp\left[\beta(\mu_1 - \mu_0)\right] = \exp\left[\beta\Delta\mu\right], \tag{3.7}$$

where $\Delta\mu$ is the difference between the chemical potentials of the solute and solvent reservoirs. At present, the (β, f) phase diagrams of the model have not been reported, however, based on the behaviours of Ising and Potts models, we can expect the sketch given in Fig. 3.3a to capture the key elements.

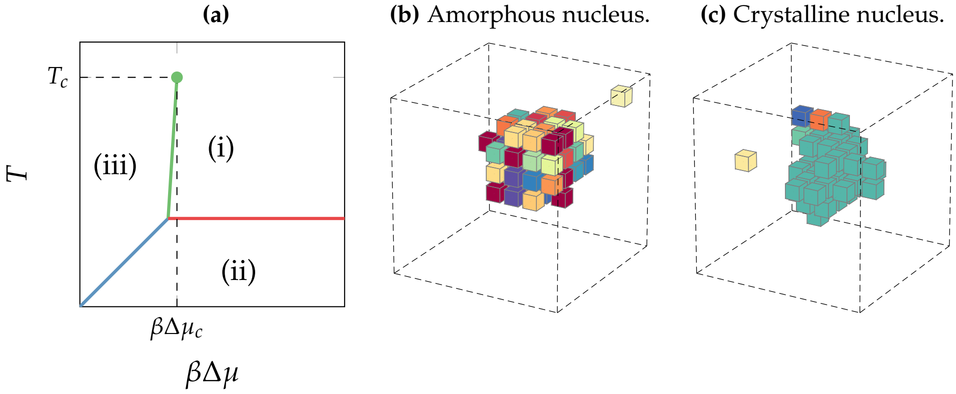

(a) **(b)** Amorphous nucleus. **(c)** Crystalline nucleus.

Figure 3.3: Schematic phase diagram for the PLG model in (a), and configurations of nuclei in coexistence with solvent in (b) and (c) for $d = 3$, $\vec{l} = (8, 8, 8)$, $Q = 24$ with $\boldsymbol{K}$ and $\boldsymbol{A}$ given by (3.6). The three regions in (a) are: (i) Amorphous solute rich (Fig. 3.2b); (ii) Crystalline solute rich (Fig. 3.2c); (iii) Solvent rich (Fig. 3.1b). Lattice configurations in (b) and (c) were obtained via standard NVT MC at $T = 0.7$ and $T = 0.3$ respectively. Solute ($s_i = 1$) lattice sites i are represented by cubes, assigned one of Q colours according to the value of q_i.

Nucleation of crystalline solute from supersaturated solvent in the PLG model under spin-flip dynamics was studied by means of free energy calculations. Duff and Peters [6] computed two dimensional free energy landscapes as functions of largest solute cluster size and its degree of internal orientational order at conditions where the ordered solute phase is thermodynamically stable in bulk. They showed that, at conditions sufficiently close to coexistence of ordered and disordered solute phases, amorphous solute nuclei (Fig. 3.3b) are thermodynamically more stable than crystalline nuclei (Fig. 3.3c), and hence the amorphous precursor nucleation pathway is thermodynamically viable. Whitelam and Hedges studied conceptually analogous models in two dimensions by mean field and simulation [78, 192], also noting the existence of amorphous precursor pathways. Using FFS, they showed that close to the crossover regime, where the free energy barriers along the ″direct″ and amorphous precursor pathways are comparable, the mobility of particles' orientational degrees of freedom can dictate the nucleation pathway [78].

More recently, the kinetics of nucleation in the $d = 3$ PLG model were studied under conditions where $K_{0,0} = K_{1,1}$, $A_{0,0} = A_{1,1}$ and $\Delta\mu \approx 0$, modelling the scenario of competitive crystallisation from a binary melt at eutectic composition [158]. Results of mean FPT calculations were reported to be in good qualitative agreement with CNT for a combination of Kawasaki and spin-flip dynamics.

3.2.6 *Other Models*

Soisson and Martin [166] studied kinetics of substitutional solid solution precipitation under vacancy diffusion in an Ising-like lattice model. They estimated the nucleation rates by measuring the rates of postcritical cluster formation at high supersaturations, showing good qualitative agreement with CNT. Jorge *et al.* used a multicomponent lattice gas system to model crystallisation of zeolite from clear solution, qualitatively reproducing experimental observations [191].

Kinetics in lattice models with spatially anisotropic interactions were explored as models of polymer aggregation and formation of amyloid fibrils, qualitatively reproducing experimental observations [194–196]. Various other lattice systems modelling thermodynamics and microscopic behaviour of polymer chains exist, however these will not be covered here.

Nucleation rates were recently measured in lattice systems by considering the kinetics of the nucleus without explicitly modelling the surrounding medium [197, 198]. In such models, nuclei kinetics are specified by saturation and particle interaction dependent attachment and detachment rates. While reasonable qualitative agreement was shown with CNT for Ising-like particle interactions, anomalous saturation dependence of nucleation rates was observed in the case of spatially anisotropic interactions [199].

3.2.7 *Heterogeneous Nucleation*

Lattice models have served as tools for exploration of mechanisms of heterogeneous nucleation. Although we will not consider heterogeneous systems in this work, for completeness, we will give a short overview of the relevant literature here.

A number of studies have been carried out on the Ising model. Page and Sear investigated nucleation in porous media by introducing a smooth surface with a shallow rectangular pit into an otherwise homogeneous $d = 2$ Ising system [200]. They showed that nucleation in a rectangular pore occurs as a two step process, with the total rate of the process varying nonmonotonically with pore width, allowing the pore geometry to be optimised to give maximum process rate. Sear considered the effect of impurity size on nucleation rate, modelling the impurity as a line of $w \in \{1, \ldots, 6\}$ "up" spins and showing that presence of even the smallest $w = 1$ impurity already gives a factor 2×10^4 increase in nucleation rate in comparison to a homogeneous system [201]. Nucleation on rough impurities in the Ising model was recently shown to give rise to nonexponential cumulative distribution of nucleation times [202]. Winter *et al.* employed a novel method of calculation of interfacial tensions, based on estimates of chemical potential in presence of a nucleus, demonstrating that the relationship between homogeneous and heterogeneous (smooth surface) interfacial tensions for varying contact angles is in line with theoretical predictions [203,204]. Nucleation on the surface was also studied under conditions where the system undergoes a crossover between regimes of surface nucleation followed by surface growth and surface nucleation followed by bulk growth [205]. Despite the change in the mechanism of phase transformation, the nucleation rate was found to vary smoothly over the parameter range where the crossover occurs.

The multi-component lattice gas analogue of the Potts model was used to illustrate the role of wetting in multi-step nucleation scenarios. It was shown that under conditions where a metastable phase interacts more favourably with impurities than the thermodynamically preferred phase, the former can nucleate ahead of the latter despite both having comparable solvent interfacial tensions [206]. Furthermore, in concave geometries, wetting by an unstable in bulk phase can occur. Under conditions of high solvent-solute but low solvent-intermediate and intermediate-solute interfacial tensions, wetting by the unstable intermediate phase was shown to accelerate nucleation of solute [207].

Mechanisms of heterogeneous freezing and condensation of water were also modelled in scenarios of surface contact at water to saturated vapour interface [208] and presence of non-volatile soluble impurities [209]. The former setting was investigated in a $d = 2$ Potts model, and nucleation was found to be fastest at the point where a liquid-liquid interface meets a smooth solid surface, though presence of liquid-liquid and liquid-solid contact lines also accelerated the process. This finding supports experimental studies of effects of partially submerged impurity particles on freezing of water. Effects of soluble non-volatile particles on liquid condensation were studied by theory and in a minimal $d = 3$ lattice model [209]. Using CNT based arguments, Sear showed that soluble impurities tend to stabilise liquid droplets, effectively eliminating the barrier to condensation at an impurity size dependent value of vapour supersaturation. Results of forward flux sampling MC in a $d = 3$ lattice model of liquid, vapour and solute particles gave a convincing qualitative verification of the finding.

Although typically in error, quantitative predictions of CNT, reported in the above studies, showed reasonable qualitative agreement with simulation.

4

MODEL AND PHASE BEHAVIOUR

Here we will introduce a novel lattice model which will be the central subject of study in this work. We will explore the phase behaviour of the model for low temperatures ($k_B T < 1.5$), mapping the phase diagram via free energy calculations and approximate analytical treatment.

4.1 THE EXTENDED POTTS LATTICE GAS MODEL

We extend the Potts lattice gas (PLG) model discussed in Sec. 3.2.5 by introducing an additional solute species. Thus, the extended PLG model is a three component system of particles on a cubic lattice with each site i having the two degrees of freedom $s_i \in \{0, 1, 2\}$ and $q_i \in \{1, \ldots, Q\}$, corresponding to the species and orientation labels respectively. We denote sites i with $s_i = 0$ as solvent and sites j with $s_j \in \{1, 2\}$ as solute, taking $Q = 24$.

4.1.1 *Particle Interactions*

As before, we specify the particle interactions in terms of the isotropic and anisotropic interaction matrices $\boldsymbol{K}$ and $\boldsymbol{A}$ respectively, which, in the case of the extended PLG, are 3×3 square matrices with entries $K_{s_i s_j}$ and $A_{s_i s_j}$ indexed by non-negative integers $s_i, s_j \in \{0, 1, 2\}$ corresponding to site species labels. The energy $E(\sigma)$ of a lattice configuration $\sigma \in \Lambda = \big\{(s, q) : s \in \{0, 1, 2\}, q \in \{1, \ldots, Q\}\big\}^N$ is given by:

$$E(\sigma) = -\sum_{\{(i,j)\}} K_{s_i s_j} - \sum_{\{(k,l)\}} \delta_{s_k s_l} A_{s_k s_l}, \tag{4.1}$$

where $\{(i, j)\}$ and $\{(k, l)\}$ are respectively the sets of unique nearest and unique diagonally neighbouring site pairs on a finite rectangular lattice with periodic boundaries. For every site i with nearest neighbours $\{j\}$, each member of the set of diagonal neighbours $\{k\}$ is a site which is a nearest neighbour of exactly two sites in $\{j\}$ (Fig. 4.1), giving 4 diagonal neighbours for every orthogonal plane in the d-dimensional lattice space for a total of

$$4\binom{d}{2} = 2\frac{d!}{(d-2)!} = 2d(d-1), \quad d \geq 2 \tag{4.2}$$

diagonal neighbours for every site i. Thus, for any d-dimensional hyperrectangular lattice with N sites, the total counts of unique nearest and unique diagonal neighbour pairs are respectively Nd and $Nd(d-1)$ for $d \geq 2$.

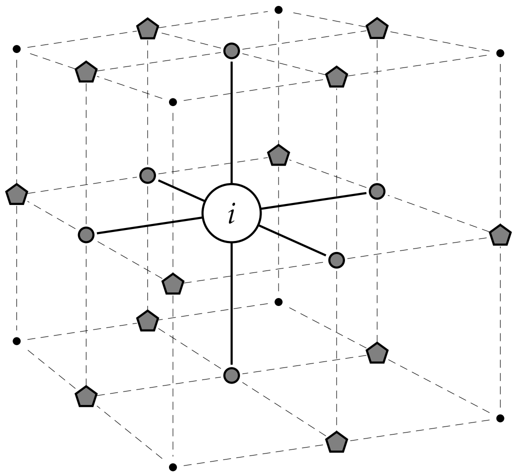

Figure 4.1: Visualisation of a $3 \times 3 \times 3$ cell of a cubic lattice showing nearest (grey circles) and diagonal (grey pentagons) neighbours of a lattice site i.

We define the isotropic and anisotropic interaction matrices as follows:

$$\boldsymbol{K} = \begin{bmatrix} 1 & 0 & 0 \\ 0 & 0 & 1 \\ 0 & 1 & 0 \end{bmatrix}, \qquad \boldsymbol{A} = \begin{bmatrix} 0 & 0 & 0 \\ 0 & c/(c+1) & 0 \\ 0 & 0 & 1/(c+1) \end{bmatrix}, \tag{4.3}$$

allowing the relative strength of anisotropic interactions between the two solute species to be controlled via the parameter $c \in [0.5, 1]$.

4.1.2 *The Hamiltonian*

The Hamiltonian $H(\sigma)$ is given by:

$$H(\sigma) = E(\sigma) - \sum_{i=0}^{2} \mu_i N_i(\sigma), \quad N_s(\sigma) = N_1(\sigma) + N_2(\sigma), \tag{4.4}$$

where μ_i and N_i are respectively the reservoir chemical potentials and particle counts for species $i \in \{0, 1, 2\}$ and we define $N_s(\sigma)$ as the number of solute sites in the lattice configuration σ. In this work, we will only consider the regime $\mu_1 = \mu_2$ where the chemical potentials of the two solute species are equal. We, therefore, define the fugacity ratio $f > 0$ as:

$$f = f_{01}, \quad f_{ss'} = \exp[\beta(\mu_{s'} - \mu_s)], \quad s, s' \in \{0, 1, 2\}, \tag{4.5}$$

as the sole parameter controlling the chemical composition of the system.

4.1.3 *Monte Carlo Move Sets*

We will consider the model in the semigrand (μVT) and canonical (NVT) ensembles, corresponding to two distinct MC move sets:

1. μVT: Transmutation-reorientation (TR) – analogous to spin-flip kinetics of the Ising model – conserving $\sum_{i=0}^{2} N_i(\sigma) = N$.
2. NVT: Diffusion-reorientation (DR) – analogous to Kawasaki [157] kinetics of the Ising model – conserving $N_s(\sigma) = n_s = \rho N$ and $N_0(\sigma) = N - n_s$, where ρ is the solute concentration.

Both move sets comprise two equally probable moves, one of which is the reorientation move attempting to replace the orientation label q_i of a randomly selected site i with an alternative label q_i' which is chosen uniformly from the set $\{1, \ldots, Q\}$ of possibilities. The transmutation move, as part of the TR move set, attempts to replace the species label s_i of a randomly chosen site i with an alternative s_i' uniformly selected on $\{0, 1, 2\}$. The diffusion move, as part of the DR move set, attempts to simultaneously swap both the species and orientation labels of a randomly chosen site and one of its randomly chosen nearest neighbours.

For any MC move $(s \to s', q \to q')$ attempting to replace the species s and orientation q labels of a single lattice site with the respective alternatives s' and q', the acceptance probability $\mathbb{P}_{\text{acc}}(s \to s', q \to q')$ is given by:

$$\mathbb{P}_{\text{acc}}(s \to s', q \to q') = \min\{1, f_{ss'} \exp[-\beta \Delta E(s \to s', q \to q')]\}, \tag{4.6}$$

where $\Delta E(s \to s', q \to q')$ is the change in the energy of the system in the case of the proposed move being accepted.

4.1.4 *Low Temperature Equilibrium States*

Exploring the parameter space $(k_B T, f)$ under the TR move set for $c = 0.5$, $k_B T < 1.5$, $Q = 24$, we find four distinct stationary system states as listed in Table 4.1. We find that the bulk solute rich states (Fig. 4.2) correspond to checkered arrangements of the two solute particle species as can be expected for the given definition of the isotropic interaction matrix $\boldsymbol{K}$. Periodic checkered particle arrangements can only be realised without interruption on rectangular periodic domains with dimensions $\vec{l}$ such that all lattice lengths l_i are even, and we will therefore only consider domains satisfying these conditions in this work.

4.2 COEXISTENCE POINT CALCULATIONS

Having established a rough sketch of the model's phase behaviour, we will now attempt to map the phase diagram. A wide selection of approaches to phase coexistence point calculations exists in the literature [210–215], and in this work we

Phase	**Label**	**Long Range q Order**	**Average Energy $-\langle E(\sigma)\rangle$**
Solvent Rich	–	–	$\sim Nd$
Disorder	**I**	–	$\sim Nd$
Partial Disorder	**II**	$s = 2$	$\sim Nd[1 + 0.5(d-1)(c+1)^{-1}]$
Order	**III**	$s \in \{1, 2\}$	$\sim 0.5Nd(d+1)$

Table 4.1: Listing of the stationary states in the extended PLG model for $k_B T < 1.5$, $c \in [0.5, 1]$, $Q = 24$ on cubic lattices with even dimensions $\vec{l}$. For all considered temperatures, the solvent rich ($\langle N_0(\sigma) \sim N$) state occurs at low values of $f < 1.0$. For $c = 0.5$, the three solute rich states ($\langle N_s(\sigma) \sim N$) are found at high values $f > 1.0$ with disordered (**I**), partially disordered (**II**) and ordered (**III**) structures being persistent at respectively high, intermediate and low values of $k_B T$. Specified in the "Long Range q Order" column are the solute species s for which long range orientational (q) order is present in the given phase.

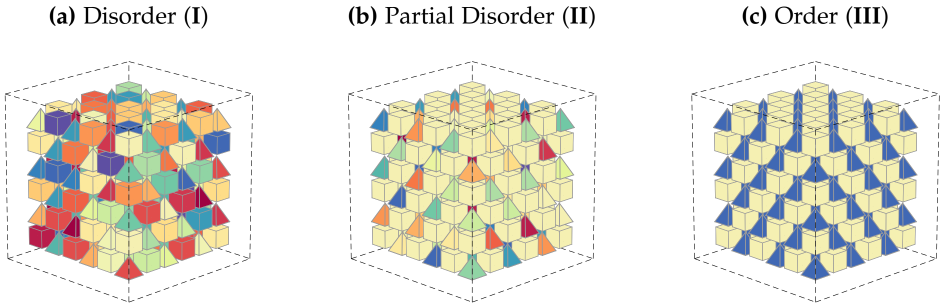
(a) Disorder (**I**) **(b)** Partial Disorder (**II**) **(c)** Order (**III**)

Figure 4.2: Visualisations of the bulk structures of the three solute rich states in the extended PLG model in $6 \times 6 \times 6$ cubic lattice cells. Lattice sites carrying species labels $s_i = 1$ and $s_i = 2$ are depicted as tetrahedra and cubes respectively, with distinct values of the orientation labels $q_i \in \{1, \ldots, Q\}$ being represented by one of the $Q = 24$ distinct colours.

will employ the combined ideas of multicanonical [216] and Wang-Landau [217] sampling strategies.

4.2.1 *Flat Histogram Method*

The central element of flat histogram sampling approaches is the observation that given the function $\eta_\lambda(\lambda) = \ln \mathbb{P}(\lambda)$, where $\mathbb{P}(\lambda)$ is the projection of the equilibrium microstate distribution $\mathbb{P}(\sigma)$ into the space of some order parameter $\lambda(\sigma)$, the distribution $\bar{\mathbb{P}}(\lambda)$ under the action of the bias $\eta_\lambda(\lambda)$ is uniform:

$$\begin{aligned} \bar{\mathbb{P}}(\lambda') &= \bar{Z}^{-1} \sum_{\{\sigma : \lambda(\sigma) = \lambda'\}} \exp\{-\beta H(\sigma) - \eta_\lambda[(\lambda(\sigma)]\} \\ &= \bar{Z}^{-1} Z \mathbb{P}(\lambda') \exp[-\eta_\lambda(\lambda')] = \bar{Z}^{-1} Z \propto 1, \end{aligned} \tag{4.7}$$

where $\bar{Z} = \sum_{\sigma \in \Lambda} \exp\{-\beta H(\sigma) - \eta_\lambda[(\lambda(\sigma)]\}$. The Wang-Landau recursion can be viewed as one of many sampling strategies for estimation of $\mathbb{P}(\lambda)$ based on utilisation of the above property of η_λ.

We implement a procedure analogous to the Wang-Landau recursion by, first, defining the range $[\lambda_{\text{min}}, \lambda_{\text{max}}]$ of a chosen one-dimensional order parameter λ. We then define a discretisation $\lambda_i \in \{\lambda_{\text{min}}, \lambda_{\text{min}} + \Delta\lambda, \ldots, \lambda_{\text{max}} - \Delta\lambda\}$ as a set of bins λ_i, $i \in \{1, \ldots, n_{\text{bin}}\}$ of width $\Delta\lambda$. Any value $\lambda(\sigma)$ of the order parameter falls into the ith bin of a histogram $h(\lambda_i)$ if $\lambda_i \leq \lambda(\sigma) < \lambda_{i+1}$. An estimate of the discrete analogue of $\eta_\lambda(\lambda)$ is obtained via iterative incremental refinement over the course of a MC simulation where a history dependent bias $\tilde{\eta}_k(\lambda_i)$ is introduced into the Metropolis acceptance criteria. At the kth iteration of the algorithm, we sample the histogram $h_k(\lambda_i)$ under the MC scheme where a move $\sigma \to \sigma'$ is accepted with probability

$$\min\left\{1, \exp\left[-\beta\{H(\sigma') - H(\sigma)\} - \{\tilde{\eta}_k[\lambda(\sigma')] - \tilde{\eta}_k[\lambda(\sigma)]\}\right]\right\}, \tag{4.8}$$

and the histogram $h_k(\lambda_i)$ and the bias $\tilde{\eta}_k(\lambda_i)$ are updated according to:

$$h_k(\lambda_i) \leftarrow h_k(\lambda_i) + 1, \quad \tilde{\eta}_k(\lambda_i) \leftarrow \tilde{\eta}_k(\lambda_i) + \Delta\eta_k, \quad \lambda_i : \lambda_i \leq \lambda(\sigma'') < \lambda_{i+1}, \tag{4.9}$$

where $\sigma'' \in \{\sigma, \sigma'\}$ is the system's microstate upon rejection or acceptance of the proposed move and $\Delta\eta_k = 2^{-k}\Delta\eta_0 \geq \Delta\eta_{\text{min}}$ is the iteration dependent bias increment. The kth iteration is terminated if the histogram $h_k(\lambda_i)$ achieves the flatness criterion:

$$0.95\bar{h}_k < h_k(\lambda_i) < 1.05\bar{h}_k \; \forall i \in \{1, \ldots, n_{\text{bin}}\}, \quad \bar{h}_k = \frac{1}{n_{\text{bin}}} \sum_{i=1}^{n_{\text{bin}}} h_k(\lambda_i), \tag{4.10}$$

and we take $\tilde{\eta}_k(\lambda_i)$ as an estimate of the discretised η_λ when the flatness criterion is satisfied for the final iteration $k : \Delta\eta_k = \Delta\eta_{\text{min}}$.

Statistical and systematic errors, convergence properties and various refinements of the above approach have been examined by multiple studies [218–220] and it is well known that the presented sampling strategy is, in many respects, not optimal. In this work, however, we will only aim to obtain approximate values of phase coexistence points for which, as we shall see, the procedure listed above is adequate.

4.2.2 *Histogram Reweighting*

Specific choices of λ can allow for estimation of $\mathbb{P}(\lambda|\beta', \vec{\mu}')$ based on a known distribution $\mathbb{P}(\lambda|\beta, \vec{\mu})$ at a different point in the parameter space. Choosing the system's energy $E(\sigma)$ as an order parameter yields:

$$\frac{\mathbb{P}(E'|\beta')}{\mathbb{P}(E'|\beta)} \propto \frac{e^{-\beta' E'} \sum_{\sigma : E(\sigma) = E'} f^{N_s(\sigma)}}{e^{-\beta E'} \sum_{\sigma : E(\sigma) = E'} f^{N_s(\sigma)}} = \exp[-(\beta' - \beta)E']. \tag{4.11}$$

Similarly, we may choose the number of solute particles N_s in the system as another order parameter yielding:

$$\frac{\mathbb{P}(N_s'|f_b)}{\mathbb{P}(N_s'|f_a)} \propto \frac{f_b^{N_s'} \sum_{\sigma:N_s(\sigma)=N_s'} e^{-\beta E(\sigma)}}{f_a^{N_s'} \sum_{\sigma:N_s(\sigma)=N_s'} e^{-\beta E(\sigma)}} = \left(\frac{f_b}{f_a}\right)^{N_s'}. \tag{4.12}$$

Thus, given a sufficiently accurate initial estimate $(\beta, \vec{\mu})$ of the phase coexistence point $(\beta^*, \vec{\mu}^*)$, by choosing an appropriate order parameter λ, the initial estimate can be refined via reweighting of the distribution $\mathbb{P}(\lambda|\beta, \vec{\mu})$ to the point where the coexistence condition is satisfied:

$$\sum_{\sigma \in A} \mathbb{P}[\lambda(\sigma)|\beta^*, \vec{\mu}^*] = \sum_{\sigma \in B} \mathbb{P}[\lambda(\sigma)|\beta^*, \vec{\mu}^*], \tag{4.13}$$

where A and B are the coexisting phases.

4.2.3 *Validation for Ising-like Lattice Gas*

We now consider solute-solvent coexistence in a two component ($s_i = 0$ for solvent and $s_i = 1$ for solute) Ising-like lattice gas model with the Hamiltonian $H_{\mathrm{LG}}(\sigma)$ given by:

$$H_{\mathrm{LG}}(\sigma) = \sum_{\{(i,j)\}} K_{s_i s_j} - N_s(\sigma) k_B T \ln f, \quad \boldsymbol{K} = \begin{bmatrix} 1 & 0 \\ 0 & 2 \end{bmatrix}, \tag{4.14}$$

where we set to solvent chemical potential $\mu_0 = 0$ without loss of generality. The exact value f_* of f at solute-solvent coexistence can be obtained by various means, and here we will employ an approach based on the Widom expression [221] for chemical potential of particle species, which, for lattice systems [76], can be derived from the following observation:

$$\begin{aligned} Z_{n_s+1} &= \frac{1}{n_s+1} \sum_{\sigma \in \Lambda_{n_s}} \sum_{\vec{x} \in X(\sigma)} \exp\{-\beta H(\sigma) - \beta \Delta H(\sigma, \vec{x})\} \\ &= Z_{n_s} \frac{N - n_s}{n_s + 1} \langle \exp\{-\beta \Delta H\} \rangle_{\sigma \in \Lambda_{n_s}} = f Z_{n_s} \frac{|\Lambda_{n_s+1}|}{|\Lambda_{n_s}|} \langle \exp\{-\beta \Delta E\} \rangle_{\sigma \in \Lambda_{n_s}}, \end{aligned} \tag{4.15}$$

where the NVT partition function Z_{n_s+1} for the system with $n_s + 1$ solute particles is constructed from a partition function Z_{n_s} by considering replacement of a solvent particle with solute at all possible $N - n_s$ positions $X(\sigma)$ in configurations $\Lambda_{n_s} = \{\sigma : N_s(\sigma) = n_s\}$ of the n_s ensemble. The symbols $\Delta H(\sigma, \vec{x})$ and ΔH in the above expression denote the change in the system's Hamiltonian due to insertion of a solute particle at respectively a specific lattice position $\vec{x}$ and a randomly chosen available position in a configuration sampled from the distribution of the n_s ensemble.

The solute chemical potential $\mu_{n_s}(\beta, f)$ of a system with n_s solute particles can be written as:

$$\mu_{n_s}(\beta, f) = F(n_s + 1|\beta, f) - F(n_s|\beta, f), \quad F(n_s|\beta, f) = -k_B T \ln \frac{Z_{n_s}(\beta, f)}{Z(\beta, f)}, \tag{4.16}$$

where $F(n_s|\beta, f)$ is the μVT free energy of the system with n_s solute particles and $Z(\beta, f)$ is the corresponding partition function. Noting that the energy of the given lattice gas can be computed by counting the unique neighbouring pairs of particles: $E_{\text{LG}}(\sigma) = \sum_{i=0}^{1} N_{ii}(\sigma) K_{ii}$, where $N_{ij}(\sigma)$ is a count of unique neighbouring pairs of particles of species i and j, it is easy to show that:

$$F(n_s|\beta, f_*) = F(N - n_s|\beta, f_*) \, \forall n_s \in \{1, \ldots, N\}, \tag{4.17}$$

by symmetry of the state space under the operation which replaces all solute particles with solvent and vice versa. Although the above condition is sufficient to obtain the exact values of $f_*(\beta)$, we can also consider the equivalent condition of equality of chemical potentials:

$$\mu_{n_s}(\beta, f_*) = -\mu_{N-n_s-1}(\beta, f_*) \, \forall n_s \in \{1, \ldots, N\}, \tag{4.18}$$

which states that the change in free energy of the system at coexistence due to insertion of a solute particle into a $N_s(\sigma) = n_s$ configuration is equal to that due to insertion of a solvent particle into a $N_s(\sigma) = N - n_s$ configuration. Solving the equation $\mu_{n_s}(\beta, f_*) + \mu_{N-n_s-1}(\beta, f_*) = 0$, with $n_s = 0$ for f_* we obtain the solute-solvent coexistence line for the given lattice model:

$$\ln f_*(\beta) = -\frac{1}{2} \left\{ \ln \langle e^{-\beta \Delta E} \rangle_{\sigma \in \Lambda_{n_s=0}} + \ln \langle e^{-\beta \Delta E} \rangle_{\sigma \in \Lambda_{n_s=N-1}} \right\} = -3\beta. \tag{4.19}$$

Taking the bin width of $\Delta\lambda = 1$ with $\lambda_{\min} = 0$, $\lambda_{\max} = N$, we now apply the procedures discussed in Secs. 4.2.1 and 4.2.2 to obtain the coexistence values $f_*(\beta)$ via MC for the cubic $\vec{l} = (4, 4, 4)$ lattice gas model by computing the free energies $F(n_s|\beta, f)$. As shown in Fig. 4.3, we find the numerical estimates of the coexistence points in excellent agreement with Eq. (4.19).

4.3 APPROXIMATE COEXISTENCE POINTS

In this section we will apply the approach of Sec. 4.2.3 along with the mean field theory for the Potts model [Eq. (3.4)] to obtain approximate expressions for the coexistence points of the four considered phases in the extended PLG model.

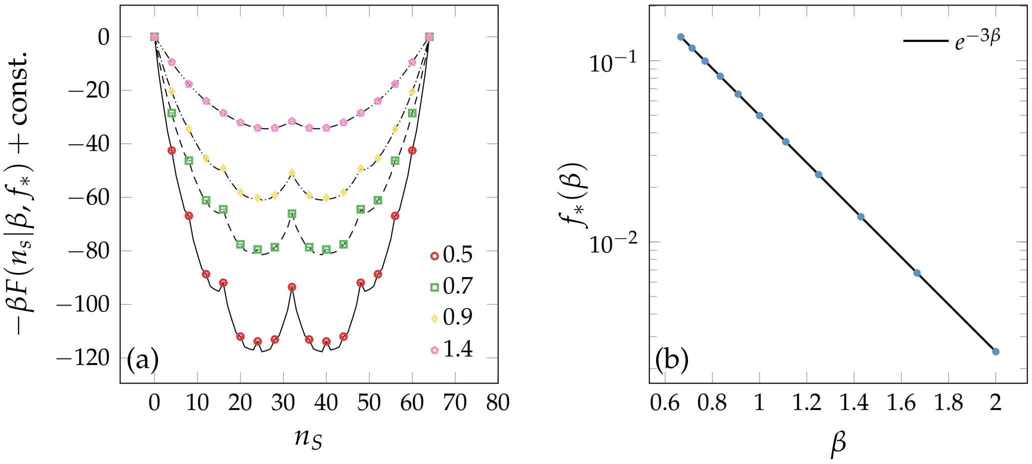

Figure 4.3: Free energies $F(n_s|\beta, f_*)$ [(a)] and solute-solvent coexistence points $f_*(\beta)$ [(b)] for the lattice gas model defined by Eq. (4.14). The four shown sets of estimates of $F(n_s|\beta, f_*)$ (lines and markers) in (a) were computed at the four values of $k_B T$, specified in the legend, by reweighting the estimates $F(n_s|\beta, f = 1.0)$, obtained via the flat histogram approach taking $\Delta\eta_0 = 2^{-2}$, $\Delta\eta_{\text{min}} = 2^{-20}$. The corresponding estimates of $f_*(\beta)$ (markers) are plotted in (b). Error bars in (a) and (b) (smaller than markers) indicate the maximum and minimum deviation from the mean value of a set of 10 independent estimates.

4.3.1 *Mean Field Solute Phase Coexistence points*

In order to determine the **I** − **II** and **II** − **III** phase coexistence points it is sufficient to consider the high f limit of the parameter space, where the extended PLG model can be thought as an interweave of two decoupled Q-state Potts lattices, each having the coordination number $N_{\text{nbr}} = 12$. The general mean field expression for the order-disorder coexistence temperature $\beta_\dagger$ in the 3D Q-state Potts model is given by:

$$\beta_\dagger^{-1}(Q) = I N_{\text{nbr}} \frac{Q-2}{Q-1} \left[2 \ln(Q-1)\right]^{-1}, \tag{4.20}$$

where I is the strength of interaction between aligned particle pairs. Taking $I = (c+1)^{-1}$ for **II** − **III** coexistence and $I = c(c+1)^{-1}$ for **I** − **II** coexistence, we obtain the mean field solution for the coexistence points of the three solute rich phases in the extended PLG model.

We sample the probability distribution $\mathbb{P}(E) = \exp[-\beta F(E)]$ over the set of the system's energy states in the range $E \in [3N, 6N]$ by applying the flat histogram method. As shown in Fig. 4.4a, the distribution $\mathbb{P}(E)$ exhibits three clear peaks at energy values close to the approximate estimates for the three solute rich phases given in Table 4.1. By reweighting the numerically computed profiles $F(E)$ we obtain estimates of coexistence points for the three solute phases (Fig. 4.4b), showing reasonable agreement with the values produced by Eq. 4.20.

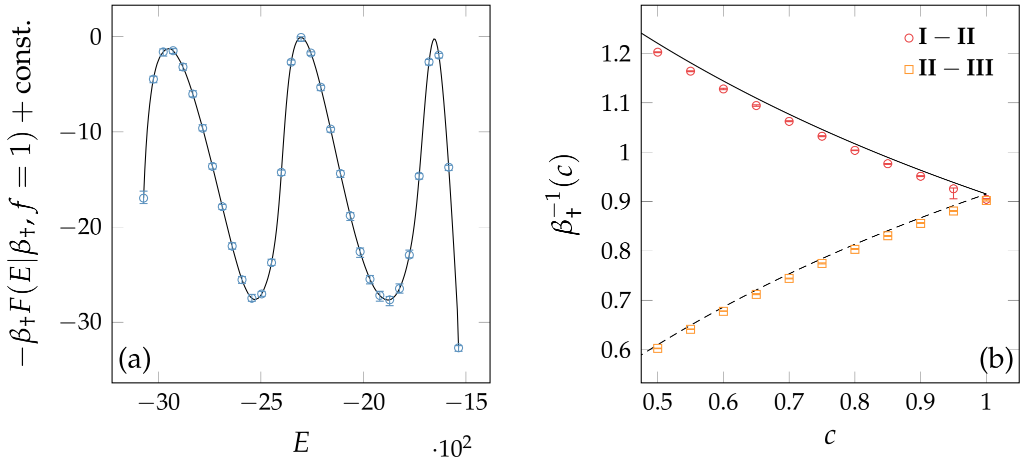

Figure 4.4: Numerically obtained free energy profile $F(E)$ at order-disorder coexistence for $f = 1$, $c = 1$ [(a)] and solute phase coexistence points [(b)] for various values of parameter $c \in [0.5, 1.0]$ [Eq. (4.3)] in the $Q = 24$ cubic $\vec{l} = (8, 8, 8)$ extended PLG model. Lines and markers in (a) correspond to values produced by the flat histogram method taking $\Delta\eta_0 = 2^{-2}$, $\Delta\eta_{\text{min}} = 2^{-20}$. Markers in (b) are the the coexistence point coordinates obtained via reweighting of numerical estimates of $F(E)$, while the lines show the corresponding mean field values as given by Eq. (4.20). Error bars (smaller than markers) indicate the ranges of numerical estimates based on at least 10 independent repetitions of the flat histogram method at every point.

4.3.2 *Solvent-Solute Coexistence in the Extended PLG*

We can derive an analogue of the Eq. (4.19) for the extended PLG model via:

$$\ln f_*(\beta) \approx -\frac{1}{2}\left\{\ln\frac{|\Lambda_{n_s=1}||\Lambda_{n_s=N}|}{|\Lambda_{n_s=0}||\Lambda_{n_s=N-1}|} + \ln\langle e^{-\beta\Delta E}\rangle_{\sigma\in\Lambda_{n_s=0}} + \ln\langle e^{-\beta\Delta E}\rangle_{\sigma\in\Lambda_{n_s=N-1}}\right\}, \tag{4.21}$$

where $|\Lambda_{n_s}| = Q^N 2^{n_s}\binom{N}{n_s}$, however, the state space symmetry argument towards Eqs. (4.17) and (4.18) does not apply here due to the presence of multiple solute species and anisotropic interactions. Additionally, due to ergodicity breaking in the large N limit, not all states in $\Lambda_{n_s=N}$ and $\Lambda_{n_s=N-1}$ are accessible to the system in the NVT ensemble, which is not taken into account by the above expression. We will now attempt to use the above expression to obtain an approximation to the solute-solvent coexistence curve for the extended model at $c = 1$.

We first note that at all considered conditions $\ln\langle e^{-\beta\Delta E}\rangle_{\sigma\in\Lambda_{n_s=0}} = e^{-6\beta}$. Assuming no short range order in **I** and perfect short range order in **III**, the respective solute insertion probabilities can be approximated by:

$$\langle e^{-\beta\Delta E}\rangle^{(\mathbf{I})}_{\sigma\in\Lambda_{n_s=N-1}} \approx \frac{1}{2} + \frac{1}{2}\sum_{i=0}^{12}\binom{12}{i} e^{(6+i/2)\beta} Q^{-i}(1-Q^{-1})^{12-i}, \tag{4.22}$$

$$\langle e^{-\beta\Delta E}\rangle^{(\mathbf{III})}_{\sigma\in\Lambda_{n_s=N-1}} \approx \frac{1}{2} + \frac{1}{2}Q^{-1}\left(Q - 1 + e^{6\beta}\right)e^{6\beta}, \tag{4.23}$$

where we take into account the possibility of interruption of the checkered arrangement of solute particles upon solute insertion. Due to ergodicity breaking at low temperatures, the disordered solute phase, like **III**, cannot easily transform between the two available checkered structures while the ordered solute phase is also unable to explore the Q^2 energetically equivalent ordered arrangements. This factors into the entropic contribution of Eq. (4.21) as follows:

$$\frac{|\Lambda_{n_s=1}||\Lambda_{n_s=N}|}{|\Lambda_{n_s=0}||\Lambda_{n_s=N-1}|} = 2N\frac{|\Lambda_{n_s=N}|}{|\Lambda_{n_s=N-1}|} = \begin{cases} 2 & \text{for } \mathbf{I}, \\ 2Q^{-1} & \text{for } \mathbf{III}. \end{cases} \tag{4.24}$$

Ignoring the negligible $\exp(-6\beta) < 2 \times 10^{-2}$, $\forall k_B T < 1.5$ term, we arrive at:

$$f_*(\beta) = \begin{cases} \left[Q\left(Q-1+e^{\beta/2}\right)^{-1}\right]^6, & \beta \leq \beta_*(Q), \\ Q\left(Q-1+e^{6\beta}\right)^{-1/2}, & \beta \geq \beta_*(Q), \end{cases} \tag{4.25}$$

where $\beta_*(Q)$ is the intersection point defined implicitly by $\left(Q-1+e^{\beta_*/2}\right)^{12} Q^{-10} = Q-1+e^{6\beta_*}$, which, we find, converges as power law to $\beta_\dagger(Q)$ [Eq. (4.20)] for large Q. As shown in Fig. 4.5b, the above expression is in reasonable agreement with the solute-solvent coexistence curve estimated via the flat histogram method.

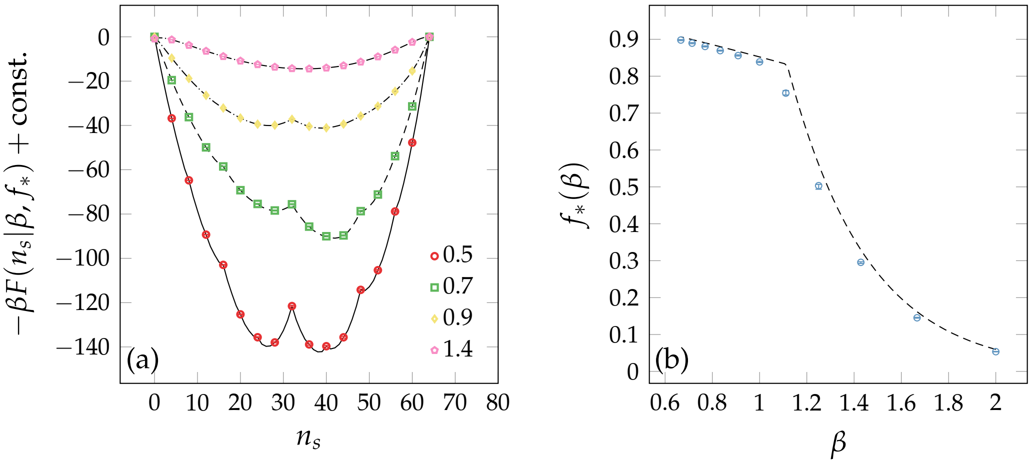

Figure 4.5: Numerically obtained free energy profiles $F(N_s|\beta, f_*)$ at solute-solvent coexistence $f_*(\beta)$ for four values of $k_B T$ (legend) [(a)]; and solute-solvent coexistence points [(b)] for $k_B T \in [0.5, 1.5]$ in the $Q = 24$, $c = 1$ cubic $\vec{l} = (4, 4, 4)$ extended PLG model. Lines and markers in (a) correspond to values produced by the flat histogram method taking $\Delta\eta_0 = 2^{-2}$, $\Delta\eta_{\min} = 2^{-20}$. Markers in (b) are the the coexistence point coordinates obtained via reweighting of numerical estimates of $F(N_s|\beta, f = 1)$, while the dashed line shows the corresponding values given by the approximation of Eq. (4.25). Error bars (smaller than markers) indicate the ranges of numerical estimates based on 10 independent repetitions of the flat histogram method for every point.

4.4 PHASE DIAGRAMS

The phase diagrams for the extended PLG model at $c \in \{0.5, 1.0\}$ are shown in Fig. 4.6. Due to the small system sizes used in MC computation of the phase coexistence points, we cannot comment on the accuracy of the approximations or the magnitude of the finite size corrections here. As we shall see in the subsequent chapters, however, the approximations developed in this chapter are sufficiently accurate for the purposes of this study.

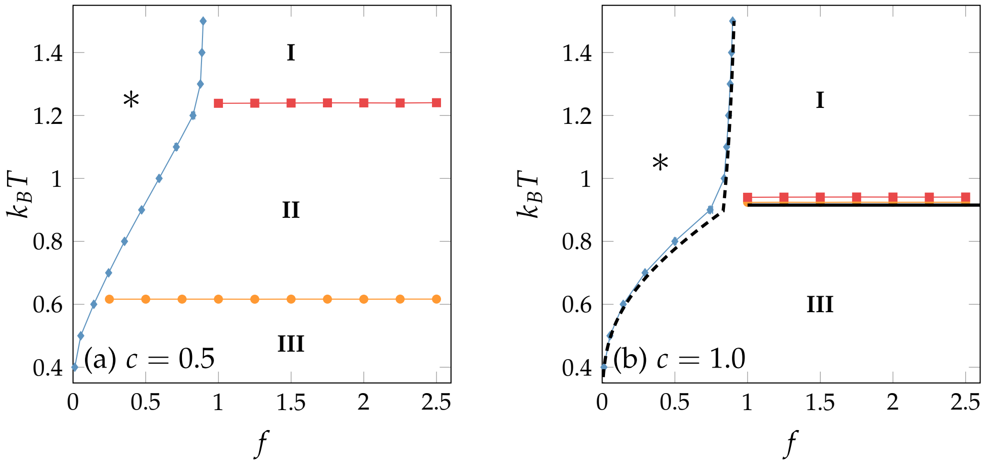

Figure 4.6: Phase diagrams for the $Q = 24$, $d = 3$ extended PLG model at $c = 0.5$ [(a)] and $c = 1.0$ [(b)], showing the boundaries of stability regions of solvent rich ($*$), disordered solute (**I**), partially ordered solute (**II**) and ordered solute (**III**) phases. Markers correspond to coexistence point estimates obtained via the flat histogram and reweighting approaches as detailed in Sec. 4.3 with error bars (smaller than markers) showing the full ranges of values over a minimum of 10 independent calculations. The solid and dashed lines in (b) are the approximate values of coexistence points obtained via respectively Eqs. (4.20) and (4.25).

4.4.1 *Solute Fugacity and Concentration*

The solute-solvent chemical potential difference can be defined as per solute monomer difference in free energy between solute rich and solvent rich states. This definition corresponds to the gradient of the straight line drawn from the point $[0, F(n_s = 0|\beta, f)]$ to the point $[N, F(n_s = N|\beta, f)]$, which can be related to the ratio $f/f_*(\beta)$ by assuming $F(n_s = 0|\beta, f_*) = F(n_s = N|\beta, f_*)$, yielding the expression:

$$\Delta\mu_{\text{coex}}(\beta, f) = \beta^{-1}[\ln f - \ln f_*(\beta)]. \tag{4.26}$$

If setting the solvent species chemical potential $\mu_0 = 0$, the above expression gives the difference in solute chemical potentials at the point (β, f) and at coexistence (β, f_*), which is the CNT definition of the driving force to nucleation [75]. In Fig. 4.7 we plot the solute concentration $\rho = N_s/N$ against f and $\Delta\mu_{\text{coex}}$, showing that the CNT assumption $\ln \rho \propto \Delta\mu_{\text{coex}}$ holds at constant temperature.

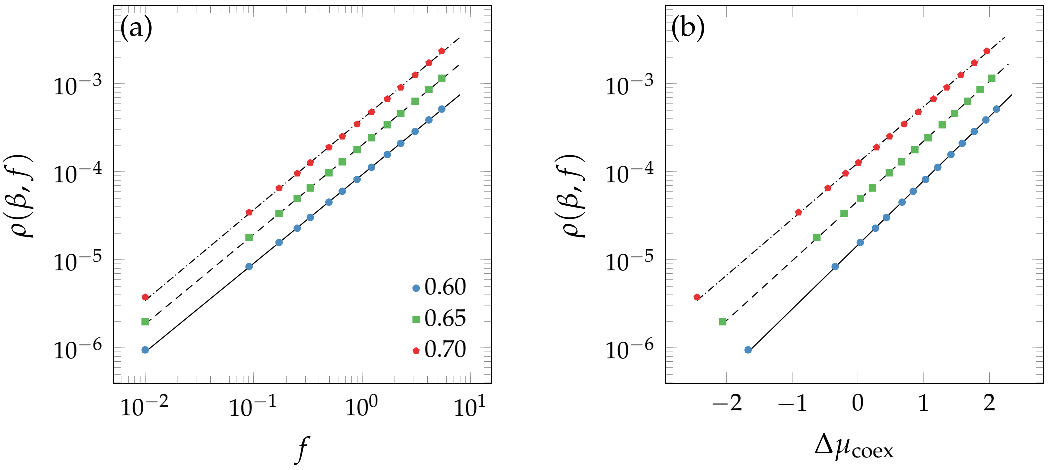

Figure 4.7: Solute concentration $\rho(\beta, f)$ plotted against solute fugacity [(a)] and solute-solvent chemical potential difference [(b)] at three values of $k_B T$ (legend) in the $c = 1$, $Q = 24$, $d = 3$ extended PLG model. Markers correspond to estimates computed from MC trajectories of 2^{20} MCS long in $\vec{l} = (64, 64, 64)$ systems, with error bars (smaller than markers) calculated by taking the means of 2^{10} MCS long trajectory segments as independent estimates and obtaining the 99% confidence intervals on the means of the resultant distributions. Lines correspond to polynomial fits to the MC estimates.

4.4.2 *Low Temperature Metastability of Disordered States*

As shown above, the extended PLG model reduces to a variant of the Potts model in the high f limit, allowing us to make use of the existing results for the Potts model here. Currently, presence of metastability in the d-dimensional Q-state Potts models is debated with recent evidence [186, 187, 222] pointing to such metastability being a finite size effect. Thus we do not expect the disordered or partially disordered phases **I** and **II** in our model at $c = 1$ to be metastable in bulk below the order-disorder transition temperature, and we will provide some evidence towards this in the next chapter.

5

EQUILIBRIUM CLUSTER DISTRIBUTIONS

In this chapter we will discuss the approaches and the results of sampling the equilibrium size and internal orientational order distributions of solute nuclei in the cubic $c = 1$, $Q = 24$, $d = 3$ extended PLG model at low temperatures. We will start by defining the relevant order parameters followed by a discussion of a path sampling approach to free energy calculations. Using the path based enhanced sampling method, we will compute the equilibrium distributions of nuclei sizes and examine the size dependence of the preferred internal orientational order of nuclei at equilibrium.

5.1 ORDER PARAMETERS

In this work, we will employ the geometric definition [1,76] of particle clusters in lattice models, i.e. a particle on the lattice is a member of a given cluster if it neighbours at least one other particle in the given cluster. It is well known that the geometric definition of particle clusters conflicts with the physical definition and leads to an incorrect treatment of the percolation transition. At the low temperatures and particle densities considered in this work, however, we do not expect to encounter any of the problems associated with the percolation transition and we will examine the thermodynamic and kinetic meaningfulness of the geometric cluster definition via appropriate calculations.

We define the order parameter $n(\sigma)$ as the size of the largest geometric cluster of solute particles present in the given microstate σ, without requiring any structure in the cluster's internal arrangement of the solute particles. By computing the proportions of aligned diagonal solute particle pairs within the largest solute cluster, we additionally quantify the degree of the cluster's internal structural order via the order parameters $v(\sigma) \in [0, 1]$ and $\chi(\sigma) \in [0, 1]$:

$$v(\sigma) = \max\left\{\phi_1(\sigma)\Phi_1^{-1}(\sigma), \phi_2(\sigma)\Phi_2^{-1}(\sigma)\right\}, \tag{5.1}$$

$$\chi(\sigma) = \begin{cases} v^{-1}(\sigma)\min\left\{\phi_1(\sigma)\Phi_1^{-1}(\sigma), \phi_2(\sigma)\Phi_2^{-1}(\sigma)\right\} & \text{if } v(\sigma) > 0, \\ 0 & \text{otherwise,} \end{cases} \tag{5.2}$$

where $\Phi_s \in \mathbb{N}$ and $\phi_s \in \mathbb{N}$ are, respectively, the total number and the number of aligned diagonal particle pairs of species $s \in \{1,2\}$ internal to the largest solute cluster.

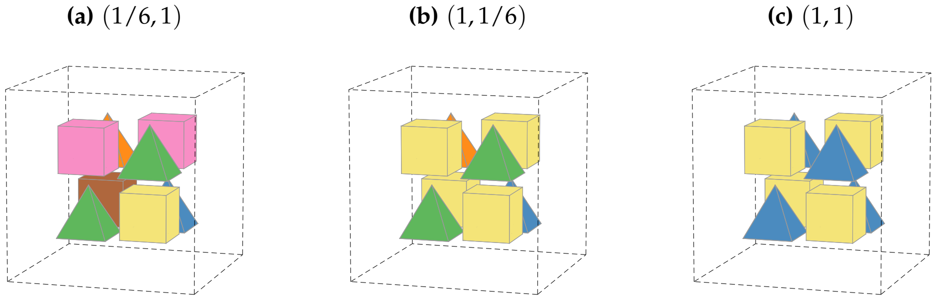
(a) $(1/6,1)$ **(b)** $(1,1/6)$ **(c)** $(1,1)$

Figure 5.1: Visualisations of cubic $\vec{l} = (2,2,2)$ lattice configurations of the $Q = 24$, $d = 3$ extended PLG model fully occupied by solute nuclei $n(\sigma) = 8$ with $\Phi_1 = \Phi_2 = 6$, showing structures with various degrees of internal orientational order and the corresponding values of the structural order parameter $[v(\sigma), \chi(\sigma)]$.

The choice of the structural order parameter (v, χ) is motivated by the energetics of the solute states in the extended PLG model: for any configuration σ such that the lattice is fully occupied by a checkered arrangement of solute particles $s \in \{1,2\}$, the energy is given by $-E(\sigma) = Nd + [c\phi_1(\sigma) + \phi_2(\sigma)]/(c+1)$. In Sec. 4.3 we have already shown that the energy $E(\sigma)$ of the system serves as a good order parameter for distinguishing between the bulk solute phases, and we can loosely classify the solute nuclei by defining three order parameter regions $\{(v,\chi)\}_\mathbf{X}$, $\mathbf{X} \in \{\mathbf{I}, \mathbf{II}, \mathbf{III}\}$:

1. Disordered nuclei: $\{(v,\chi)\}_\mathbf{I} = \{(v,\chi) : v \in [0, 0.5],\ \chi \in [0,1]\}$.
2. Partially disordered nuclei: $\{(v,\chi)\}_\mathbf{II} = \{(v,\chi) : v \in (0.5, 1],\ \chi \in [0, 0.5]\}$.
3. Ordered nuclei: $\{(v,\chi)\}_\mathbf{III} = \{(v,\chi) : v \in (0.5, 1],\ \chi \in (0.5, 1]\}$.

Upon a rapid quench to low temperatures, order-disorder transitions in Potts-like spin systems are known to proceed via domain coarsening, where multiple domains (grains) of aligned spins form, leading to a frustrated "polycrystalline" state or extremely slow relaxation towards a globally ordered – "monocrystalline" – state [223]. For the purposes of this work, we identify "polycrystalline" states as subsets of their corresponding ordered phases (**II** or **III**), as is achieved by the above classification scheme over the considered range of temperatures.

5.2 ENHANCED SAMPLING METHOD

Once again, a multitude of methods for enhanced sampling of order parameter distributions exist [224], many of which have already been mentioned in Sec. 4.2.

In this chapter, we consider the equilibrium path sampling (EPS) or "BOLAS" approach [225], thereby providing an introduction to the path sampling methodology which will be useful in Chapter 7.

5.2.1 *Equilibrium Path Sampling*

A path through the system's configuration space can be viewed as a sequence $\vec{\sigma} = (\sigma_1, \sigma_2, \dots, \sigma_\tau)$ of configurations $\sigma_i \in \Lambda$, such that any microstate σ_{i+1} in the sequence can be constructed from σ_i via acceptance of a single MC move, i.e. $\mathbb{P}(\sigma_i \to \sigma_{i+1}) > 0\, \forall i \in \{1, \dots, \tau - 1\}$. By the Markov property, the probability $\mathbb{P}(\vec{\sigma})$ of any path $\vec{\sigma}$ can be written in the form of Eq. (2.12), which allows us to develop a MC approach for path sampling.

We now consider sampling of the equilibrium distribution $\mathbb{P}(\vec{\sigma})$ of paths $\vec{\sigma} \in \Lambda^\tau$ of fixed length τ via the "shooting" MC move $\vec{\sigma} \to \vec{\sigma}'$ [130], which constructs a path $\vec{\sigma}' \in \Lambda^\tau$ from path $\vec{\sigma}$ by:

- Choosing a starting configuration σ_a from the sequence $\vec{\sigma}$ and setting $\sigma'_b = \sigma_a$ in the sequence $\vec{\sigma}'$, for some independently generated a and b uniform on $\{1, \dots, \tau\}$.
- Sampling the forward and backward path segments of $\vec{\sigma}'$, comprising respectively $\tau - b$ and $b - 1$ sequentially generated microstates, by initiating two independent MC trajectories starting from $\sigma'_b = \sigma_a$.

Correct sampling of the equilibrium path distribution can be achieved by imposing the detailed balance conditions on the shooting move acceptance [$\mathbb{P}_{\text{acc}}(\vec{\sigma} \to \vec{\sigma}')$] and path generation [$\mathbb{P}_{\text{gen}}(\vec{\sigma} \to \vec{\sigma}')$] probabilities:

$$\frac{\mathbb{P}_{\text{acc}}(\vec{\sigma} \to \vec{\sigma}')\mathbb{P}_{\text{gen}}(\vec{\sigma} \to \vec{\sigma}')}{\mathbb{P}_{\text{acc}}(\vec{\sigma}' \to \vec{\sigma})\mathbb{P}_{\text{gen}}(\vec{\sigma}' \to \vec{\sigma})} = \frac{\mathbb{P}(\vec{\sigma}')}{\mathbb{P}(\vec{\sigma})} = \frac{\mathbb{P}(\sigma'_1) \prod_{i=1}^{\tau-1} \mathbb{P}(\sigma'_i \to \sigma'_{i+1})}{\mathbb{P}(\sigma_1) \prod_{j=1}^{\tau-1} \mathbb{P}(\sigma_j \to \sigma_{j+1})}. \tag{5.3}$$

The reversibility condition [Eq. (2.8)] on the microstate transition probabilities implies that the dynamics of the systems studied in this work are invariant under time reversal, allowing the path generation probability $\mathbb{P}_{\text{gen}}(\vec{\sigma} \to \vec{\sigma}')$ to be written as the product of probabilities of the forward and backward path segments:

$$\frac{\mathbb{P}_{\text{gen}}(\vec{\sigma} \to \vec{\sigma}')}{\mathbb{P}_{\text{gen}}(\vec{\sigma}' \to \vec{\sigma})} = \frac{\prod_{i=2}^{b} \mathbb{P}(\sigma'_i \to \sigma'_{i-1}) \prod_{j=b}^{\tau-1} \mathbb{P}(\sigma'_j \to \sigma'_{j+1})}{\prod_{k=2}^{a} \mathbb{P}(\sigma_k \to \sigma_{k-1}) \prod_{m=a}^{\tau-1} \mathbb{P}(\sigma_m \to \sigma_{m+1})}. \tag{5.4}$$

Combining and simplifying the above equations, we arrive at:

$$\frac{\mathbb{P}_{\text{acc}}(\vec{\sigma} \to \vec{\sigma}')}{\mathbb{P}_{\text{acc}}(\vec{\sigma}' \to \vec{\sigma})} \times \frac{\prod_{i=2}^{b} \mathbb{P}(\sigma'_i \to \sigma'_{i-1})}{\prod_{k=2}^{a} \mathbb{P}(\sigma_k \to \sigma_{k-1})} = \frac{\mathbb{P}(\sigma'_1) \prod_{i=1}^{b-1} \mathbb{P}(\sigma'_i \to \sigma'_{i+1})}{\mathbb{P}(\sigma_1) \prod_{j=1}^{a-1} \mathbb{P}(\sigma_j \to \sigma_{j+1})},$$

which can be further simplified by noting that:

$$\prod_{i=2}^{b} \mathbb{P}(\sigma'_i \to \sigma'_{i-1}) = \prod_{i=2}^{b} \mathbb{P}(\sigma'_{i-1} \to \sigma'_i) \frac{\mathbb{P}(\sigma'_{i-1})}{\mathbb{P}(\sigma'_i)} = \frac{\mathbb{P}(\sigma'_1)}{\mathbb{P}(\sigma'_b)} \prod_{i=1}^{b-1} \mathbb{P}(\sigma'_i \to \sigma'_{i+1}), \tag{5.5}$$

leading to:

$$\frac{\mathbb{P}_{\text{acc}}(\vec{\sigma} \to \vec{\sigma}')}{\mathbb{P}_{\text{acc}}(\vec{\sigma}' \to \vec{\sigma})} = \frac{\mathbb{P}(\sigma'_b)}{\mathbb{P}(\sigma_a)} = 1, \tag{5.6}$$

since $\sigma_a = \sigma'_b$. Thus, any shooting move can be accepted with probability 1, given that the microscopic stochastic dynamics obey detailed balance and the shooting point $\sigma_a = \sigma'_b$ appears in the generated trajectory $\vec{\sigma}'$ unaltered.

Acceptance criteria for shooting moves which perturb the microstate σ_a prior to generating the forward and backward segments of $\vec{\sigma}'$ are straightforward to derive by including appropriate considerations in the expression for the path generation probability $\mathbb{P}_{\text{gen}}(\vec{\sigma} \to \vec{\sigma}')$. Under the Metropolis kinetics discussed in Sec. 4.1.3, however, shooting point perturbation is not required for decorrelation of the generated path, and the MC scheme described above is sufficient for the purposes of this work.

5.2.2 *Recovering Marginal Distributions*

The EPS algorithm provides a straightforward approach to sampling of conditional distributions $\mathbb{P}[\sigma|\lambda(\sigma) \in \{\lambda\}]$ over the portion of state space which realises values of the order parameter $\lambda(\sigma)$ belonging to some set or window $\{\lambda\}$. This is achieved by accepting only the trajectories $\vec{\sigma} \in \Lambda^{\tau}$ which contain at least one configuration σ_i such that $\lambda(\sigma_i) \in \{\lambda\}$. The obtained conditional ensemble of configurations can be used to estimate the conditional distribution of the order parameter $\mathbb{P}[\lambda|\lambda \in \{\lambda\}]$, which, given a set of overlapping windows $\{\lambda\}_i$, can be used to reconstruct a substantial portion of the equilibrium distribution $\mathbb{P}(\lambda)$.

Several methods of reconstruction of the equilibrium distribution $\mathbb{P}(\lambda)$ from a finite set of overlapping conditional distributions $\mathbb{P}[\sigma|\lambda(\sigma) \in \{\lambda\}_i]$ exist in the literature [226, 227]. In this work, we will consider the weighted histogram (WHAM) [228, 229] and least squares (LSQ) approaches.

In a given range of order parameter values $\lambda \in [\lambda_{\min}, \lambda_{\max}]$, we partition the order parameter space into m bins of equal width $\Delta\lambda$ and define w overlapping windows. For every window $i \in \{1, \ldots, w\}$, the EPS scheme samples some number $g_{ij} \in \mathbb{N}$, $j \in \{1, \ldots, m\}$ of hits in the jth bin of the discretised order parameter space. The set of probabilities $\{p_j\}$, corresponding to an estimate of the discretised equilibrium distribution $\mathbb{P}(\lambda)$, can be recovered from the histograms g_{ij} via WHAM by simultaneously solving the equations:

$$p_j = \frac{\sum_{i=1}^{w} g_{ij}}{\sum_{i=1}^{w} u_{ij} \sum_{k\in\{j\}_i} g_{ik}}, \quad u_{ij} = \begin{cases} \left(\sum_{k\in\{j\}_i} p_k\right)^{-1} & \text{if } j \in \{j\}_i, \\ 0 & \text{otherwise,} \end{cases} \tag{5.7}$$

where $\{j\}_i$ is the set of indices of bins included in the ith EPS window. The more computationally straightforward LSQ approach attempts to match the free energy estimates of adjacent overlapping windows by sequentially reconstructing the overall estimated free energy profile $G_j^{(w)}$, $j \in \{1, \ldots, m\}$ as follows:

$$\begin{aligned} G_j^{(1)} &= \begin{cases} \ln g_{1j} & \text{if } j \in \{j\}_1, \\ 0 & \text{otherwise,} \end{cases} \quad \{j\}^{(1)} = \{j\}_1, \quad \{j\}^{(i)} = \{j\}^{(i-1)} \cup \{j\}_i, \\ G_j^{(i)} &= \begin{cases} \ln g_{ij} + \kappa^{(i)} & \text{if } j \in \{j\}_i \text{ and } j \notin \nu^{(i)}, \\ \left(G_j^{(i-1)} + \ln g_{ij} + \kappa^{(i)}\right)/2 & \text{if } j \in \nu^{(i)}, \\ G_j^{(i-1)} & \text{otherwise,} \end{cases} \\ \nu^{(i)} &= \{j\}^{(i-1)} \cap \{j\}_i, \quad \kappa^{(i)} = |\nu^{(i)}|^{-1} \sum_{k\in\nu^{(i)}} G_k^{(i-1)} - \ln g_{ik}, \end{aligned} \tag{5.8}$$

where $\kappa^{(i)}$ determine the vertical offsets required for least squares matching of values $G_k^{(i-1)}$ and $\ln g_{ik}$ in the window overlaps $\nu^{(i)}$.

5.2.3 *Validation*

We now verify our implementation of the EPS method by computing the equilibrium distribution of the order parameter (n, χ_{PLG}) in the PLG model as defined in Sec. 3.2.5 at $k_B T = 0.7$, $f = 2.25$, where the product $n(\sigma)\chi_{\text{PLG}}(\sigma)$ corresponds to the size of the largest cluster of aligned solute particles inside the largest cluster of solute particles in configuration σ. We consider cubic $\vec{l} = (32, 32, 32)$ systems and sample paths of length $\tau = 6N = 6 \times 32^3$ counting and storing only 7 configurations, obtained at intervals of 1 MC sweep, per accepted path. We estimate the conditional probabilities of every possible value of the order parameter in the range $n \in [1, 320]$, $\chi_{\text{PLG}} \in (0, 1]$ by defining an array of 6400 windows as illustrated in Fig. 5.2a. For each window we carry out EPS equilibration and sampling stages which terminate upon accepting respectively 5×10^4 and 10^5 new lattice configurations, i.e. accepting at most 5×10^4 and 10^5 or at least $5 \times 10^4/7$ and $10^5/7$ shooting moves. Reconstructing the estimate of the free energy landscape $\mathcal{F}(n, \chi_{\text{PLG}})$ via the LSQ procedure [Eq. (5.8)] we obtain a result (Fig. 5.2b) which is in good quantitative agreement with that reported in Ref. [6].

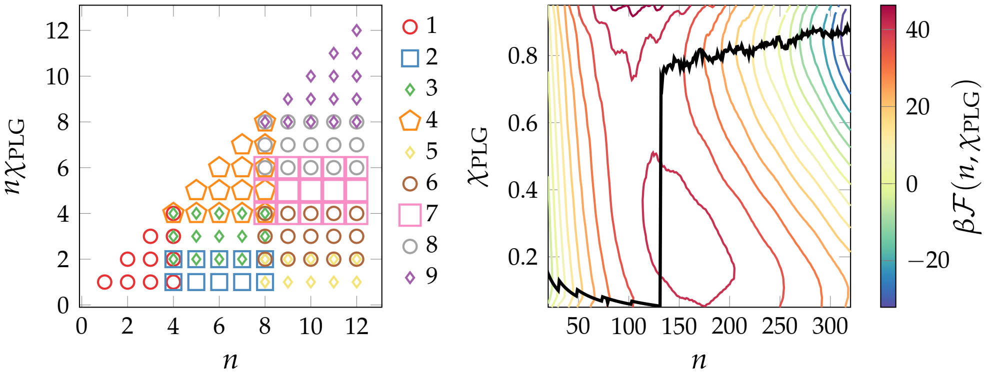

Figure 5.2: EPS windowing scheme (left) and the reconstructed free energy profile (right) for the PLG model at $k_B T = 0.7$, $f = 2.25$. Markers in the left panel are drawn at each of the possible order parameter values in the range $n \in [1, 12]$, $\chi_{\mathrm{PLG}} \in (0, 1]$, with distinct marker shapes corresponding to distinct overlapping order parameter windows $i \in \{1, \ldots, 9\}$ (legend). In the left panel, the contour lines are drawn at intervals of $8k_B T$ and the black line is drawn through coordinates $\chi^*_{\mathrm{PLG}}(n) = \mathrm{argmin}_{\chi_{\mathrm{PLG}}}\{\mathcal{F}(n, \chi_{\mathrm{PLG}})\}$.

Due to the high computational expense of solving the set of coupled equations Eq. (5.7) via fixed point iteration, we have not attempted to employ WHAM in reconstruction of multi-dimensional free energy landscapes in this work. While the computational expense of the WHAM approach can be dramatically reduced by applying the more advanced numerical methods [229], we do not observe any significant discrepancies between profiles reconstructed via Eqs. (5.7) and (5.8) (Fig. 5.3) and, for this reason, do not employ WHAM throughout the rest of this work.

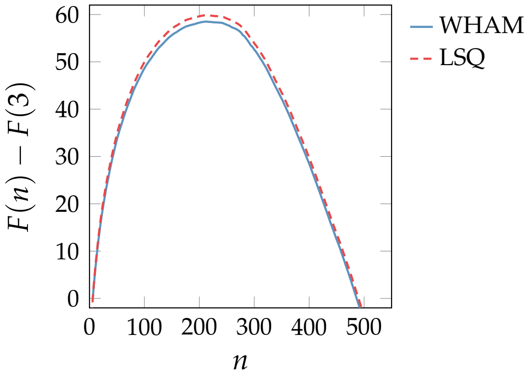

Figure 5.3: Reconstructions of the free energy $F(n) = -k_B T \ln \mathbb{P}[n | n(\sigma) \in \{3, \ldots, 603\}] +$ const. as function of the largest solute cluster size n via Eqs. (5.7) and (5.8) for the $c = 1$, $Q = 24$ extended PLG model on a cubic $\vec{l} = (32, 32, 32)$ lattice at $k_B T = 0.7$, $f = 2.0$. The conditional distributions $\mathbb{P}[n | n(\sigma) \in \{n\}_i]$ were sampled via EPS, defining 200 overlapping windows of width $\Delta n = 4$ over the range $n \in [3, 603]$. For each window, the EPS equilibration and sampling stages terminated upon accepting respectively 5×10^4 and 10^5 new configurations. The EPS algorithm sampled paths of length $\tau = 6 \times 32^3$ in the μVT ensemble, counting and storing only 7 configurations per path.

We now apply the EPS sampling and LSQ reconstruction procedures to obtain estimates of portions of the equilibrium distributions $\mathbb{P}(n)$ and $\mathbb{P}(n, v, \chi)$ for the $Q = 24$, $c = 1$ extended PLG model on a cubic $\vec{l} = (32, 32, 32)$ lattice in the region $k_B T \in \{0.6, 0.65, 0.7\}$, $f \in \{2, 2.25, 3, 4, \ldots, 7\}$ of parameter space, i.e. at conditions where the ordered solute phase is the most stable thermodynamic state of the system. In all applications of the EPS method, we sample paths of length $\tau = 6 \times 32^3$ in the μVT ensemble, i.e. under the transmutation-reorientation move set (Sec. 4.1.3), counting and storing only 7 configurations per path and allow the equilibration and sampling stages to terminate upon acceptance of respectively 5×10^4 and 10^5 new configurations.

5.3.1 *Cluster Size Distributions*

We estimate the 1D conditional distributions $\mathbb{P}[n|n(\sigma) \in \{n\}_i]$ via EPS, defining 200 overlapping windows $\{n\}_i = \{3 + (i-1)(\Delta n - 1), \ldots, 3 + i(\Delta n - 1)\}$ of width $\Delta n = 4$ in the range $n \in [3, 603]$. Additionally, we obtain estimates of the conditional probabilities $\mathbb{P}[n|n(\sigma) \in \{1, \ldots, 8\}]$ from 10^2 brute force MC generated trajectories of length 10^4. Applying the LSQ reconstruction procedure to the obtained EPS and brute force histograms, we estimate the free energies $F(n) = -k_B T \ln \mathbb{P}[n|n(\sigma) \in \{1, \ldots, 603\}] + \text{const.}$ computing the barriers $\Delta F(n) = F(n) - F(1)$ (Fig. 5.4).

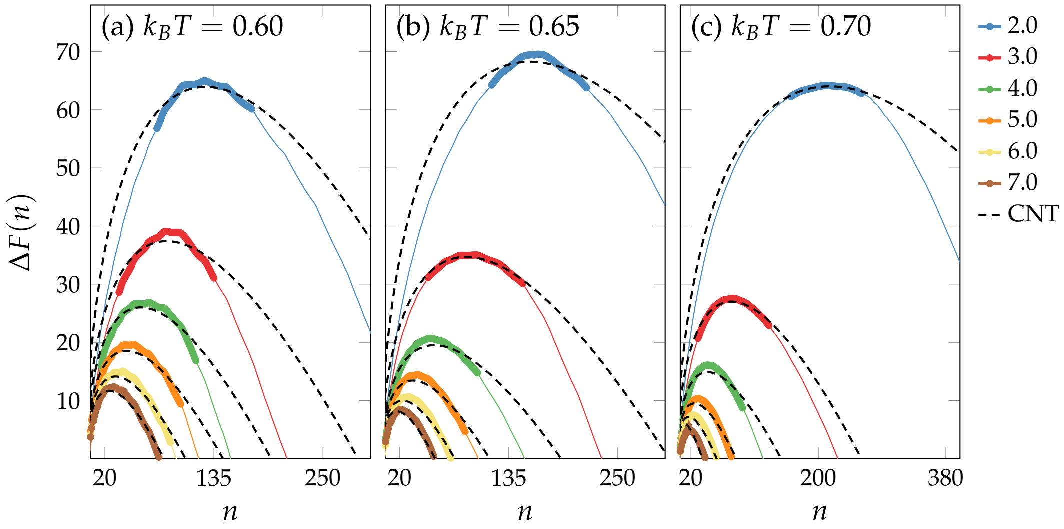

Figure 5.4: Estimates of the free energy barriers $\Delta F(n)$ to nucleation (solid lines) for the $c = 1$, $Q = 24$, $d = 3$ extended PLG model at $k_B T \in \{0.6, 0.65, 0.7\}$, $f \in \{2, 3, \ldots, 7\}$, showing the corresponding fits of the CNT expression Eq. (2.54) (dashed lines). The CNT fits were obtained by computing the coefficients a and b yielding the least squares solutions to the sets of simultaneous equations $\Delta F(n_i) - b n_i^{2/3} + a n_i = 0$, $n_i \in \{n_{\text{mn}}, n^\dagger + 50\}$, where $n_{\text{mn}} = \max\{n^\dagger - 50, 1\}$, $n^\dagger = \text{argmax}_n\{\Delta F(n)\}$ and the sets of coordinates $[n_i, \Delta F(n_i)]$ used in the fits correspond to the thicker portions of the solid lines.

Although Eq. (2.54) appears to give reasonable fits to the obtained estimates of $\Delta F(n)$ close to the top of the barrier $n^{\dagger} = \mathrm{argmax}_n\{\Delta F(n)\}$, we find the overall quality of the CNT description of the free energy barriers rather poor, which has previously been recognised in multiple other studies of nucleation phenomena [175, 176] (Table 3.2). We also find that the least squares values of the CNT coefficients $\Delta\mu_{\mathrm{CNT}}$ do not correspond to the approximate values of the thermodynamic solute-solvent chemical potential difference $\Delta\mu_{\mathrm{coex}}$ [Eq. (4.26)], while the estimates of the nuclei surface tensions γ_{CNT} are not independent of solute supersaturation as typically assumed by CNT (Fig. 5.5). The CNT prediction $\Delta F(n^{\dagger}) \propto \Delta\mu_{\mathrm{coex}}^{-2}$, however, appears to hold well at higher solute supersaturations $f \geq 3$ as shown in Fig. 5.5c. Additionally, we verify the absence of finite size effects in the calculations presented here by obtaining estimates of $\Delta F(n)$ from EPS simulations on cubic systems of $\vec{l} = (16, 16, 16)$ at $k_B T = 0.7$, $f = 2$, i.e. where the critical nuclei are largest, which we find in excellent agreement with the data computed for $\vec{l} = (32, 32, 32)$ systems.

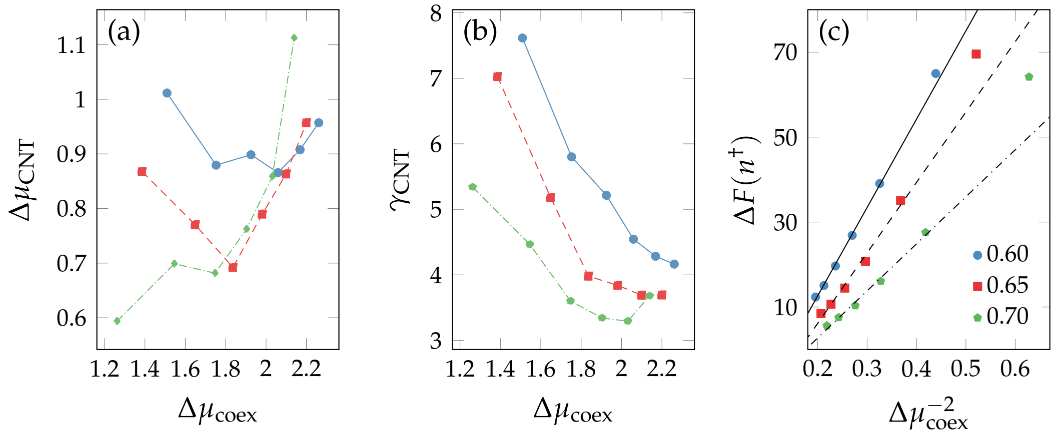

Figure 5.5: Values of the least squares estimates of CNT volume and surface coefficients [(a) and (b)], and heights of the free energy barriers to nucleation [(c)] for the $c = 1$, $Q = 24$, $d = 3$ extended PLG model plotted against $\Delta\mu_{\mathrm{coex}}$ for three values of $k_B T$ (legend). Lines and markers in (a) and (b) correspond to the least squares coefficient estimates producing the CNT fits shown in Fig. 5.4. Markers in (c) are the EPS estimates of the free energy barrier heights while lines show the corresponding least squares linear fits to the leftmost 5 points, i.e. for $f \geq 3$.

It is important to note that our estimates of $\mathbb{P}(n)$ do not take into account the possibility of existence of multiple clusters in a single lattice configuration, which can be expected to result in a systematic underestimation of $\mathbb{P}(n)$ for low values of n [73]. Furthermore, we do not assess the thermodynamic relevance of the geometric definition of solute clusters which may be a significant factor in our application of CNT [75]. Due to the relatively high computational expense of the necessary calculations, we cannot give a rigorous account of the statistical uncertainties in our estimates of nucleation barrier heights here. Therefore, we cannot comment conclusively on the predictive power of Eq. (2.54) based on the data presented in this section. In the chapters that follow, however, we will explore the applicability of CNT's treatment of nucleation kinetics in the extended PLG model, making use of the explicit estimates of the free energy barrier heights given here.

5.3.2 *Equilibrium Internal Orientational Order of Nuclei*

In this section, we estimate the equilibrium distributions $\mathbb{P}(n, v, \chi)$ of the three-dimensional order parameter introduced in Sec. 5.1 via EPS at $k_B T \in \{0.6, 0.65, 0.7\}$ and $f = 2.25$. For simplicity, we coarsen the space of the orientational order parameter (v, χ) by defining 16 equally sized bins along v and χ and only consider the range of cluster sizes $n \geq 22$, where the density of order parameter values is sufficiently high to allow at least one value per bin. Keeping the bin width of 1 along the n coordinate, we define 2500 cubic overlapping EPS windows 4 bins wide along each coordinate in the range $n \in [22, 322]$, $v \in [0, 1]$, $\chi \in [0, 1]$. Using the EPS trajectory parameters and termination criteria specified in Sec. 5.3.1, we obtain estimates of the free energies $\mathcal{F}(n, v, \chi) = -k_B T \ln \mathbb{P}(n, v, \chi) + \text{const.}$ via Eq. (5.8), interpolating for the unsampled values via Delaunay triangulation.

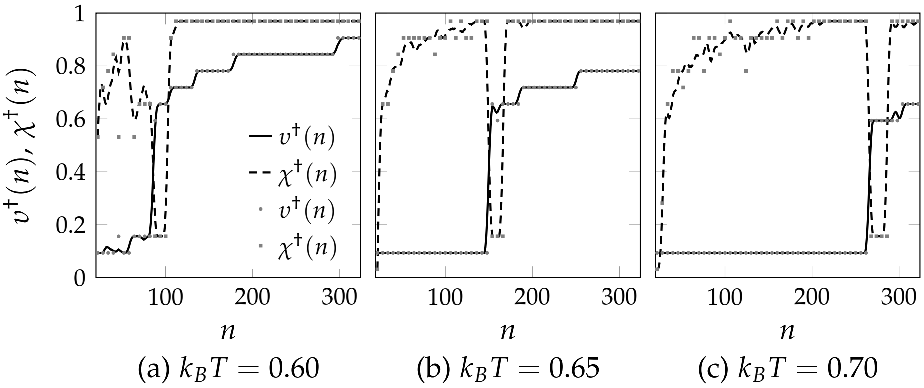

(a) $k_B T = 0.60$ (b) $k_B T = 0.65$ (c) $k_B T = 0.70$

Figure 5.6: Coordinates of minima $(v^\dagger, \chi^\dagger)(n) = \text{argmin}_{(v,\chi)}\{\mathcal{F}(n, v, \chi)\}$ plotted against n at three temperatures for the $c = 1$, $Q = 24$, $d = 3$ extended PLG model. Markers correspond to the values obtained directly from the EPS estimates of $\mathcal{F}(n, v, \chi)$ while lines show the data upon application of a smoothing filter.

Examining the reconstructed profiles $\mathcal{F}(n, v, \chi)$, we observe a strong dependence on n and $k_B T$ of the equilibrium distributions $\mathbb{P}(v, \chi | n)$ of the orientational order parameter, where small solute clusters ($n < 80$) are highly likely to exhibit a low degree of internal orientational order, i.e. $\mathbb{P}[(v, \chi) \in \{(v, \chi)\}_{\mathrm{I}} | n < 80] \approx 1$, while large solute nuclei ($n > 310$) are typically highly ordered, i.e. $\mathbb{P}[(v, \chi) \in \{(v, \chi)\}_{\mathrm{III}} | n > 310] \approx 1$. We illustrate this by computing the n dependent coordinates of the local minima $(v^\dagger, \chi^\dagger)(n) = \text{argmin}_{(v,\chi)}\{\mathcal{F}(n, v, \chi)\}$ (Fig. 5.6), which can be thought of as metrics of the thermodynamically preferred degrees of nuclei orientation order. As can be seen in Fig. 5.6, partially disordered states appear to be preferable for a range of intermediate nuclei sizes, which suggests that we can expect multi-stage nucleation pathways of the ordered solute phase, proceeding sequentially via disordered and partially disordered precursor states, to be viable under microscopic kinetics characterised by slow nucleus growth and fast relaxation of nucleus' orientational order.

In Fig. 5.7 we visualise the orientational order distributions of critical nuclei, i.e. of size $n = n^\dagger = \operatorname{argmax}_n\{\Delta F(n)\}$, showing that their thermodynamically preferred degrees of orientational order are temperature dependent. This, however, does not imply that nucleation of disordered and partially disordered solute structures can occur at the studied temperatures. In fact, for $n \geq 300$ we see no barriers to transformation of nuclei to ordered structures from either of the two possible precursors, suggesting that, in the studied parameter regime, the scenario of competitive nucleation of the three solute structures is unlikely in the extended PLG model. Computing portions of the distributions $\mathbb{P}(n, v, \chi)$ at $k_B T \in \{0.6, 0.65, 0.7\}$, $f \in \{1, 7\}$, we find no significant dependence of the thermodynamically preferred nuclei structures on solute concentration, suggesting that the maximum nucleus size below which non-ordered structures are thermodynamically viable is largely determined by temperature.

$$\mathcal{F}^\dagger(v,\chi) = \mathcal{F}(n^\dagger, v, \chi) - \mathcal{F}(n^\dagger, v^\dagger, \chi^\dagger)$$

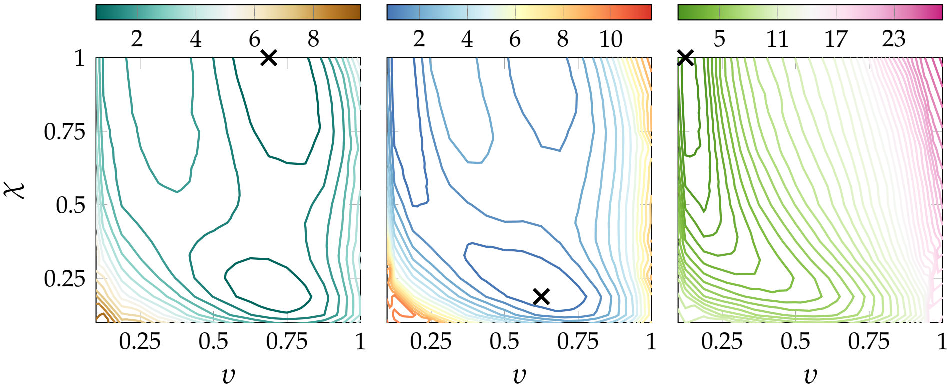

(a) $n^\dagger = 103$, $k_B T = 0.6$.

(b) $n^\dagger = 150$, $k_B T = 0.65$.

(c) $n^\dagger = 152$, $k_B T = 0.7$.

Figure 5.7: Contour plots of 2D segments $\mathcal{F}^\dagger(v,\chi)$ of free energy landscapes $\mathcal{F}(n, v, \chi)$ at three temperatures, $f = 2.25$ and for fixed values of $n = n^\dagger = \operatorname{argmax}_n\{\Delta F(n)\}$ for the $c = 1$, $Q = 24$, $d = 3$ extended PLG model. Contour lines are drawn at intervals of $1 k_B T$ and crosses indicate the coordinates of the local minima $(v^\dagger, \chi^\dagger) = \operatorname{argmin}_{(v,\chi)}\{\mathcal{F}(n^\dagger, v, \chi)\}$.

A possible interpretation of the findings presented in this section can be constructed within the framework of CNT. We can consider treating the three solute structures as distinct solute polymorphs, defining the barriers $\mathcal{F}_{\mathbf{X}}(n)$, $\mathbf{X} \in$

$\{\mathbf{I}, \mathbf{II}, \mathbf{III}\}$ by integrating the distributions $\mathbb{P}(n, v, \chi)$ within the appropriate basins $\{(v, \chi)\}_{\mathbf{X}}$ of orientational order, as defined in Sec. 5.1:

$$\mathcal{F}_{\mathbf{X}}(n) = -k_B T \ln \int_{\{v\}_{\mathbf{X}}} \int_{\{\chi\}_{\mathbf{X}}} dv d\chi \mathbb{P}(n, v, \chi) + \text{const.}. \tag{5.9}$$

We find that the curves $\mathcal{F}_{\mathbf{X}}(n)$ (Fig. 5.8) are well fitted by the CNT-like expression: $\gamma_{\mathbf{X}} n^{2/3} - \Delta\mu_{\mathbf{X}} n + \text{const.}$, yielding values of coefficients of the surface and volume contributions to the nuclei free energies which are consistent with the energetics of the extended PLG model: $\gamma_{\mathbf{I}} < \gamma_{\mathbf{II}} < \gamma_{\mathbf{III}}$ and $\Delta\mu_{\mathbf{I}} < \Delta\mu_{\mathbf{II}} < \Delta\mu_{\mathbf{III}}$ – i.e. the cost of forming solute-solvent interface and the gain associated with the growth of solute domain both increase with the degree of nucleus order. The observed dependence of $\mathcal{F}_{\mathbf{X}}(n)$ on temperature suggests that in some parameter regime $k_B T \in (0.6, 0.65)$ the heights of the barriers to nucleation of the three solute structures are equal, which, in the framework of CNT, implies the possibility of comparable nucleation rates for the three solute structures.

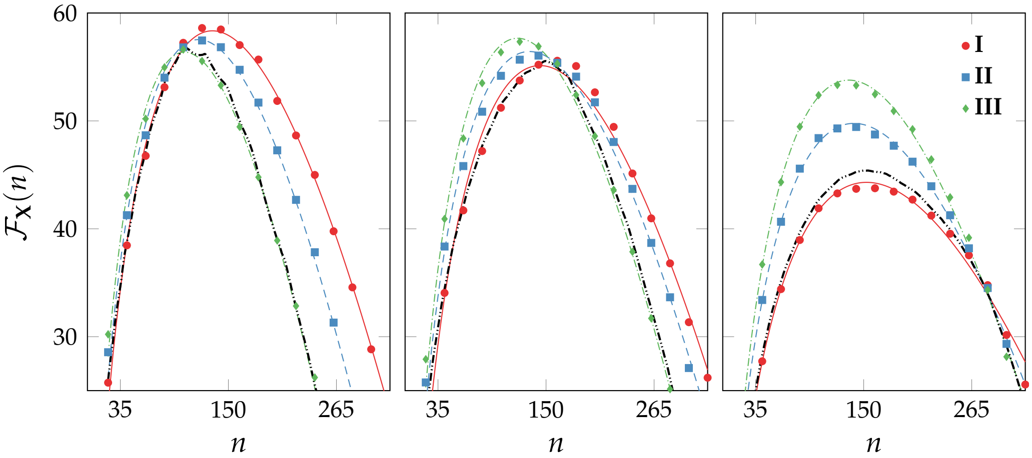

(a) $k_B T = 0.60$ (b) $k_B T = 0.65$ (c) $k_B T = 0.70$

Figure 5.8: Free energy barriers $\mathcal{F}_{\mathbf{X}}(n)$ (markers) to nucleation of the three solute structures at three temperatures for the $c = 1$, $Q = 24$, $d = 3$ extended PLG model, showing the corresponding fits of the CNT-like expression $\gamma_{\mathbf{X}} n^{2/3} - \Delta\mu_{\mathbf{X}} n + C_{\mathbf{X}}$ (lines). Black lines show estimates of the one-dimensional free energies $\Delta F(n)$ obtained via the EPS procedure outlined in Sec. 5.3.1.

Regimes where different solute structures nucleate on similar timescales could be useful for investigation of the, so far, poorly understood microscopic kinetics of dissolution-recrystallisation processes [152] in scenarios where structural transformation is also a viable mechanism of formation of the stable solute phase. While such scenarios can be realised in the present model, e.g. by generating postcritical solute clusters of the three different structures, due to the absence of barriers to structural transformation between the three solute phases, however, the physical relevance of such realisations is unclear. Although we will not consider the route to a lattice model with higher barriers to structural transformations in solute nuclei in this work, in the next section we will provide evidence towards barrierless orientational ordering within solute nuclei being a feature of any ferromagnetic Potts-like lattice model of anisotropic particles.

5.4 SAMPLING EQUILIBRIUM CLUSTER CONFIGURATIONS

Similar dependence of the distributions of the orientational order parameter (v, χ) to that discussed in Sec. 5.3.2 can be observed in the solute rich state of the extended PLG model on small cubic $\vec{l} = (l+2, l+2, l+2)$ lattices of length $l+2$ with a static layer of solvent particles at each boundary of the lattice (Fig. 5.9). With transmutation MC moves disabled, this setup corresponds to the two component Q-state Potts model with diagonal interactions and reflecting boundary conditions, and can be used to sample the distribution of equilibrium structures of cubic nuclei $n = l^3$.

The tendency of small nuclei to adopt disordered structures at higher temperatures, as seen in Fig. 5.9, can, therefore, be understood as a consequence of finite size stability of disordered states in the Potts model. Recent reports on d-dimensional Q-state Potts models [186, 187, 222] argue that the range of temperatures where disordered states persist is a function of system size, approaching zero as $l \to \infty$. This is consistent with our observation that at low temperatures $k_B T \in \{0.6, 0.65, 0.7\}$ there exists a finite solute cluster size n_{III} such that for nuclei of size $n > n_{\text{III}}$ the ordered structure is thermodynamically preferred and no barriers to transformation to the ordered structure are present.

The same arguments can be used to interpret the stability of small disordered nuclei in the PLG model [6] and we can expect similar behaviour in any lattice model of anisotropic particles where the solute rich state reduces to the ferromagnetic Q-state Potts model.

5.4.1 *Constrained Cluster Size Ensemble*

Various methods for analysis and generation of nuclei have previously been explored in the Ising model [165,230]. In this section we develop a straightforward MC based approach for sampling the equilibrium distributions of nuclei in the extended PLG model.

We first generate a cluster of n solute particles by simulating an Eden-like growth process [231], starting from a single solute particle at the centre of a three-dimensional lattice occupied entirely by solvent. The growth process corresponds to iterative insertion of solute particles (s, q), with s and q chosen uniformly on respectively $\{1, 2\}$ and $\{1, \ldots, Q\}$, into randomly chosen sites neighbouring the solute cluster. After $n-1$ iterations of the process, we obtain a rough and structurally disordered cluster of size n (Fig. 5.10a).

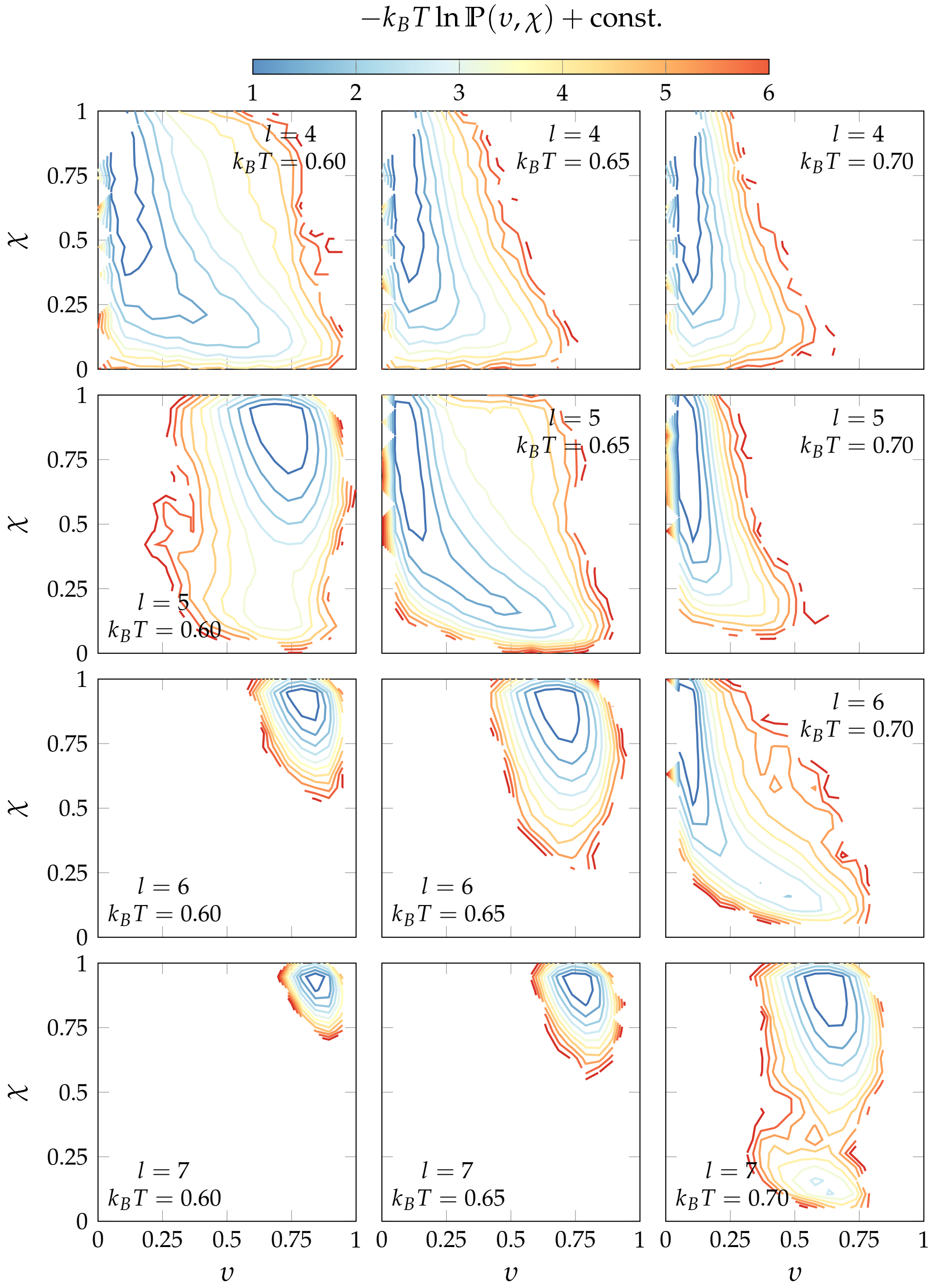

Figure 5.9: Estimated distributions of the orientational order parameter (v, χ) in the $c = 1$, $Q = 24$ extended PLG model on small cubic lattices of length $l + 2$ with static solvent (reflecting) boundaries at three temperature values. The estimates shown are computed from MC trajectories of length 10^6MCS employing reorientation particle moves only. Contour lines are drawn at intervals of $1k_B T$.

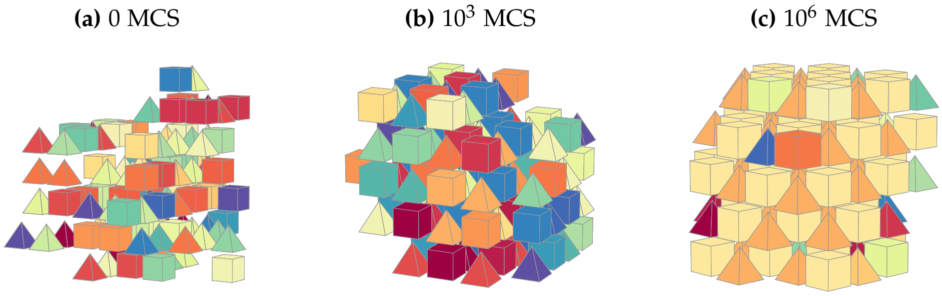

Figure 5.10: Typical initial, short time and long time cluster configurations for $n = 103$, $k_B T = 0.6$ as generated by the constrained cluster MC algorithm for the $c = 1$, $Q = 24$, $d = 3$ extended PLG model. Here 1MCS corresponds to n applications of the constrained cluster MC update. The configurations are visualised in accordance with the convention used in Fig. 4.2.

Having generated a solute cluster of the required size, we define the subset $S = S_\text{u} \cup S_\text{v}$ of the lattice as the union of the set S_u of solute particles belonging to the generated solute cluster and the set S_v of solvent particles which are nearest neighbours of at least one solute particle in the cluster. Subsequently, we initiate a Metropolis MC scheme comprising three equally probable moves: (1) Reorientation of a particle in S_u. (2) Change of species of a particle in S_u to some species $s \in \{1, 2\}$. (3) Interchange of species and orientation labels between a particle in S_u and a particle in S_v. It is important to note that acceptance of move (3) leads to modification of sets S_u and S_v which we take into account in the calculation of the corresponding acceptance probabilities $\mathbb{P}^{(3)}_\text{acc}(\sigma \to \sigma')$ to assure detailed balance:

$$\mathbb{P}^{(3)}_\text{acc}(\sigma \to \sigma') = \begin{cases} \min\left\{1, \frac{|S_\text{v}(\sigma)|}{|S_\text{v}(\sigma')|} e^{-\beta[E(\sigma')-E(\sigma)]}\right\} & \text{if } |S_\text{u}(\sigma)| = |S_\text{u}(\sigma')|, \\ 0 & \text{otherwise,} \end{cases} \tag{5.10}$$

where $S_\text{u}(\sigma)$ is the set of solute particles belonging to the largest solute cluster in a lattice configuration σ and $S_\text{v}(\sigma)$ is the set of solvent nearest neighbours of particles in $S_\text{u}(\sigma)$. We find that the described MC scheme yields compact solute clusters (Fig. 5.10) characterised by a probability distribution of the orientational order parameter (v, χ) which matches that obtained via EPS (Fig. 5.11).

5.4.2 *Committor Distributions*

Having verified that the MC scheme of Sec. 5.4.1 correctly samples the equilibrium distribution of solute clusters, we now consider the suitability of the geometric definition of solute clusters at low temperatures. A useful quantity for this purpose is the committor $\mathcal{Q}_n$ [7], which can be defined as the probability of a solute cluster of size n growing to macroscopic size rather than dissolving com-

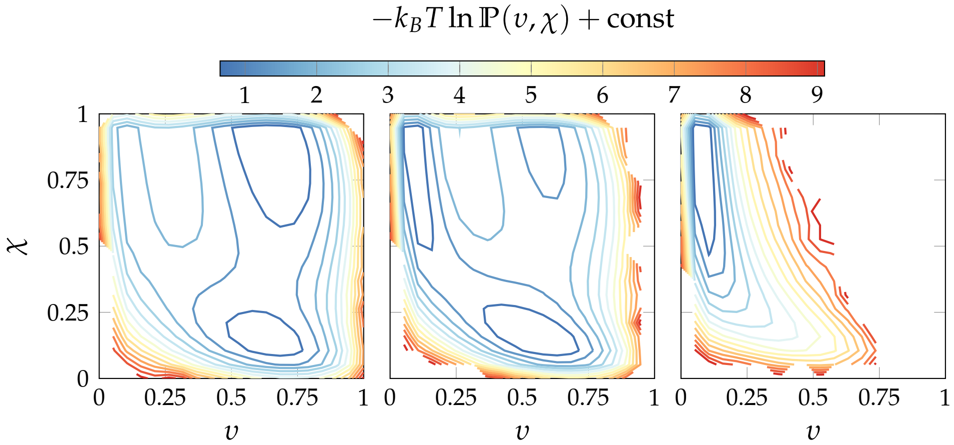

(a) $n = 103$, $k_B T = 0.6$. (b) $n = 150$, $k_B T = 0.65$. (c) $n = 152$, $k_B T = 0.7$.

Figure 5.11: Estimates of distributions of the order parameter (v, χ) obtained under the Metropolis MC sampling equilibrium configurations of solute clusters of fixed size n at three temperatures for the $c = 1$, $Q = 24$, $d = 3$ extended PLG model. The shown estimates were computed based on 10^2 samples of MC trajectories of length 10^6MCS, with 1MSC corresponding to n MC updates of the cluster configuration. Contour lines are drawn at intervals of $1 k_B T$. The shown data appear in good agreement with those presented in Fig. 5.7.

pletely. This quantity can be expressed in terms of the microscopic committors q_σ^+ defined in in Sec. 2.3.5 via the equation:

$$\mathcal{Q}_{n'} = \sum_{\sigma \in \Lambda} q_\sigma^+ \mathbb{P}[\sigma | n(\sigma) = n'], \tag{5.11}$$

which corresponds to the conditional average of q_σ^+ with respect to the equilibrium distribution $\mathbb{P}(\sigma)$ over the ensemble of configurations $\sigma \in \Lambda$ for which $n(\sigma) = n'$ is the size of the largest solute cluster. Within the frameworks of CNT and TST, it is expected that the ensemble of critical clusters of size $n = n^\dagger$ yields the value of committor $\mathcal{Q}_{n^\dagger} = 0.5$.

Exact evaluation of the committor is infeasible for large values of n, and we instead compute the distributions $\mathbb{P}(\widetilde{\mathcal{Q}}_{n^\dagger})$ of the committor estimator $\widetilde{\mathcal{Q}}_{n^\dagger}$ defined as the fraction of 10 μVT MC trajectories, initiated from a configuration containing a solute cluster of size $n^\dagger$, where the size of the largest solute cluster exceeds $n = 10^3$ before dissolving to $n \leq 10$. Applying the constrained cluster size MC scheme to generation of solute clusters of critical size $n^\dagger = \text{argmax}_n\{\Delta F(n)\}$, as estimated based on EPS calculations, we obtain reasonable forms (Fig. 5.12) of distributions of the committor estimators $\widetilde{\mathcal{Q}}_{n^\dagger}$. Although we find that the critical cluster sizes, as estimated based on explicit free energy calculations, likely do not realise the value $\mathcal{Q}_{n^\dagger} = 0.5$ on average, the sharply peaked forms of the committor estimator distributions suggest that the definition of solute clusters employed in this work is kinetically relevant under the μVT kinetics.

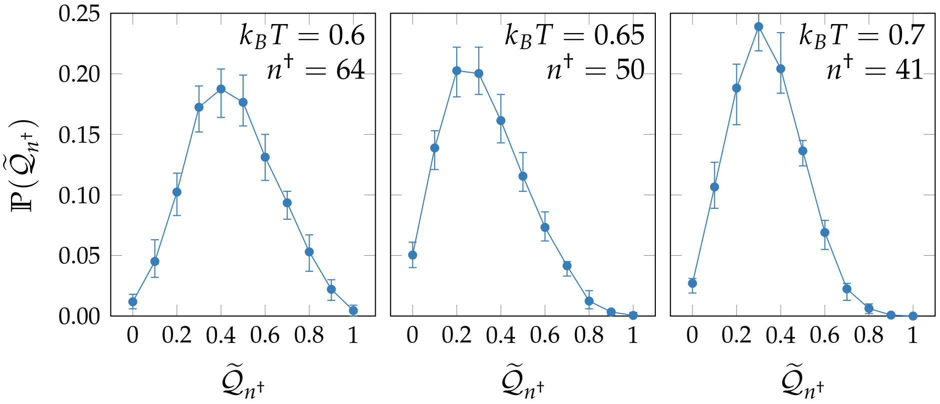

Figure 5.12: Distributions of the committor estimator $\widetilde{\mathcal{Q}}_{n^\dagger}$ at three temperatures and $f = 4$ under the transmutation-reorientation (μVT) MC move set in the $c = 1$, $Q = 24$, $d = 3$ extended PLG model. The distributions were estimated based on 10 sets of 10^3 independent samples of $\widetilde{\mathcal{Q}}_{n^\dagger}$. Each MC trajectory was initiated from a configuration containing a solute cluster of size $n^\dagger$ generated via the procedure outlined in Sec. 5.4.1, allowing 10^4MCS for equilibration of the solute cluster. Samples of $\widetilde{\mathcal{Q}}_{n^\dagger}$ were computed as fractions of 10 independent MC trajectories for which the solute cluster size exceeded 10^3 particles before ever dissolving to a size of 10 or fewer particles. Error bars correspond to maximum and minimum deviations from the average values across 10 independent estimates of the distributions.

It is important to note that the constrained cluster size MC scheme does not sample nuclei configurations according to the distribution of the transition state ensemble, as required under TST for realisation of the value $\mathcal{Q}_{n^\dagger} = 0.5$ of the committor. The results presented in this section, therefore, cannot be give a rigorous assessment of our definition of the solute cluster size for the role of a reaction coordinate. A more thorough report on such assessment would require implementation of MC schemes which sample the kinetically relevant distributions of critical nuclei, e.g. TPS, TIS and FFS.

5.5 CHAPTER SUMMARY

We have shown that, under microscopic kinetics where structural relaxation of solute nuclei occurs on a significantly faster timescale than nucleus growth, low temperature solute nucleation pathways in the $c = 1$, $Q = 24$, $d = 3$ extended PLG model proceed via disordered and partially disordered precursor solute structures. The apparent sequential ripening mechanism of the growth limited nucleation process can be understood as a manifestation of the finite size effect in Potts-like models of anisotropic particles: at any given temperature below the order-disorder transition, the thermodynamically favoured nucleus structure is fully determined by the nucleus size. We have additionally highlighted that, under the current understanding, metastability of disordered states below the order-disorder transition temperature in Potts-like models occurs only in finite systems. Thus solid-state transformation into the ordered solute structure is, energetically, a barrier free process for sufficiently large disordered solute nuclei below the order-disorder transition in the PLG and the extended PLG models. This suggests that pure Potts-like models of anisotropic particles in solution such as the PLG or the extended PLG are not sufficient for modelling of dissolution-recrystallisation processes observed in systems of polymorphic minerals.

6

SEEDING METHOD

The recently introduced ”seeding” method [232] is showing promise in obtaining reasonable estimates of nucleation rates and free energy barrier heights for solid-liquid transitions in multiple systems and over broad ranges of parameter space [112,118,124]. By inserting an artificially constructed crystalline nucleus into a system in a metastable liquid state, the approach attempts to obtain fragments of nucleation trajectories of the system, which are then used for formulating a one-dimensional quantitative model of the nucleation process based on CNT. Among several advantages of the ”seeding” method over explicit techniques for free energy barrier and nucleation rate estimation are its simplicity of implementation and significantly lower computational expense, since the estimation procedure only requires a relatively small sample of short trajectories of the nucleus size coordinate. However, the method relies heavily on the assumptions of CNT, typically ignoring the variability of structure within crystalline nuclei over the course of the nucleation process, and hence the resultant approximate quantitative treatment requires verification against the more robust rate and barrier estimation strategies. The ”seeding” method has also recently been applied in studies of nucleation from solution [102, 114], however validation of the obtained nucleation rate estimates against those computed via alternative means has, so far, not been carried out in this particular context.

In this chapter we will consider the ”seeding” method in the context of nucleation from solution in the $c = 1$, $Q = 24$, $d = 3$ extended PLG model. We will first outline the approach in the context of overdamped Langevin dynamics and consider the statistical properties of the typically computed quantities. Within the framework of the seeding method, we will then derive an estimator for the CNT coefficient γ_{CNT} and provide the analytical form of its probability distribution under a specific set of assumptions. Finally we will apply the method to reconstruction of the nucleation free energy barriers in the extended PLG model under the two sets of microscopic kinetics defined in Sec. 4.1.3.

6.1 LANGEVIN EQUATION FOR THE REACTION COORDINATE

The one-dimensional overdamped Langevin equation for the time evolution of a coordinate $x(t) \in \mathbb{R}$ can be written as:

$$\dot{x}(t) = \frac{dx}{dt} = -\beta D_x \nabla_x F_x[x(t)] + \xi_x(t) = -\beta D_x \left.\frac{dF_x}{dx}\right|_{x(t)} + \xi_x(t), \tag{6.1}$$

where D_x is the diffusion coefficient, F_x is the one-dimensional potential of mean force and $\xi_x(t)$ is a random process satisfying the conditions $\langle \xi_x(t) \rangle = 0$ and $\langle \xi_x(t)\xi_x(t') \rangle = 2D_x\delta(t - t')$, with $\delta(t)$ being the Dirac delta function. Central to the "seeding" method is the observation that for any trajectory $x(t) : x(0) = x_0$ the initial drift $\langle \dot{x}_0 | x_0 \rangle$ along the x coordinate can be obtained by taking the ensemble averages of both sides of the above equation:

$$\langle \dot{x}_0 | x_0 \rangle = \langle \dot{x}(0) | x(0) = x_0 \rangle = -\beta D_x \left.\frac{dF_x}{dx}\right|_{x_0}, \tag{6.2}$$

which offers the possibility of reconstructing the one-dimensional potential F_x based on MC measurements of the initial drifts and the diffusion coefficient:

$$F_x(x) = -k_B T D_x^{-1} \int_{-\infty}^{x} dx_0 \langle \dot{x}_0 | x_0 \rangle. \tag{6.3}$$

6.1.1 *Estimators and Their Properties*

Within the framework of the "seeding" method, the drifts $\langle \dot{x}_0 | x_0 \rangle$ are estimated by obtaining averages of linear least squares fits to the time evolutions $\Delta x(x_0, t) = x(t) - x_0$, $x(0) = x_0$ over a narrow range of time values $t \in [0, t_{\max}]$. It is expected that at the top of the potential barrier $x_0 = x^* = \mathrm{argmax}_x\{F_x(x)\}$, the average deviation from the initial coordinate is zero for the specified short time interval, i.e. $\langle \Delta x(x^*, t) \rangle \approx 0$ for $t \in [0, t_{\max}]$, allowing the diffusion coefficient to be estimated via the average gradient of the linear fits to the time series $\mathrm{SD}(x_0, t) = [x(t) - \langle x(t) \rangle]^2$, $x(0) = x_0$. Noting that $\Delta x(x_0, 0) = 0$ and $\mathrm{SD}(x_0, 0) = 0$ for all x_0, we argue that linear models of the form $g(t) \propto t$, i.e. without vertical offsets, are a reasonable choice for the purposes of extraction of initial gradients of the two time series.

For a sample of M independent trajectories $x_j(t_i) : x_j(0) = x_0, j \in \{1, \ldots, M\}$, where values of the x coordinate are evaluated at W points $t_i = i\Delta t$, $i \in \{1, \ldots, W\}$ with $\Delta t = t_{\max}/W$, the least squares estimators $v_x(x_0)$ and $\zeta_x(x_0)$ of, respectively, the coordinate dependent average drift and diffusivity can be explicitly written as:

$$
\begin{aligned}
v(x_0) &= \frac{\sum_{i=1}^{W} t_i \sum_{j=1}^{M} \Delta x_j(x_0, t_i)}{M \sum_{i=1}^{W} t_i^2}, \\
\zeta_x(x_0) &= \frac{\sum_{i=1}^{W} t_i \sum_{j=1}^{M} \mathrm{SD}_x^{(j)}(x_0, t_i)}{2M \sum_{i=1}^{W} t_i^2},
\end{aligned}
\tag{6.4}
$$

where $\Delta x_j(x_0, t_i)$ and $\mathrm{SD}_x^{(j)}(x_0, t_i)$ are computed from the independent trajectories $x_j(t_i) : x_j(0) = x_0$. Assuming that over the range of times $t \in [0, t_{\max}]$ trajectories $x(t) : x(0) = x_0$ are well described by: $\dot{x}(t) = -\beta D_x \nabla_x F_x(x_0) + \xi_x(t)$, it is possible to show that the distributions of $\Delta x(x_0, t)$ and $\mathrm{SD}(x_0, t)$ are, respectively, normal – $\mathcal{N}[-t\nabla_x F_x(x_0), 2D_x t]$ and gamma – $\Gamma(0.5, 4D_x t)$. While this clearly implies normality of the distribution of $v_x(x_0)$, the distribution of $\zeta_x(x_0)$ is more complex, converging to normal only for large M as shown in Fig. 6.1.

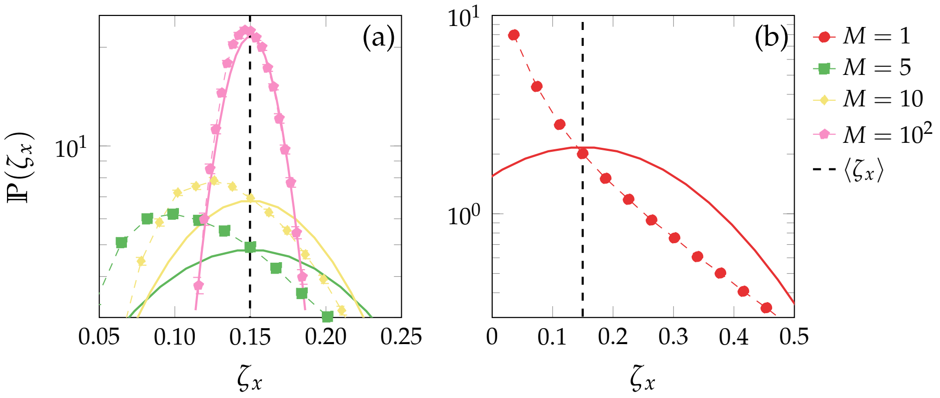

Figure 6.1: Probability densities of estimator $\zeta_x(x_0)$ for trajectories of pure Brownian motion $\dot{x}(t) = \xi_x(t)$, i.e. $F_x(x_0) = 0$, at $k_B T = D_x = 0.15$ for various sample sizes M. Distribution estimates (markers and thin dashed lines) and the corresponding 95% confidence intervals, shown by the error bars (smaller than markers), were obtained based on a sample of 10^5 estimates ζ_x, i.e. $M \times 10^5$ trajectories $x(t)$, taking $t_{\max} = 10^{-3}$ and $\Delta t = 10^{-4}$. For comparison, drawn in solid lines are the normal probability densities $\mathcal{N}[\langle \zeta_x \rangle, \mathrm{Var}(\zeta_x)]$ with the average $\langle \zeta_x \rangle$ indicated by the dashed black lines. Deviation of $\mathbb{P}(\zeta_x)$ from normality is noticeable even for $M = 100$.

6.1.2 *Drifts, Diffusion Coefficients and Escape Rates*

We now apply the estimators given by Eq. (6.4) in the context of Brownian motion in a bistable potential $F_x(x) = x^4 - 2x^2$, simulated via the BAOAB-limit method presented in Ref. [233]. Taking $W = M = 100$ and $\Delta t = 10^{-4}$, $t_{\max} = 10^{-2}$, we find that, on average, both estimators yield excellent linear fits of the form $\langle \Delta x(x_0, t) \rangle = v_x(x_0) t$ and $\langle \mathrm{SD}(x_0, t) \rangle = 2\zeta_x(x_0) t$ (Fig. 6.2), with $v_x(x_0)$ in good agreement with $F_x(x_0)$ (Fig. 6.3a), since $\beta D_x = 1$.

While the quantity $v_x(x_0)$ appears to accurately estimate the drifts $\langle \dot{x}_0 | x_0 \rangle$, we find that the estimator $\zeta_x(x_0)$ does not, on average, yield the value of $\zeta_x(x^*) = D_x$,

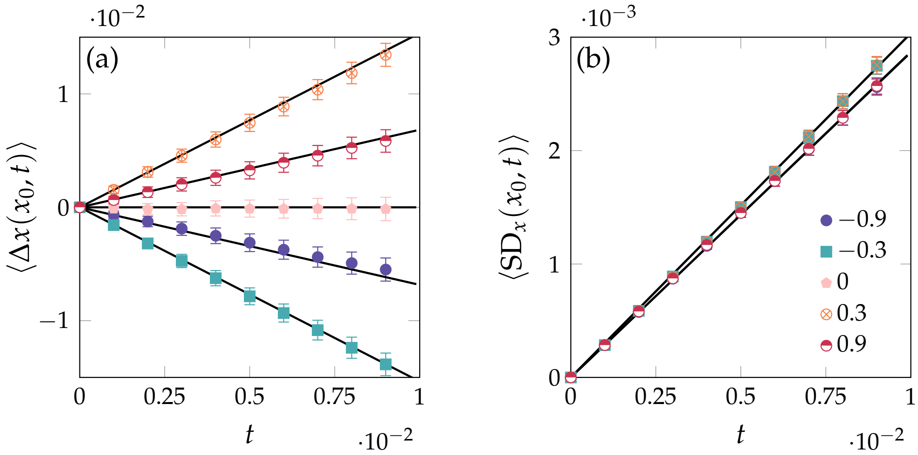

Figure 6.2: Mean displacements [(a)] and mean squared deviations from the mean $\langle x(t)\rangle$ [(b)] of trajectories $x(t) : x(0) = x_0$ at $k_BT = 0.15$ for the 5 values of x_0 given in the legend. Estimates (markers) and the corresponding 95% confidence intervals, as shown by the error bars (smaller than markers), were obtained based on 10^4 sets of $M = 100$ trajectories. Gradients of the solid lines are given by the averages of $\langle v_x(x_0)\rangle \approx F_x(x_0)$ [in (a)] and $\langle \zeta_x(x_0)\rangle$ [in (b)] over the 10^4 trajectory sets.

where $x^* = 0 = \mathrm{argmax}_x\{F_x(x)\}$. As shown in Fig. 6.3b, we observe parabolic variation of $\zeta_x(x_0)$ in the vicinity of the top of the potential barrier, with $\zeta_x(x^*) > D_x$ over a range of k_BT values. Thus, we conclude that the estimator $\zeta_x(x^*)$ is systematically in error, which, we speculate, may be attributable to the acceleration of the evolution $x(t)$ due to the curvature of F_x near $x^* = 0$.

The rate j_x of escape of trajectories starting at $x_0 = -1$ to $x = 1$ is expressed in terms of the barrier height $\Delta F_x = F_x(x^*) - F_x(-1)$ via the Kramers' [234] approximate formula:

$$j_x \approx \frac{\beta}{2\pi} D_x e^{-\beta \Delta F_x} \sqrt{|F_x''(-1)||F_x''(0)|}, \quad F_x''(x') = \left.\frac{d^2 F_x}{dx^2}\right|_{x'} \tag{6.5}$$

where $\cos\pi = -1$ and $|.|$ denotes the absolute value operator in this context. For a barrier height reconstruction procedure of the form:

$$\bar{F}_x(x_i) = -\frac{k_BT}{\zeta_x(x^*)} \sum_{x_0 = x_{\min}}^{x_i} \Delta x v_x(x_0), \quad x_i = x_{\min} + i\Delta x, \tag{6.6}$$

as motivated by Eq. (6.3), the exact form of the probability distribution of barrier height estimates $\bar{F}_x(x_i)$ can be obtained under the assumption of normality of the distribution of $\zeta_x(x^*)$. While in the next section, we will consider a similar approach to estimation of error in barrier reconstruction, here we wish only to examine the effect of the systematic error in $\zeta_x(x^*)$.

For reference, we carry out calculations of mean first passage times from $x = -1$ to $x = 1$ for a set of temperatures (Fig. 6.3c) and obtain the corresponding exact values of the stationary current via the Kramers' expression:

$$j_x = D_x \mathcal{P}_x(-1) \frac{e^{\beta F_x(-1)}}{\int_{-1}^{1} dx e^{\beta F_x(x)}}, \quad \mathcal{P}_x(x) = \frac{e^{-\beta F_x(x)}}{\int_{-2}^{0} dx e^{-\beta F_x(x)}}, \tag{6.7}$$

using numerical integration. Considering the narrow range of variation and the low magnitude of the systematic error of the estimator $\zeta_x(x^*)$, we do not expect the overestimation of D_x to impact significantly the estimates of escape rates j_x, as demonstrated in Fig. 6.3c, since the systematic error is partially cancelled by the errors in the harmonic approximations employed in the derivation of Eq. (6.5).

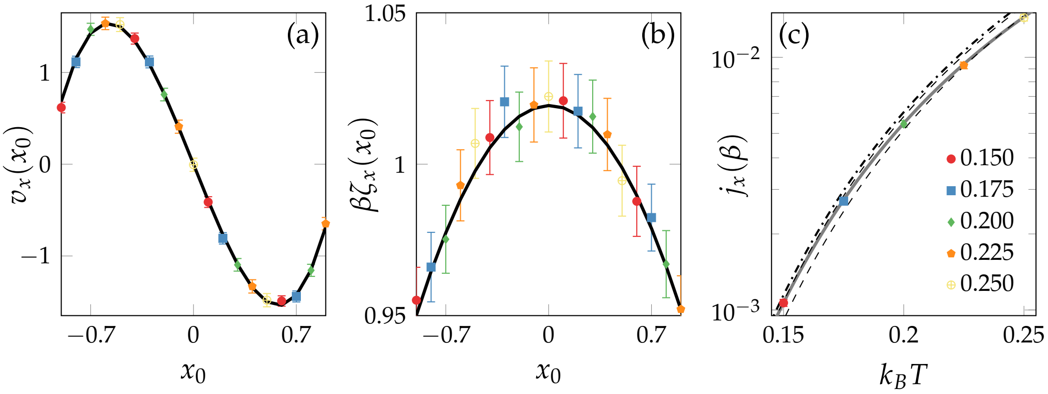

Figure 6.3: Average estimates of drifts $\langle \dot{x}_0 | x_0 \rangle$ [(a)] and coordinate dependent diffusivities [(b)], and escape rates j_x [(c)] at the 5 values of $k_B T$ specified in the legend. The values and the corresponding 95% confidence intervals, as shown by the error bars (smaller than markers), in (a) and (b) are based on 10^4 sets of $M = 100$ trajectories. Solid lines in (a) and (b) are given by, respectively, the curve dF_x/dx and a parabolic fit to the shown data. Markers in (c) correspond to means of 10^6 brute force estimates of the inverse mean first passage times, with error bars (smaller than markers) showing the corresponding 95% confidence intervals. Dashed lines in (c) show the range of j_x estimates obtained via Eq. (6.5), assuming overestimation by 1% to 4% of the barrier height and the prefactor βD_x due to the systematic error in $\zeta_x(x^*)$. The dashed-dotted line in (c) shows the values of j_x obtained via Eq. (6.5) using exact values of ΔF_x and βD_x. The grey line in (c) is given by Eq. (6.7).

6.2 SEEDING METHOD IN THE CONTEXT OF CNT

We now consider the "seeding" approach in the context of nucleation in the extended PLG model under the assumption that the largest solute cluster size $n(\sigma)$, as defined in Sec. 5.1, is a good candidate for the reaction coordinate, and the time evolution $n(t) = n[\sigma(t)]$ is well described by the Langevin equation of the form of Eq. (6.1). While in the results of committor calculations (Sec. 5.4.2) we do not find any evidence for our definition of $n(\sigma)$ being an inappropriate choice of the reaction coordinate, the assumption of $n(t)$ resembling Brownian motion is problematic, since $n(t)$ is clearly a non-Markovian process [159, 160] under both the transmutation-reorientation (TR) and the diffusion-reorientation

(DR) sets of microscopic kinetics (Sec 4.1.3). As we will discuss in Chapter 7, non-Markovian effects under the DR move set are expected to be stronger than under TR kinetics due to the stronger correlations of solute density fluctuations. Furthermore, nucleation pathways in Potts-like models of anisotropic particles are known to be strongly dependent on the relative rates of nuclei structural relaxation and particle attachment under the given set of microscopic kinetics [78]. Due to the diffusion limited character of nuclei growth under the DR kinetics, we expect substantially lower rates of particle attachment under DR than under TR kinetics, allowing much greater timescales for nuclei structural relaxation between successive particle attachment events under the DR move set.

In the context of modelling of nucleation kinetics, the central aim of the "seeding" method is to recover thermodynamic properties of the system, namely the invariant under the choice of microscopic kinetics height of the nucleation barrier, based on kinetic information, i.e. the properties of $n(t)$. In light of the above observations, we argue that the DR and TR kinetic variants of the present model offer an interesting test case for the "seeding" method, since the effects of the non-Markovian behaviour of $n(t)$ and the significance of nuclei growth pathways in this context are not clear.

6.2.1 *Estimation of Drifts and Diffusivities along the Cluster Size Coordinate*

We employ the standard "seeding" approach in obtaining values of $v_n(n_0)$ and $\zeta_n(n_0)$ for $n \in [3, 498]$ at $k_B T \in \{0.6, 0.65, 0.7\}$ and $f \in \{2, 3, \ldots, 7\}$ in cubic $\vec{l} = (64, 64, 64)$ systems, preparing the initial configurations $\sigma_0 : n(\sigma) = n_0$ in two steps: (1) Generation of solute cluster via the procedure detailed in Sec. 5.4.1, allowing $n_0 \times 10^3$ applications of the constrained cluster Metropolis MC scheme for relaxation of the initial cluster to its equilibrium structure. (2) Insertion of $N\rho(\beta, f)$ solute particles of species s chosen uniformly on $\{1, 2\}$ into the system away from the generated nucleus. Sampling $M = 10^2$ trajectories $n(t) : n(0) = n_0$ for each value of $n_0 \in [3, 498]$ we compute the estimators $v_n(n_0)$ and $\zeta_n(n_0)$ via an analogous procedure to that covered in Sec. 6.1.1, taking $\Delta t = 10\text{MCS}$ and $t_{\max} = 10^3\text{MCS}$, with $W = 10^2$. Within the considered time interval, we find that the magnitude of fluctuations in the nucleus size coordinate under the DR kinetics is negligible in comparison to $N\rho(\beta, f)$, suggesting that no significant solute depletion effects are to be expected.

The linear fits produced by $v_n(n_0)$ appear to capture the short time ($t \leq 10^2\text{MCS}$) behaviour of $n(t)$ well (Figs. 6.4a and 6.4b), however, examining the fits with respect to the time series $\Delta n(n_0, t)$, we find that the quality of the fits is not consistent and large relative errors in $v_n(n_0)$ can be expected for DR kinetics (Figs. 6.4c and 6.4d). From the drift estimates, we estimate the size n^* of the critical nucleus as:

$$n^* = \underset{n \in [3,498]}{\operatorname{argmax}} \left\{ - \sum_{n_0=3}^{n} v_n(n_0) \right\}, \tag{6.8}$$

in accordance with Eq. 6.3. While we find that $v_n(n_0)$ typically changes sign in the vicinity of $n_0 = n^*$ as expected, it is not uncommon for drift estimates $v_n(n^*)$ to deviate from zero (Fig. 6.4c).

In the obtained sample of trajectories, the nuclei growth rates under the DR kinetics appear to be approximately two orders of magnitude slower than those under the TR move set, which is attributable to the differences in the underlying character of the two particle attachment processes as discussed above. We observe reasonably linear behaviour of $\langle \mathrm{SD}_n(n^*, t) \rangle$ for $t \leq 10^2$MCS and slow variation of estimates $\zeta_n(n_0)$ in the vicinity of $n_0 = n^*$ (Fig. 6.5). We, therefore, use the data points $\zeta_n(n_0) : n_0 \in [n^* - 20, n^* + 20]$ for estimation of uncertainty in the measurement $\zeta_n(n^*)$ of diffusivity D_n.

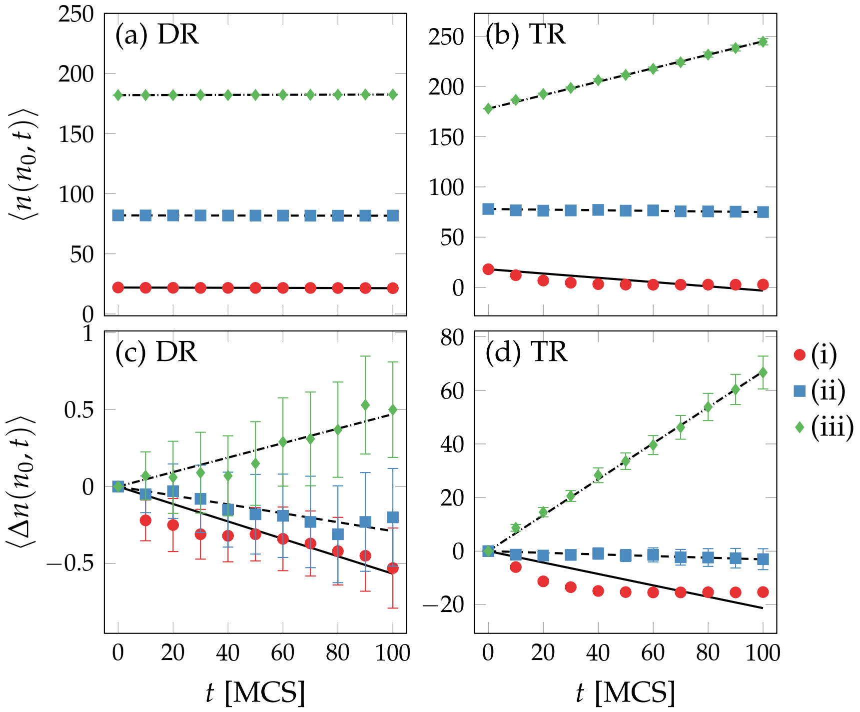

Figure 6.4: Average trajectories [(a) and (b)] and displacements [(c) and (d)] along the cluster size coordinate at $k_BT = 0.7$, $f = 3$ under DR ($n^* = 82$) and TR ($n^* = 78$) kinetics for the $c = 1$, $Q = 24$, $d = 3$ extended PLG model at three values of n_0: (i) $n_0 = n^* - 60$, (ii) $n_0 = n^*$, (iii) $n_0 = n^* + 10^2$. Markers show the data points obtained via MC, with error bars specifying the 95% confidence intervals based on $M = 10^2$ estimates, while lines correspond to the linear fits $v_n(n_0)$.

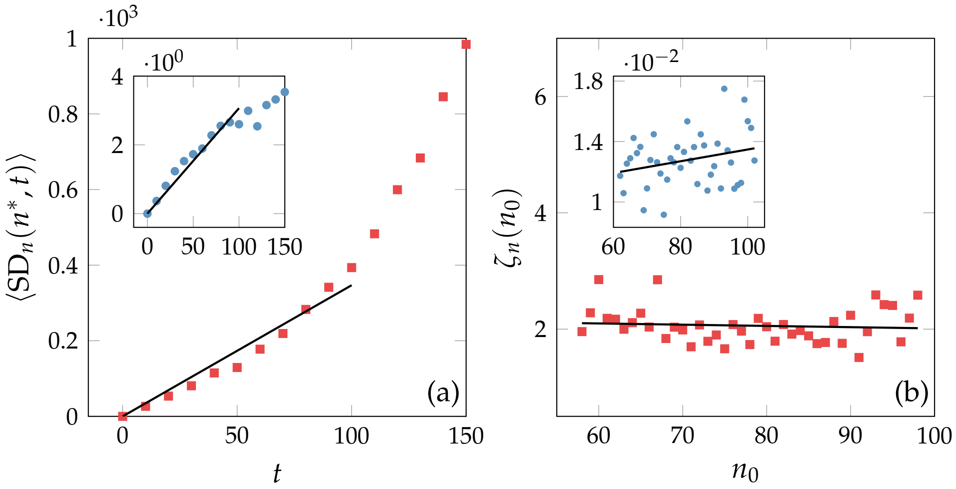

Figure 6.5: Mean squared deviation $\langle \mathrm{SD}_n(n^*, t)\rangle$ from the mean at the estimated value of critical cluster size [(a)] and estimates $\zeta_n(n_0)$, $n_0 \in [n^* - 20, n^* + 20]$ of coordinate dependent diffusivity along n [(b)] under TR (main panels) and DR (insets) kinetics for the $c = 1$, $Q = 24$, $d = 3$ extended PLG model at $k_B T = 0.7$, $f = 3$. Lines in (a) correspond to linear fits to the MC data (markers) as defined by $\zeta_n(n^*)$. Lines in (b) show the linear fits used for detrending the values of $\zeta_n(n_0)$ for estimation of uncertainty in the measurement of $\zeta_n(n^*)$.

6.2.2 *Fitting of a CNT model*

Substituting Eq. (2.54) into an analogous equation to Eq. (6.2) for $n(t)$, we obtain a relationship between the parameters $(\gamma_{\mathrm{CNT}}, \Delta\mu_{\mathrm{CNT}})$ of the CNT droplet model and the drifts $\langle \dot{n}_0 | n_0\rangle$ along the solute cluster size coordinate under the assumption of $n(t)$ obeying Langevin dynamics:

$$-\frac{\langle \dot{n}_0 | n_0\rangle}{\beta D_n} = \frac{2}{3}\gamma_{\mathrm{CNT}} n_0^{-1/3} - \Delta\mu_{\mathrm{CNT}} \quad \Rightarrow \quad \gamma_{\mathrm{CNT}} = \frac{3}{2}\left[\Delta\mu_{\mathrm{CNT}} - \frac{\langle \dot{n}_0 | n_0\rangle}{\beta D_n}\right] n_0^{1/3}. \tag{6.9}$$

We, therefore, expect that the quantity $\gamma^\dagger(n_0)$ is independent of n_0 under the assumptions of CNT and the "seeding" method:

$$\gamma^\dagger(n_0) = \frac{3}{2}\left[\Delta\mu_{\mathrm{CNT}} - \frac{v_n(n_0)}{\beta \zeta_n^*}\right] = \gamma_{\mathrm{CNT}}, \quad \zeta_n^* = \zeta_n(n^*), \tag{6.10}$$

and we define the least squares estimator γ_{LS} of γ_{CNT} as an average of $\gamma^\dagger(n_0)$ over some range $n_0 \in [a, b]$:

$$\gamma_{\mathrm{LS}} = \frac{1.5}{b - a + 1}\left[\Delta\mu_{\mathrm{CNT}} \sum_{n_0=a}^{b} n_0^{1/3} - \frac{k_B T}{\zeta_n^*} \sum_{n_0=a}^{b} v_n(n_0) n_0^{1/3}\right]. \tag{6.11}$$

Assuming that the quantities $\sum_{n_0=a}^{b} v_n(n_0) n_0^{1/3}$ and ζ_n^* are normally distributed, the probability distribution of γ_{LS} corresponds to the distribution of the quotient of noncentral normal variates [235, 236], which can be accurately computed via integration of the bivariate normal probability density function [237]. Thus, based on our sample of $v_n(n_0)$ and $\zeta_n(n_0)$ it is possible to estimate the confidence interval on γ_{LS} and, therefore, deduce the error in the estimate of the nucleation free energy barrier height.

6.2.3 *Quotient of Noncentral Normal Variates*

We now outline the approach for calculation of confidence intervals on the quantity $\sum_{n_0=a}^{b} v_n(n_0) n_0^{1/3}/\zeta_n^*$, assuming $\sum_{n_0=a}^{b} v_n(n_0) n_0^{1/3}$ and ζ_n^* are normally distributed and independent. For any two normally distributed independent random variates X_i, $i \in \{1,2\}$ with respective means $\langle X_i \rangle$ and variances $\text{Var}(X_i)$, the cumulative distribution of the quotient $Y = X_1/X_2$ is given by [236]:

$$
\begin{aligned}
\mathbb{P}(Y \leq y) &= \mathcal{L}[\omega(y), -a_2, \psi(y)] + \mathcal{L}[-\omega(y), a_2, \psi(y)], \quad a_i = \frac{\langle X_i \rangle}{\sqrt{\text{Var}(X_i)}}, \\
b(y) &= y\sqrt{\frac{\text{Var}(X_2)}{\text{Var}(X_1)}}, \quad \omega(y) = \frac{a_1 - a_2 b(y)}{\sqrt{1 + b^2(y)}}, \quad \psi(y) = \frac{b(y)}{\sqrt{1 + b^2(y)}}, \\
\mathcal{L}[h, k, \varrho] &= \frac{1}{2\pi\sqrt{1 - \varrho^2}} \int_h^\infty \int_k^\infty dx dz \exp\left\{ -\frac{x^2 + z^2 - 2xz\varrho}{2\sqrt{1 - \varrho^2}} \right\}.
\end{aligned}
\tag{6.12}
$$

In Fig. 6.6 we verify the above set of equations against numerically computed probability density distributions $\mathbb{P}(Y)$.

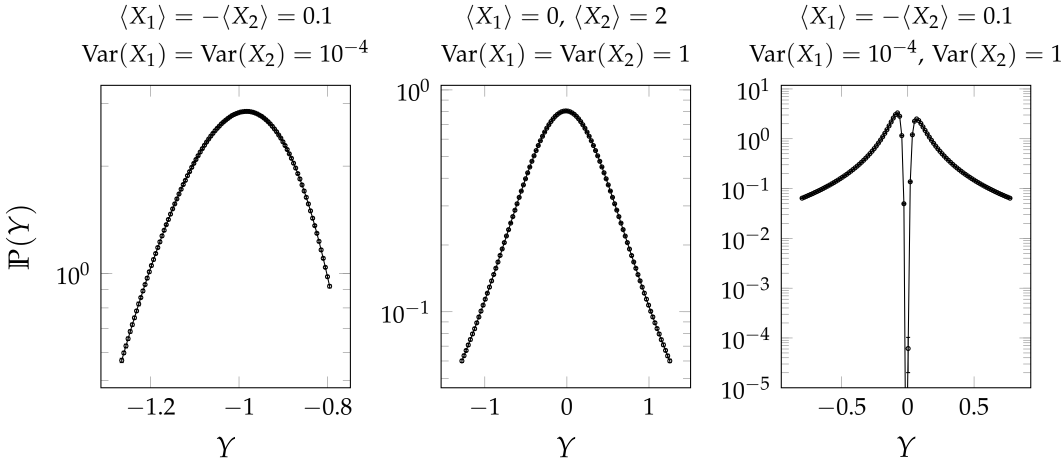

Figure 6.6: Numerically computed distributions of quotients of noncentral normal variates for three sets of parameters. The numerical estimates (markers) are based on 10^7 independent samples of $Y = X_1/X_2$ with error bars (smaller than markers) showing the 95% confidence intervals computed based on 50 independent sample sets. Lines correspond to numerically computed derivatives $d\mathbb{P}(Y \leq y)/dy$ of $\mathbb{P}(Y \leq y)$ as given by Eq. (6.12).

Setting $X_1 = \sum_{n_0=a}^{b} v_n(n_0) n_0^{1/3}$ and $X_2 = \zeta_n^*$ the 95% confidence interval on $\sum_{n_0=a}^{b} v_n(n_0) n_0^{1/3}/\zeta_n^*$ can be estimated by numerically solving the equations:

$$
\mathbb{P}(Y \leq y_{\text{min}}) - 0.025 = 0, \quad \mathbb{P}(Y \leq y_{\text{max}}) - 0.975 = 0,
\tag{6.13}
$$

for $y_{\min}$ and $y_{\max}$, and the corresponding confidence interval on the value γ_{LS} can be computed via the appropriate scaling and translation operations on the obtained interval $[y_{\min}, y_{\max}]$.

6.3 NUCLEATION BARRIER RECONSTRUCTION

The fitted CNT model yields estimates of the form of the free energy barrier $\Delta F(n)$ and the height of the barrier $\Delta F(n^{\dagger})$ via:

$$\Delta F(n) = n^{2/3}\gamma_{\mathrm{LS}} - n\Delta\mu_{\mathrm{CNT}}, \quad \Delta F(n^{\dagger}) = \frac{1}{2}n^{\dagger}\Delta\mu_{\mathrm{CNT}}, \quad n^{\dagger} = \left(\frac{2\gamma_{\mathrm{LS}}}{3\Delta\mu_{\mathrm{CNT}}}\right)^{3}, \tag{6.14}$$

Clearly, all the necessary computations, including the calculation of γ_{LS}, require a precise definition of $\Delta\mu_{\mathrm{CNT}}$ and we consider the following three options:

1. $\Delta\mu_{\mathrm{CNT}} = \Delta\mu_{\mathrm{coex}}$ – the per solute monomer free energy difference between bulk solute rich and solvent rich states, i.e. the thermodynamic solute-solvent chemical potential difference.

2. $\Delta\mu_{\mathrm{CNT}} = \Delta\mu_{\mathrm{fit}}$ – the values of the CNT volume coefficient obtained via two parameter fits of Eq. (6.9).

3. $\Delta\mu_{\mathrm{CNT}} = \Delta\mu_{\mathrm{EPS}}$ – the values of the CNT volume coefficient obtained via fits of Eq. (2.54) to the explicitly computed via EPS free energy barriers as presented in Sec. 5.3.1.

We obtain fits of the three classes of CNT models to the estimates of scaled initial drifts $-k_B T v_n(n_0)/\zeta_n^*$ in the range $n_0 \in \{n^* - 20, n^* + 20\}$ via Eq. (6.11) as illustrated in Fig. 6.7. Although we occasionally arrive at exceptionally poor fits of the $\Delta\mu_{\mathrm{CNT}} = \Delta\mu_{\mathrm{coex}}$ model, with noticeable dependence on n_0 of $\gamma^{\dagger}(n_0)$ (Figs. 6.7a and 6.7e), the resultant three fits of Eq. (6.9) are typically of comparable quality. The obtained reconstructions of the nucleation barriers [Eq. (6.14)], however, appear highly sensitive to the choice of the $\Delta\mu_{\mathrm{CNT}}$ value, as can be seen in Figs. 6.7f, 6.7g and 6.7h, where the values $\Delta\mu_{\mathrm{CNT}} \neq \Delta\mu_{\mathrm{EPS}}$ result in significantly overestimated barrier heights.

To illustrate the sensitivity of the "seeding" method's barrier reconstruction approach further, we compare the barrier height values obtained via EPS and the "seeding" method in Fig. 6.8. Here we show that usage of the model $\Delta\mu_{\mathrm{CNT}} = \Delta\mu_{\mathrm{coex}}$ results in systematic errors of up to a factor of 3 in the obtained estimates of nucleation barrier heights, while usage of values $\Delta\mu_{\mathrm{CNT}} = \Delta\mu_{\mathrm{fit}}$ leads to poor consistency of the estimation procedure, often yielding barrier reconstructions which vary strongly with the underlying microscopic kinetics of the system. Taking $\Delta\mu_{\mathrm{CNT}} = \Delta\mu_{\mathrm{EPS}}$ results in reasonable agreement between the barrier height estimates of the "seeding" method and those of EPS under both sets of kinetics

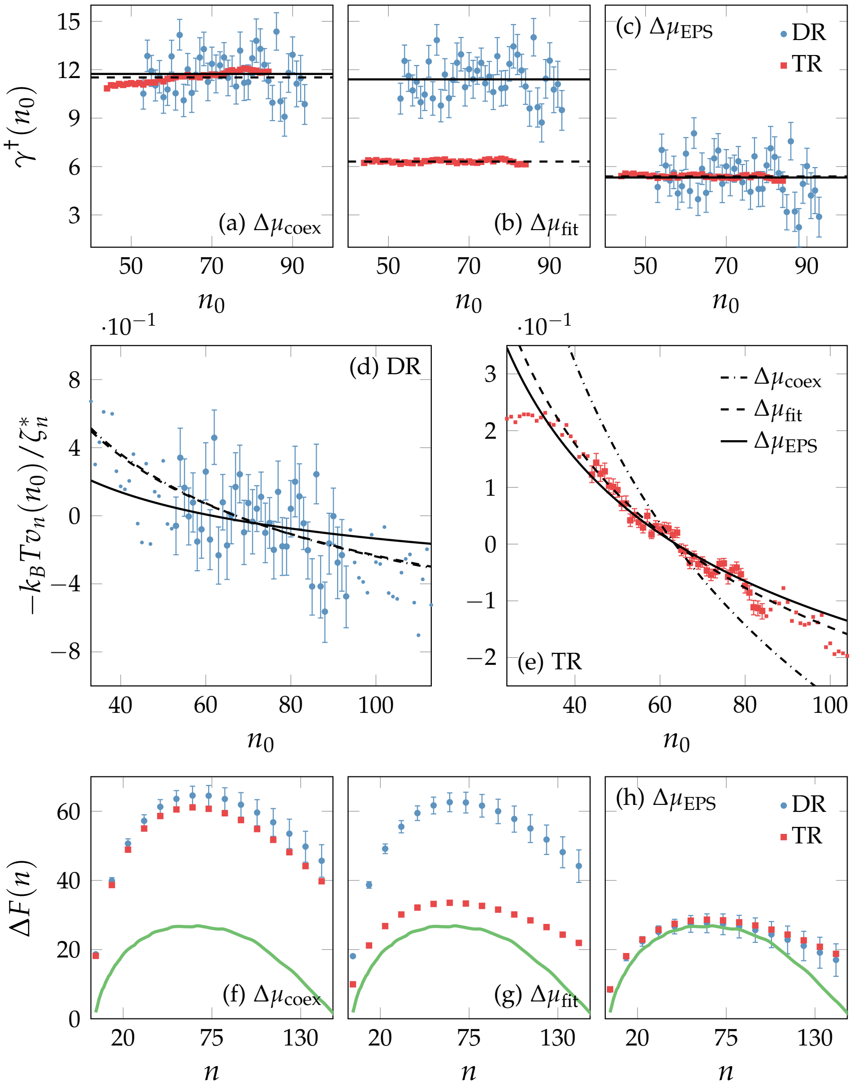

Figure 6.7: Comparison of the three fitted CNT models based on the three values of $\Delta\mu_{\mathrm{CNT}}$ for DR (circles) and TR (squares) kinetics for the $c = 1$, $Q = 24$, $d = 3$ extended PLG model at $k_BT = 0.7$, $f = 4$. Panels (a), (b) and (c) show the obtained values of $\gamma^\dagger(n_0)$ [Eq. (6.10)] (markers) and the corresponding linear fits γ_{LS} [Eq. (6.11)] (lines). Panels (d) and (e) compare the numerical estimates (markers) and the fitted CNT models (lines) for the Eq. (6.9), using the three values of $\Delta\mu_{\mathrm{CNT}}$ specified in the legend of (e). The smaller markers in (d) and (e) correspond to data points outside the ranges $n_0 \in [n^* - 20, n^* + 20]$ of the data values used for computation of the CNT fits. Panels (f), (g) and (h) show the forms of the reconstructed via CNT fits profiles $\Delta F(n)$ [Eq. (6.14)] (markers) in relation to those explicitly computed via EPS (Fig. 5.4) (lines). Error bars show the 95% confidence intervals obtained using the procedure outlined in Sec. 6.2.3.

for $f \geq 3$, although at lower supersaturations ($f = 2$) we find that the "seeding" method overestimates the barrier heights by up to 43%.

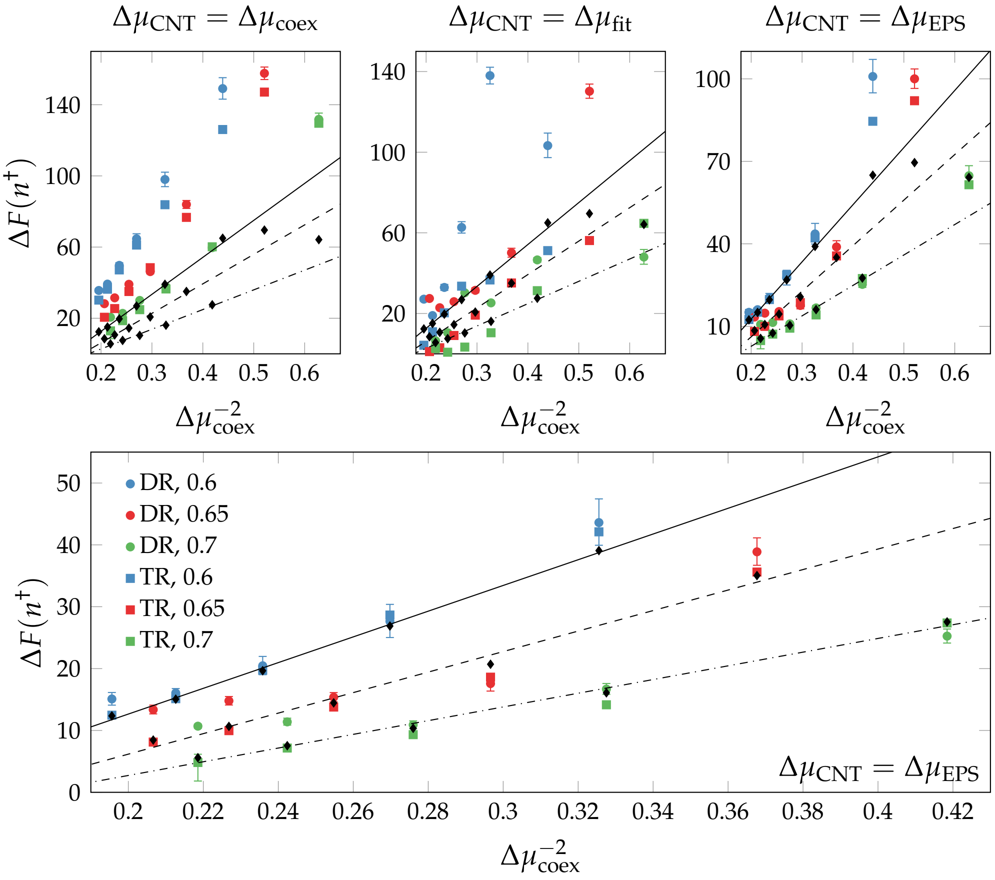

Figure 6.8: Comparison of nucleation barrier height estimates obtained via EPS (diamonds and lines corresponding to the data shown in Fig. 5.5c) and the "seeding" method (markers), using the three definitions of $\Delta\mu_{\mathrm{CNT}}$ for DR (circles) and TR (squares) kinetics for the $c = 1$, $Q = 24$, $d = 3$ extended PLG model at $k_B T \in \{0.6, 0.65, 0.7\}$ and $f \in \{2, 3, \ldots, 7\}$. Error bars show the 95% confidence intervals obtained using the procedure outlined in Sec. 6.2.3.

6.3.1 *Nucleation Rate Estimates*

We now compare the nucleation rate values obtained via Eq. 2.53 using barrier height estimates of the "seeding" method and of EPS. We estimate the monomer attachment rates J_*^+ via the measurements $\zeta_n(n_0)$ of diffusivity D_n along the nucleus size coordinate, taking $J_*^+ = \zeta_n(n^*)$ with n^* given by Eq. (6.8) for the "seeding" method, and $J_*^+ = \zeta_n(n^{\dagger})$ for EPS where $n^{\dagger} = \mathrm{argmax}_n\{\Delta F(n)\}$ with $\Delta F(n)$ being the explicitly computed free energy barrier. The values of the Zeldovich factor $\mathcal{Z}$ are given by $\mathcal{Z} = 3(\Delta\mu_{\mathrm{CNT}})^2\sqrt{\beta(\gamma_{\mathrm{LS}})^{-3}}/4$ in the case of the "seeding" method and are estimated via the curvature of parabolic fits to the top of the explicitly computed barrier $\Delta F(n)$ for EPS. We use the solute density values $\rho(\beta, f)$, shown in Fig. 4.7, in estimation of rates based on both the "seeding" method and the EPS data sets.

The resultant nucleation rate estimates are shown in Fig. 6.9 from which we arrive at the same set of conclusions regarding the sensitivity of the ”seeding” method to the choice of $\Delta\mu_{\text{CNT}}$ value as when analysing Fig. 6.8. The systematic errors in barrier height estimates of the $\Delta\mu_{\text{CNT}} = \Delta\mu_{\text{coex}}$ model lead to factors of tens of orders of magnitude disagreement between the rate estimates of the ”seeding” method and those obtained via the CNT formula [Eq. (2.53)] using the EPS estimates $\Delta F(n^{\dagger})$ of the nucleation barrier heights. The poor consistency and the large scatter of rate values using the $\Delta\mu_{\text{CNT}} = \Delta\mu_{\text{fit}}$ fits are attributable to the large errors in drift and diffusivity estimates for DR kinetics. The systematic deviation of rate values estimated based on the $\Delta\mu_{\text{CNT}} = \Delta\mu_{\text{EPS}}$ model from those obtained via EPS is likely due to the differences in the estimates $\zeta_n(n^*)$ and $\zeta_n(n^{\dagger})$ of diffusivity along the n coordinate and the differences in the computed values of $\mathcal{Z}$.

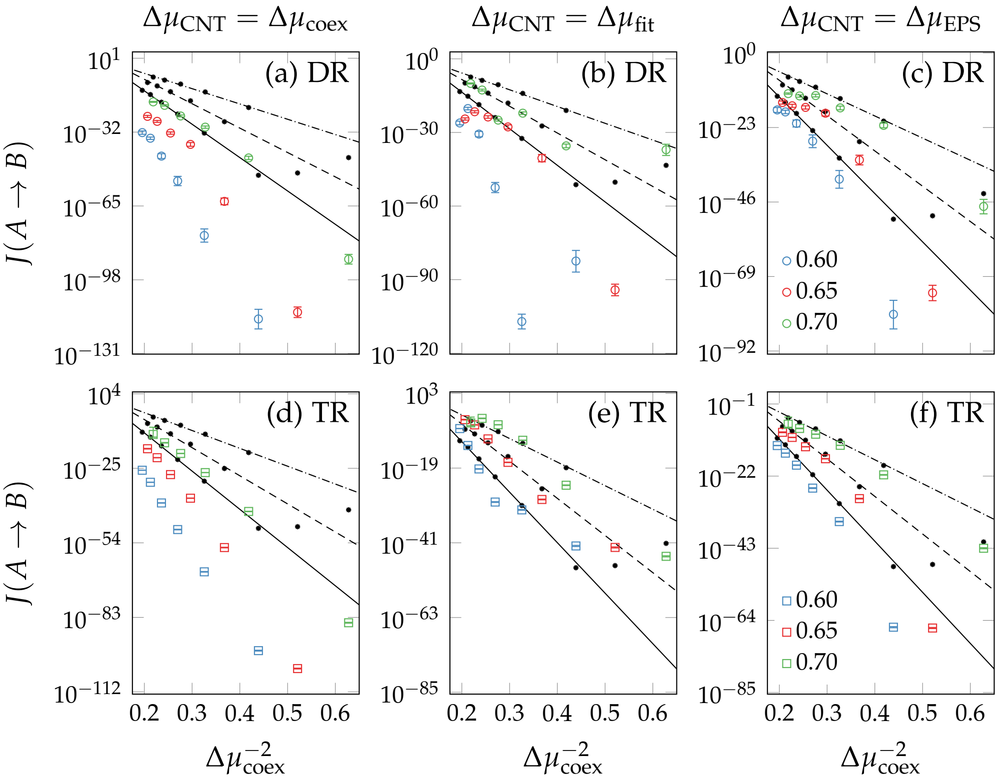

Figure 6.9: Comparison of nucleation rate estimates obtained via EPS (lines and black markers) and the ”seeding” method (hollow markers), using the three definitions of $\Delta\mu_{\text{CNT}}$ for DR (circles) and TR (squares) kinetics for the $c = 1$, $Q = 24$, $d = 3$ extended PLG model at $k_B T \in \{0.6, 0.65, 0.7\}$ and $f \in \{2, 3, \ldots, 7\}$. Error bars are based on the 95% confidence intervals on γ_{LS}.

Thus, we have shown that barrier reconstruction and rate estimation procedures of the ”seeding” method are highly sensitive to the values of $\Delta\mu_{\text{CNT}}$, yet, given an appropriate value of the CNT volume coefficient, reasonable estimates of these quantities can be obtained based on seeded trajectories of $n(t)$ at high solute supersaturations. Although we expect differences in the accuracy of the Langevin description of $n(t)$ as well as differences in growth pathways for the two studied sets of kinetics, the barrier reconstructions for DR and TR move sets appear in good agreement at high supersaturations suggesting that the differences between the respective $n(t)$ kinetics do not play a significant role here.

From the available to us data we cannot comment conclusively on the discrepancies between the barrier height and nucleation rate estimates of the ”seeding” method and those informed by explicit free energy calculations at $f = 2$. The apparent deviation of explicit barrier height estimates from the CNT scaling $\Delta F(n^{\dagger}) \propto \Delta\mu_{\mathrm{coex}}^{-2}$ at the lower supersaturations may be an artefact of our solute cluster size metric or may indicate the onset of a distinct scaling regime for $f \leq 2$. The latter scenario, while previously unseen in lattice models, is not implausible since, unlike for $f \geq 3$, we expect the equilibrium structures of the critical nuclei at lower supersaturations to be partially or fully ordered, as shown in Sec. 5.3.2. Thus it is not unreasonable to suppose that the scaling of nucleation barrier heights with solute-solvent chemical potential difference in the lower supersaturation regime may be distinct to that seen at higher supersaturations due to the distinction between energetics and surface properties of fully disordered and partially or fully ordered nuclei. Furthermore, it is possible that the appropriate nuclei structures were not adequately sampled in our application of the ”seeding” method, since $n \times 10^3$ applications of the constrained cluster size MC scheme may be insufficient to relax the initially generated large nuclei to their equilibrium structures, which would explain the observed discrepancies.

7

EXPLICIT RATE CALCULATIONS

We start by briefly reviewing the formalism of transition path theory and its connection to the theory of Markov chains and rare event methods in the context of reversible Markov jump processes. Since detailed comparison of the well established rare event methods is still lacking in the literature, we will provide an illustration of the implemented methods by studying transition events a simple system. The results of rare event simulations for the $c = 1$, $Q = 24$, $d = 3$ extended PLG model will be covered towards the end of the chapter.

7.1 IRREDUCIBLE MARKOV CHAINS

Computational study of kinetics of lattice models, in our case, is concerned with properties of a Markov jump process $\sigma(m) \in \Lambda$, $m \in \mathbb{N}$ evolving at discrete time intervals m on a discrete and finite state space Λ. Every configuration $\sigma \in \Lambda$ encodes states of N lattice sites, no more than two of which may change over any jump $\sigma(m) \to \sigma(m+1)$ due to single site update or site exchange moves as used in MC (Sec. 4.1.3). For simplicity, we will set a constant rate R for all possible jumps, including the self loops $\sigma \to \sigma$, which can be used to map the discrete time process $\sigma(m)$ onto its continuous analogue $\sigma(t)$, $t \in [0, \infty)$. Setting $R = N$ we state that, on average, N jumps occur per unit time, i.e. one time unit is equivalent to a single MC sweep (Sec. 2.2.6).

In this setting, the continuous time process $\sigma(t)$ is fully defined by the jump rate R and the jump (transition) matrix $\boldsymbol{P}$:

$$P_{ij} = \mathbb{P}(\sigma_i \to \sigma_j),\ i, j \in \{1, \ldots, |\Lambda|\}, \tag{7.1}$$

where $\boldsymbol{P}$ remains constant after every jump and is such that the set Λ of microstates forms a single communicating class, i.e. there exists at least one path of non zero probability between any two microstates states in Λ. We will now outline some elegant computations on $\boldsymbol{P}$ which will be useful in later sections.

7.1.1 *The Fundamental Matrix*

In studies of transition events, we are interested in aggregate properties of trajectories $\sigma(t)$ which start in some subset $A \subset \Lambda$ and end in some other subset $B \subset \Lambda$, such that A and B are disjoint. Much of rare event methodology, for example, is concerned with computing the average first passage times from A to B.

In the context of irreducible Markov chains [238], as discussed in Sec. 2.2.1, problems of this kind can be very elegantly formulated in terms of the fundamental matrix $\boldsymbol{G}$ of an absorbing Markov chain with a transition matrix $\boldsymbol{M}$, which is easily constructed from $\boldsymbol{P}$. To study properties of trajectories $\sigma(t)$, ending in some subset $C \subset \Lambda$ and starting anywhere but C, one constructs $\boldsymbol{M}(C)$ by modifying $\boldsymbol{P}$ as follows:

$$M_{ij}(C) = \begin{cases} P_{ij} & \text{if } \sigma_i, \sigma_j \in \Lambda \setminus C, \\ 0 & \text{if } \sigma_i \in C,\, \sigma_j \in \Lambda \setminus C, \\ 1 & \text{if } \sigma_i = \sigma_j \in C, \text{ i.e. otherwise.} \end{cases} \tag{7.2}$$

Thus $\boldsymbol{M}(C)$ corresponds to $\boldsymbol{P}$ modified such that all states $\sigma \in C$ are absorbing. The fundamental matrix $\boldsymbol{G}(C)$ is extracted by first rearranging the rows of $\boldsymbol{M}(C)$ and partitioning it into portions corresponding to absorbing and non-absorbing states:

$$\boldsymbol{M}(C) = \begin{bmatrix} \boldsymbol{M}_l(C) & \boldsymbol{M}_r(C) \\ \boldsymbol{0}_C & \boldsymbol{I}_C \end{bmatrix}, \tag{7.3}$$

where $\boldsymbol{I}$ is a $|C| \times |C|$ identity matrix, $\boldsymbol{0}_C$ is a $|C| \times |\Lambda \setminus C|$ matrix of zeroes, $\boldsymbol{M}_l(C)$ is a $|\Lambda \setminus C| \times |\Lambda \setminus C|$ matrix of transition probabilities between states $\sigma, \sigma' \in \Lambda \setminus C$ and $\boldsymbol{M}_r(C)$ is a $|\Lambda \setminus C| \times |C|$ matrix of jump probabilities from states $\sigma \in \Lambda \setminus C$ to states $\sigma' \in C$. The fundamental matrix is then defined as:

$$\boldsymbol{G}(C) = \lim_{\tau \to \infty} \sum_{k=0}^{\tau} \left[\boldsymbol{M}_l(C)\right]^k = \left[\boldsymbol{I}_{\Lambda \setminus C} - \boldsymbol{M}_l(C)\right]^{-1}. \tag{7.4}$$

7.1.2 *Mean First Passage Times*

The significance of $\boldsymbol{G}(C)$ is that it encodes the mean numbers of jumps in $\Lambda \setminus C$ before absorption by C of trajectories which started in $\Lambda \setminus C$. It is possible to show that the column vector $\vec{m}_C$, where each entry $m_C^{(i)}$ gives the mean number of jumps before absorption in C from a state $\sigma_i \in \Lambda \setminus C$, $i \in \{1, \dots, |\Lambda \setminus C|\}$, is given by:

$$\vec{m}_C = \boldsymbol{G}(C)\vec{e}_{\Lambda \setminus C}, \quad \Rightarrow \quad m_C^{(i)} = \sum_{j=1}^{|\Lambda \setminus C|} G_{ij}(C), \tag{7.5}$$

where $\vec{e}_{\Lambda \setminus C}$ is a column vector of $|\Lambda \setminus C|$ ones. To specify the mean number of jumps before entry into C, one has to provide the initial distribution $\widetilde{\mathbb{P}}_{\Lambda \setminus C}(\sigma)$ of states $\sigma \in \Lambda \setminus C$. Expressing $\widetilde{\mathbb{P}}_{\Lambda\setminus C}(\sigma)$ as a row vector $\vec{\pi}_{\Lambda\setminus C} : \pi^{(i)}_{\Lambda\setminus C} = \widetilde{\mathbb{P}}_{\Lambda\setminus C}(\sigma_i)$, the mean number of jumps $\langle m_C | \vec{\pi}_{\Lambda\setminus C} \rangle$ before hitting C can be written as a scalar product:

$$\langle m_C | \vec{\pi}_{\Lambda\setminus C} \rangle = \vec{\pi}_{\Lambda\setminus C} \vec{m}_C = \vec{\pi}_{\Lambda\setminus C} \boldsymbol{G}(C) \vec{e}_{\Lambda\setminus C}, \tag{7.6}$$

which, in the case of a constant jump rate R, also yields the mean first passage time $\langle t_C | \vec{\pi}_{\Lambda\setminus C} \rangle$:

$$\langle t_C | \vec{\pi}_{\Lambda\setminus C} \rangle = \langle m_C | \vec{\pi}_{\Lambda\setminus C} \rangle / R. \tag{7.7}$$

7.1.3 *Absorption Probabilities*

The probability of eventual absorption of a trajectory $\sigma(t) : \sigma(0) = \sigma_i \in \Lambda \setminus C$ by a particular state $\sigma_j \in C$ is given by a matrix $\boldsymbol{A}(C) = \left[A_{ij}(C)\right]$:

$$\boldsymbol{A}(C) = \boldsymbol{G}(C)\boldsymbol{M}_r(C), \tag{7.8}$$

which yields the distribution row vector $\vec{\pi}_C$, whose jth entry gives the average absorbed by the particular state $\sigma_j \in C$ fraction of trajectories $\sigma(t) : \sigma(0) \in \Lambda \setminus C$, given the initial distribution $\vec{\pi}_{\Lambda\setminus C}$ of staring points $\sigma(0)$ in $\Lambda \setminus C$:

$$\vec{\pi}_C = \vec{\pi}_{\Lambda\setminus C} \boldsymbol{A}(C). \tag{7.9}$$

7.1.4 *General Applicability*

It is worth noting that computations of mean first passage times and absorption probabilities do not require explicit evaluation of the fundamental matrix. Nevertheless, computations on transition matrices for even the smallest lattice models are generally impractical due to the large volume of the models' configuration space. In addition, jump probabilities in low temperature and saturation regions of the parameter space are typically small, which limits the precision with which useful quantities can be evaluated numerically.

7.2 TRANSITION PATH THEORY

Path sampling methods for rate calculations are often derived in the context of the effective positive flux formalism. In this chapter we will explore the transition path theoretic (TPT) approach [54] in the context of reversible Markov chains, as introduced in Sec. 2.2.2. We will first outline the relationship between TPT and the quantities discussed in Sec. 7.1.

7.2.1 *Rate and Effective Reactive Current*

In Sec. 2.3.5 we presented an expression for the rate of transition from metastable state A to stable state B as a sum of effective reactive probability currents $\mathcal{J}^+(\sigma \to \sigma')$ from A to B through a dividing surface. For reversible Markov jump processes

[Eq. (2.8)], there is no distinction between the forward and backward hitting times $\tau_C^+(\sigma)$ and $\tau_C^-(\sigma)$:

$$\tau_C^+(\sigma) = \tau_C^-(\sigma) = \tau_C(\sigma), \tag{7.10}$$

leading to the following relation for the forward and backward committors q_σ^+, q_σ^-:

$$q_\sigma^+ = \mathbb{P}[\tau_B(\sigma) < \tau_A(\sigma)] = 1 - \mathbb{P}[\tau_B(\sigma) > \tau_A(\sigma)] = 1 - q_\sigma^-. \tag{7.11}$$

Further noting that $q^+(\sigma) = 0\,\forall\sigma \in A$ and assuming a constant jump rate R, we can write Eq. (2.43) as:

$$J(A \to B) = R \sum_{\sigma\in A} \sum_{\sigma'\in\Lambda\setminus A} \mathbb{P}(\sigma)\mathbb{P}(\sigma \to \sigma')\mathbb{P}[\tau_B(\sigma') < \tau_A(\sigma')]. \tag{7.12}$$

7.2.2 *Paths, Hitting Times and Committors*

In Sec. 5.2.1, we have sketched a derivation for a MC approach to sampling the equilibrium distribution $\mathbb{P}(\vec{\sigma}_\tau)$ of paths $\vec{\sigma}_\tau$ of fixed length $\tau \in \mathbb{N}$. It is easy to see that the distribution $\mathbb{P}[\tau_C(\sigma)]$ of hitting times $\tau_C(\sigma)$ can be related to the distribution of paths $\mathbb{P}(\vec{\sigma}_\tau)$:

$$\mathbb{P}[\tau_C(\sigma) = \tau] = \sum_{\sigma_1\in\Lambda\setminus C} \sum_{\sigma_2\in\Lambda\setminus C} \cdots \sum_{\sigma_\tau\in C} \mathbb{P}(\sigma \to \sigma_1) \prod_{i=1}^{\tau-1} \mathbb{P}(\sigma_i \to \sigma_{i+1}), \tag{7.13}$$

by expressing the total probability of reaching some state space subset $C \subset \Lambda$ from state $\sigma \in \Lambda$ for the first time after $\tau \in \mathbb{Z}^+$ jumps, as a sum over paths of length $\tau + 1$ (since the initial state σ is included) which only visit the set C after τ jumps from σ. Using the notation of Sec. 7.1, it is easy to see that $\mathbb{P}[\tau_C(\sigma) = \tau]$ is the sum of entries of the row vector: $\vec{\pi}_{\Lambda\setminus C}\boldsymbol{M}_l^{\tau-1}(C)\boldsymbol{M}_r(C)$, where the row vector $\vec{\pi}_{\Lambda\setminus C}$ corresponds to the distribution $\mathbb{P}(\sigma \to \sigma_1)$ over $\sigma_1 \in \Lambda \setminus C$, i.e. entries $P_{ij} : \sigma_i = \sigma, \sigma_j = \sigma_1$ of the transition matrix $\boldsymbol{P}$.

The above expression does not exclude the possible contributions from trajectories which hit other disjoint from C subsets of Λ in less that τ jumps from σ. Such contributions are important to consider when computing the committor $\mathbb{P}[\tau_B(\sigma) < \tau_A(\sigma)]$. Let $\Theta = \Lambda \setminus (A \cup B)$ be the subset of the state space Λ excluding the reactant and product states. For any jump $\sigma_i \to \sigma_{i+1}$ we can write:

$$\sum_{\sigma_{i+1}\in\Lambda\setminus B} \mathbb{P}(\sigma_i \to \sigma_{i+1}) = \sum_{\sigma_{i+1}\in\Theta} \mathbb{P}(\sigma_i \to \sigma_{i+1}) + \sum_{\sigma_{i+1}\in A} \mathbb{P}(\sigma_i \to \sigma_{i+1}). \tag{7.14}$$

This allows us to separate the contributions to $\mathbb{P}[\tau_B(\sigma) = \tau]$ from two types of trajectories: (1) Those that remain in Θ until the final jump τ. (2) Those that decay to A after $\tau' < \tau$ jumps:

$$\begin{aligned}
\mathbb{P}[\tau_B(\sigma) = \tau] = &\sum_{\sigma_1 \in \Theta} \sum_{\sigma_2 \in \Theta} \cdots \sum_{\sigma_\tau \in B} \mathbb{P}(\sigma \to \sigma_1) \prod_{i=1}^{\tau-1} \mathbb{P}(\sigma_i \to \sigma_{i+1}) \\
&+ \sum_{\sigma_1 \in A} \sum_{\sigma_2 \in \Lambda \backslash B} \cdots \sum_{\sigma_\tau \in B} \mathbb{P}(\sigma \to \sigma_1) \prod_{i=1}^{\tau-1} \mathbb{P}(\sigma_i \to \sigma_{i+1}) \\
&+ \sum_{\sigma_1 \in \Theta} \sum_{\sigma_2 \in A} \sum_{\sigma_3 \in \Lambda \backslash B} \cdots \sum_{\sigma_\tau \in B} \mathbb{P}(\sigma \to \sigma_1) \prod_{i=1}^{\tau-1} \mathbb{P}(\sigma_i \to \sigma_{i+1}) + \ldots
\end{aligned} \tag{7.15}$$

Introducing the joint probability $\mathbb{P}[\tau_A(\sigma), \tau_B(\sigma)]$ of trajectories originating at $\sigma \in \Lambda$ and hitting the sets A and B at respective first times τ_A and τ_B:

$$\mathbb{P}[\tau_A, \tau_B] = \sum_{\sigma_1 \in \Theta} \cdots \sum_{\sigma_{\tau_A} \in A} \sum_{\sigma_3 \in \Lambda \backslash B} \cdots \sum_{\sigma_{\tau_B} \in B} \mathbb{P}(\sigma \to \sigma_1) \prod_{i=1}^{\tau_B - 1} \mathbb{P}(\sigma_i \to \sigma_{i+1}), \tag{7.16}$$

we can rewrite Eq. 7.15 in the more compact form:

$$\begin{aligned}
\mathbb{P}[\tau_B(\sigma) = \tau] &= \mathbb{P}[\tau_A(\sigma) > \tau, \tau_B(\sigma) = \tau] + \sum_{i=1}^{\tau-1} \mathbb{P}[\tau_A(\sigma) = i, \tau_B(\sigma) = \tau] \\
&= \mathbb{P}[\tau_A(\sigma) > \tau, \tau_B(\sigma) = \tau] + \mathbb{P}[\tau_A(\sigma) < \tau, \tau_B(\sigma) = \tau],
\end{aligned} \tag{7.17}$$

where the contribution:

$$\mathbb{P}[\tau_A(\sigma) > \tau, \tau_B(\sigma) = \tau] = \sum_{\sigma_1 \in \Theta} \sum_{\sigma_2 \in \Theta} \cdots \sum_{\sigma_\tau \in B} \mathbb{P}(\sigma \to \sigma_1) \prod_{i=1}^{\tau-1} \mathbb{P}(\sigma_i \to \sigma_{i+1}) \tag{7.18}$$

is related to the committor as:

$$\mathbb{P}[\tau_B(\sigma) < \tau_A(\sigma)] = \lim_{\tau \to \infty} \sum_{k=1}^{\tau} \mathbb{P}[\tau_A(\sigma) > k, \tau_B(\sigma) = k]. \tag{7.19}$$

Thus, the committor can be thought of as the total absorption probability by subset B of trajectories $\sigma(t) : \sigma(0) = \sigma \in \Theta$ in a Markov chain where all states in $A \cup B$ are absorbing. In the framework of Sec. 7.1, the vector of committor values for states $\sigma \in \Theta$ can be expressed as: $\boldsymbol{A}(A \cup B)\vec{e}_B$, where $\vec{e}_B$ is a column vector with $|A \cup B|$ entries such that $e_B^{(i)} = 1$ for $\sigma_i \in B$ and $e_B^{(j)} = 0$ for $\sigma_j \in A$.

7.2.3 *Escape Rates and Quasi-equilibrium*

When considering transitions from metastable to stable macroscopic states, we assume that the initial probability distribution $\widetilde{\mathbb{P}}(\sigma)$ of the system's microstates is concentrated in A and transforms into the concentrated in B equilibrium distribution $\mathbb{P}(\sigma)$ at a sufficiently slow rate that $\widetilde{\mathbb{P}}(\sigma)$ can be treated as stationary. Under the stationarity assumption on $\widetilde{\mathbb{P}}(\sigma)$, we can write the approximately constant with time total probability flux J_A^+ leaving the state A as a sum over all possible escape routes out of A:

$$J_A^+ = R \sum_{\sigma \in A} \sum_{\sigma' \in \Lambda \setminus A} \widetilde{\mathbb{P}}(\sigma)\mathbb{P}(\sigma \to \sigma'). \tag{7.20}$$

Thus, for time invariant $\widetilde{\mathbb{P}}(\sigma)$, J_A^+ is equivalent to the inverse mean residence time in A and the inverse mean first passage time $\langle t_{\Lambda\setminus A} | \vec{\pi}_A \rangle$ from A to $\Lambda \setminus A$ for trajectories $\sigma(t) \, : \, \sigma(0) \in A$, with the distribution $\vec{\pi}_A$ of initial microstates corresponding to the concentrated in A distribution $\widetilde{\mathbb{P}}(\sigma)$. Defining:

$$\mathbb{P}(\sigma' | A \to \sigma') = R \left(J_A^+\right)^{-1} \sum_{\sigma \in A} \widetilde{\mathbb{P}}(\sigma)\mathbb{P}(\sigma \to \sigma'), \tag{7.21}$$

as the distribution of microstates the system takes upon first leaving A, we can rewrite Eq. (7.12) as:

$$J(A \to B) = J_A^+ \sum_{\sigma \in \Lambda \setminus A} \mathbb{P}(\sigma | A \to \sigma)\mathbb{P}[\tau_B(\sigma) < \tau_A(\sigma)]. \tag{7.22}$$

Noting that $\sum_{\sigma \in \Lambda \setminus A} \mathbb{P}(\sigma | A \to \sigma) = 1$, the above expression can be interpreted as the product of the probability flux out of A and the average with respect to $\mathbb{P}(\sigma | A \to \sigma)$ committor for microstates $\sigma \in \Lambda \setminus A$.

Using the notation of Sec. 7.1, the above can be expressed as:

$$J(A \to B) = \langle t_{\Lambda\setminus A} | \vec{\pi}_A \rangle^{-1} \left[\vec{\pi}_\Theta \boldsymbol{A}(A \cup B)\vec{e}_B + \sum_{\sigma \in B} \mathbb{P}(\sigma | A \to \sigma) \right], \tag{7.23}$$

where $\vec{\pi}_A$ is a row vector with $|A|$ elements representing $\widetilde{\mathbb{P}}(\sigma)$, $\vec{\pi}_\Theta$ is a row vector with $|\Theta|$ entries representing the portion of $\mathbb{P}(\sigma | A \to \sigma)$ falling on Θ, $\vec{e}_B$ is a column vector with $|A \cup B|$ elements such that $e_B^{(i)} = 1$ for $\sigma_i \in B$ and $e_B^{(j)} = 0$ for $\sigma_j \in A$ and the sum inside the square brackets takes into account the possibility of trajectories arriving from A to B in one jump.

7.2.4 *Application to the Ising Model*

We now consider transition events in the 3×3 two-dimensional Ising model under the Metropolis realisation of spin flip kinetics with periodic boundaries, without examining in detail the transition mechanism. The transition matrix $\boldsymbol{P}$ has $(2^9)^2$ entries $\mathbb{P}(\sigma_i \to \sigma_j)$ given by:

$$P_{ij} = \begin{cases} 0 & \text{if } |N_+(\sigma_j) - N_+(\sigma_i)| > 1, \\ \frac{1}{2N}\left\{e^{\beta\left[E(\sigma_i)-E(\sigma_j)\right]}\right\}\left\{f^{N_+(\sigma_j)-N_+(\sigma_i)}\right\} & \text{if } |N_+(\sigma_j) - N_+(\sigma_i)| = 1, \\ 1 - \sum_{k\neq i} P_{ik} & \text{if } i = j, \text{ i.e. otherwise.} \end{cases} \tag{7.24}$$

which can be calculated and represented with sufficient accuracy for a range in (k_BT, f) numerically, where $N_+(\sigma)$ gives the count of "up" spins in the configuration σ, $f = \exp[\beta(\mu_+ - \mu_-)]$, with μ_+ and μ_- being the reservoir chemical potentials of respectively the "up" and "down" spins, and we have already covered the relationship between f and the external magnetic field h in Sec. 3.2.1. In Fig. 7.1 we verify that the above matrix is consistent with the Metropolis MC by computing the equilibrium distribution $\mathbb{P}(N_+)$ via MC and by taking the principal eigenvector of $\boldsymbol{P}$.

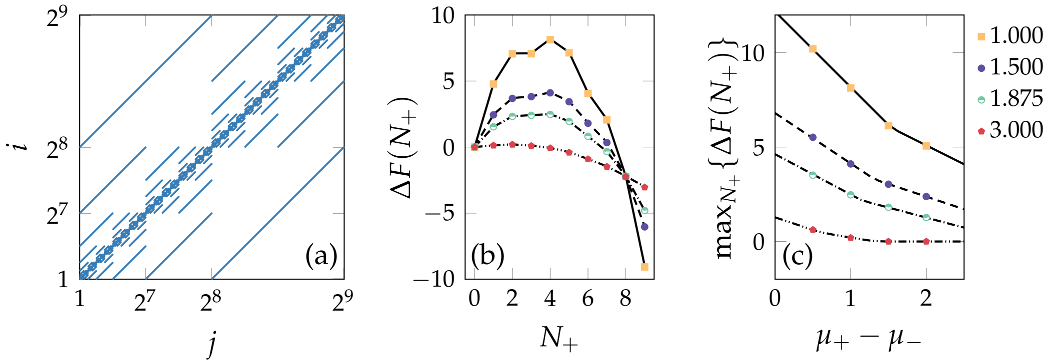

Figure 7.1: Validation of the jump matrix $\boldsymbol{P}$ for the 3×3 Ising model. The sparsity pattern of $\boldsymbol{P}$ is shown in (a) with blue dots marking the nonzero entries. In (b) free energies $\Delta F(N_+) = -\ln \mathbb{P}(N_+) + \ln \mathbb{P}(N_+ = 0)$ are plotted for four values of k_BT (legend) at $\mu_+ - \mu_- = 1$. In (c) we plot the maxima of $\Delta F(N_+)$ as a possible metric for the heights of the free energy barriers to transition from spin "down" to spin "up" state. The markers in (b) and (c) correspond to the data obtained via the multicanonical flat histogram MC, with the minimum bias increment of 2^{-30}, while the lines show the values obtained by computing the principal eigenvector of $\boldsymbol{P}$.

We define $A = \{\sigma : N_+(\sigma) = 0\}$ and consider transitions from A to $B = \{\sigma : N_+(\sigma) = N\}$, starting from a nonequilibrium initial distribution $\widetilde{\mathbb{P}}(\sigma \in A) = 1$. Taking the jump rate as $R = 1$, it is easy to see that the escape rate J_A^+ is equivalent to the inverse mean first passage time $\langle t_{\Lambda\setminus A} | \vec{\pi}_A \rangle^{-1}$ and is given by the probability of appearance of a single "up" spin in a lattice with all spins being in the "down" state:

$$J_A^+ = \langle t_{\Lambda\setminus A} | \vec{\pi}_A \rangle^{-1} = 1 - \mathbb{P}(\sigma_A \to \sigma_A), \tag{7.25}$$

where $\sigma_A \in A$ is such that $N_+(\sigma_A) = 0$. We find that the rate of escape from A is well defined for all k_BT and $\Delta\mu_\pm = \mu_+ - \mu_-$ (Fig. 7.2), including the low barrier regimes, if the initial distribution $\widetilde{\mathbb{P}}(\sigma \in A) = 1$ is artificially kept constant in time. In other words, the distribution of first passage times $t_{\Lambda\backslash A}$ is exponential with rate parameter J_A^+ independent of the free energy barrier height, provided that all sampled trajectories $\sigma(t)$ start at $\sigma(0) \in A$, i.e. $N_+[\sigma(0)] = 0$.

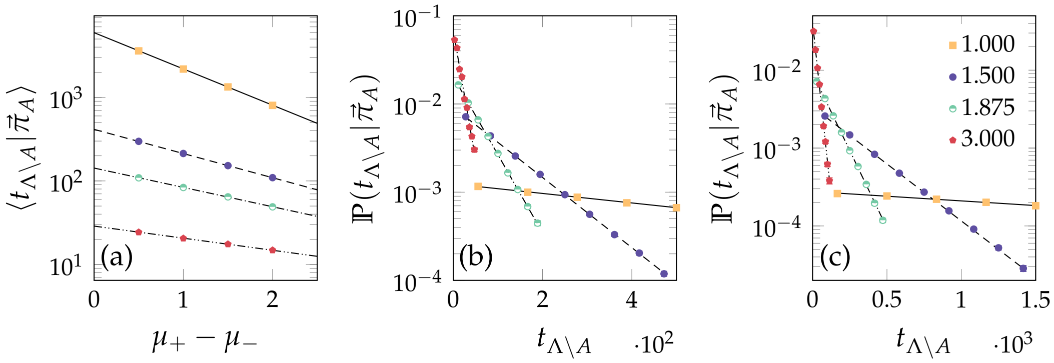

Figure 7.2: Averages [(a)] and probability density distributions [(b) and (c)] of escape times $t_{\Lambda\backslash A}$ for four temperature values (legend) and at various values of $\Delta\mu_\pm$, covering regimes of low [(b) $\Delta\mu_\pm = 2$] and high [(c) $\Delta\mu_\pm = 0.5$] barriers. Markers correspond to MC estimates based on 10^3 independent samples of $t_{\Lambda\backslash A}$, with error bars (smaller than markers) showing the 95% confidence intervals based on 10^2 repetitions of the sampling procedure. Lines in (a) are the exact values for residence times in state A. Lines in (b) and (c) are the exponential probability densities with rate parameters given by $\langle t_{\Lambda\backslash A}|\vec{\pi}_A\rangle^{-1}$.

The escape rate J_A^+ can also be estimated as the number of jumps $\sigma \to \sigma'$ leading from $N_+(\sigma) = 0$ to $N_+(\sigma') = 1$ per unit time over any sufficiently long trajectory starting in A. While this procedure yields estimates which agree with the inverse mean first passage time in high barrier regimes, it is not applicable in low barrier regimes since any long trajectory will spend a significant amount of time in B before returning to A thus severely underestimating the escape rate.

The distribution $\mathbb{P}(\sigma|A \to \sigma)$ of the system's states immediately upon leaving A is uniform over the 9 states $\sigma : N_+(\sigma) = 1$. Thus, due to the symmetry of the system, the average committor $\mathbb{P}[\sigma \to B|N_+(\sigma) = 1]$ over states $\sigma : N_+(\sigma) = 1$ is given simply by $\mathbb{P}[\tau_B(\sigma) < \tau_A(\sigma)] : N_+(\sigma) = 1$, which corresponds to any entry $A_{ij}(A \cup B)$ of the matrix $\boldsymbol{A}(A \cup B)$ such that $N_+(\sigma_i) = 1$ and $N_+(\sigma_j) = N$. Defining $\vec{\pi}_{\Lambda\backslash B}$ as the row vector form of $\widetilde{\mathbb{P}}(\sigma)$, i.e. $\pi^{(i)}_{\Lambda\backslash B} = 1$ if $N_+(\sigma_i) = 0$ and $\pi^{(i)}_{\Lambda\backslash B} = 0$ otherwise, we find the brute force MC estimates of the committor and the mean first passage times $\left\langle t_B|\vec{\pi}_{\Lambda\backslash B}\right\rangle$ in excellent agreement with those obtained via operations on the fundamental matrix of $\boldsymbol{P}$ (Fig. 7.3).

Having verified the exactness of Eqs. (7.20), (7.19) and (7.6) in computing respectively the escape rates, committor values and mean first passage times, we now show that the TPT Eq. (7.22) yields a good approximation to the inverse mean first passage times in high barrier regimes. As shown in Fig. 7.3c, in the high barrier regime at $k_B T = 1$ the TPT rate is in excellent agreement with the inverse mean first passage times computed via Eq. (7.6). With increasing temper-

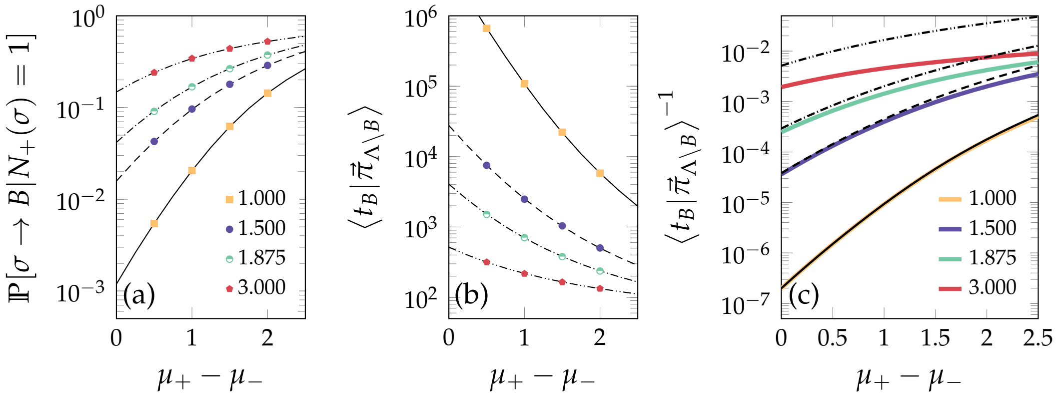

Figure 7.3: Committor values [(a)], mean first passage times [(b)] and comparison of rate values given by TPT and corresponding inverse mean first passage times [(c)] for four values of k_BT (legends) over a range of $\Delta\mu_\pm$. Markers correspond to MC estimates based on 10^2 independent samples of t_B, with error bars (smaller than markers) giving the 95% confidence intervals computed based on 10^2 repetitions of the sampling procedures. Lines in (a) and (b) correspond to the values obtained via the operations on the transition matrix $\boldsymbol{P}$ discussed in Sec. 7.1. In (c), the approach of Sec. 7.1 is compared to the TPT formula (black lines) for the transition rate, making use of the exact values of the escape rates and the committor.

atures and $\Delta\mu_\pm$, the quasi-stationary assumption on $\widetilde{\mathbb{P}}(\sigma)$ gradually breaks down, yielding non-exponential distributions of first passage times (Fig. 7.4a) which, in contrast to those at high barrier regimes (Fig. 7.4b), are not well described by a single rate parameter. Consequently, the TPT rate values are not meaningful in low barrier regimes, since significant time dependent contributions to the, now time dependent, arrival rate $J(A \to B)$ into B can be expected from all states in $\Lambda \setminus B$. Various approaches to the study of transition processes under non-stationary conditions exist in the literature [239, 240], however, in this work, we will not discuss transitions in low barrier regimes further.

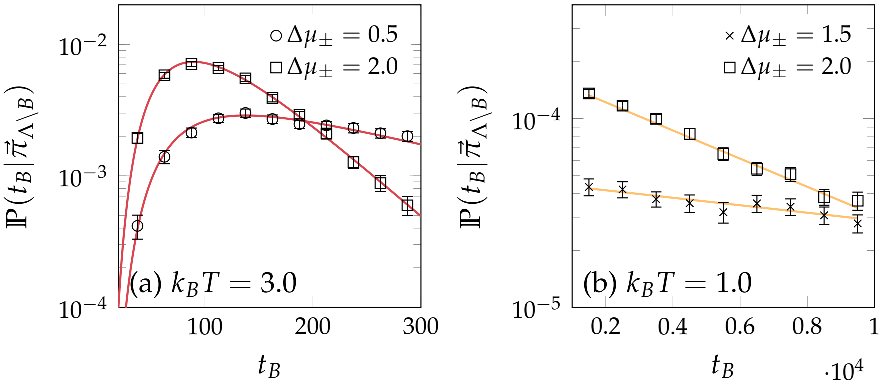

Figure 7.4: Probability density distributions of first passage times in low [(a)] and high [(b)] barrier regimes. Markers correspond to MC estimates based on 10^2 independent samples of t_B, with error bars being the 95% confidence intervals obtained via 10^2 repetitions of the sampling procedure. Lines in (a) are the exact distributions of hitting times as given by Eq. (7.13), computed via the appropriate matrix operations on $\boldsymbol{P}$. Lines in (b) are the exponential probability densities with rate parameters given by $\langle t_B\rangle^{-1}$.

7.3 RARE EVENT METHODS

Modern rare event methods, such as transition interface sampling (TIS), partial path TIS (PPTIS) and forward flux sampling (FFS) (Sec. 7.3), compute transition rates via an equation of the form:

$$J(A \to B) = J_A^+ \prod_{i=1}^{k} \mathbb{P}(\lambda_i \to \lambda_{i+1}), \tag{7.26}$$

where J_A^+ is the rate of system's escape of state A and $\mathbb{P}(\lambda_i \to \lambda_{i+1})$ are the system's transition probabilities in some collective variable space. For a carefully chosen collective variable, we can interpret $\{\lambda_i : i \in \{1, \ldots, k\}\}$ as a collection of disjoint subsets $\lambda_i \subset \Theta$, such that every reactive trajectory must pass through λ_i before passing through λ_{i+1} on its way towards B. Path sampling algorithms of FFS, TIS and PPTIS employ different strategies for estimating the transition probabilities $\mathbb{P}(\lambda_i \to \lambda_{i+1})$, while the estimator for J_A^+ is the same in all three cases: J_A^+ is given by the average number of times the system leaves A in the "direction" of B per unit time, in other words – the inverse residence time in A as discussed in Sec. 7.2.3. Here we will briefly discuss the justification of Eq. (7.26) in the framework of TPT, exploring the differences between the three rare event methods and validating our implementation.

7.3.1 *Connection to Transition Path Theory*

Clearly, Eqs. (7.22) and (7.26) are equivalent if the number of interfaces in the rare event scheme is set to 2:

$$\mathbb{P}(\lambda_1 \to \lambda_2) = \mathbb{P}(A^+ \to B) = \sum_{\sigma \in A^+} \mathbb{P}(\sigma | A \to \sigma) \mathbb{P}[\tau_B(\sigma) < \tau_A(\sigma)], \tag{7.27}$$

where we have defined $\lambda_2 = B$ and $A^+ = \lambda_1$ is the set of microstates accessible by the system immediately upon leaving A:

$$A^+ = \{\sigma \in \Lambda \setminus A : \exists\, \sigma' \in A : \mathbb{P}(\sigma' \to \sigma) > 0\}. \tag{7.28}$$

Suppose every reactive trajectory must pass through some subset $C \subseteq \Theta$ of microstates before it may enter B. Then for any $\sigma \in \Theta$ the joint probability $\mathbb{P}[\tau_A(\sigma) > \tau_B, \tau_B(\sigma) = \tau_B, \tau_C(\sigma) = \tau_C]$ is given by:

$$\mathbb{P}[\tau_B, \tau_C] = \sum_{\sigma_1 \in \Theta \setminus C} \sum_{\sigma_2 \in \Theta \setminus C} \cdots \sum_{\sigma_{\tau_C} \in C} \sum_{\sigma_{\tau_C+1} \in \Theta} \cdots \sum_{\sigma_{\tau_B} \in B} \mathbb{P}(\sigma \to \sigma_1) \prod_{i=1}^{\tau_B - 1} \mathbb{P}(\sigma_i \to \sigma_{i+1}), \tag{7.29}$$

where the contributions from trajectories recrossing C are included, since Θ includes C, and by construction we have:

$$\mathbb{P}[\tau_B, \tau_C > \tau_B] = 0, \quad \sum_{\tau_C < \tau_B} \mathbb{P}[\tau_B, \tau_C] = \mathbb{P}[\tau_A(\sigma) > \tau_B, \tau_B(\sigma) = \tau_B]. \tag{7.30}$$

We can, therefore, rewrite Eq. (7.19) as follows:

$$\mathbb{P}[\tau_A(\sigma) > \tau_B(\sigma)] = \lim_{\tau\to\infty} \lim_{\tau'\to\infty} \sum_{k=1}^{\tau} \sum_{l=1}^{\tau'} \mathbb{P}[\tau_A(\sigma) > k+l, \tau_B(\sigma) = k+l, \tau_C(\sigma) = k], \tag{7.31}$$

where we count contributions to the committor from all possible trajectories entering B in l jumps after entering C in k jumps from σ. Defining the distribution $\mathbb{P}(\sigma_C|\sigma \to C)$ of arrival points $\sigma_C \in C$ for trajectories coming from $\sigma \in \Lambda$:

$$\begin{aligned} &\mathbb{P}(\sigma_C|\sigma \to C) = \{\mathbb{P}[\tau_A(\sigma) > \tau_C(\sigma)]\}^{-1} \times \dots \\ &\lim_{\tau\to\infty} \sum_{k=1}^{\tau} \sum_{\sigma_1 \in \Lambda\setminus C} \cdots \sum_{\sigma_{k-1} \in \Lambda\setminus C} \mathbb{P}(\sigma \to \sigma_1)\mathbb{P}(\sigma_{k-1} \to \sigma_C) \prod_{i=1}^{k-1} \mathbb{P}(\sigma_i \to \sigma_{i+1}), \end{aligned} \tag{7.32}$$

it is straightforward to show that:

$$\mathbb{P}[\tau_A(\sigma) > \tau_B(\sigma)] = \mathbb{P}[\tau_A(\sigma) > \tau_C(\sigma)] \sum_{\sigma_C \in C} \mathbb{P}(\sigma_C|\sigma \to C)\mathbb{P}[\tau_A(\sigma_C) > \tau_B(\sigma_C)]. \tag{7.33}$$

The expression for the rate now reads:

$$J(A \to B) = J_A^+ \sum_{\sigma \in A^+} \sum_{\sigma_C \in C} \mathbb{P}(\sigma|A \to \sigma)\mathbb{P}(\sigma \to C)\mathbb{P}(\sigma_C|\sigma \to C)\mathbb{P}(\sigma_C \to B), \tag{7.34}$$

where $\mathbb{P}(\sigma \to C) = \mathbb{P}[\tau_A(\sigma) > \tau_C(\sigma)]$ and $\mathbb{P}(\sigma_C \to B) = \mathbb{P}[\tau_A(\sigma_C) > \tau_B(\sigma_C)]$ and in order to write it in the form of Eq. (7.26), we can take the same approach as when writing Eq. (7.12) in the form of Eq. (7.22). We first define the average with respect to $\mathbb{P}(\sigma|A \to \sigma)$ committor $\mathbb{P}(A^+ \to C)$:

$$\begin{aligned} \mathbb{P}(A^+ \to C) &= \sum_{\sigma \in A^+} \sum_{\sigma_C \in C} \mathbb{P}(\sigma|A \to \sigma)\mathbb{P}(\sigma \to C)\mathbb{P}(\sigma_C|\sigma \to C) \\ &= \sum_{\sigma \in A^+} \mathbb{P}(\sigma|A \to \sigma)\mathbb{P}(\sigma \to C), \end{aligned} \tag{7.35}$$

which gives the total probability of a trajectory arriving in C before returning to A after having entered A^+, i.e. left A. Additionally, the distribution $\mathbb{P}(\sigma_C|A^+ \to C)$ of arrival points $\sigma_C \in C$ for trajectories coming from anywhere in A^+ is given by:

$$\mathbb{P}(\sigma_C|A^+ \to C) = [\mathbb{P}(A^+ \to C)]^{-1} \sum_{\sigma \in A^+} \mathbb{P}(\sigma|A \to \sigma)\mathbb{P}(\sigma \to C)\mathbb{P}(\sigma_C|\sigma \to C), \tag{7.36}$$

which finally leads to:

$$\begin{aligned} J(A \to B) &= J_A^+ \mathbb{P}(A^+ \to C) \sum_{\sigma_C \in C} \mathbb{P}(\sigma_C|A^+ \to C)\mathbb{P}(\sigma_C \to B) \\ &= J_A^+ \mathbb{P}(A^+ \to C)\mathbb{P}(C \to B). \end{aligned} \tag{7.37}$$

Following analogous steps to those listed above, we can expand the committor $\mathbb{P}(\sigma_C \to B)$ further by introducing additional intermediate checkpoint sets for reactive trajectories along the path from C to B.

7.3.2 *Distinctions between Sampling Strategies*

Let us now compare the approaches of the FFS, TIS and PPTIS algorithms to calculating the expanded committor $\mathbb{P}(A^+ \to C)\mathbb{P}(C \to B)$.

The FFS algorithm proceeds by first collecting a sample of configurations $\sigma \in A^+$ according to the distribution $\mathbb{P}(\sigma|A \to \sigma)$ by storing the end points of all configurations escaping A. Selecting the starting points uniformly from the obtained pool of configurations, the algorithm generates a sample of trajectories $\sigma(t) : \sigma(0) \in A^+$, computing the fraction of the sample which arrived in C and storing the corresponding arrival points. Thus, for every stored microstate $\sigma \in A^+$, the algorithm estimates the probability $\mathbb{P}(\sigma \to C)$ while simultaneously storing with probability $\mathbb{P}(\sigma \to C)\mathbb{P}(\sigma_C|\sigma \to C)$ a starting point $\sigma_C \in C$ for the subsequent calculation of $\mathbb{P}(C \to B)$. Estimates of $\mathbb{P}(\sigma \to C)$ and the stored configurations $\sigma_C \in C$ are implicitly weighted by $\mathbb{P}(\sigma|A \to \sigma)$, since starting points of all trajectories launched from A^+ are sampled from $\mathbb{P}(\sigma|A \to \sigma)$. It is, therefore, easy to see that $\mathbb{P}(A^+ \to C)$ is correctly estimated and, by an analogous argument, the same can be shown for the computation of $\mathbb{P}(C \to B)$.

For each pair of interfaces, e.g. (A^+, C), the algorithm of TIS samples the equilibrium ensemble of paths of variable length, accepting only those trajectories which, having originated in A and eventually entered A^+, either: (1) return to A or (2) proceed to C. The probability $\mathbb{P}(A^+ \to C)$ is estimated as the fraction of trajectories of type (2) in the entire pool of accepted trajectories. Clearly, each increment to the count of trajectories of type (2) is implicitly weighted by the distribution $\mathbb{P}(\sigma|A \to \sigma)$ of arrival points in A^+, while the likelihood of the count being incremented is $\mathbb{P}(\sigma \to C)$. In contrast to FFS however, when estimating $\mathbb{P}(C \to B)$, the TIS algorithm does not make use of the sampled information on the distribution $\mathbb{P}(\sigma_C|A^+ \to C)$ of arrival points $\sigma_C \in C$ as obtained from the calculation of $\mathbb{P}(A^+ \to C)$. Instead, the arrival points $\sigma_C \in C$ are sampled explicitly over the course of the calculation of $\mathbb{P}(C \to B)$, since for the interface pair (C, B) the accepted trajectories must again originate in A.

From the above it is reasonable to conclude that, in the context of spatially discrete reversible Markov chains, the FFS and TIS algorithms sample the same quantities, provided that the collective variable is defined as discussed at the beginning of Sec. 7.3. The approach of PPTIS, however, departs substantially from those listed above by, effectively, constructing a Markov chain in the collective variable space to describe the kinetics of the transition from A to B. Given a set of interfaces $\{\lambda_i\}$, the algorithm estimates a set of four conditional jump probabilities:

1. $\mathcal{P}_i^{\pm} = \mathcal{P}(\lambda_i \to \lambda_{i+1}|\lambda_{i-1} \to \lambda_i)$.
2. $(1 - \mathcal{P}_i^{\pm}) = \mathcal{P}(\lambda_i \to \lambda_{i-1}|\lambda_{i-1} \to \lambda_i)$.
3. $\mathcal{P}_i^{\mp} = \mathcal{P}(\lambda_i \to \lambda_{i-1}|\lambda_{i+1} \to \lambda_i)$.
4. $(1 - \mathcal{P}_i^{\mp}) = \mathcal{P}(\lambda_i \to \lambda_{i+1}|\lambda_{i+1} \to \lambda_i)$,

between pairs of interfaces in every window defined by triples $(\lambda_{i-1}, \lambda_i, \lambda_{i+1})$. This is achieved by sampling the equilibrium ensembles of the four corresponding types of paths of variable length in the restricted to the PPTIS window region of state space. Upon completion, the coarse grained Markov representation of the transition is constructed by recovering the jump probabilities $\mathcal{P}(\lambda_i \to \lambda_{i+1})$ via the recursion:

$$\mathcal{P}(\lambda_i \to \lambda_{i+1}) = \mathcal{P}_i^{\pm}\mathcal{P}(\lambda_{i-1} \to \lambda_i) + \left(1 - \mathcal{P}_i^{\mp}\right)\mathcal{P}(\lambda_{i+1} \to \lambda_i), \tag{7.38}$$

where the Markov assumption:

$$\mathcal{P}(\lambda_i \to \lambda_{i+1}|\lambda_{i-1} \to \lambda_i) = \mathcal{P}(\lambda_i \to \lambda_{i+1}|\lambda_{i-1} \to \lambda_i, \lambda_{i-2} \to \lambda_{i-1}, \dots),$$

is implicit and the resultant Markov chain can be solved exactly, taking $\lambda_0 = \lambda_1$, to approximate the mean committors $\mathbb{P}(\lambda_i \to \lambda_{i+1})$. The conditions under which the above corresponds to Eq. (7.37) are not obvious within the TPT framework, although the validity of the approximation can be assessed by studying the memory loss properties of the system in the collective variable space [140].

7.3.3 *Application to the Ising Model*

The collective variable N_+ is a good candidate for ordering the state space of the Ising model in the study of transitions from $N_+ = 0$ to $N_+ = N$, since any single jump $\sigma \to \sigma'$ in the configuration space can lead to a change in N_+ by no more than ± 1. Thus, any reactive trajectory must realise each of the possible values of N_+ in an increasing sequence along the path from A to B, allowing any strictly increasing sequence of N_+ values to construct a valid set of interfaces $\{\lambda_i\}$ for use in a rare event sampling scheme. Considering rare event methods in the context of the Ising model is particularly interesting since it is easy to see that the collective variable N_+ evolves in time in a non-Markovian fashion, as the probabilities of transitions $N_+ \to N_+ \pm 1$ are dependent not only on N_+ but also on the involved lattice configurations. In addition, the estimated by FFS, TIS and PPTIS quantities can be computed exactly by appropriate manipulations of the transition matrix $\boldsymbol{P}$ which we will now summarise.

We have already seen that the committor $\mathbb{P}(\sigma \to B)$ can be computed via the matrix $\boldsymbol{A}(A \cup B)$ as the fraction of absorbed by the subset B trajectories $\sigma(t)$: $\sigma(0) = \sigma \in \Theta$ in the Markov chain described by $\boldsymbol{P}$ with all microstates in A and B being absorbing. The same procedure can be applied to compute any committor $\mathbb{P}(\sigma \to \lambda_i)$, where:

$$\lambda_i = \{\sigma \in \Lambda \setminus A : N_+(\sigma) = i\}, \tag{7.39}$$

is the set of microstates realising the value i of the collective variable N_+. To compute exactly the quantities estimated by TIS and FFS for any pair $(\lambda_i, \lambda_j) : j > i > 1$ of interfaces, we first obtain the matrix $\boldsymbol{A}(A \cup \lambda_i)$ which, if post-multiplied by a column vector $\vec{e}_{\lambda_i}$ of $|A \cup \lambda_i|$ entries such that $e^{(k)}_{\lambda_i} = 1$ for $\sigma_k \in \lambda_i$ and $e^{(l)}_{\lambda_i} = 0$ for $\sigma_l \in A$, gives the column vector form of $\mathbb{P}(\sigma \to \lambda_i)$ for every σ not included in $A \cup \lambda_i$. Pre-multiplying $\boldsymbol{A}(A \cup \lambda_i)$ by the row vector $\vec{\pi}_{A^+}$, which comprises 9 nonzero entries corresponding to $\mathbb{P}(\sigma | A \to \sigma)$, gives the row vector form of $\mathbb{P}(A^+ \to \lambda_i)\mathbb{P}(\sigma | A^+ \to \lambda_i)$, which, if conditioned on $A^+ \to \lambda_i$, is the distribution $\mathbb{P}(\sigma | A^+ \to \lambda_i)$ of arrival points in λ_i from all possible trajectories starting in A. At this point, the average committor $\mathbb{P}(\lambda_i \to \lambda_j)$ can be computed via the scalar product:

$$\mathbb{P}(\lambda_i \to \lambda_j) = \vec{\pi}_{\lambda_i} \boldsymbol{A}(A \cup \lambda_j) \vec{e}_{\lambda_j}, \tag{7.40}$$

where $\vec{\pi}_{\lambda_i}$ is the obtained row vector form of $\mathbb{P}(\sigma | A^+ \to \lambda_i)$ and $\vec{e}_{\lambda_j}$ is a column vector with $e^{(k)}_{\lambda_j} = 1$ for $\sigma_k \in \lambda_j$ and $e^{(l)}_{\lambda_j} = 0$ for $\sigma_l \in A$ and we should also clarify that $\vec{\pi}_{\lambda_1} = \vec{\pi}_{A^+}$ and $\lambda_9 = B$.

The procedure for computing exactly the PPTIS conditional jump probabilities for any triple of interfaces $(\lambda_i, \lambda_j, \lambda_k) : k > j > i \geq 1$ is more involved, and, for simplicity, we will only illustrate the approach for computing $\mathcal{P}^{\pm}_j$. We first isolate a portion of the transition matrix $\boldsymbol{P}$, keeping only the entries P_{lm} which correspond to $\mathbb{P}(\sigma_l \to \sigma_m) : N_+(\sigma_l), N_+(\sigma_m) \in \{i, i+1, \dots, k\}$ and normalising the rows of the resultant matrix $\boldsymbol{P}'$ to sum to 1. Taking the principal eigenvector of $\boldsymbol{P}'$, we obtain the equilibrium distribution $\mathcal{P}(\sigma)$ for the isolated portion of the Markov chain. To compute $\mathcal{P}_j^{\pm}$, we must determine the conditional distribution $\mathcal{P}(\sigma|\lambda_i \to \sigma)$ as the fraction of absorbed by λ_j trajectories $\sigma(t) : \sigma(0) \in \lambda_i$ with starting points distributed according to the equilibrium distribution $\mathcal{P}(\sigma|\sigma \in \lambda_i)$ over λ_i. Generating the matrix $\boldsymbol{A}'(\lambda_j)$ from $\boldsymbol{P}'$ and providing the conditional equilibrium distribution $\mathcal{P}(\sigma|\sigma \in \lambda_i)$ in row vector form $\vec{w}_{\lambda_i}$, the row vector form $\vec{w}_{\lambda_j}$ of $\mathcal{P}(\sigma|\lambda_i \to \sigma)$ can be obtained via $\vec{w}_{\lambda_j} = \vec{w}_{\lambda_i}\boldsymbol{A}'(\lambda_j)$. The conditional distribution $\mathcal{P}_j^{\pm}$ can now be obtained by an analogous to Eq. (7.40) operation:

$$\mathcal{P}_j^{\pm} = \vec{w}_{\lambda_j}\boldsymbol{A}'(\lambda_i \cup \lambda_k)\vec{e}_{\lambda_k}. \tag{7.41}$$

We apply the three rare event methods to the 3×3 Ising model, taking the sets of interfaces to be $\{\lambda_1, \lambda_2 \ldots, \lambda_9\}$ for FFS and TIS, and $\{\lambda_0, \lambda_1, \lambda_2 \ldots, \lambda_9\}$ for PPTIS, verifying that the results of the performed calculations do not change if varying interface separation. Performing 10 independent calculations under each rare event scheme for each of the parameter points $k_B T \in \{1, 3\}$, $\Delta\mu_{\pm} \in \{0.5, 1.0, 1.5, 2.0\}$, we find Eqs. (7.40) and (7.41) in excellent agreement with MC as shown in Fig. 7.5.

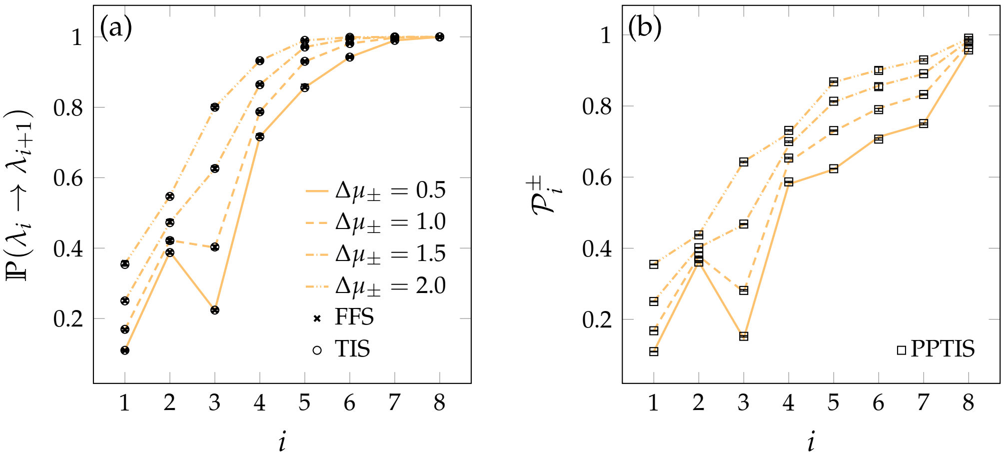

Figure 7.5: Comparison of Eqs. (7.40) and (7.41) (lines) with data produced by FFS, TIS and PPTIS (markers) at $k_B T = 1$, $\Delta\mu_{\pm} \in \{0.5, 1.0, 1.5, 2.0\}$. Estimates due to FFS are based on 10^4 successful trials at each interface. Runs of TIS and PPTIS comprised an equilibration stage and sampling stage, both of which continued until 10^5, for TIS, or 10^6, for PPTIS, shooting moves were accepted. Error bars (smaller than markers) represent the minima and maxima of 10 independent estimates.

Rate and committor estimates, produced by the three rare event schemes also appear in excellent agreement with TPT (Fig. 7.6) both in high and low barrier regimes, suggesting that the Markov assumption on the evolution of the collective variable N_+, as made by the PPTIS approach to committor estimation, is reasonable for the 3×3 Ising model under spin flip kinetics.

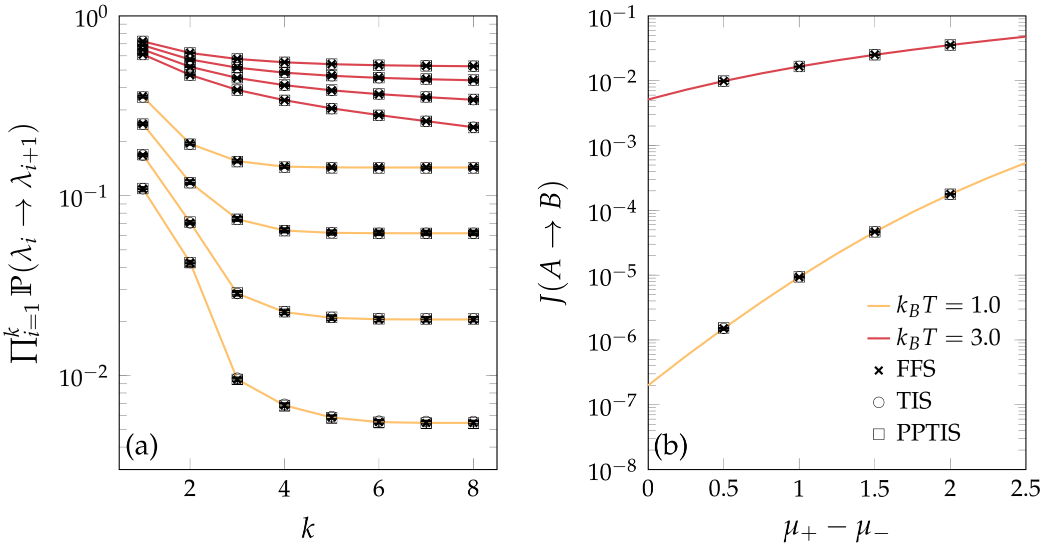

Figure 7.6: Comparison of the three rare event methods at two values of k_BT (legend) and four values of $\Delta\mu_\pm \in \{0.5, 1, 1.5, 2\}$. Lines correspond to exact values [Eq. (7.40)] of the cumulative product of mean committors $\mathbb{P}(\lambda_i \to \lambda_{i+1})$ [(a)] and rates [(b)] as given by Eq. (7.22). Estimates due to FFS are based on 10^4 successful trials at each interface. Runs of TIS and PPTIS comprised an equilibration stage and sampling stage, both of which continued until 10^5, for TIS, or 10^6, for PPTIS, shooting moves were accepted. Error bars (smaller than markers) represent the minima and maxima of 10 independent estimates.

7.4 MODELLING OPEN SYSTEM KINETICS

In order to study nucleation from solution in a finite lattice system at low solute concentrations, we must consider an open system where the solute concentration is allowed relax to its quasi-stationary level without being depleted completely by nucleus growth. This is adequately achieved by the unphysical transmutation-reorientation kinetics (TR), where solute particles are allowed to appear and disappear in the finite system, thus correctly maintaining the solute chemical potentials. For the more realistic diffusion-reorientation (DR) model of solute transport, we can view the finite system $\Omega \subset \mathbb{Z}^d$ as a subregion of an infinite d-dimensional lattice domain $\mathbb{Z}^d$ whose spatially homogeneous solute concentration does not change in time. In this setting, the subdomain Ω must be allowed to exchange particles with the surrounding infinite system $\mathbb{Z}^d$. In this section, we will illustrate, in the context of an open system of non-interacting random walkers on $\mathbb{Z}^d$, the implications of implementing the open system by allowing particle exchange.

7.4.1 *Random Walker on $\mathbb{Z}^d$*

We consider a particle $\vec{x}(m) \in \mathbb{Z}^d$ performing an unbiased random walk on a d-dimensional lattice $\mathbb{Z}^d$ in discrete time m. For our purposes, it is useful to write down the probability distribution $\mathbb{P}_d(\vec{x}|m)$ of particle positions after m jumps, given that $\vec{x}(0) = 0$:

$$\mathbb{P}_d(\vec{x}|m) = (2d)^{-m} m! \sum_{\{m_i^+, m_i^-\}} \left[\prod_{i=1}^{d} m_i^+! m_i^-! \right]^{-1}, \tag{7.42}$$

where the sum carries over the set $\{m_i^+, m_i^-\} : i \in \{1, \ldots, d\}$ such that $\sum_{i=1}^{d} m_i^+ + m_i^- = m$ and $x_i = m_i^+ - m_i^-$ and for $d = 1$ we have:

$$\mathbb{P}_1(\vec{x}|m) = \frac{(2d)^{-m} m!}{m_1^+! m_1^-!} = \frac{2^{-m} m!}{[(m - x_1)/2]! [(m + x_1)/2]!}.$$

Using the above, we also obtain the probability of the particle arriving in m jumps at any point $\vec{x} \in \mathbb{Z}^d$ having started at any $\vec{x}_0 \in \mathbb{Z}^d$ via $\mathbb{P}_d(\vec{x} - \vec{x}_0|m)$.

7.4.2 *Density Autocorrelation Function*

We can define Ω as a cubic subdomain $\Omega = \{-l/2, \ldots, l/2\}^d$ of length l of a much larger cubic domain $\Phi = \{-L/2, \ldots, L/2\}^d$ with periodic boundaries for which we can take the limit $L \to \infty$ to consider it an infinite system. Given a constant density $\rho = M/|\Phi|$ of M unbiased random walkers in Φ, the particle density X_m in Ω is a stationary stochastic process:

$$X_m = |\Omega|^{-1} \sum_{i=1}^{M} \mathbb{1}_\Omega[\vec{x}_i(m)], \quad \mathbb{1}_\Omega[\vec{x}] = \begin{cases} 1 & \text{if } \vec{x} \in \Omega, \\ 0 & \text{otherwise,} \end{cases} \tag{7.43}$$

where $\vec{x}_i(m)$ is the position of the ith particle at discrete time m. For non-interacting particles with multiple lattice site occupancy, X_m can exceed the value of 1 with nonzero probability, however, for our purposes this is not important, since we are only concerned with the relaxation properties of X_m, which can be quantified via the time autocorrelation function $\mathcal{R}_X(m)$ as defined in Sec. 2.2.4.

It is possible to show that, due to the mutual independence of the M random walkers, the autocorrelation function for the $L \to \infty$ limit is equal to the one particle autocorrelation function:

$$\mathcal{R}_X(m) = \frac{\langle \mathbb{1}_\Omega[\vec{x}(k)] \mathbb{1}_\Omega[\vec{x}(k+m)] \rangle - \langle \mathbb{1}_\Omega[\vec{x}(k)] \rangle}{\langle \mathbb{1}_\Omega^2[\vec{x}(k)] \rangle - \langle \mathbb{1}_\Omega[\vec{x}(k)] \rangle} = |\Omega|^{-1} \sum_{\vec{x} \in \Omega} \sum_{\vec{y} \in \Omega} \mathbb{P}_d(\vec{x} - \vec{y}|m), \tag{7.44}$$

which is analogous to the result for systems of spatially and time continuous random walkers [241]. Thus, $\mathcal{R}_X(m)$ can be computed as the probability of an unbiased random walker being in Ω after m jumps, having started its journey at a lattice site drawn uniformly from Ω. Examining the analytical and MC estimated $R_X(m)$ for $d \in \{1, 3\}$ (Fig. 7.7) we find that the random walker density autocorrelation functions vary slowly with m, exhibiting power law tails $\sim m^{-d/2}$.

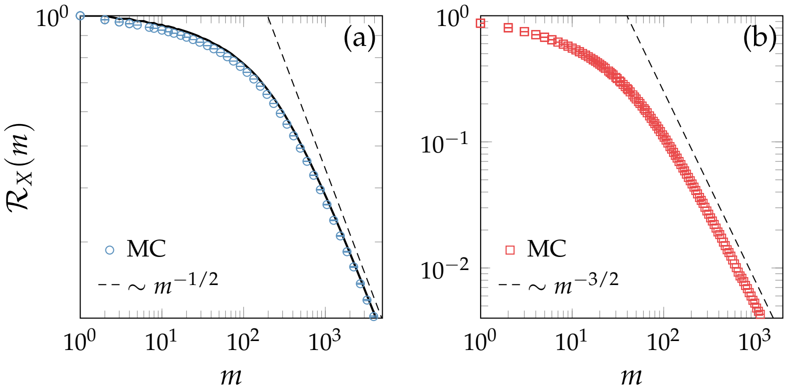

Figure 7.7: Density autocorrelation functions for $d \in \{1,3\}$. In (a), the solid line is the plot of Eq. (7.44) while markers correspond to estimates of the ACF sequence obtained from 10^2 independent realisations of X_m for $m \in [0, 10^6]$, $\rho = 0.5$, $l = 128$ on a $L = 2^{21}$ 1D lattice with error bars showing the 95% confidence intervals. In (b), the markers correspond to averages of 10^2 MC estimates of the probability $|\Omega|^{-1} \sum_{\vec{x} \in \Omega} \sum_{\vec{y} \in \Omega} \mathbb{P}_d(\vec{x} - \vec{y}|m)$ for $m \in [0, 10^4]$ in a $l = 32$ subdomain of a 3D lattice with error bars showing the variance of the computed estimates.

7.4.3 *Implications for Modelling*

Clearly any model of an open system must reproduce the particle density fluctuations which are consistent with the underlying model of particle transport. While we cannot accurately quantify solute density relaxation for DR kinetics in 3D, even at $\beta = 0$, we can expect qualitatively similar behaviour of the autocorrelation functions to that depicted in Fig. 7.7 at low solute concentrations. Various memory kernel methods for generating stationary correlated sequences exist [7, 32], although generation of sequences with slowly decaying memory is challenging since the time range of any numerical kernel is limited by the available physical memory. Simple models of barrier crossing processes in presence of fluctuations with slowly decaying memory have been considered [242–245], however, realising power law correlated density fluctuations in finite particle systems via Metropolis style kinetics has not been attempted in the literature.

Thus, at present, we cannot formulate a model open system which reproduces particle density fluctuations consistent with the underlying particle transport process for DR kinetics.

7.5 EXPLICIT RATES FOR THE EXTENDED PLG

In this section we consider an approximate treatment of the solute nucleation process in the $c = 1$, $Q = 24$, $d = 3$ extended PLG model under DR and TR kinetics via seeded PPTIS simulations. We implement the PPTIS algorithm taking the size of the largest solute nucleus as the collective variable. Given a fixed

PPTIS interface separation of $n_i - n_{i-1} = \Delta n \in \mathbb{Z}^+$ along the largest solute cluster size coordinate $n \in \mathbb{N}$, the maximum change in solute particle count within any given PPTIS window (n_{i-1}, n_i, n_{i+1}) is $n_{i+1} - n_{i-1} = 2\Delta n$. Noting that each PPTIS simulation can be seeded with a trajectory starting from a configuration σ such that $n(\sigma) = n_i$ and the solute particle count $N_s(\sigma)$ is set to $N_s(\sigma) = (N - n_i)\rho + n_i$, the solute density depletion and augmentation fall within $\pm\Delta n/N$.

Thus the solute depletion within PPTIS simulations can be easily tuned to fall well within confidence bounds on the density fluctuations in an open system, which, assuming a quasi-static uniform density profile, follow a binomial distribution over the domain $\{0, 1, \ldots, N\}$ with "success" probability ρ. Since we consider the process over a range of solute concentrations $\rho \in [5 \times 10^{-4}, 3 \times 10^{-3}]$ in cubic systems of $l = 32$ using the same PPTIS implementation, we take the maximum PPTIS interface separation of $\Delta n_{\max} = 4$, corresponding to the 75% confidence bound on density fluctuations for $\rho = 5 \times 10^{-4}$.

7.5.1 *Validation at High Solute Concentration*

We consider the sensitivity of our PPTIS implementation to variation of the interface separation Δn by obtaining rate estimates at $k_B T = 0.7$, $f = 8$ under DR kinetics. The interface coordinates $\{n_i\}$ are defined by $\Delta n \in \{1, 2, 3, 4\}$ and the respective values $n_1 \in \{5, 6, 8, 10\}$, $n_{\text{end}} \in \{49, 48, 47, 46\}$ as the increasing sequence $\{n_i\} = \{n_1, n_1 + \Delta n, n_1 + 2\Delta n, \ldots, n_{\text{end}}\}$. In all runs of PPTIS we employ equilibration and sampling stages, which terminate after accepting at least 10^4 and 2×10^4 shooting moves respectively.

Defining B as the region of state space where the size of the largest solute nucleus exceeds 50 particles, we obtain brute force MC samples of first passage times t_B. Despite the relatively high supersaturation at $f = 8$, we find that the barrier remains high enough for the quasi-static approximation of the transition process to hold, yielding an exponential distribution of first passage times (Fig. 7.8a). We find that rate estimates obtained by our PPTIS implementation, though consistent across 10 independent sampling repetitions, vary over the explored range of Δn (Fig. 7.8b). Rate estimates for $\Delta n \in \{3, 4\}$ appear in good agreement, yet deviate by approximately a factor of 2 from the obtained estimate of the inverse mean first passage time.

Several factors contributing to the disagreement between PPTIS rates and the inverse mean first passage time value can be identified for our PPTIS implementation. Along with the questionable validity of the memory loss assumption on $n(t)$, we can expect errors in PPTIS due to large time intervals between successive tests of trajectory acceptance criteria. Based on the discussion of Sec. 7.3, we can see that, in the context of Markov chains, reaching of a PPTIS interface by a trajectory must be detected accurate to the smallest available time unit – a single jump. Since

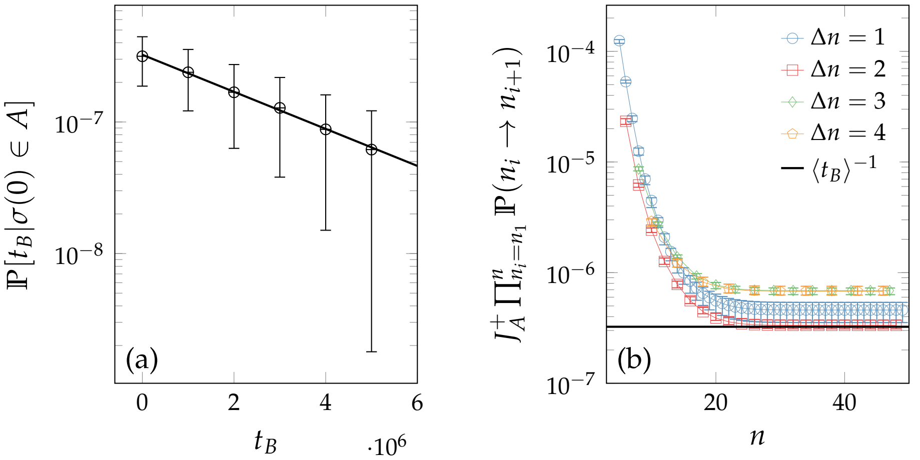

Figure 7.8: First passage time distribution [(a)] and PPTIS cumulative committor product [(b)] for the $c = 1$, $Q = 24$, $d = 3$ extended PLG model under DR kinetics at $k_B T = 0.7$, $f = 8$, demonstrating the sensitivity of the PPTIS implementation to the choice of window width Δn in (b). Markers in (a) are averages of 67 sets of 10^2 independent estimates obtained via brute force MC, with error bars showing the 95% confidence intervals. The solid line in (a) represents the exponential probability density with the rate parameter set to the inverse mean first passage time $\langle t_B|\sigma(0) \in A\rangle^{-1}$. Markers in (b) are the averages of 10 independent runs of PPTIS with error bars showing the minimum and maximum deviation from the mean value across the 10 runs. The solid black line in (b) is the inverse mean first passage time $\langle t_B|\sigma(0) \in A\rangle^{-1}$.

in our implementation the order parameter is computed after a single MC sweep, it is not unlikely that valid trajectories are rejected or incorrectly classified due to crossing the required interfaces mid-sweep, although the corresponding effect on the resultant rate estimate is not obvious.

7.5.2 *Estimates at Lower Solute Concentrations*

We carry out two PPTIS simulations taking $\Delta n = 4$, $n_1 = 3$, $n_{\text{end}} = 83$ for every pair $(k_B T, f)$ of values $k_B T \in \{0.60, 0.65, 0.70\}$ and $f \in \{5.5, 6.0, 6.5, 7.0\}$, computing the largest solute cluster size n at intervals of 20 MCS for both TR and DR kinetics. For each window (n_{i-1}, n_i, n_{i+1}) in the cluster size coordinate, we initialise a simulation generating an acceptable trajectory by "shooting" from an artificially constructed configuration comprising a cluster of size n_i surrounded by a supersaturated solution with the total number of solute particles in the configuration given by $(N - n_i)\rho + n_i$. In all PPTIS simulations we carry out equilibration and sampling stages terminating upon acceptance of at least 10^4 and 2×10^4 shooting moves respectively.

In Fig. 7.9 we show typical nuclei configurations seen in the sampled PPTIS trajectory ensembles for the window with the largest limits along n. We find that the typical nuclei are reasonably compact and disordered, which is consistent with results of EPS for $n < 100$ at the three temperatures as can be expected since PPTIS samples the equilibrium path ensemble.

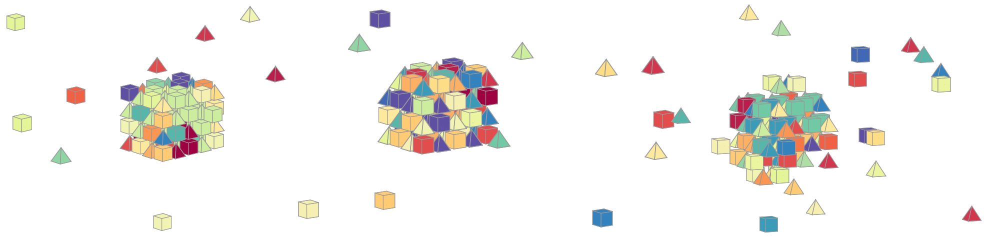

DR, $k_BT = 0.6$ DR, $k_BT = 0.65$ DR, $k_BT = 0.7$

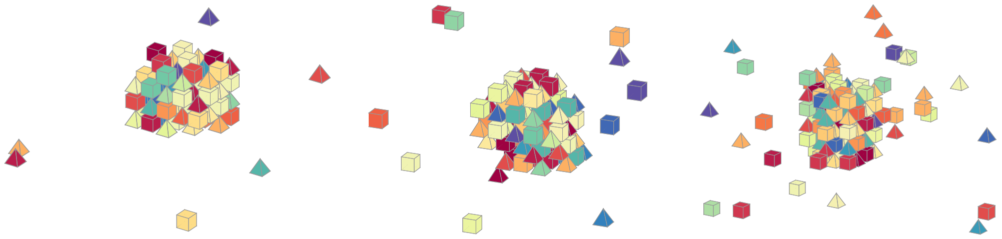

TR, $k_BT = 0.6$ TR, $k_BT = 0.65$ TR, $k_BT = 0.7$

Figure 7.9: Visualisations of typical nuclei configurations in PPTIS path segments for the window $n \in [75, 83]$ for the $c = 1$, $Q = 24$, $d = 3$ PLG model at three temperatures and $f = 7$ for the two sets of microscopic kinetics. The configurations are visualised in accordance with the convention used in Fig. 4.2.

The obtained cumulative committor products appear to converge well within the specified range along the cluster size coordinate (Fig. 7.10). We find the resultant PPTIS rate estimates in reasonable agreement with those obtained via CNT using explicitly computed free energy barrier heights (Fig. 7.11) at all considered conditions except $k_BT = 0.6$ for DR kinetics, where we see PPTIS rate estimates deviate from CNT by between 2 and 3 orders of magnitude. The PPTIS rate estimate for $k_BT = 0.6$, $f = 6.5$ for DR kinetics (Fig 7.11a) is greater than that for the same temperature at $f = 7.0$, suggesting that our error estimates for PPTIS based on two independent samples are not representative of the statistical errors in the procedure. We also expect a systematic error due to incorrectly implemented PPTIS trajectory acceptance conditions: trajectories were only considered part of the PPTIS ensemble when crossing the appropriate interfaces. Based on the discussion of Sec. 7.3 it is clear that such implementation is not correct, and we can expect the resultant rate estimates to be lower than if trajectories were accepted upon hitting the appropriate interfaces.

Finally, we cannot comment on the role of the Markov assumption on evolution of $n(t)$ based on the results presented here, since both CNT and PPTIS assume Markovian behaviour, albeit to different extents.

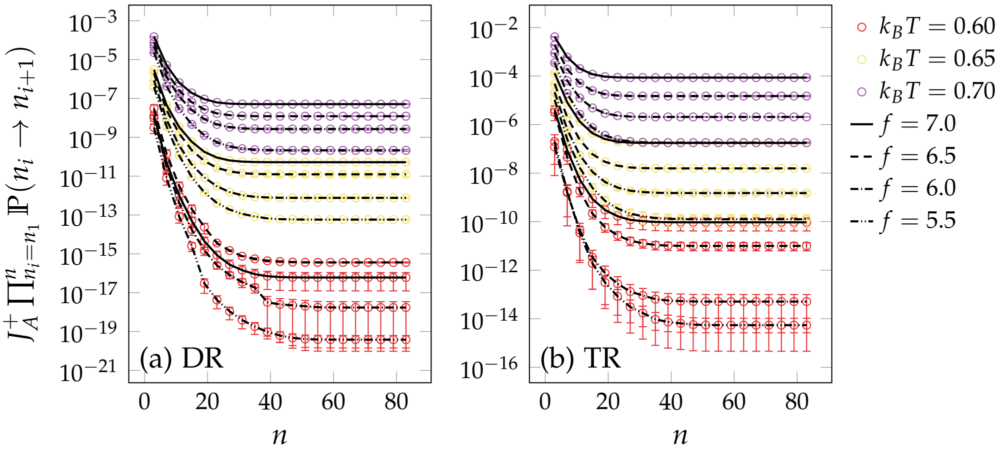

Figure 7.10: Plots of PPTIS estimates of cumulative committor products multiplied by the escape rates J_A^+ for the $c = 1$, $Q = 24$, $d = 3$ extended PLG model. Markers and lines correspond to averages and error bars give the maxima and minima of two independent sets of estimates of committor values. Escape rates J_A^+ were estimated based on 10^2 independent trajectories of $n(t)$, each 10^4 MCS long. All PPTIS simulations carried out equilibration and sampling stages continuing until respectively 10^4 and 2×10^4 shooting moves were accepted.

7.6 CHAPTER SUMMARY

In this chapter we have carefully examined the connection between the TPT formalism and modern rare event methodology in the context of reversible Markov chains, demonstrating the mathematical equivalence of FFS and TIS approaches to rate calculation. In addition to the "seeding" method discussed in the previous chapter, here we have considered two strategies for rate calculation in lattice models of nucleation from solution under realistic particle transport kinetics: (1) Simulating kinetics of a finite subdomain of an infinite system at constant solute density. (2) Carrying out seeded PPTIS simulations of closed systems conserving solute density. Due to the slow relaxation of local particle density fluctuations in large systems, we have concluded that, at present, approach (1) is difficult to realise via standard Metropolis MC methods employed throughout this work. While we have shown that approach (2) is feasible and does yield reasonable with respect to CNT nucleation rate estimates in the $c = 1$, $Q = 24$, $d = 3$ extended PLG, we have not assessed the role of the memory loss assumption, as made by PPTIS, in simulations with diffusive particle transport.

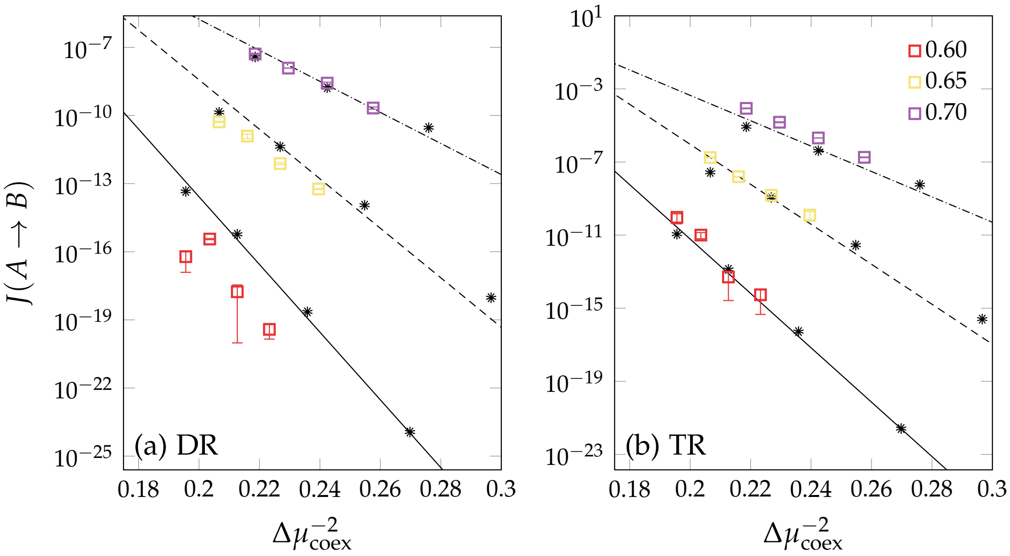

Figure 7.11: Comparison of rate estimates due to PPTIS (square markers) against rate estimates obtained via the CNT formula [Eq. (2.53)] using the explicitly computed via EPS free energy barriers (black markers) for the $c = 1$, $Q = 24$, $d = 3$ extended PLG model. Attachment rates J_*^+ for the CNT expression were estimated via the diffusion coefficient at the top of the free energy barrier and Zeldovich factors $\mathcal{Z}$ were computed by taking the curvature of the corresponding quadratic fits. Lines correspond to linear fits to the CNT rate estimates as show in Fig. 6.9.

8

SUMMARY AND CONCLUSIONS

We now provide an overview and a general discussion of the presented results before summarising our main contributions and potential areas for future work in the field of modelling nucleation from solution via lattice models.

8.1 SUMMARY AND DISCUSSION OF KEY FINDINGS

We have introduced a multicomponent lattice model of a solution, where solute can adopt disordered, partially ordered and fully ordered structures, by extending the PLG model of Duff and Peters [6], providing accurate estimates as well as approximate analytical expressions for the corresponding phase diagrams. Noting the similarity of the PLG and the extended model, it is likely that the approach for derivation of the solute-solvent coexistence line, as discussed in Sec. 4.3, can be applied to the PLG model, while the solute rich states of both models can be easily mapped on to the Q-state three-dimensional Potts model, for which the order-disorder coexistence temperature is known.

Using the path based enhanced sampling method (EPS) of Radhakrishnan and Schlick [225] we have obtained equilibrium distributions of orientational order of solute nuclei at conditions where the ordered solute phase is thermodynamically preferred. We found that the degree of orientational order of solute nuclei is temperature and size dependent, although, based on our calculations, we expect sufficiently large nuclei to prefer high degrees of internal order in equilibrium, with disordered and partially disordered states being short lived. This observation is consistent with the results of the recent studies of metastability of disordered states in the Potts model below the order-disorder coexistence temperature, which suggest that such metastability is present only in finite systems. Thus the size dependence of internal orientational order of solute nuclei in our model can be thought of as a finite size effect. We have also developed and validated against EPS a simple MC move set for sampling of equilibrium distributions of solute nuclei, which can be easily applied to the Ising and PLG models.

Employing the constrained cluster size MC scheme introduced in Sec. 5.4.1 for generation of seed system configurations, we have assessed the performance of the

″seeding″ approach to nucleation rate calculations in the extended PLG model under two sets of microscopic kinetics. We found that the accuracy of the obtained barrier height and nucleation rate estimates varied greatly with the set value of the CNT chemical potential difference parameter, i.e. the volume coefficient of the CNT droplet model (Sec 2.4.2). While this has not been previously demonstrated, the poor performance of the ″seeding″ method, when using the bulk value of the solute-solvent chemical potential difference in the underlying CNT model, is not surprising since the application of bulk phase properties to microscopic nuclei as well as the functional form of CNT have been criticised in multiple studies of lattice and off-lattice models [1, 110, 175, 176] (Table 3.2). Although we found that the ″seeding″ method can produce reasonable nucleation barrier reconstructions at high solute supersaturations, given the values of CNT chemical potential difference parameter obtained based on explicit free energy calculations, we observed significant disagreement between the estimates produced by the ″seeding″ method and those computed via EPS at lower solute supersaturations.

Applying the statistical error estimation approach for the ″seeding″ method, as derived in Sec. 6.2.2, we found that the observed disagreement between explicit nucleation barrier height estimates and those produced by the ″seeding″ method cannot be explained by the statistical errors associated with determining the parameters of a CNT model based on the kinetics of the largest solute nucleus size coordinate. It is important to note, however, that the error estimation approach of Sec. 6.2.2 is based on the assumptions of normality and independence of the probability distributions of the involved quantities. The normality assumption is difficult to verify even in the context of the relatively computationally inexpensive lattice model, and it is, therefore, possible that the derived by us error estimation approach for the ″seeding″ method does not yield the correct confidence bounds on barrier height and rate estimates. Although we obtained reasonable results of the committor histogram tests (Sec. 5.4.2), we cannot rule out the possibilities of our definition of the nucleus size coordinate not satisfying the criteria of CNT [75] or being erroneous at low supersaturations. The observations that EPS tends to underestimate the critical nucleus size (Sec. 5.4.2) and that the explicit barrier height estimates at low solute supersaturations deviate from the expected CNT scaling with respect to the bulk solute-solvent chemical potential difference (Sec. 5.3.1) may also be partially explained by the inaccuracies of our definition of nucleus size and the possibility of structural transformation of nuclei over the course of the transition process, although we cannot make any conclusive comments here without additional data in the low supersaturation regime.

In Sec. 7.3, we have thoroughly examined the connection between TPT and rare event methods in the context of reversible Markov chains, showing that FFS and TIS methods are conceptually equivalent, provided that the collective variable λ

is defined such that every reactive trajectory must realise the value λ_i before the value λ_{i+1} can be achieved, where $\{\lambda_i\}$ are the values of the collective variable at the interfaces defined by FFS and TIS. Such definitions of the collective variable are straightforward to provide in the context of lattice models, e.g. number of solute particles in the system, which is not the case in the off-lattice systems. At present we do not find any thorough analysis of FFS and TIS methods in the literature under conditions where the definition of λ does not satisfy the given criterion. While we did not explore such scenarios in this work, it would be interesting to see if the framework of TPT can be used to provide a rigorous analysis of FFS and TIS under suboptimal definitions of λ, and, as illustrated in Chapter 7, reversible Markov chains can provide an ideal starting point for such analysis.

Despite the clear existence of nonclassical growth pathways of solute nuclei (Sec. 5.3.2) and the known non-Markovian character of microscopic kinetics of nuclei growth [159, 160], we found that the framework of CNT can be used to construct a quantitatively reasonable effective treatment of the solute-solvent transition both in our examination of the "seeding" method and in results of explicit nucleation rate calculations via PPTIS (Sec. 7.5) at high supersaturations. This is not surprising since assumptions of CNT are known to not hold in most numerically studied model particle systems [3, 175] (Table 3.1), yet Eq. (2.53) appears to yield reasonable nucleation rate estimates. Additionally, at the conditions of our PPTIS simulations we only expect to observe disordered structures over the considered range of values of the nucleus size coordinate, meaning no structural transformations occurred within the sampled PPTIS paths. It is worth noting that, for interface separation of $\Delta n = 1$, the rate estimation approach of PPTIS, in the context of nucleation, closely resembles the one-dimensional Markov treatment of the process in the derivation of Eq. (2.53), which suggests that PPTIS may not be the appropriate choice of sampling strategy if strongly non-Markovian character or nonclassical kinetics of the transition process are expected. As discussed in Sec. 7.5, out of the considered rate calculation approaches, the implemented by us PPTIS scheme is the only viable choice of path sampling strategy for study of nucleation under diffusive particle transport while avoiding the unphysical solute depletion effects.

This brings us to the discussion of the seldom studied nucleation kinetics of open systems under diffusive particle transport where, as shown in Sec. 7.4.2, we expect solute density fluctuations to exhibit slow relaxation, making such systems difficult to model via the standard MC methods. Barrier crossing processes in presence of strongly correlated fluctuations have been studied in one-dimensional systems [243, 245] showing escape characteristics which depart substantially from those described by the Kramers' rate theory. However, it is not clear whether inclusion of realistic density fluctuations into models of open particle systems would significantly affect the models' nucleation kinetics, which offers an interesting direction for future study.

8.2 CONCLUSIONS

We have considered nucleation of the ordered solute phase in a Q-state Potts-like lattice model of solution of anisotropic particles, where the solute particles exhibit a Potts-like anisotropic interaction. We have provided evidence for such models not being appropriate candidates for modelling of competing nucleation pathways, where large nuclei of solute structures of different degrees of internal orientational order may form, and the subsequent formation of the most thermodynamically stable bulk structure proceeds via a combination of structural transformation, dissolution and recrystallisation of the formed nuclei. This is largely due to the absence of metastability of disordered structures in the large system limit of the Q-state Potts models below the order-disorder temperature.

We have demonstrated the connections between transition path theory and the popular path sampling based rare event methods in the context of reversible Markov chains, verifying that the FFS and TIS methods employ equally valid MC sampling strategies assuming a well defined collective variable.

We found that, over a broad range of parameter space, the CNT framework is sufficient to formulate a reasonable quantitative treatment of the nucleation process in our model at high solute supersaturations, both in the context of the Auer and Frenkel [125] approach and the procedure of the "seeding" method [102].

8.3 FUTURE WORK

At present, we do not find a lattice model of anisotropic particles in solution which can capture the nonclassical nucleation mechanisms thought to occur in systems of polymorphic minerals. While we cannot rule out the potential for development of such models based on Potts-like representation of anisotropic particles, where a particle's orientation in space is represented by an integer label, it is clear that, for an accurate model, the Potts-like anisotropic interaction would have to be modified to allow bulk metastability of disordered states below the order-disorder transition temperature. It is worth noting that, even if an appropriate set of particle interactions is found, showing that the corresponding disordered solute structures are metastable in bulk may not be straightforward, as is evident from the ongoing debate in the context of the Q-state Potts model.

It is clear that much further work is required in the assessment of the performance of the "seeding" method, in particular with respect to the statistical properties of the estimators defined in Sec. 6.1.1 in the context of kinetics of the nucleus size coordinate. It would, additionally, be useful to consider alternative functional forms of the CNT droplet free energy model as well as performance of the method at ever lower supersaturations.

Finally, it would be particularly interesting to examine the nucleation kinetics in lattice models with strongly temporally correlated particle density fluctuations. Such kinetics have, so far, not been considered even in the context of the spin-flip Ising model, which would serve a good starting point here. While the implementation of the appropriate MC scheme for such kinetics is not immediately clear, various methods for generation of correlated stationary time series exist. This research direction is particularly appealing since it may lead to general advances in methodology for modelling of open systems, which are necessary for future studies of nucleation from solution.

BIBLIOGRAPHY

[1] K. Binder and P. Virnau. Overview: Understanding nucleation phenomena from simulations of lattice gas models. *J. Chem. Phys.*, 145(21):211701, 2016.

[2] V. Agarwal and B. Peters. *Solute Precipitate Nucleation: A Review of Theory and Simulation Advances*, pages 97–160. John Wiley & Sons, Inc., 2014.

[3] G. C. Sosso, J. Chen, S. J. Cox, M. Fitzner, P. Pedevilla, A. Zen, and A. Michaelides. Crystal Nucleation in Liquids: Open Questions and Future Challenges in Molecular Dynamics Simulations. *Chem. Rev.*, 116(12):7078, 2016.

[4] H. Vehkamäki. *Classical nucleation theory in multicomponent systems*. Springer Science & Business Media, 2006.

[5] R. P. Sear. The non-classical nucleation of crystals: microscopic mechanisms and applications to molecular crystals, ice and calcium carbonate. *Internat. Materials Rev.*, 57(6):328, 2012.

[6] N. Duff and B. Peters. Nucleation in a Potts lattice gas model of crystallization from solution. *J. Chem. Phys.*, 131(18):184101, 2009.

[7] M. E. Tuckerman. *Statistical mechanics: theory and molecular simulation*. Oxford University Press, New York, 2010.

[8] P. Ehrenfest and T. Ehrenfest. *The conceptual foundations of the statistical approach in mechanics*. Dover Publications, Inc., New York, 1990.

[9] C. C. Moore. Ergodic theorem, ergodic theory, and statistical mechanics. *Proc. Natl. Acad. Sci.*, 112(7):1907, 2015.

[10] C. R. de Oliveira and T. Werlang. Ergodic hypothesis in classical statistical mechanics. *Revista Brasileira de Ensino de Física*, 29(2):189, 2007.

[11] R. Frigg. A Field Guide to Recent Work on the Foundations of Statistical Mechanics., 2008.

[12] D. Lavis. An Objectivist Account of Probabilities in Statistical Physics. In C. Beisbart and S. Hartmann, editors, *Probabilities in Physics*, page 51. Oxford University Press, 2011.

[13] L. D. Landau and E. M. Lifshitz. *Statistical physics, part 1*, volume 1. Science, PhysMatLit, 1995.

[14] D. Chandler. *Introduction to modern statistical mechanics*. Oxford University Press, New York, 1987.

[15] D. Frenkel and B. Smit. *Understanding molecular simulation: from algorithms to applications*. Academic press, 2002.

[16] J. Sethna. *Statistical mechanics: entropy, order parameters, and complexity*. Oxford University Press, 2006.

[17] L. A. Bunimovich, I. P. Cornfeld, R. L. Dobrushin, N. B. Maslova, Y. B. Pesin, A. M. Vershik, M. V. Jakobson, Y. M. Sukhov, and Y. G. Sinai. *Dynamical Systems II: Ergodic Theory with Applications to Dynamical Systems and Statistical Mechanics*, volume 2. Springer Science & Business Media, 2013.

[18] J. Earman and M. Rédei. Why Ergodic Theory Does Not Explain the Success of Equilibrium Statistical Mechanics. *Brit. J. Philos. Sci.*, 47(1):63, 1996.

[19] D. A. Levin, Y. Peres, and E. L. Wilmer. *Markov chains and mixing times*. American Mathematical Soc., 2009.

[20] T. P. Hayes and A. Sinclair. A General Lower Bound for Mixing of Single-Site Dynamics on Graphs. *Ann. Appl. Probab.*, 17(3):931, 2007.

[21] M. Lubin and A. D. Sokal. Comment on "Antiferromagnetic Potts models". *Phys. Rev. Lett.*, 71(11):1778, 1993.

[22] I. Ya. Korenblit and E. F. Shender. Spin glasses and nonergodicity. *Phys. Usp.*, 32(2):139, 1989.

[23] H. Bauer, K. Schulten, and W. Nadler. Generalized moment expansion of dynamic correlation functions in finite Ising systems. *Phys. Rev. B*, 38(1):445, 1988.

[24] C. E. Shannon. A Mathematical Theory of Communication. *ACM SIGMOBILE Mob. Comput. Commun. Rev.*, 5(1):3, 2001.

[25] E. T. Jaynes. Information Theory and Statistical Mechanics. *Phys. Rev.*, 106(4):620, 1957.

[26] Harvey R. Brown, Wayne Myrvold, and Jos Uffink. Boltzmann's H-theorem, its discontents, and the birth of statistical mechanics. *Studies in History and Philosophy of Science Part B: Studies in History and Philosophy of Modern Physics*, 40(2):174, 2009.

[27] D. P. Landau and K. Binder. *A guide to Monte Carlo simulations in statistical physics*. Cambridge university press, New York, 2009.

[28] K. Binder and D. W. Heermann. *Monte Carlo Simulation in Statistical Physics*. Springer-Verlag Berlin Heidelberg, 5th edition, 2010.

[29] M. P. Nightingale and H. W. J. Blöte. Dynamic Exponent of the Two-Dimensional Ising Model and Monte Carlo Computation of the Subdominant Eigenvalue of the Stochastic Matrix. *Phys. Rev. Lett.*, 76(24):4548, 1996.

[30] J. C. Angles d'Auriac, R. Maynard, and R. Rammal. Critical dynamics of finite Ising model. *J. Stat. Phys.*, 28(2):307, 1982.

[31] J.-S. Wang and R. H. Swendsen. Cluster Monte Carlo algorithms. *Physica A*, 167(3):565, 1990.

[32] G. E. P. Box, G. M. Jenkins, and G. C. Reinsel. *Time series analysis: forecasting and control*. John Wiley & Sons, 4th edition, 2008.

[33] W. A. Link and M. J. Eaton. On thinning of chains in MCMC. *Methods Ecol. Evol.*, 3(1):112, 2012.

[34] G. R. Grimmett and D. R. Stirzaker. *Probability and random processes*. Oxford university press, New York, 3rd edition, 2001.

[35] S. M. Ross. *Introduction to probability models*. Academic press, 10th edition, 2010.

[36] R. Durrett. *Essentials of stochastic processes*. Springer Science & Business Media, 2nd edition, 2012.

[37] S. A. Serebrinsky. Physical time scale in kinetic Monte Carlo simulations of continuous-time Markov chains. *Phys. Rev. E*, 83(3):037701, 2011.

[38] D. T. Gillespie. Exact stochastic simulation of coupled chemical reactions. *J. Phys. Chem.*, 81(25):2340, 1977.

[39] K. Binder. Theory of first-order phase transitions. *Rep. Prog. Phys.*, 50(7):783, 1987.

[40] T. D. Lee and C. N. Yang. Statistical Theory of Equations of State and Phase Transitions. II. Lattice Gas and Ising Model. *Phys. Rev.*, 87(3):410, 1952.

[41] S. Bangu. *Why Does Water Boil? Fictions in Scientific Explanation*, pages 319–330. Springer International Publishing, 2015.

[42] M. Kastner. Phase transitions and configuration space topology. *Rev. Mod. Phys.*, 80(1):167, 2008.

[43] H. E. Stanley. *Introduction to phase transitions and critical phenomena*. Oxford : Clarendon Press, 1971.

[44] V. V. Slezov. *Nucleation versus Spinodal Decomposition in Confined Binary Solutions*, pages 353–397. Wiley-VCH Verlag GmbH & Co. KGaA, 2009.

[45] J. Wedekind, G. Chkonia, J. Wölk, R. Strey, and D. Reguera. Crossover from nucleation to spinodal decomposition in a condensing vapor. *J. Chem. Phys.*, 131(11):114506, 2009.

[46] K. Binder and P. Fratzl. *Spinodal Decomposition*, pages 409–480. Wiley-VCH Verlag GmbH & Co. KGaA, 2005.

[47] D. Yoshioka. *Statistical physics: an introduction*. Springer Science & Business Media, 2007.

[48] P. D. Olmsted. Lectures on Landau Theory of Phase Transitions. *University of Leeds, Department of Physics*, 2000.

[49] E. E. Santiso and B. L. Trout. A general set of order parameters for molecular crystals. *J. Chem. Phys.*, 134(6):064109, 2011.

[50] D. Moroni. *Efficient sampling of rare event pathways: from simple models to nucleation*. PhD thesis, Universiteit van Amsterdam, 2005.

[51] D. Heidrich. *The reaction path in chemistry: current approaches and perspectives*. Springer Science & Business Media, 1995.

[52] W. Koch and M. C. Holthausen. *A chemist's guide to density functional theory*. Wiley-VCH Verlag GmbH, 2nd edition, 2001.

[53] M. Ferrario, G. Ciccotti, and K. Binder. *Computer simulations in condensed matter: from materials to chemical biology*, volume 1 of *Lecture notes in Physics, 703*. Springer, Berlin Heidelberg, 2006.

[54] P. Metzner, C. Schütte, and E. Vanden-Eijnden. Transition Path Theory for Markov Jump Processes. *Multiscale Model. Simul.*, 7(3):1192, 2009.

[55] F. A. Tal and E. Vanden-Eijnden. Transition state theory and dynamical corrections in ergodic systems. *Nonlinearity*, 19(2):501, 2006.

[56] P. Metzner, C. Schütte, and E. Vanden-Eijnden. Illustration of transition path theory on a collection of simple examples. *J. Chem. Phys.*, 125(8):084110, 2006.

[57] M. Lapelosa and C. F. Abrams. Transition-path theory calculations on non-uniform meshes in two and three dimensions using finite elements. *Comput. Phys. Commun.*, 184(10):2310, 2013.

[58] P. Hänggi, P. Talkner, and M. Borkovec. Reaction-rate theory: fifty years after Kramers. *Rev. Mod. Phys.*, 62(2):251, 1990.

[59] B. Peters and B. L. Trout. Obtaining reaction coordinates by likelihood maximization. *J. Chem. Phys.*, 125(5):054108, 2006.

[60] W. Li and A. Ma. Recent developments in methods for identifying reaction coordinates. *Mol. Simul.*, 40(10-11):784, 2014.

[61] I. V. Markov. *Crystal growth for beginners*. World Scientific, 1995.

[62] D. T. Wu. Nucleation Theory. In H. Ehrenreich and F. Spaepen, editors, *Advances in Research and Applications*, volume 50 of *Solid State Physics*, pages 37 – 187. Academic Press, 1996.

[63] S. Auer and D. Frenkel. Quantitative prediction of crystal-nucleation rates for spherical colloids: A computational approach. *Annu. Rev. Phys. Chem.*, 55(1):333, 2004.

[64] D. Reguera, , and H. Reiss. Extended Modified Liquid DropDynamical Nucleation Theory (EMLDDNT) Approach to Nucleation:A New Theory. *J. Phys. Chem. B*, 108(51):19831, 2004.

[65] V. I. Kalikmanov. Mean-field kinetic nucleation theory. *J. Chem. Phys.*, 124(12):124505, 2006.

[66] S. Prestipino, A. Laio, and E. Tosatti. Systematic Improvement of Classical Nucleation Theory. *Phys. Rev. Lett.*, 108(22):225701, 2012.

[67] J. Wedekind, J. Wölk, D. Reguera, and R. Strey. Nucleation rate isotherms of argon from molecular dynamics simulations. *J. Chem. Phys.*, 127(15):154515, 2007.

[68] M. Horsch, J. Vrabec, and H. Hasse. Modification of the classical nucleation theory based on molecular simulation data for surface tension, critical nucleus size, and nucleation rate. *Phys. Rev. E*, 78(1):011603, 2008.

[69] V. I. Kalikmanov, J. Wölk, and T. Kraska. Argon nucleation: Bringing together theory, simulations, and experiment. *J. Chem. Phys.*, 128(12):124506, 2008.

[70] I. Napari, J. Julin, and H. Vehkamäki. Performance of some nucleation theories with a nonsharp droplet-vapor interface. *J. Chem. Phys.*, 133(15):154503, 2010.

[71] K. K. Tanaka, H. Tanaka, T. Yamamoto, and K. Kawamura. Molecular dynamics simulations of nucleation from vapor to solid composed of Lennard-Jones molecules. *J. Chem. Phys.*, 134(20):204313, 2011.

[72] T. P. Bennett and J. C. Barrett. Water nucleation: A comparison between some phenomenological theories and experiment. *J. Chem. Phys.*, 137(12):124702, 2012.

[73] L. Maibaum. Comment on "Elucidating the Mechanism of Nucleation near the Gas-Liquid Spinodal". *Phys. Rev. Lett.*, 101(1):019601, 2008.

[74] G. T. Beckham and B. Peters. Optimizing Nucleus Size Metrics for Liquid-Solid Nucleation from Transition Paths of Near-Nanosecond Duration. *J. Phys. Chem. Lett.*, 2(10):1133, 2011.

[75] B. Cheng, G. A. Tribello, and M. Ceriotti. Solid-liquid interfacial free energy out of equilibrium. *Phys. Rev. B*, 92(18):180102, 2015.

[76] F. Schmitz, P. Virnau, and K. Binder. Monte Carlo tests of nucleation concepts in the lattice gas model. *Phys. Rev. E*, 87(5):053302, 2013.

[77] E. Sanz, C. Valeriani, D. Frenkel, and M. Dijkstra. Evidence for Out-of-Equilibrium Crystal Nucleation in Suspensions of Oppositely Charged Colloids. *Phys. Rev. Lett.*, 99(5):055501, 2007.

[78] L. O. Hedges and S. Whitelam. Limit of validity of Ostwald's rule of stages in a statistical mechanical model of crystallization. *J. Chem. Phys.*, 135(16):164902, 2011.

[79] R. P. Sear. Quantitative studies of crystal nucleation at constant supersaturation: experimental data and models. *CrystEngComm*, 16(29):6506, 2014.

[80] D. Gebauer, M. Kellermeier, J. D. Gale, L. Bergstrom, and H. Colfen. Pre-nucleation clusters as solute precursors in crystallisation. *Chem. Soc. Rev.*, 43(7):2348, 2014.

[81] D. W. Oxtoby. Nucleation of first-order phase transitions. *Acc. Chem. Res.*, 31(2):91, 1998.

[82] J. L. F. Abascal and C. Vega. A general purpose model for the condensed phases of water: TIP4P/2005. *J. Chem. Phys.*, 123(23):234505, 2005.

[83] J. L. F. Abascal, E. Sanz, R. Garca Fernndez, and C. Vega. A potential model for the study of ices and amorphous water: Tip4p/ice. *J. Chem. Phys.*, 122(23):234511, 2005.

[84] V. Molinero and E. B. Moore. Water Modeled As an Intermediate Element between Carbon and Silicon. *J. Phys. Chem. B*, 113(13):4008, 2009.

[85] F. G. Fumi and M. P. Tosi. Ionic sizes and born repulsive parameters in the NaCl-type alkali halides. *J. Phys. Chem. Solids*, 25(1):31, 1964.

[86] D. E. Smith and L. X. Dang. Computer simulations of NaCl association in polarizable water. *J. Chem. Phys.*, 100(5):3757, 1994.

[87] I. S. Joung and Cheatham T. E. Determination of Alkali and Halide Monovalent Ion Parameters for Use in Explicitly Solvated Biomolecular Simulations. *J. Phys. Chem. B*, 112(30):9020, 2008.

[88] S. V. Lishchuk. Role of three-body interactions in formation of bulk viscosity in liquid argon. *J. Chem. Phys.*, 136(16):164501, 2012.

[89] T. Palberg. Crystallization kinetics of colloidal model suspensions: recent achievements and new perspectives. *J. Phys.: Condens. Matter*, 26(33):333101, 2014.

[90] C. Vega and J. L. F. Abascal. Simulating water with rigid non-polarizable models: a general perspective. *Phys. Chem. Chem. Phys.*, 13(44):19663, 2011.

[91] J. L. Aragones, E. Sanz, C. Valeriani, and C. Vega. Calculation of the melting point of alkali halides by means of computer simulations. *J. Chem. Phys.*, 137(10):104507, 2012.

[92] J. L. Aragones, E. Sanz, and C. Vega. Solubility of NaCl in water by molecular simulation revisited. *J. Chem. Phys.*, 136(24):244508, 2012.

[93] J. P. Mithen, A. J. Callison, and R. P. Sear. Nucleation of crystals that are mixed composites of all three polymorphs in the Gaussian core model. *J. Chem. Phys.*, 142(22):224505, 2015.

[94] K. Kratzer and A. Arnold. Two-stage crystallization of charged colloids under low supersaturation conditions. *Soft Matter*, 11(11):2174, 2015.

[95] A. Cuetos and M. Dijkstra. Kinetic Pathways for the Isotropic-Nematic Phase Transition in a System of Colloidal Hard Rods: A Simulation Study. *Phys. Rev. Lett.*, 98(9):095701, 2007.

[96] R. Ni and M. Dijkstra. Crystal nucleation of colloidal hard dumbbells. *J. Chem. Phys.*, 134(3):034501, 2011.

[97] I. Saika-Voivod, P. H. Poole, and R. K. Bowles. Test of classical nucleation theory on deeply supercooled high-pressure simulated silica. *J. Chem. Phys.*, 124(22):224709, 2006.

[98] T. Li, D. Donadio, and G. Galli. Nucleation of tetrahedral solids: A molecular dynamics study of supercooled liquid silicon. *J. Chem. Phys.*, 131(22):224519, 2009.

[99] S. Bonella, S. Meloni, and G. Ciccotti. Theory and methods for rare events. *Eur. Phys. J. B*, 85(3):1, 2012.

[100] P. G. Bolhuis and C. Dellago. Practical and conceptual path sampling issues. *Eur. Phys. J. ST*, 224(12):2409, 2015.

[101] J. Wedekind, R. Strey, and D. Reguera. New method to analyze simulations of activated processes. *J. Chem. Phys.*, 126(13):134103, 2007.

[102] B. C. Knott, V. Molinero, M. F. Doherty, and B. Peters. Homogeneous nucleation of methane hydrates: Unrealistic under realistic conditions. *J. Am. Chem. Soc.*, 134(48):19544, 2012.

[103] C. Dellago, P. G. Bolhuis, F. S. Csajka, and D. Chandler. Transition path sampling and the calculation of rate constants. *J. Chem. Phys.*, 108(5):1964, 1998.

[104] R. J. Allen, D. Frenkel, and P. R. ten Wolde. Simulating rare events in equilibrium or nonequilibrium stochastic systems. *J. Chem. Phys.*, 124(2):024102, 2006.

[105] Titus S. van Erp, Daniele Moroni, and Peter G. Bolhuis. A novel path sampling method for the calculation of rate constants. *J. Chem. Phys.*, 118(17):7762, 2003.

[106] A. Laio and M. Parrinello. Escaping free-energy minima. *Proc. Natl. Acad. Sci.*, 99(20):12562, 2002.

[107] F. Trudu, D. Donadio, and M. Parrinello. Freezing of a Lennard-Jones Fluid: From Nucleation to Spinodal Regime. *Phys. Rev. Lett.*, 97(10):105701, 2006.

[108] L. Maragliano, A. Fischer, E. Vanden-Eijnden, and G. Ciccotti. String method in collective variables: Minimum free energy paths and isocommittor surfaces. *J. Chem. Phys.*, 125(2):024106, 2006.

[109] E. E. Santiso and B. L. Trout. A general method for molecular modeling of nucleation from the melt. *J. Chem. Phys.*, 143(17):174109, 2015.

[110] L. Filion, M. Hermes, R. Ni, and M. Dijkstra. Crystal nucleation of hard spheres using molecular dynamics, umbrella sampling, and forward flux sampling: A comparison of simulation techniques. *J. Chem. Phys.*, 133(24):244115, 2010.

[111] L. Filion, R. Ni, D. Frenkel, and M. Dijkstra. Simulation of nucleation in almost hard-sphere colloids: The discrepancy between experiment and simulation persists. *J. Chem. Phys.*, 134(13):134901, 2011.

[112] J. R. Espinosa, C. Vega, C. Valeriani, and E. Sanz. Seeding approach to crystal nucleation. *J. Chem. Phys.*, 144(3):034501, 2016.

[113] J. Diemand, R. Angélil, K. K. Tanaka, and H. Tanaka. Large scale molecular dynamics simulations of homogeneous nucleation. *J. Chem. Phys.*, 139(7):074309, 2013.

[114] N. E. R. Zimmermann, B. Vorselaars, D. Quigley, and B. Peters. Nucleation of NaCl from Aqueous Solution: Critical Sizes, Ion-Attachment Kinetics, and Rates. *J. Am. Chem. Soc.*, 137(41):13352, 2015.

[115] T. Schilling, S. Dorosz, H. J. Schpe, and G. Opletal. Crystallization in suspensions of hard spheres: a Monte Carlo and molecular dynamics simulation study. *J. Phys.:Condens. Matter*, 23(19):194120, 2011.

[116] J. Russo, A. C. Maggs, D. Bonn, and H. Tanaka. The interplay of sedimentation and crystallization in hard-sphere suspensions. *Soft Matter*, 9(30):7369, 2013.

[117] M. Radu and T. Schilling. Solvent hydrodynamics speed up crystal nucleation in suspensions of hard spheres. *EPL*, 105(2):26001, 2014.

[118] J. R. Espinosa, C. Vega, C. Valeriani, and E. Sanz. The crystal-fluid interfacial free energy and nucleation rate of NaCl from different simulation methods. *J. Chem. Phys.*, 142(19):194709, 2015.

[119] T. Li, D. Donadio, G. Russo, and G. Galli. Homogeneous ice nucleation from supercooled water. *Phys. Chem. Chem. Phys.*, 13(44):19807, 2011.

[120] T. Li, D. Donadio, and G. Galli. Ice nucleation at the nanoscale probes no mans land of water. *Nat. Commun.*, 4:1887, 2013.

[121] A. Haji-Akbari, R. S. DeFever, S. Sarupria, and P. G. Debenedetti. Suppression of sub-surface freezing in free-standing thin films of a coarse-grained model of water. *Phys. Chem. Chem. Phys.*, 16(47):25916, 2014.

[122] A. Haji-Akbari and P. G. Debenedetti. Direct calculation of ice homogeneous nucleation rate for a molecular model of water. *Proc. Natl. Acad. Sci.*, 112(34):10582, 2015.

[123] E. Sanz, C. Vega, J. R. Espinosa, R. Caballero-Bernal, J. L. F. Abascal, and C. Valeriani. Homogeneous Ice Nucleation at Moderate Supercooling from Molecular Simulation. *J. Am. Chem. Soc.*, 135(40):15008, 2013.

[124] J. R. Espinosa, E. Sanz, C. Valeriani, and C. Vega. Homogeneous ice nucleation evaluated for several water models. *J. Chem. Phys.*, 141(18):18C529, 2014.

[125] S. Auer and D. Frenkel. Prediction of absolute crystal-nucleation rate in hard-sphere colloids. *Nature*, 409(6823):1020, 2001.

[126] J. D. Weeks, D. Chandler, and H. C. Andersen. Role of Repulsive Forces in Determining the Equilibrium Structure of Simple Liquids. *J. Chem. Phys.*, 54(12):5237, 1971.

[127] F. H. Stillinger. Phase transitions in the Gaussian core system. *J. Chem. Phys.*, 65(10):3968, 1976.

[128] S. M. A. Malek, G. P. Morrow, and I. Saika-Voivod. Crystallization of Lennard-Jones nanodroplets: From near melting to deeply supercooled. *J. Chem. Phys.*, 142(12):124506, 2015.

[129] B. W. H. van Beest, G. J. Kramer, and R. A. van Santen. Force fields for silicas and aluminophosphates based on *ab initio* calculations. *Phys. Rev. Lett.*, 64(16):1955, 1990.

[130] T. S. van Erp. *Dynamical Rare Event Simulation Techniques for Equilibrium and Nonequilibrium Systems*, pages 27–60. John Wiley & Sons, Inc., 2012.

[131] S. Jungblut and C. Dellago. Caveats of mean first-passage time methods applied to the crystallization transition: Effects of non-Markovianity. *J. Chem. Phys.*, 142(6):064103, 2015.

[132] J. Julin, I. Napari, and H. Vehkamki. Comparative study on methodology in molecular dynamics simulation of nucleation. *J. Chem. Phys.*, 126(22):224517, 2007.

[133] J.-M. Leyssale, J. Delhommelle, and C. Millot. Hit and miss of classical nucleation theory as revealed by a molecular simulation study of crystal nucleation in supercooled sulfur hexafluoride. *J. Chem. Phys.*, 127(4):044504, 2007.

[134] V. G. Baidakov, A. O. Tipeev, K. S. Bobrov, and G. V. Ionov. Crystal nucleation rate isotherms in Lennard-Jones liquids. *J. Chem. Phys.*, 132(23):234505, 2010.

[135] V. G. Baidakov and A. O. Tipeev. Crystal nucleation and the solid-liquid interfacial free energy. *J. Chem. Phys.*, 136(7):074510, 2012.

[136] M. J. McGrath, J. N. Ghogomu, N. T. Tsona, J. I. Siepmann, B. Chen, I. Napari, and H. Vehkamki. Vapor-liquid nucleation of argon: Exploration of various intermolecular potentials. *J. Chem. Phys.*, 133(8):084106, 2010.

[137] T. Zykova-Timan, C. Valeriani, E. Sanz, D. Frenkel, and E. Tosatti. Irreducible Finite-Size Effects in the Surface Free Energy of NaCl Crystals from Crystal-Nucleation Data. *Phys. Rev. Lett.*, 100(3):036103, 2008.

[138] M. N. Joswiak, N. Duff, M. F. Doherty, and B. Peters. Size-Dependent Surface Free Energy and Tolman-Corrected Droplet Nucleation of TIP4P/2005 Water. *J. Phys. Chem. Lett.*, 4(24):4267, 2013.

[139] S. Jungblut and C. Dellago. Crystallization of a binary Lennard-Jones mixture. *J. Chem. Phys.*, 134(10):104501, 2011.

[140] D. Moroni, P. G. Bolhuis, and T. S. van Erp. Rate constants for diffusive processes by partial path sampling. *J. Chem. Phys.*, 120(9):4055, 2004.

[141] S. E. M. Lundrigan and I. Saika-Voivod. Test of classical nucleation theory and mean first-passage time formalism on crystallization in the Lennard-Jones liquid. *J. Chem. Phys.*, 131(10):104503, 2009.

[142] J. Wedekind and D. Reguera. Kinetic Reconstruction of the Free-Energy Landscape. *J. Phys. Chem. B*, 112(35):11060, 2008.

[143] C. Valeriani, E. Sanz, and D. Frenkel. Rate of homogeneous crystal nucleation in molten NaCl. *J. Chem. Phys.*, 122(19):194501, 2005.

[144] S. Jungblut and C. Dellago. Pathways to self-organization: Crystallization via nucleation and growth. *Eur. Phys. J. E*, 39(8):77, 2016.

[145] J. Russo and H. Tanaka. Nonclassical pathways of crystallization in colloidal systems. *MRS Bulletin*, 41(5):369, 2016.

[146] H. J. Schöpe, G. Bryant, and W. van Megen. Effect of polydispersity on the crystallization kinetics of suspensions of colloidal hard spheres when approaching the glass transition. *J. Chem. Phys.*, 127(8):084505, 2007.

[147] T. Schilling, H. J. Schöpe, M. Oettel, G. Opletal, and I. Snook. Precursor-Mediated Crystallization Process in Suspensions of Hard Spheres. *Phys. Rev. Lett.*, 105(2):025701, 2010.

[148] C. Desgranges and J. Delhommelle. Molecular Mechanism for the Cross-Nucleation between Polymorphs. *J. Am. Chem. Soc.*, 128(32):10368, 2006.

[149] D. Chakraborty and G. N. Patey. How Crystals Nucleate and Grow in Aqueous NaCl Solution. *J. Phys. Chem. Lett.*, 4(4):573, 2013.

[150] P. Raiteri and J. D. Gale. Water Is the Key to Nonclassical Nucleation of Amorphous Calcium Carbonate. *J. Am. Chem. Soc.*, 132(49):17623, 2010.

[151] L. C. Jacobson, W. Hujo, and V. Molinero. Amorphous Precursors in the Nucleation of Clathrate Hydrates. *J. Am. Chem. Soc.*, 132(33):11806, 2010.

[152] J. Ihli, W. C. Wong, E. H. Noel, Y.-Y. Kim, A. N. Kulak, H. K. Christenson, M. J. Duer, and Meldrum F. C. Dehydration and crystallization of amorphous calcium carbonate in solution and in air. *Nat. Commun.*, 5(3169), 2014.

[153] A. F. Wallace, L. O. Hedges, A. Fernandez-Martinez, P. Raiteri, J. D. Gale, G. A. Waychunas, S. Whitelam, J. F. Banfield, and J. J. De Yoreo. Microscopic Evidence for Liquid-Liquid Separation in Supersaturated CaCO3 Solutions. *Science*, 341(6148):885, 2013.

[154] J. J. De Yoreo. In-situ liquid phase TEM observations of nucleation and growth processes. *Prog. Cryst. Growth Charact. Mater.*, 62(2):69, 2016.

[155] C. Rottman and M. Wortis. Equilibrium crystal shapes for lattice models with nearest-and next-nearest-neighbor interactions. *Phys. Rev. B*, 29(1):328, 1984.

[156] M. Hasenbusch, S. Meyer, and M. Pütz. The roughening transition of the three-dimensional Ising interface: A Monte Carlo study. *J. Stat. Phys.*, 85(3):383, 1996.

[157] K. Kawasaki. Diffusion Constants near the Critical Point for Time-Dependent Ising Models. I. *Phys. Rev.*, 145(1):224, 1966.

[158] V. Agarwal and B. Peters. Nucleation near the eutectic point in a Potts-lattice gas model. *J. Chem. Phys.*, 140(8):084111, 2014.

[159] J. Kuipers and G. T. Barkema. Non-Markovian dynamics of clusters during nucleation. *Phys. Rev. E*, 79(6):62101, 2009.

[160] J. Kuipers and G. T. Barkema. Limitations of a Fokker-Planck description of nucleation. *Phys. Rev. E*, 82(1):11128, 2010.

[161] O. Penrose and A. Buhagiar. Kinetics of nucleation in a lattice gas model: Microscopic theory and simulation compared. *J. Stat. Phys.*, 30(1):219, 1982.

[162] O. Penrose, J. Lebowitz, J. Marro, M. Kalos, and J. Tobochnik. Kinetics of a first-order phase transition: computer simulations and theory. *J. Stat. Phys.*, 34(3):399, 1984.

[163] D. Stauffer, A. Coniglio, and D. W. Heermann. Monte Carlo Experiment for Nucleation Rate in the Three-Dimensional Ising Model. *Phys. Rev. Lett.*, 49(18):1299, 1982.

[164] V. A. Shneidman, K. A. Jackson, and K. M. Beatty. On the applicability of the classical nucleation theory in an Ising system. *J. Chem. Phys.*, 111(15):6932, 1999.

[165] H. Vehkamäki and I. J. Ford. Nucleation theorems applied to the Ising model. *Phys. Rev. E*, 59(6):6483, 1999.

[166] F. Soisson and G. Martin. Monte Carlo simulations of the decomposition of metastable solid solutions: Transient and steady-state nucleation kinetics. *Phys. Rev. B*, 62(1):203, 2000.

[167] K. Binder and E. Stoll. Scaling Theory for Metastable States and Their Lifetimes. *Phys. Rev. Lett.*, 31(1):47, 1973.

[168] K. Binder and H. Müller-Krumbhaar. Investigation of metastable states and nucleation in the kinetic Ising model. *Phys. Rev. B*, 9(5):2328, 1974.

[169] D. W. Heermann, A. Coniglio, W. Klein, and D. Stauffer. Nucleation and metastability in three-dimensional Ising models. *J. Stat. Phys.*, 36(3):447, 1984.

[170] M. Acharyya and D. Stauffer. Nucleation and hysteresis in Ising model: classical theory versus computer simulation. *Eur. Phys. J. B*, 5(3):571, 1998.

[171] V. A. Shneidman, K. A. Jackson, and K. M. Beatty. Nucleation and growth of a stable phase in an Ising-type system. *Phys. Rev. B*, 59(5):3579, 1999.

[172] S. Wonczak, R. Strey, and D. Stauffer. Confirmation of classical nucleation theory by Monte Carlo simulations in the 3-dimensional Ising model at low temperature. *J. Chem. Phys.*, 113(5):1976, 2000.

[173] K. Binder and D. Stauffer. Monte Carlo study of the surface area of liquid droplets. *J. Stat. Phys.*, 6(1):49, 1972.

[174] A. C. Pan and D. Chandler. Dynamics of Nucleation in the Ising Model. *J. Phys. Chem. B*, 108(51):19681, 2004.

[175] S. Ryu and W. Cai. Validity of classical nucleation theory for Ising models. *Phys. Rev. E*, 81(3):30601, 2010.

[176] S. Ryu and W. Cai. Numerical tests of nucleation theories for the Ising models. *Phys. Rev. E*, 82(1):11603, 2010.

[177] K. Binder and M. H. Kalos. "Critical clusters" in a supersaturated vapor: Theory and Monte Carlo simulation. *J. Stat. Phys.*, 22(3):363, 1980.

[178] H. Furukawa and K. Binder. Two-phase equilibria and nucleation barriers near a critical point. *Phys. Rev. A*, 26(1):556, 1982.

[179] G Jacucci, A. Perini, and G. Martin. Monte Carlo computation of cluster free energies in the Ising model: a test for the validity of the capillarity approximation. *J. Phys. A*, 16(2):369, 1983.

[180] A. Perini, G. Jacucci, and G. Martin. Cluster free energy in the simple-cubic Ising model. *Phys. Rev. B*, 29(5):2689, 1984.

[181] J. Marro and R. Toral. Equilibrium cluster distributions of the three-dimensional Ising model in the one phase region. *Physica A*, 122(3):563, 1983.

[182] K. Brendel, G. T. Barkema, and H. van Beijeren. Nucleation times in the two-dimensional Ising model. *Phys. Rev. E*, 71(3):31601, 2005.

[183] A. Bazavov, B. A. Berg, and S. Dubey. Phase transition properties of 3D Potts models. *Nucl. Phys. B*, 802(3):421, 2008.

[184] S.-H. Tsai and D. P. Landau. Phase diagram of a two-dimensional large-Q Potts model in an external field. *Comput. Phys. Commun.*, 180(4):485, 2009.

[185] L. Mittag and M. J. Stephen. Mean-field theory of the many component Potts model. *J. Phys. A*, 7(9):L109, 1974.

[186] M. Ibáñez Berganza, A. Petri, and P. Coletti. Dynamic metastability in the two-dimensional potts ferromagnet. *Phys. Rev. E*, 89(5):052115, 2014.

[187] M. Ibáñez Berganza, P. Coletti, and A. Petri. Anomalous metastability in a temperature-driven transition. *EPL*, 106(5):56001, 2014.

[188] S. B. Rutkevich. Monte-Carlo simulation of nucleation in the two-dimensional Potts model. *Int. J. Mod. Phys. C*, 13(4):495, 2002.

[189] David P. Sanders, Hernán Larralde, and Fran çois Leyvraz. Competitive nucleation and the Ostwald rule in a generalized Potts model with multiple metastable phases. *Phys. Rev. B*, 75(13):132101, 2007.

[190] A. Okamoto, T. Kuwatani, T. Omori, and K. Hukushima. Free-energy landscape and nucleation pathway of polymorphic minerals from solution in a potts lattice-gas model. *Phys. Rev. E*, 92(4):042130, 2015.

[191] M. Jorge, S. M. Auerbach, and P. A. Monson. Modeling Spontaneous Formation of Precursor Nanoparticles in Clear-Solution Zeolite Synthesis. *J. Am. Chem. Soc.*, 127(41):14388, 2005.

[192] S. Whitelam. Nonclassical assembly pathways of anisotropic particles. *J. Chem. Phys.*, 132(19):194901, 2010.

[193] N. Duff and B. Peters. Erratum: "Nucleation in a Potts lattice gas model of crystallization from solution" [J. Chem. Phys.131, 184101 (2009)]. *J. Chem. Phys.*, 132(12):129901, 2010.

[194] J. Zhang and M. Muthukumar. Monte Carlo simulations of single crystals from polymer solutions. *J. Chem. Phys.*, 126(23):234904, 2007.

[195] J. Zhang and M. Muthukumar. Simulations of nucleation and elongation of amyloid fibrils. *J. Chem. Phys.*, 130(3):035102, 2009.

[196] Irbäck, A. and Wessén, J. Thermodynamics of amyloid formation and the role of intersheet interactions. *J. Chem. Phys.*, 143(10):105104, 2015.

[197] J. H. ter Horst and D. Kashchiev. Determining the nucleation rate from the dimer growth probability. *J. Chem. Phys.*, 123(11):114507, 2005.

[198] J. H. ter Horst and D. Kashchiev. Rate of Two-Dimensional Nucleation: Verifying Classical and Atomistic Theories by Monte Carlo Simulation. *J. Phys. Chem. B*, 112(29):8614, 2008.

[199] R. Cabriolu, D. Kashchiev, and S. Auer. Breakdown of nucleation theory for crystals with strongly anisotropic interactions between molecules. *J. Chem. Phys.*, 137(20):204903, 2012.

[200] A. J. Page and R. P. Sear. Heterogeneous Nucleation in and out of Pores. *Phys. Rev. Lett.*, 97(6):065701, 2006.

[201] R. P. Sear. Heterogeneous and Homogeneous Nucleation Compared: Rapid Nucleation on Microscopic Impurities. *J. Phys. Chem. B*, 110(10):4985, 2006.

[202] R. P. Sear. Non-self-averaging nucleation rate due to quenched disorder. *J. Phys. Condens. Matter*, 24(5):052205, 2012.

[203] D. Winter, P. Virnau, and K. Binder. Monte Carlo Test of the Classical Theory for Heterogeneous Nucleation Barriers. *Phys. Rev. Lett.*, 103(22):225703, 2009.

[204] D. Winter, P. Virnau, and K. Binder. Heterogeneous nucleation at a wall near a wetting transition: a Monte Carlo test of the classical theory. *J. Phys. Condens. Matter*, 21(46):464118, 2009.

[205] R. P. Sear. Continuity of the nucleation of bulk and surface phases. *J. Chem. Phys.*, 129(16):164510, 2008.

[206] R. P. Sear. Formation of a metastable phase due to the presence of impurities. *J. Phys. Condens. Matter*, 17(25):3997, 2005.

[207] R. P. Sear. Nucleation via an unstable intermediate phase. *J. Chem. Phys.*, 131(7):074702, 2009.

[208] R. P. Sear. Nucleation at contact lines where fluid-fluid interfaces meet solid surfaces. *J. Phys. Condens. Matter*, 19(46):466106, 2007.

[209] R. P. Sear. Nucleation of a liquid on aerosol nanoparticles. *EPL*, 83(6):66002, 2008.

[210] D. Frenkel and A. J. C. Ladd. New Monte Carlo method to compute the free energy of arbitrary solids. Application to the fcc and hcp phases of hard spheres. *J. Chem. Phys.*, 81(7):3188, 1984.

[211] A. Z. Panagiotopoulos. Direct determination of phase coexistence properties of fluids by Monte Carlo simulation in a new ensemble. *Mol. Phys.*, 61(4):813, 1987.

[212] D. A. Kofke. Gibbs-Duhem integration: a new method for direct evaluation of phase coexistence by molecular simulation. *Mol. Phys.*, 78(6):1331, 1993.

[213] N. B. Wilding and A. D. Bruce. Freezing by monte carlo phase switch. *Phys. Rev. Lett.*, 85(24):5138, 2000.

[214] J.-S. Wang and Robert H. Swendsen. Transition Matrix Monte Carlo Method. *J. Stat. Phys.*, 106(1):245, 2002.

[215] E. G. Noya, C. Vega, and E. de Miguel. Determination of the melting point of hard spheres from direct coexistence simulation methods. *J. Chem. Phys.*, 128(15):154507, 2008.

[216] N. B. Wilding. Computer simulation of fluid phase transitions. *Am. J. Phys.*, 69(11):1147, 2001.

[217] F. Wang and D. P. Landau. Efficient, Multiple-Range Random Walk Algorithm to Calculate the Density of States. *Phys. Rev. Lett.*, 86(10):2050, 2001.

[218] R. E. Belardinelli and V. D. Pereyra. Wang-Landau algorithm: A theoretical analysis of the saturation of the error. *J. Chem. Phys.*, 127(18):184105, 2007.

[219] T. Vogel, Y. W. Li, T. Wüst, and D. P. Landau. Generic, Hierarchical Framework for Massively Parallel Wang-Landau Sampling. *Phys. Rev. Lett.*, 110(21):210603, 2013.

[220] R. E. Belardinelli, V. D. Pereyra, R. Dickman, and B. J. Lourenço. Intrinsic convergence properties of entropic sampling algorithms. *J. Stat. Mech. Theor. Exp.*, 2014(7):P07007, 2014.

[221] B. Widom. Some Topics in the Theory of Fluids. *J. Chem. Phys.*, 39(11):2808, 1963.

[222] T. Nogawa, N. Ito, and H. Watanabe. Static and dynamical aspects of the metastable states of first order transition systems. In *Proceedings of the 24th Workshop on Computer Simulation Studies in Condensed Matter Physics (CSP2011)*, volume 15, pages 76 – 80, 2011.

[223] J. Olejarz, P. L. Krapivsky, and S. Redner. Zero-temperature coarsening in the 2d potts model. *J. Stat. Mech. Theor. Exp.*, 2013(6):P06018, 2013.

[224] C. Abrams and G. Bussi. Enhanced Sampling in Molecular Dynamics Using Metadynamics, Replica-Exchange, and Temperature-Acceleration. *Entropy*, 16(1):163, 2014.

[225] R. Radhakrishnan and T. Schlick. Biomolecular free energy profiles by a shooting/umbrella sampling protocol, "BOLAS". *J. Chem. Phys.*, 121(5):2436, 2004.

[226] M. R. Shirts and J. D. Chodera. Statistically optimal analysis of samples from multiple equilibrium states. *J. Chem. Phys.*, 129(12):124105, 2008.

[227] B. W. Zhang, J. Xia, Z. Tan, and R. M. Levy. A Stochastic Solution to the Unbinned WHAM Equations. *J. Phys. Chem. Lett.*, 6(19):3834, 2015.

[228] A. M. Ferrenberg and R. H. Swendsen. Optimized Monte Carlo data analysis. *Phys. Rev. Lett.*, 63(12):1195, 1989.

[229] F. Zhu and G. Hummer. Convergence and error estimation in free energy calculations using the weighted histogram analysis method. *J. Comput. Chem.*, 33(4):453, 2012.

[230] V. A. Shneidman and G. M. Nita. On the critical cluster in the two-dimensional Ising model: Computer-assisted exact results. *J. Chem. Phys.*, 121(22):11232, 2004.

[231] M. Eden. A Two-dimensional Growth Process. In *Proceedings of the Fourth Berkeley Symposium on Mathematical Statistics and Probability, Volume 4: Contributions to Biology and Problems of Medicine*, pages 223–239, Berkeley, Calif., 1961. University of California Press.

[232] X.-M. Bai and M. Li. Calculation of solid-liquid interfacial free energy: A classical nucleation theory based approach. *J. Chem. Phys.*, 124(12):124707, 2006.

[233] B. Leimkuhler and C. Matthews. Rational Construction of Stochastic Numerical Methods for Molecular Sampling. *AMRX*, 2012.

[234] H. A. Kramers. Brownian motion in a field of force and the diffusion model of chemical reactions. *Physica*, 7(4):284, 1940.

[235] S. Cabuk and Springer M. D. Distribution of the quotient of noncentral normal random variables. *Commun. Stat. Theory Methods*, 19(3):1157, 1990.

[236] D. ÖKsoy and L. a Aroian. The quotient of two correlated normal variables with applications. *Commun. Stat. Simul. Comput.*, 23(1):223, 1994.

[237] Z. Drezner and G. O. Wesolowsky. On the computation of the bivariate normal integral. *J. Stat. Comput. Simul.*, 35(1-2):101, 1990.

[238] T. J. Sheskin. *Markov chains and decision processes for engineers and managers*. CRC Press, 2011.

[239] J. T. Berryman and T. Schilling. Sampling rare events in nonequilibrium and nonstationary systems. *J. Chem. Phys.*, 133(24):244101, 2010.

[240] N. B. Becker, R. J. Allen, and P. R. ten Wolde. Non-stationary forward flux sampling. *J. Chem. Phys.*, 136(17):174118, 2012.

[241] G. Mazenko, J. R. Banavar, and R. Gomer. Diffusion coefficients and the time auto-correlation function of density fluctuations. *Surf. Sci.*, 107(2):459, 1981.

[242] A. Fuliński. Transitions through fluctuating barrier: Role of asymmetry and memory. *J. Chem. Phys.*, 107(11):4225, 1997.

[243] W. Min and X. S. Xie. Kramers model with a power-law friction kernel: Dispersed kinetics and dynamic disorder of biochemical reactions. *Phys. Rev. E*, 73(1):010902, 2006.

[244] S. Chaudhury and B. J. Cherayil. Approximate first passage time distribution for barrier crossing in a double well under fractional Gaussian noise. *J. Chem. Phys.*, 125(11):114106, 2006.

[245] I. Goychuk and P. Hänggi. Anomalous Escape Governed by Thermal $1/f$ Noise. *Phys. Rev. Lett.*, 99(20):200601, 2007.